# On the pristine nature of cometary nuclei : coupled modeling of their thermal and dynamical evolution

Anastasios Gkotsinas

**THESE de DOCTORAT DE**
**L'UNIVERSITE CLAUDE BERNARD LYON 1**

**Ecole Doctorale n°52**
**Physique et Astrophysique de Lyon (PHAST)**

**Discipline** : Sciences de la Terre et de l'Univers

Soutenue publiquement le 21/09/2023, par :
**Anastasios GKOTSINAS**

# On the pristine nature of cometary nuclei : Coupled modeling of their thermal and dynamical evolution

---

Devant le jury composé de :

| | |
|---|---|
| **Cathy QUANTIN-NATAF**<br>Professeure des Universités, Université de Lyon 1 | Présidente |
| **Matthew M. KNIGHT**<br>Assistant Professor, U.S. Naval Academy | Rapporteur |
| **Emmanuel LELLOUCH**<br>Astronome, Observatoire de Paris - PSL | Rapporteur |
| **Cécile FERRARI**<br>Professeure des Universités, Université Paris Cité | Examinatrice |
| **Aurélie GUILBERT-LEPOUTRE**<br>Chargée de Recherche, CNRS | Directrice de thèse |
| **Sean N. RAYMOND**<br>Chargé de Recherche, CNRS | Co-Directeur de thèse |
| **Jean-François GONZALEZ**<br>Maître des Conférences, Université de Lyon 1 | Invité |

# Abstract

Comets are a population of small Solar System bodies, often described as the most primitive population in our Solar System, holding valuable information on its formation and evolution. Formed early, at the same time as the giant planets, in the outer parts of the protoplanetary disk and scattered outwards shortly after their formation towards distant and cold reservoirs, they are considered to have preserved their primordial composition and properties to a great extent.

However, the level of this primitive nature has started to be reevaluated recently, as a growing body of observational evidence and an important number of theoretical studies are suggesting the possibility of thermally-induced alterations before their return to the inner parts of the Solar System, where they are usually studied and observed.

In this context, our work aims to examine the level of the primitive nature of different cometary families in our Solar System. To do so, we developed a dedicated thermal evolution model, designed for an efficient coupling to $N$-body simulations, tracking the long-term orbital evolution of planetesimals, originating in the outer parts of the protoplanetary disk and evolving into planetary-crossing orbits after a prolonged stay in outer Solar System reservoirs.

Our results reveal the possibility of thermal processing, affecting mainly the primordial condensed hyper-volatile content and on a lesser extent the primordial moderately-volatile and amorphous water ice content, during the early phases of a comet's lifetime. A comparative study is indicating that long-period comets are expected to be the least altered population. Intense, yet sporadic, activity is also recorded in the planetary region, as comets return in the inner Solar System, compatible with the current observables on the Centaur population. These results indicate that the thermal evolution of cometary nuclei is inextricably related to their orbital evolution. They are also indicating that the cometary activity observed in the inner parts of the Solar System is very likely triggered from thermally processed subsurface layers, highlighting the necessity of considering the past evolutionary history of comets when interpreting the current observations in a broader context.

# Résumé

Les comètes sont une population de petits corps du Système Solaire souvent décrits comme les objets les plus primitifs de notre Système Solaire, détenant des informations précieuses sur sa formation et son évolution. Formées tôt, au même temps que les planètes géantes, dans les parties externes du disque protoplanétaire et dispersées vers l'extérieur peu après leur formation pour être stockées dans des réservoirs lointains et froids, elles sont considérées comme ayant largement conservé leurs propriétés et composition primordiales.

Cependant, le niveau de leur nature primitive a commencé à être revu, car un nombre croissant d'observables et d'études théoriques suggèrent la possibilité d'altérations thermiques avant leur retour dans les parties internes du Système Solaire où elles sont généralement étudiées et observées.

Dans ce contexte, ce travail vise à examiner le niveau de cette nature primitive pour les différentes familles cométaires de notre Système Solaire. Dans ce but, nous avons développé un modèle d'évolution thermique dédié, conçu pour un couplage efficace aux simulations $N$-corps capables de suivre l'évolution orbitale à long terme des planétésimaux, provenant des parties externes du disque protoplanétaire et évoluant vers des orbites dans la région planétaire, après un séjour prolongé dans les réservoirs extérieurs du système solaire.

Nos résultats révèlent la possibilité d'altérations thermiques, affectant principalement le contenu condensé primordial d'hyper-volatiles et dans un second lieu le contenu primordial modérément volatile et la glace d'eau amorphe, au cours des premières phases de la vie des comètes. Une étude comparative indique que les comètes à longue période devraient être la population la moins altérée. Une activité intense, mais sporadique, est également enregistrée dans la région des planètes géantes, alors que les comètes reviennent dans le Système Solaire interne, compatible avec les observables actuelles concernant la population de Centaures. Ces résultats indiquent que l'évolution thermique des noyaux cométaires est inextricablement liée à leur évolution orbitale. Ils indiquent également que l'activité cométaire observée dans les parties internes du Système Solaire provient très probablement de couches déjà altérées, soulignant la nécessité de prendre en compte l'histoire dynamique des comètes lors de l'interprétation des observations actuelles.

# Contents

# Symbols and Constants

**Table 1:** List of Symbols

| Symbol | Meaning/Description | Units (SI) |
|---|---|---|
| a | Semimajor axis of cometary orbits | au |
| $\mathcal{A}$ | Albedo | - |
| $a_{eq}$ | Equivalent semimajor axis | au |
| $a_J$ | Semimajor axis of Jupiter | au |
| c | Specific heat capacity | J $kg^{-1}$ $K^{-1}$ |
| d | Depth | m |
| D | Local diffusion coefficient | $m^2s^{-1}$ |
| $D_{eff}$ | Effective diffusion coefficient | $m^2s^{-1}$ |
| $d_H$ | Heliocentric distance | au |
| e | Eccentricity | - |
| $E$ | Complete elliptic integral of the second order | - |
| $E_a$ | Crystallization activation energy | J |
| $f$ | Solid to radiative component ratio | - |
| { | Numerical weighing factor | - |
| h | Hertz factor | - |
| J | Vapor flux | kg $m^{-2}$ $s^{-1}$ |
| m | Molecular mass | m |
| P | Orbital period | s |
| $P_{sat}$ | Saturation vapor pressure | Pa |
| q | Energy flux | W $m^{-2}$ |
| Q | Mass release rate | kg $m^{-2}$ $s^{-1}$ |
| R | Cometary nucleus' radius | m |
| $r_i$ | Radial distance of nodal points | m |
| $r_p$ | Average pore radius | m |
| $\bar{r}_t$ | Time-averaged radius | m |
| $\bar{r}_T$ | Effective thermal radius | m |
| $\bar{r}_{tF}$ | Time-averaged flux radius | m |
| $\bar{r}_\theta$ | True-anomaly-averaged radius | m |
| $\bar{r}_{\theta F}$ | True-anomaly-averaged flux radius | m |
| S | Energy sources and sinks | - |

| | | |
|---|---|---|
| T | Temperature | K |
| t | Time | s |
| $T_J$ | Tisserand parameter | - |
| V | Control volume | $m^3$ |
| $v_{th}$ | Thermal velocity | m $s^{-1}$ |
| X | Mass fraction of species | - |
| $\delta$ | Skin depth | m |
| $\Delta r_i$ | Control volume size | m |
| $\Delta t$ | Time step | s |
| $\epsilon$ | Emissivity | - |
| $\zeta$ | Local zenith angle | deg |
| $\theta$ | Azimuthal angle or true anomaly | deg or rad |
| $\kappa$ | Effective thermal conductivity | W $m^{-1}$ $K^{-1}$ |
| $\kappa_{rad}$ | Radiative conductivity | W $m^{-1}$ $K^{-1}$ |
| $\kappa_{solid}$ | Solid component conductivity | W $m^{-1}$ $K^{-1}$ |
| $\xi$ | Tortuosity | - |
| $\rho$ | Solid components' partial density | kg $m^{-3}$ |
| $\rho_{bulk}$ | Nucleus bulk density | kg $m^{-3}$ |
| $\rho^c$ | Solid components' compact density | kg $m^{-3}$ |
| $\tau$ | Crystallization timescale | s |
| $\tau_{gas}$ | Gas diffusion timescale | s |
| $\tau_{sub}$ | Sublimation timescale | s |
| $\tau_{th}$ | Thermal diffusion timescale | s |
| $\phi$ | Polar angle | deg |
| $\phi$ | Russel's correction factor | - |
| $\Phi$ | Radial energy flux | W $m^{-2}$ |
| $\psi$ | Porosity | - |

**Table 2:** List of Constants

| Constant | Symbol | Value | Units (SI) |
|---|---|---|---|
| Astronomical unit | au | $1.496 \times 10^{11}$ | m |
| Boltzmann constant | $k$ (or $k_B$) | $1.380649 \times 10^{23}$ | J K$\times 10^{-1}$ |
| Crystallization constant | $A$ | $9.54 \times 10^{-14}$ | s |
| Solar constant | $F_\odot$ or $L_\odot$ | 1360 | W $m^{-2}$ |
| Solar year | yr | $3.15576 \times 10^7$ | s |
| Universal gas constant | $R_g$ | 8.314462 | J $mol^{-1}$ $K^{-1}$ |

# Chapter 1

# Introduction

## 1.1 Comets: The Fossils of our Solar System

Comets are celestial objects known to mankind for thousands of years, with the earlier recorded sightings dating back to 1000 BC (Figure 1.1 and Festou et al., 2004). Yet, it is only in the last decades of the 20th century, that their true nature and significance in the understanding of our Solar System started to be revealed. Today, we know that these bright apparitions in the night sky are not some kind of God sign or a bad omen, but rather the manifestation of periodic activity from small-sized bodies orbiting around the Sun.

If we seek a somewhat more descriptive, but always simple, definition, S.A. Stern, the principal investigator of NASA's New Horizons space mission, described comets as a population of "*small bodies with sizes between 1-15 km, usually detected as they approach the Sun when their near-surface volatiles sublimate under the increasing insolation, in turn generating an extensive, highly visible gas-and-dust atmosphere, called the* coma [...] *the cometary nucleus is the source of the escaping gas and dust that make up both the coma, and its extension, called the* tail" (Stern, 2003).

Analyzing Stern's short definition, we note that the main feature of a comet is its nucleus. Despite thousands of years of observations, the first accurate prediction of its nature was given by American astronomer F.L. Whipple in 1950 (Whipple, 1950). Whipple, hypothesized the nucleus as a conglomerate of volatile ices, responsible for the observed activity, embedded in "*a matrix of meteoric material with little structural strength*". This description, known as the *dirty snowball*, was confirmed three decades later by the flyby of comet 1P/Halley by the Giotto mission (Reinhard, 1982), the first to closely observe a comet. Since then, five more missions have successfully approached and studied cometary nuclei, revealing a variety of irregular shapes and forms (see for example Figure 1.2). They confirmed the predictions for low tensile strength ($<$ 100 Pa) and established cometary

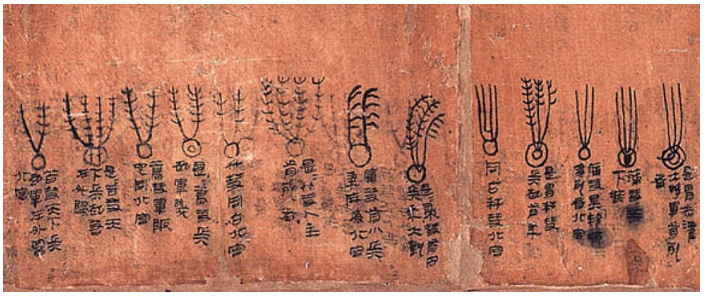

**Figure 1.1:** Part of manuscript on silk from the Early Western Han Dynasty (China, 206 to 168 BC), representing in total 29 comets, each with his own name, depicted with a head and a tail pointing away from the Sun (Credit: Hunan Museum)

.

nuclei as objects with low densities (∼600 kg $m^{-3}$) and very high porosities (∼70-80%) (Groussin et al., 2019). The detection of organic compounds on the nuclei (e.g. Kissel and Krueger, 1987) provided an explanation for their very dark surfaces, with average albedos[1] of 0.04 (Knight et al., 2023). The prevalence of the non-volatile/refractory over the ice component (e.g. Choukroun et al., 2020) led to the term *icy dirtball* (Keller, 1989), describing that the structure of cometary nuclei is primarily determined by the non-volatile component, unlike Whipple's initial assumption.

When cometary nuclei approach the Sun, an intense activity is developed as the embedded ice components heat up and sublimate, i.e. pass from the solid to the gas phase directly, dragging along with them dust particles from the surface. This activity is the source of the two other characteristic features of comets: their comae and their tails. Comae can be described as tenuous atmospheres surrounding cometary nuclei, similar to the outer layers of planetary atmospheres, extending at large distances of the order of thousands of kilometers (Rodgers et al., 2004). Due to the revolution of nuclei around the Sun and the interactions between the gas and dust particles with the solar wind, tail-like features can be produced as presented in Figure 1.3. Three tails have been identified so far around comets: (a) a dust tail produced by the dust particles entrained by gas drag and further pushed away by the solar radiation pressure, typically extending at distances of the order of $10^4$ km reaching $10^8$ km in some cases (Fulle, 2004), (b) an ion tail composed of escaping particles ionized by solar radiation and forming this narrow structure due to interactions with the solar wind (Behar et al., 2018) and (c) a sodium (Na) tail for which the origins are still uncertain and which is rarely detected (Cremonese et al., 1997; Wilson et al., 1998; Cremonese

[1] A physical quantity measuring the fraction of the incident radiation scattered back into space over all angles and wavelengths (Knight et al., 2023)

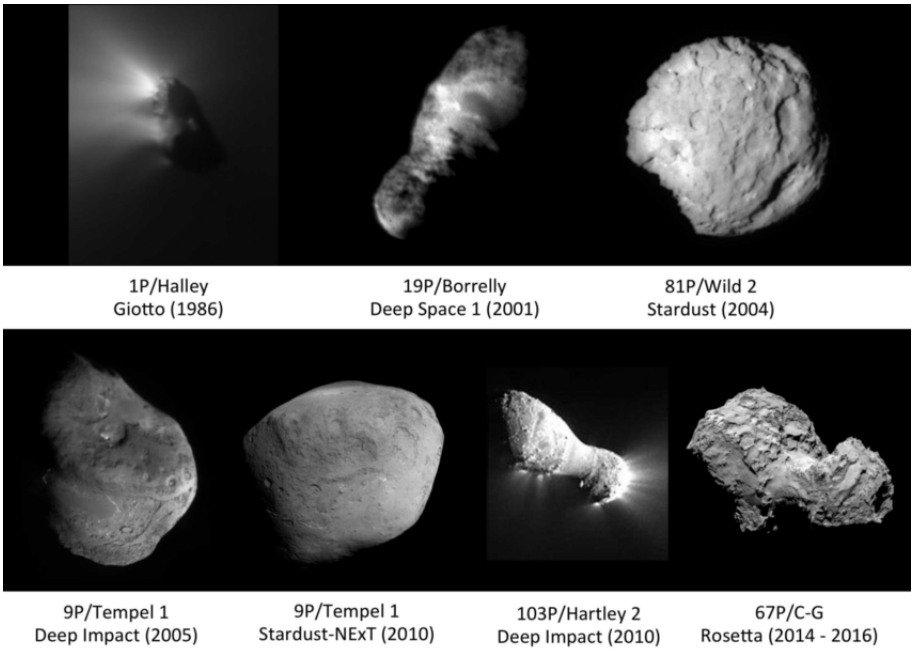


**Figure 1.2:** Images of six cometary nuclei visited by spacecraft: 1P/ Halley (credit ESA-MPAE), 19P/Borrelly (credit NASA/ JPL), 81P/ Wild 2 (credit NASA/JPL), 9P/ Tempel 1 (credit NASA/ JPL/UMD and NASA/JPL/Caltech-Cornell), 103P/Hartley 2 (credit NASA/ JPL/ UMD), and 67P/Churyumov-Gerasimenko (Credit: Groussin et al. (2019))

.

et al., 2002).

Aside from their spectacular apparitions on the night skies over the centuries, comets have drawn the attention of the scientific community over the last decades due to their assumed primitive nature. The current thinking suggests an early formation for comets, at the same time as the giant planets, of which they are often considered to be the building blocks, on the outer parts of the planetesimal disk. Scattered away at outer Solar System reservoirs, where they stayed at very low temperatures for timescales comparable to the Solar System's age, they are considered to have remained relatively unaltered, conserving almost intact valuable information from the initial moments of the Solar System. As they return to inner Solar System[2] where they are usually detected and observed, this information can finally become available and are expected to clarify numerous aspects regarding the primitive Solar System, such as its initial composition, its physical, chemical and dynamical evolution, the formation of the giant planets (e.g. Levison

[2]Here the terms inner and outer Solar System are used to describe the area within and outside the orbit of Neptune respectively.

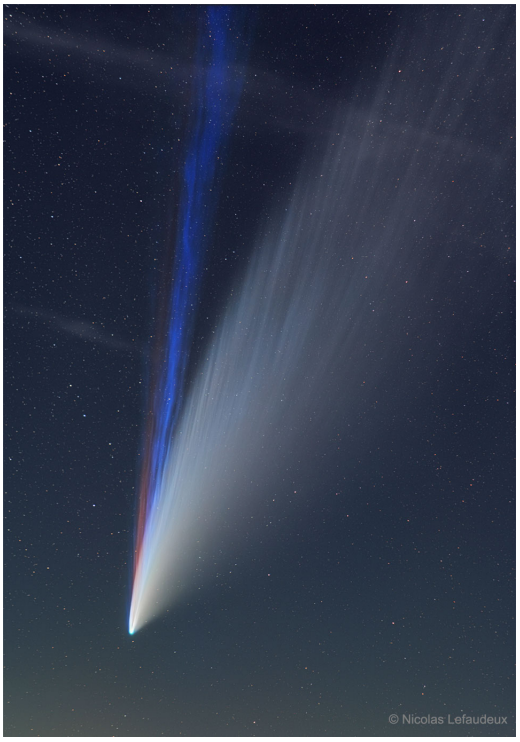


**Figure 1.3:** The three tails of comet C/2020 F3 (NEOWISE), as captured in July 2020 from Bretagne, France: (a) a peculiar wavy dust tail in white, (b) an ion tail pointing directly away from the Sun in blue and (c) a sodium tail in red (Credit: Nicolas Lefaudeux, 2020).

and Duncan, 1994; Filacchione et al., 2019; Weissman et al., 2020; Wierzchos and Womack, 2020), or even shed some light on the mystery surrounding the delivery of water on Earth (e.g. Raymond and Izidoro, 2017).

However, this 'primitiveness' concept has been challenged by a rising number of studies these last years. Indeed, a growing body of evidence, both from theoretical studies (e.g. Davidsson, 2021; Kral et al., 2021; Kaib, 2022; Lisse et al., 2022; Parhi and Prialnik, 2023) and observations (e.g. Hui et al., 2019; Farnham et al., 2021; Jewitt et al., 2021; Zhang et al., 2022) are suggesting that thermal processing and therefore activity and alterations on cometary nuclei occur from the early phases of their existence and at greater distances from the Sun, when and where they were previously expected to remain unaltered. We have to make clear that none of these studies, at least to our understanding, seeks to defy the status of comets as one of the most pristine populations in the Solar System. Nevertheless, they all point to the necessity of a re-assessment of the primitiveness level, in order to better interpret current observations and improve theoretical models and predictions.

It is this necessity of reevaluating the degree of the primitive nature of comets that motivates this work. To do so, we propose a novel theoretical approach, allowing the examination of thermal processing on long timescales for a large number of simulated cometary nuclei, providing the necessary background for a first-order assessment of the primitiveness of cometary populations on our Solar System. However, before developing our method, it seems necessary to give an overview of the current considerations and proposed approaches regarding comets and their evolution on the Solar System, in order to place this study on the current context.

## 1.2 Cometary Nuclei Formation

The formation of the progenitors of what we identify today as cometary nuclei, the *planetesimals*, in the protoplanetary disk, the disk of gas and dust that formed after the collapse of the solar nebula, is probably the least understood stage in planetary evolution (e.g. Chiang and Youdin, 2010). Despite a good understanding of the mechanisms leading to the creation of sub-meter structures from grains (e.g. Blum et al., 2022) and of the mechanisms acting on km-sized objects, leading to the formation of planets (e.g. Raymond et al., 2009), the intermediate step linking these sub-meter structures to the km-sized bodies (i.e. the planetesimals), remains open to interpretations.

We can identify two predominant scenarios for the formation of comet nuclei, both supported by recent observations by the Rosetta mission (e.g Davidsson et al., 2016; Blum et al., 2017), although neither is conclusive: (a) hierarchical coagulation (e.g. Weidenschilling et al., 1997) and (b) gravitational instabilities (e.g. Cuzzi et al., 2008). The first mechanism considers collisions between small aggregates driven by differential motions due to gas drag. These collisions form clumps that can grow further through inelastic collisions, during which the larger aggregates sweep up smaller ones in their vicinity, hence the term *hierarchical*, to form km-sized objects (Weidenschilling et al., 1997; Cuzzi et al., 2008). In the gravitational instability scenario, particle concentrations collapse when their density exceeds a certain threshold, known as the Roche density (Goldreich and Ward, 1973), to form km-sized objects, with sizes ranging from 10 to 1000 km, increasing with the distance from the Sun (Cuzzi et al., 2010). For the creation of these particle concentrations a variety of mechanisms have been proposed: weak turbulences in the nebula (Cuzzi et al., 2008), streaming instabilities due to the relative motion between the gas and the solid component in the disk (Youdin and Goodman, 2005), large vortices created by radial buoyancy in the solar nebula (Raettig et al., 2015), concentrations of drifting dust at pressure bumps (Drążkowska and Dullemond, 2014; Drążkowska et al., 2016; Izidoro et al., 2021) as well as sublimation and recondensation of silicates (Morbidelli et al., 2022). These processes are very likely to be key

in the pile-up of dust particles triggering instabilities in the disk, such as the streaming instability (Johansen and Youdin, 2007; Simon et al., 2016; Yang et al., 2017). The possibility of a direct passage from sub-meter structures, to km-sized objects invoked by the gravitational instability scenario, lead to an assumption for planetesimals with initial sizes of 100 km or more, with the smaller ones being the result of collisional fragmentation (Morbidelli et al., 2009). However, this scenario have been contested by following studies (Weidenschilling, 2011; Davidsson et al., 2016), as it produces objects with incompatible physical properties (e.g. elevated densities of the order of 600-1000 kg $m^{-3}$, low porosities ($\sim$40%) and high tensile strength (1-10 MPa)) to those observed on cometary nuclei and especially on comet 67P, where a low bulk density (535 kg $m^{-3}$), a high porosity ($\sim$70%) and a low tensile strength ($<$ 0.15 kPa) were measured (Davidsson et al., 2016).

Despite the uncertainties surrounding their formation, a consensus regarding their place of formation, on the outer parts of the protoplanetary disk, seems to have been established (Dones et al., 2015). Initially considered to have formed at distances between 15 and 30 au (e.g. Levison and Morbidelli, 2003), the latest studies constrain this range furthermore to 20-30 au (e.g. Nesvorný, 2015). Interestingly, this area of the protoplanetary disk is beyond the distances at which the condensation of volatile species becomes possible (Lecar et al., 2006; Dodson-Robinson et al., 2009), allowing the incorporation of volatiles, even those of high volatility, in the planetesimals.

## 1.3 Orbital evolution

Once planetesimals form, a complex journey begins, marked by a series of gravitational interactions with the giant planets, bringing them to their current positions in the outskirts of the Solar System. This journey is intimately related to the evolutionary mechanisms that led our Solar System from the protoplanetary disk to its current orbital architecture.

### 1.3.1 Planetary Migration

In the last decades, many different works have tried to resolve the mystery of our Solar System's formation (e.g Tsiganis et al., 2005; Walsh et al., 2011; Levison et al., 2011; Nesvorný and Morbidelli, 2012). All of them considered that the Solar System's giant planets underwent a dynamical instability, forcing Uranus and Neptune to migrate outwards from their initial positions. It was during this migration that the planetesimals were scattered all over the Solar System, populating, among other endings, their current source reservoirs (e.g Gomes, 2003; Brasser and Morbidelli, 2013).

Modeling the nature and the timeline of this dynamical instability was the main concern of these studies. Thommes et al. (1999) were the first to propose an outwards migration for Uranus and Neptune due to interactions

with the other giant planets, inspired from the failure of previous models to form these planets in their actual positions. The *Nice* model (Tsiganis et al., 2005), the most prominent work at the time, managed to successfully reproduce the giant planets' orbital architecture by considering that they were initially in a compact configuration at distances between 5 and 14 au. Due to gravitational interactions with the planetesimals, Jupiter and Saturn drifted, with Jupiter moving slightly inwards and Saturn, Uranus and Neptune outwards. During this migration, the giant planets dispersed the planetesimals remaining in the protoplanetary disk, forming the cometary source reservoirs as we know them today. It's worth noting at this point, that most of the planetesimals were ejected from the Solar System ($\simeq$90%), a small percentage ($\simeq$7-10%) was captured in the Oort Cloud (Brasser and Morbidelli, 2013; Raymond et al., 2020b) and a tiny fraction ($<$1%) was captured in the Kuiper Belt and the scattered disk, or other populations of small Solar System bodies (Nesvorný, 2018), such as the Jupiter Trojans (Morbidelli et al., 2005), the irregular satellites of the giant planets (Nesvorný et al., 2007) or the asteroids located between Mars and Jupiter (Levison et al., 2009).

Other scenarios for the migration of the giant planets have been proposed as well. For example, Walsh et al. (2011), demonstrated that some of the characteristic features of the inner Solar System, in particular the low masses of Mars and the asteroid belt, as well as the presence of ice in small bodies occupying the outer parts of the latter, can be better explained if the migration took place in two phases. A first one where the giant planets migrate inwards, with Jupiter and Saturn reaching distances of approximately 1.5 and 2 au respectively and a second where they reverse (or '*tack*') and start moving outwards to reach their current positions after 100 kyr from the dynamical instability.

Several studies followed the original *Nice* model, attempting to address a variety of issues, such as the arbitrary initial conditions or the effects on the terrestrial planets (e.g. Morbidelli et al., 2007; Brasser et al., 2009; Levison et al., 2011; Nesvorný and Morbidelli, 2012). Morbidelli et al. (2007) proposed an initial multi-resonant placement[3] which breaks down due to interactions between the planets and the planetesimal disk, leading to a late dynamical instability. Nesvorný and Morbidelli (2012) examined the possibility of more planets in the initial setup, testing configurations with four, five and six giant planets. They concluded that a scenario with an additional ice giant, ejected from the Solar System by Jupiter during migration, provoking a discontinuity in the migration, manages to better reproduce the current orbits of the giant planets.

[3] A state occuring when the ratio of the orbital periods of two or more bodies is close to the ratio of small integers. For example, a 3:2 motion resonance, such as the one Neptune and Pluto are in, means that Pluto will complete two orbits at the time Neptune completes three.

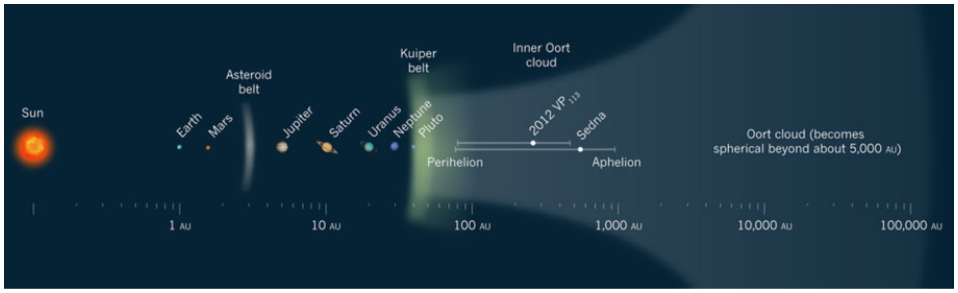


**Figure 1.4:** Schematic representation of the current considerations on the structure and the populations of the inner and outer parts of the Solar System. We can identify, aside from the terrestrial and the giant planets, the asteroid belt at distances between 2 and 3.5 au, the Kuiper Belt, starting beyond the orbit of Neptune, Pluto and the inner and outer parts of the Oort Cloud. We also note the orbits of the two first objects considered to reside in the latter: Sedna (Brown et al., 2004) and 2012 $VP_{113}$ (Trujillo and Sheppard, 2014). (Credit: Schwamb (2014) adapted from Stern (2003)).

Another crucial issue was the timescale of this dynamical instability. Initially it was considered to take place relatively late, after ∼700 Myr (Gomes et al., 2005; Levison et al., 2011), compatible with the timeline of the Late Heavy Bombardment, an hypothesized event thought to have occurred 3.9 billion years ago, during which a significant amount of small bodies collided with the terrestrial planets (Tera et al., 1974; Wetherill, 1975; Bottke and Norman, 2017). However, several studies showed that sampling biases are probably the reason for the Late Heavy Bombardment model (Boehnke and Harrison, 2016; Zellner, 2017). The current thinking suggests an earlier occurrence, no later than 50 Myr after the dispersal of the protosolar nebula, although the exact timing is still a matter of a debate. Some studies advocate for an instability at the moment of the gas disk dissipation and while the rocky planets were still forming (e.g. Clement et al., 2018; Liu et al., 2022), while others propose a delayed event by 10-50 Myr (e.g. Nesvorný, 2015).

### 1.3.2 Reservoir Formation and Implantation Mechanisms

Regardless of the considerations surrounding the migration scenario, the fate of the planetesimals seems to be widely accepted. If they are not completely ejected from the Solar System (e.g Charnoz and Morbidelli, 2003; Raymond et al., 2020b), fall into the Sun or one of planets (e.g. Gomes et al., 2005), they end up in the outskirts of the Solar System, forming two cometary reservoirs, known as the Edgeworth-Kuiper Belt (Edgeworth, 1943; Kuiper, 1951) and the Oort Cloud (Oort, 1950).

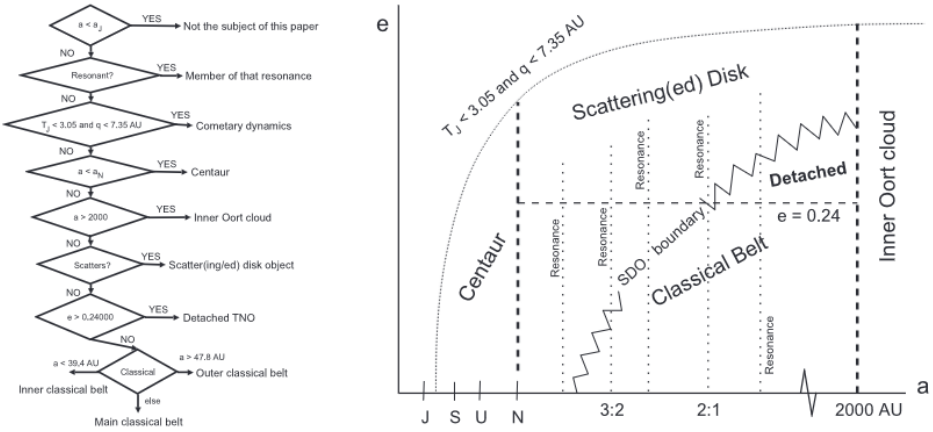


**Figure 1.5:** *Left panel:* Schematic flow diagram for the Transneptunian region nomenclature. *Right panel:* Schematic not-in-scale representation of the giant-planet and Transneptunian region, until the Inner Oort Cloud, at the a-e plane, with the different small-body populations (Credit: Gladman et al. (2008)).

### Edgeworth-Kuiper Belt

The presence of a large population of small bodies beyond the orbit of Neptune was first hypothesized by two astronomers, K.E. Edgeworth (Edgeworth, 1943; Edgeworth, 1949) and G. Kuiper (Kuiper, 1951) in the late forties, early fifties. Its existence was confirmed four decades later, in 1992, by the detection of the first member of this population of Trans-Neptunian Objects (TNOs), 1992 $QB_1$, by astronomers D. Jewitt and J. Luu (Jewitt and Luu, 1993). It is considered to extend at distances between 30 and 50 au from the Sun with its outer limit defined by orbits at the 2:1 resonance with that of Neptune (e.g. Allen et al., 2001). Traditionally, small bodies in the Kuiper Belt are considered to be on relatively stable orbits that do not cross the orbit of Neptune, allowing them to remain in the reservoir on timescales comparable to the age of the Solar System (Duncan et al., 1995). Subsequent studies proposed an extension to the Kuiper Belt, starting at distances larger than 50 au, known as the scattered disk. This population unlike the Kuper Belt, contains objects in unstable orbits, as their perihelia cross the orbit of Neptune (Duncan and Levison, 1997) and are expected to feed the inner parts of the Solar System with comets.

Advances in observational capabilities and a rise in the discoveries of TNOs with a diversity in orbital characteristics, led to a more complex and more comprehensive, description of the populations residing in the Trans-Neptunian region. Today we can identify four main subpopulations (Figure 1.5), classified by their dynamical properties (Gladman et al., 2008):

- **Resonant populations:** Containing TNOs trapped in a mean-motion resonance (MMR) with Neptune. A variety of objects have been detected to occupy at least 10 different resonances (3:2 (Plutinos), 5:2, 2:1 (Twotinos), 3:1, 5:1, 4:3, 5:3, 7:3, 5:4, and 7:4) (see also Gladman et al., 2012). These populations despite having perihelia close to the orbit of Neptune, are considered to be in stable orbits, as the resonances help them avoid close encounters with the planet.

- **Scattered Disk Objects (SDOs)**: Defined as objects that are *scattering actively off Neptune*, meaning that they are in unstable orbits with large eccentricities and long orbital periods, crossing that of Neptune. Interactions with Neptune, tend to remove them from the transneptunian area, and force them back in the giant-planet region (Duncan and Levison, 1997). More concrete definitions, propose to consider as SDOs all objects with q $>$ 30 au (Brasser and Morbidelli, 2013), while others consider larger perihelia (q $>$ 33 au) and long orbits (a $>$ 50 au) (Volk and Malhotra, 2008).

- **Detached Objects**: Objects in orbits with large eccentricities (e $>$ 0.24) and semimajor axis below 2000 au, so that they are not considerably influenced by forces external to the Solar System. These objects have perihelia well outside the orbit of Neptune (q $>$ 38 au) (Emel'yanenko et al., 2003) and they do not interact as strongly with it, hence the *detached* characterization.

- **Classical Belt Objects**: Objects characterized by low eccentricity orbits (e $<$ 0.24) and semimajor axis roughly constrained by the 3:2 and the 2:1 MMR, although some lightly populated orbits outside of these limits are also considered to belong to this group. This population can be roughly said to contain all low eccentricity non-resonant TNOs. Several subcategories for this population have been proposed. For example a classification based on the semimajor axis divides the Classical Belt to:

  - *Inner* for orbits with semimajor axis a $<$ 39.4 au.
  - *Outer* for orbits with semimajor axis a $>$ 48.4 au.
  - *Main* for orbits with semimajor axis in between.

  A more prominent subdivision of the Classical Belt is based on the inclination. Brown (2001), identified two distinct Classical Belt populations, one of very low inclinations i $<$ 5°, known as the *cold* classical and one with a wide range of inclinations above 5°, known as the *hot* classical.

**From the Protoplanetary Disk to the Edgeworth-Kuiper Belt:** An implantation mechanism was proposed by Gomes (2003), based on an initial proposition by Malhotra (1993) and Malhotra (1995), to describe how the planetesimals from the outer planetesimal disk end up in the Trans-Neptunian region. This mechanism can be reduced to the three following steps (see also Nesvorný, 2015):

1. The planetesimals are scattered outwards as a series of close encounters[4] with the migrating Neptune result in an excitation of their inclinations and eccentricities. The planetesimals are placed in orbits similar to the ones described for the SDOs, with semimajor axis a $>$ 30 au and perihelia below or very close to the orbit of Neptune.

2. The planetesimals are captured in one of the MMRs described previously, at orbits with high libration amplitudes. A variety of complex secular dynamic effects (such as large-amplitude Kozai oscillations) act to reduce their eccentricities. This eccentricity decrease allows the planetesimals (which we can now call TNOs) to decouple their orbit from the gravitational influence of Neptune.

3. As the migration of Neptune continues, the planetesimals have two options: either move into more stable orbits inside the resonance with decreased libration amplitudes or to escape it and move into stable orbits with high inclination and perihelia above 35 au (see also Levison and Duncan, 1997; Levison and Morbidelli, 2003).

Nesvorný (2015) demonstrated that although this implantation mechanism was proposed before the Nice model and its follow-up works, that changed the view regarding Neptune's migration, it is still a valid mechanism, permitting the population of the Trans-Neptunian region (see also Kaib and Sheppard, 2016; Nesvorný et al., 2016). However, it should be noted that the implantation efficiency is quite low, of the order of $10^{-3}$, meaning that only a few of the scattered planetesimals will be lucky enough to reach the Kuiper Belt, while most of the others will be ejected from the Solar System (e.g. Nesvorný, 2015; Nesvorný et al., 2017; Raymond et al., 2020b).

### The Oort Cloud

As in the case of the Kuiper Belt, the existence of the Oort Cloud was initially hypothesized by the theoretical works of J. Oort in 1950 (Oort, 1950). In his works, Oort observed a spike on the reciprocal semimajor axis (1/a),

[4] An encounter is considered to be "close" when a planetesimal enters a planet's Hill sphere, a quantity defining the area where the gravitational influence of the planet is stronger than the influence of the Sun

also known as binding or orbital energy, a measure of how strongly an object is bound to the Sun, around values of $\sim 10^{-4}$ au$^{-1}$, on a small sample of comets with long orbital periods and large semimajor axis. He concluded that these long-period comets should arrive from "*a huge cloud of comets extending from a distance a = 10000 au to distances of at least 150000 au* ". Unlike the Kuiper Belt its existence remains theoretical to this day as no direct observation of the Oort Cloud has been made so far (Portegies Zwart et al., 2021), despite the recent discoveries of the first objects in its inner (Sedna (Brown et al., 2004), 2012 $VP_{113}$ (Trujillo and Sheppard, 2014), 2015 $TG_{387}$ (Sheppard et al., 2019)) and outer parts (2014 $FE_{72}$ (Sheppard and Trujillo, 2016)).

Similarly to the subpopulations of the Kuiper Belt, two main substructures can be identified in the Oort Cloud, separated by the Oort spike at $10^{-4}$ au$^{-1}$ (or a$\simeq$10000 au) (Figure 1.6) : (a) a bound region, where the orbital energy is above zero, containing comets bound to the Sun and (b) an unbound region, where the orbital energy is negative and comets are mainly on hyperbolic orbits that allow them to escape the Solar System (Dones et al., 2004). Comets on orbits with semimajor axis above the Oort spike (a $>$ 10000 au) are considered to be *dynamically new*, meaning that they are statistically more likely to visit the planetary region for the first time, while those below the spike are considered to be *dynamically old* or *returning* comets, meaning that they have probably visited at least once the planetary region. We have to note here that recent studies have pushed this limit further away at 25000 au or even 50000 au (Dybczyński and Królikowska, 2015; Królikowska and Dybczyński, 2017; Vokrouhlický et al., 2019).

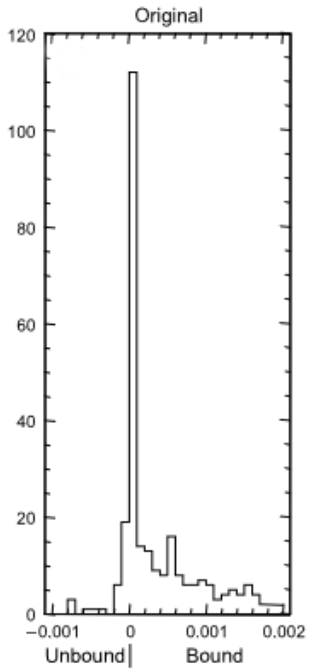


**Figure 1.6:** Distribution of the 'original' orbital energies (au$^{-1}$) (see below) for a sample of 386 comets. The Oort spike and the separation between *bound* and *unbound* populations is evident at $10^{-4}$ au$^{-1}$ (Credit: Dones et al. (2004)).

Duncan et al. (1987), placed the inner edge of the Oort Cloud at approximately 3000 au, and proposed a division into classical or Outer Oort Cloud (a $>$ 20000 au) and Inner or Hills[5] Oort

[5]Named after astronomer J.G. Hills who first proposed a similar separation in 1981

Cloud (a $<$ 20000 au), with the former being less populated and therefore less massive, by a factor of five. The Inner Oort Cloud is harder to populate as galactic torques are too weak to circularize the orbits of planetesimals with semimajor axis lower than $\sim 10^4$. However if the planetesimals were scattered during the stellar cluster phase, then it might be much more massive (Tremaine, 1993; Wyatt et al., 2017). Fouchard et al. (2017) proposed a relatively different separation based on the governing forces acting on the Oort Cloud objects: (a) an inner part governed by planetary perturbations and (b) an outer part governed by perturbations by passing stars and galactic tides. They placed their transition zone from the one regime to the other at 1000-2000 au, slightly closer to the Sun compared to the distance proposed by Duncan et al. (1987).

**From the Protoplanetary Disk to the Oort Cloud:** A mechanism similar to the one placing planetesimals in the Kuiper Belt is responsible for populating the Oort Cloud. A series of close encounters with the giant planets in the planetesimal disk, led to an increase of the orbital energy (i.e. the semimajor axis and the eccentricity) of planetesimals while their perihelion distance remained relatively stable at the giant planet region. This increase in the orbital energy in most cases continued until the planetesimals became unbound from the Sun, escaping the Solar System to become interstellar objects, which was the fate of most planetesimals orbiting close to Jupiter and Saturn (Dones et al., 2015). However galactic tides, torques created by changes in the galaxy's gravitational field, mainly of the vertical density gradient (Heisler and Tremaine, 1986; Duncan et al., 1987; Kaib and Quinn, 2008) or random approaches of a passing star (Pfalzner et al., 2018), can act as stabilizing factors and inverse the above procedure, by increasing the planetesimals' perihelion distance instead of their orbital size (i.e. the semimajor axis). This allowed them to reach stable orbits in the Oort Cloud (Duncan et al., 1987; Dones et al., 2015). This stabilizing condition helped astronomers to constrain the size of the Oort Cloud. By imposing that the timescale of the changes in the semimajor axis must be comparable to the timescale of the changes in the perihelion distance provoked by the passage of a star, Duncan et al. (1987) and Tremaine (1993) estimated the Oort Cloud to extend at distances $\sim$10000-100000 au. As the interest for the Oort Cloud grew over the years, additional mechanisms contributing on its formation and structure were proposed such as the gravitational scattering of planetesimals on the protoplanetary disk by other stars on the Sun's birth cluster (e.g. Fernández, 1997; Kaib and Quinn, 2008; Brasser et al., 2012) or galactic tides affecting the planetesimals during the radial migration of the Solar System within the Galaxy (e.g. Kaib et al., 2011; Portegies Zwart et al., 2021). Levison et al. (2010) considered also the possibility of cap-

(Hills, 1981).

turing comets originating from other stars in the Sun's birth cluster, in the Oort Cloud. The implantation efficiency in the Oort Cloud is also quite small, of the order of 0.05-0.07 (e.g. Brasser and Morbidelli, 2013; Raymond et al., 2020b), which is an order of magnitude higher than for the Kuiper Belt, suggesting a higher probability for a planetesimal to end up in the Oort Cloud than the Kuiper Belt.

### 1.3.3 Return to the Inner Solar System

Even if the scattered planetesimals find their way to stable orbits in the Kuiper Belt, the scattered disk or the Oort Cloud, a variety of destabilizing mechanisms can act to force them back into the inner Solar System.

TNOs revolving in high-eccentricity, unstable orbits in the scattered disk, but also TNOs in the Classical Belt and rarely some Resonant TNOs managing to escape the MMRs, can gravitationally interact with the giant planets and enter into a regime of chaotic motions, gradually reducing their perihelion distance until they reach low inclination Neptune-crossing orbits, in a mechanism very similar to that described previously for the implantation. This mechanism is supplying the inner Solar System with objects, that upon their return are characterized by low inclinations and relatively short orbital periods (P $<$ 200 yr), historically known as the Short-period Comets (SPCs) (Duncan et al., 1988; Torbett, 1989; Duncan et al., 1995).

Objects in the Oort Cloud, as was implied by Fouchard's et al. (2017) proposed structure, can be destabilized by planetary perturbations if they are in the inner Oort Cloud (see also Wiegert and Tremaine, 1999; Kaib and Quinn, 2009) or from galactic tides and passing stars if they are in the outer Oort Cloud (e.g. Rickman et al., 2008; Fouchard et al., 2011; Wysoczańska et al., 2020). As with SDOs, the return mechanism can be considered to be the inverse process of the one that brought them there. The gravitational perturbations tend to decrease their perihelion distances while the semimajor axis remains nearly constant. Progressively, the objects will be in planetary-crossing orbits provoking random changes in their semimajor axis and a drift towards the planetary region (e.g. Duncan et al., 1987; Kaib and Quinn, 2009). This procedure is feeding the inner Solar System, with comets characterized by an isotropic distribution of their inclinations and long orbital periods (P $>$200 yr), historically known as the Long-Period Comets (LPCs). Interestingly, this return procedure can take place in two different ways: by a slow and progressive decrease of the perihelion distance, implying several passages through the planetary region, or by an abrupt decrease bringing the comet on orbits with very low perihelia (q $<$ 5 au), without any previous passage in the planetary area. LPCs of the first type are known as *creepers*, and the ones arriving in the second way as *jumpers* (Kaib and Quinn, 2009; Fouchard et al., 2017; Vokrouhlický et al., 2019). A similar distinction can be made for SPCs, as the delivery can be rather

hasty or delayed if the comet is trapped between Saturn and Neptune, with times reaching the order of Gyr (Di Sisto and Brunini, 2007).

### 1.3.4 Inner Solar System Cometary Populations

As they return to the inner Solar System, objects that we initially called '*planetesimals*', then '*TNOs*' (or *KBOs*, *SDOs* and *Oort-Cloud Objects*) when they were located in the outer Solar System, can finally be called *comets*.

As mentioned in the previous section, the historical division of comets is based on their orbital period. Comets with with P $<$ 200 yr, are known as the Short-period Comets and comets with P $>$ 200 yr are called Long-period Comets. However, as noted in Nesvorný et al. (2017), this orbital period of 200 yr does not hold any particular significance and it was used only because it guarantees at least one perihelion passage in modern times.

In the same historical context, SPCs were divided in two populations:

- The **Jupiter-family Comets (JFCs):** a population with low inclinations (i $<$ 30°) and short orbital periods (P $<$ 20 yr), implying semimajor axis a $<$ 7.4 au. They owe their name to the strong influence of Jupiter, which they encounter at low velocities, on their orbits (Di Sisto et al., 2009; Dones et al., 2015; Nesvorný et al., 2017).
- The **Halley-type Comets (HTCs):** a population with more dispersed inclinations and orbital periods between 20 and 200 yr, implying semimajor axis between 7.4 au and 34.2 au (Dones et al., 2015). They were named after comet 1P/Halley, the first recognized member of this particular population.

This historical classification can sometimes be confusing, as these two subpopulations often overlap in the orbital parameter space (Nesvorný et al., 2017). Levison (1996), inspired by a classification proposition by Carusi et al. (1995), proposed an alternative taxonomy, based on the Tisserand parameter with respect to Jupiter, which conveniently combines the orbital period and the inclination into a single expression. It is defined as:

$$T_J = \frac{a_J}{a} + 2\sqrt{(1-e^2)\frac{a}{a_J}}\cos i \tag{1.1}$$

where $a_J$ is Jupiter's semimajor axis, and $a, e, i$ the comet's semimajor axis, eccentricity and inclination respectively. This parameter is an approximation of the Jacobi constant, an integral of the motion in the circular restricted three-body motion, which also provides a measure of the relative velocity between a comet and Jupiter during close encounters $v_{rel} \propto \sqrt{3 - T_J}$. This implies that comets with $T_J$ just below three can have low-velocity encounters with Jupiter. It has the advantage of being globally conserved over a

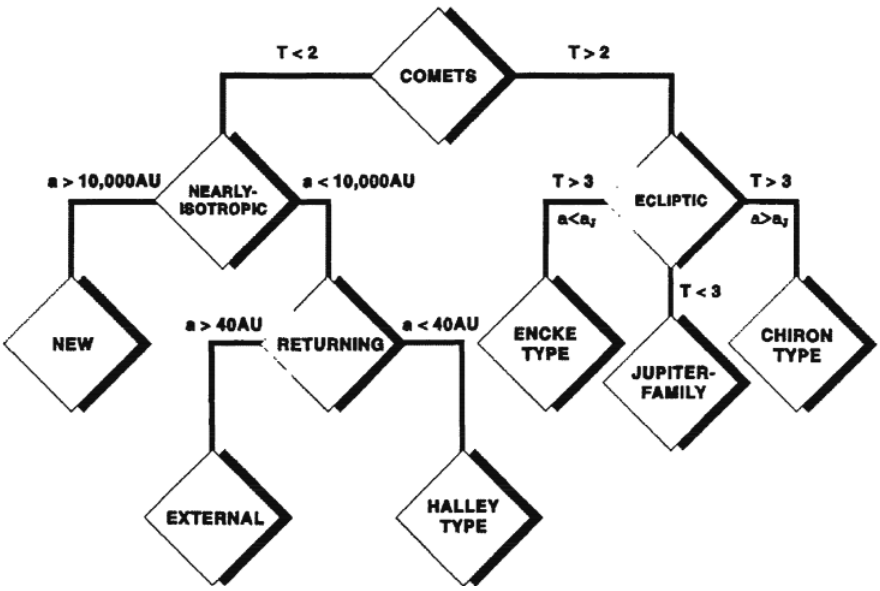


**Figure 1.7:** Levison (1996) proposed cometary taxonomy, based on the Tisserand parameter with respect to Jupiter. (Source: Levison (1996)).

comet's orbital evolution, despite small fluctuations due to Jupiter's eccentricity, unlike the orbital period which can change significantly.

Levison's (1996) taxonomy suggests the separation of comets in two main classes (see also Figure 1.7 adapted from the original publication):

1. **The Ecliptic Comets (ECs) ($T_J > 2$)**: Comets originating from low-inclination reservoirs such as the scattered disk and the Kuiper Belt, hence the *ecliptic* characterization. This class contains most of the comets previously known as SPCs. It is further divided in three subclasses:

    - The Jupiter-family Comets ($2 < T_J < 3$): A subclass that contains comets dynamically controlled by Jupiter. Although the typical upper limit for this subclass is 3, values above three are also possible as Jupiter's orbit is also slightly eccentric. The highest $T_J$ value for a JFC is recorded for comet 133P/Elst-Pizarro with 3.184 (Di Sisto et al., 2010).
    - The Chiron-type Comets ($T_J > 3$ and $a > a_J$): A subclass commonly known as Centaurs, named by Levison after its first identified member at the time. Unlike JFCs, their orbits do not cross that of Jupiter and they orbit in the giant planet area. $T_J$ values for Centaurs can extend well above 4.5 as in the case of Centaur (2015 BH518) where $T_J = 4.7$ according to JPL's Small-Body

Database Search Engine[6].

- The Encke-type Comets ($T_J > 3$ and $a < a_J$): Named after the first identified member of this subclass, comet 2P/Encke. Comets in this class have their entire orbit within that of Jupiter, implying very short orbital periods. The highest value for an Encke-type Comet is recorded for C/2020 P4-B with 5.43 according to JPL's Small-Body Database Search Engine, with the majority of values being constrained between 3.01 and 3.2.

2. **The Nearly-isotropic Comets (NICs) ($T_J < 2$)**: A name chosen to designate the isotropic distribution of the inclinations for the comets in this class. This distribution suggests an origin from an isotropic or spherically distributed parent population such as the Oort Cloud. With a few differences, we can say that it is the class that replaced comets previously known as LPCs (although the term LPCs is still widely used). Two further subclasses were proposed: *New* and *Returning*, holding the same significance as before. However a further subdivision for the Returning subclass was proposed. Comets with semimajor axis low enough to be trapped in a MMR with a giant planet are designated as *Halley-type Comets* and those with semimajor axis larger than this threshold as *Externals*. The threshold between these two subclasses was set to be Pluto's semimajor axis at 40 au, at the time, the most distant object in a MMR (3:2 with Neptune).

We should note that variations in the definitions for the aforementioned subclasses are quite frequent. We described previously the current thinking about the boundary between *dynamically new* and *returning* LPCs. We can also cite small differences in the definition of the Centaur population, which are commonly defined to be objects with semimajor axis larger than that of Jupiter and perihelia within the orbit of Neptune (Jewitt, 2009). Seligman et al. (2021), gave a very comprehensive overview of the existing definitions for Levison's ECs, where we can note on the one hand these small changes in designations and definitions and on the other hand the efficiency of the Tisserand parameter, 25 years later.

A very interesting consequence of the Tisserand parameter classification and its conservation quality, is that a comet will mostly stay in his primary class (ECs or NICs), although some interlopers might exist (Brasser et al., 2012). On the contrary, changes between subclasses are frequent, suggesting a connection between the different populations. These connections were highlighted by Jewitt (2015) (Figure 1.8), who summarized the different possibilities for a planetesimal starting his journey from the protoplanetary disk until its return to the inner Solar System in the current epoch.

[6] `http://ssd.jpl.nasa.gov/sbdb_query.cgi`

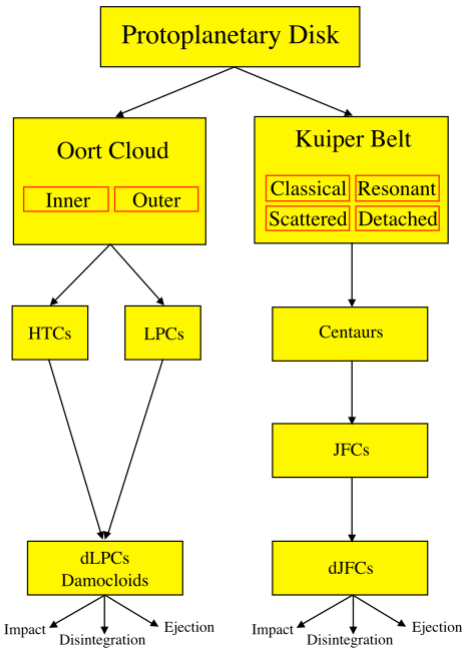


**Figure 1.8:** Flow diagram highlighting the main suspected connections between cometary populations. The "d" in the last two boxes is used to designate dormant comets (Credit: Jewitt (2015)).

To illustrate these connections, we can take the example of a Jupiter-family Comet. As demonstrated in Figure 1.8 it originates from the Kuiper Belt, and more precisely from the scattered disk as it is implied by its low inclination orbit, where it is designated as a SDO (Duncan and Levison, 1997). Once the return mechanism (see Section 1.3.3) places it on a Neptune-crossing orbit, a dynamical cascade involving the giant planets is set in motion to bring it closer to the Sun. The comet passes from the dynamical control of one giant planet to the giant planet interior to it, until it reaches Jupiter-crossing orbits, where it will be designated as a JFC (Levison and Duncan, 1994; Tancredi, 1995; Levison and Duncan, 1997; Tancredi, 1998). In the intermediate phases, during its orbital evolution in the giant planet area, the comet will be designated as a Centaur (Di Sisto and Brunini, 2007). We should note that this procedure, although it might appear straightforward in Figure 1.8, it is actually very chaotic (Tiscareno and Malhotra, 2003), as the passage from one planet to the other might take place in many different ways, due to the stochastic nature of the encounters of a comet with the giant planets.

An interesting parameter is the timescale of the different evolutionary phases, knowing that this flow chart describes procedures with timescales comparable to the Solar System's age. The first phase, that of the implan-

tation of the planetesimals to their respective reservoirs, is usually completed in timescales of the order of tenths to hundreds of millions years (e.g. Nesvorný, 2015). The reservoir phase is the longest one, with timescales reaching the order of the Solar System's age (see for example Nesvorný et al. (2017) and references therein). The return phase is the shortest one, as the ejection process from the planetary region can be rather quick. As an indication, Dones et al. (1996) estimated 0.5 Myr for JFCs and a maximum of 5 Myr for the Centaurs in their data set. Di Sisto and Brunini (2007) and Di Sisto et al. (2009) are estimating a mean lifetime of 72 Myr in the Centaur area and lifetimes of the order of thousands of years once the objects evolve into JFCs. Similar lifetimes have been proposed by other works (e.g. 3-32 Myr (Horner et al., 2004a; Horner et al., 2004b) or 22 Myr (Bailey and Malhotra, 2009)), with these discrepancies being indicative of the chaotic nature of the trajectories in the giant planet region.

### 1.3.5 Possible Endings for Comets

As highlighted in Jewitt's (2015) flow chart, once a comet reaches the inner Solar System it has mainly three options: (a) being ejected from the Solar System, in most cases by Jupiter (Dones et al., 1996), although ejection by other planets during its Centaur phase is also quite possible (e.g. Di Sisto and Brunini, 2007; Bailey and Malhotra, 2009; Fraser et al., 2022), (b) impacting a giant planet or the Sun (e.g. Fernández et al., 2018), or (c) going through a catastrophic disintegration of its nucleus (Boehnhardt, 2004; Fernández, 2009; Knight et al., 2023). It has been also suggested that it is possible to exhaust its volatile content and become a *dormant* or *extinct* comet, a fate that however does not protect comets from the other possible fates (e.g. Oort, 1950; Hartmann et al., 1987; Coradini et al., 1997; Weissman et al., 2002).

## 1.4 Thermal Processing of Cometary Nuclei

In the previous sections, a brief presentation of the main orbital evolutionary stages of a comet's life was given. Nonetheless, to discuss the primitiveness of cometary populations, we should look into the physical evolution of the cometary nucleus itself during this long journey in and out of the Solar System. Before going through that, it is thus necessary to briefly review the current knowledge around cometary nuclei, and especially their bulk composition, as it can be considered one of the main indicators of primitiveness.

### 1.4.1 Composition of Comets

Following Whipple (1950) description (see Section 1.1) we can identify two main components on a comet's nucleus: a non-volatile, refractory component and a frozen volatile component. Recent observations from the Rosetta mission are pointing to the possible presence of a third component of semi-volatile salts, potentially dominant over the other components with derived abundance upper limits of 40vol% (Poch et al., 2020), but further investigations are necessary. Our knowledge on the composition of these components is mainly based on ground-based observations and techniques, such as spectroscopy at different wavelengths, but also flybys and a few *in situ* observations by spacecrafts visiting cometary nuclei (see for example Figure 1.2).

#### Non-volatile or Refractory Component

Our knowledge about the non-volatile component was greatly boosted by space mission flybys and *in situ* observations, managing to study closely the nuclei, often hidden from ground-based observations by the bright coma. They revealed a very complex and rich composition with a wide variety of organic and inorganic compounds such as silicates, metal and mineral species alongside carbon, hydrogen, nitrogen and oxygen compounds, collectively known as CHONs, in the majority of comets (Cochran et al., 2015).

**Inorganic compounds** The inorganic non-volatile component consists mainly of different types of silicate species, as confirmed by a wide range of observations both on SPCs and LPCs. The Giotto spacecraft was the first to detect silicates rich in magnesium, silicon, calcium and iron, both in crystalline and amorphous form, in the coma and the nucleus of comet 1P/Halley (Kissel et al., 1986a; Kissel et al., 1986b). Amorphous pyroxene and olivine were detected in the coma of comet C/1995 O1 (Hale-Bopp) during his last perihelion passage by infrared spectroscopy (Crovisier et al., 1997). Magnesium-rich olivine and pyroxene in crystalline form has also been detected in comet 9P/Tempel 1 by the Deep Impact mission (A'Hearn et al., 2005) providing evidence for possible heating of cometary interiors, early on, in the protoplanetary disk (Harker et al., 2005; Sugita et al., 2005). Ferro-magnesian silicates, among other refractory minerals (pyroxene and olivine), were also detected in the dust sample collected from comet 81P/Wild 2 by the Stardust mission (Brownlee et al., 2003; Zolensky et al., 2006). Features of amorphous and crystalline silicates were also identified in the mid-infrared spectra of Oort Cloud Comets (Kelley et al., 2013) and other periodic comets (10P/Tempel 2 and 49P/Arend-Rigaux) (Kelley et al., 2017). Although no straightforward information is available for the mineralogy of the dust on comet 67P/Churyumov-Gerasimenko (hereafter

67P/C-G) (Levasseur-Regourd et al., 2018), analysis from the COSIMA mass spectrometer and the GIADA grain and dust analyzer, suggest the presence of silicates and sulphides in 67P/C-G as well (Bardyn et al., 2017).

**Organic Compounds** These missions revealed also the presence of organic compounds in cometary surfaces, the presence of which was already suspected by the dark nature of their surfaces and low albedos (e.g Kissel and Krueger, 1987). Surprisingly, organics proved to be the dominant composite of the dust component (e.g. Brownlee et al., 2003). Their existence, in both amorphous and crystalline form, was confirmed in all the aforementioned comets visited by spacecrafts (Krueger et al., 1991; Kissel et al., 2004). However, it was the Rosetta mission, that revealed the abundance and complexity of organic compounds on comet 67P/C-G (Levasseur-Regourd et al., 2018). The COSAC and Ptolemy instruments onboard of the Philae lander, the first ever to study a cometary surface from so close, discovered 16 organic compounds, mainly nitrogen-bearing species, such as amines, nitriles and amides, but also compounds from the chemical groups of alcohols and carbonyls (Capaccioni et al., 2015; Goesmann et al., 2015; Altwegg et al., 2017; Boehnhardt et al., 2017).

### Volatile or Icy Component

Information on comets' volatile components was somewhat easier to acquire, as it is, mainly, the result of ground-based observations of their comae. These observations although restricted to a relatively limited amount of molecules allowed detections on a large number of comets. Significant contributions came from space missions as well, which although limited to a few comets, provided a view on the wealth of volatile material present on cometary nuclei (Bockelée-Morvan and Biver, 2017).

In Figure 1.9, an overview of detected volatile species in cometary atmospheres is given (Bockelée-Morvan and Biver, 2017). It reveals a rich inventory of ice molecules, with 25 being detected in more than two different comets, without considering isotopes, ions, atoms or radicals. This non-exhaustive representation of cometary ice species can be further extended if additional detections from comet 67P/C-G are considered (Altwegg et al., 2019). We note that the main component is water ice (all abundances are relative to water), followed by carbon dioxide ($CO_2$) and carbon monoxide (CO). High relative abundances for methanol ($CH_3OH$) and formaldehyde ($H_2CO$) have been detected as well in more than ten comets. Ammonia ($NH_3$) is the most abundant among the nitrogen-bearing species, while hydrogen sulphide ($H_2S$) is the most abundant among sulfur-bearing ones.

We observe that the range of molecular abundances vary between comets, with the bigger discrepancies concerning the CO molecule. This is somehow expected due to its highly volatile nature and the differences in the dynam-

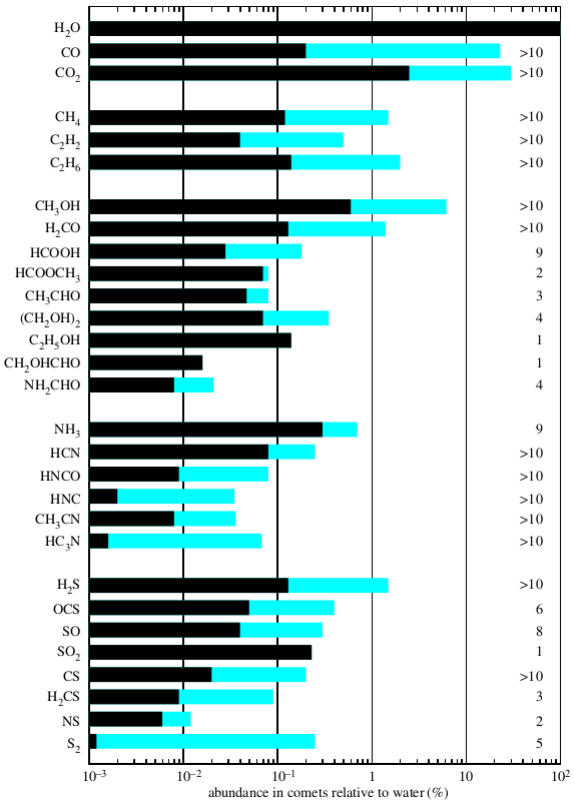


**Figure 1.9:** Molecules detected in comets and their abundances relative to water. Bars in blue show the range of measured abundances in comets, indicating composition diversity between comets. The number of comets in which abundance measurements are available is indicated on the right.(Credits: Bockelée-Morvan et al. (2004); Bockelée-Morvan and Biver (2017)).

ical history observed between different cometary populations (e.g. JFCs vs LPCs) (Dello Russo et al., 2016). An analysis of the chemical diversity between comets from different dynamical families (JFCs vs LPCs) (Biver and Bockelée-Morvan, 2016) do not demonstrate any particular trends. This is considered to be consistent with the Nice model and its follow-up studies presented previously, that predict a common origin for all comets, leaving any observed differences to be explained, most possibly by particularities in the orbital evolution of each comet.

Although abundant in cometary atmospheres, ice species have rarely been detected on cometary surfaces as they are usually covered by dust (see for example Figure 1.10). Direct observations, made possible through space missions, revealed for the first time chunks of ice particles in the surface of comets 9P/Tempel 1 and 103P/Hartley 2 (Kelley et al., 2013). Exposed ice

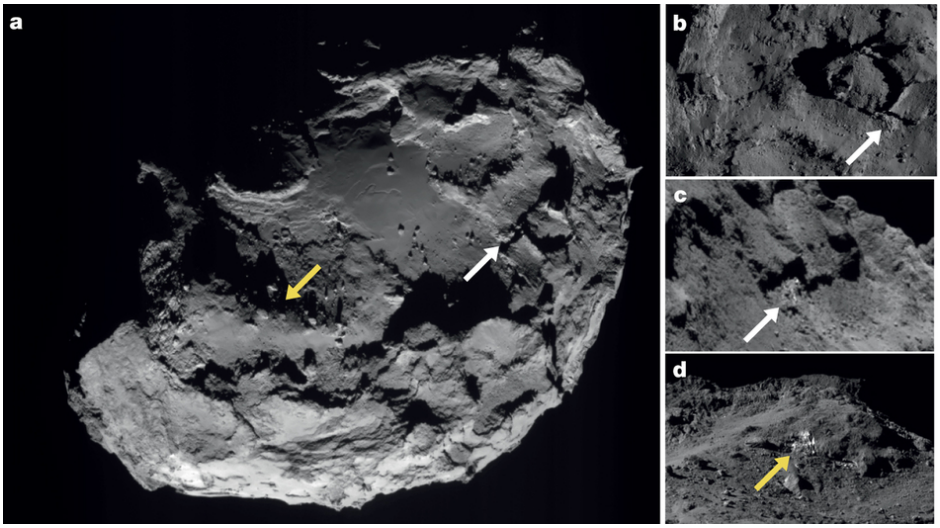


**Figure 1.10:** Rosetta NAVCAM images revealing the presence of water ice on the surface of comet 67P/C-G on the Imhotep region, located on the largest lobe of the nucleus near the equator. The white and yellow arrows indicate chunks of exposed water ice from different viewing geometries (Credits: Filacchione et al. (2016a)).

was also discovered, on the surface of comet 67P/C-G, where $H_2O$ (Pommerol et al., 2015; Filacchione et al., 2016a; Fornasier et al., 2016; Fornasier et al., 2023) and $CO_2$ ice patches have been detected (Filacchione et al., 2016b).

### 1.4.2 An Overview of Thermal Evolution Models

From the different evolutionary phases outlined in Figure 1.8, comets have been considered historically to undergo thermal processing due to solar irradiation, during their inner Solar System phase (e.g. their JFC phase), where intense water-driven activity is observed. In the previous phases, they were considered to have remained relatively unaltered, with slight alterations from cosmic ray radiation, heating from passing stars or random supernovae events affecting mainly their surfaces and upper subsurface layers (e.g. Meech and Svoren, 2004).

In Section 1.1 we briefly presented how a growing number of studies is resetting this traditional concept and suggests that activity and therefore alterations are possible during the other phases of evolution as well. For example, an increasing number of observations indicate long-distance activity either from Centaurs (Jewitt, 2009; Lin et al., 2014; Mazzotta Epifani et al., 2017; Mazzotta Epifani et al., 2018; Wierzchos et al., 2017; Wierzchos and Womack, 2020; Steckloff et al., 2020; De la Fuente Marcos et al., 2021; Bockelée-Morvan et al., 2022) or comets passing through the Centaur area

(Jewitt et al., 2017; Meech et al., 2017b; Hui et al., 2019; Yang et al., 2021; Farnham et al., 2021; Kokotanekova et al., 2021; Kelley et al., 2022). In most cases this activity is suspected to be CO-driven, breaking down the traditional concept of water-driven activity. Of course not all Centaurs or comets passing through the Centaur area have been found to be active (Cabral et al., 2019; Li et al., 2020; Lilly et al., 2021), indicating that some activation mechanism should exist.

Unfortunately, in the pro-JWST era the observational capabilities did not allow the detection of activity at distances beyond the giant planet region, despite indications for a more distant and earlier onset (Jewitt et al., 2021). This obstacle was surmounted by theoretical studies and the use of thermal evolution models, allowing for predictions of thermal processing and alterations at different distances and evolutionary phases. These models were initially conceived in order to understand the observed cometary activity, driven by surface sublimation of cometary ices, and its underlying mechanisms in the innermost parts of the Solar System, during the water-driven activity phase, but also to infer some of its internal properties (e.g. Weissman and Kieffer, 1981; Kuhrt, 1984; Fanale and Salvail, 1984; Herman and Podolak, 1985). The main focus at the time was comet 1P/Halley, target of the upcoming Giotto mission. They considered a simplified composition of dust and water ice for the most part, and examined the heat, gas and dust transport in cometary nuclei.

The flyby of comet 1P/Halley and the revelation of its highly porous nature, motivated a new wave of thermal evolution models, focusing on understanding the sublimation mechanism from a porous nucleus (e.g. Mekler et al., 1990; Prialnik and Bar-Nun, 1990). The possibility of a dust mantle formation and its effects on the activity was also a prominent modeling field (e.g. Prialnik and Bar-Nun, 1988; Rickman et al., 1990). Gradually, thermal evolution models started also to consider more elaborated compositions, including H, CO, $CO_2$ as well as $H_2O$ ice (Fanale and Salvail, 1987; Bar-Nun and Prialnik, 1988; Fanale and Salvail, 1990; Espinasse et al., 1991; Espinasse et al., 1993). Additional activity mechanisms such as the crystallization of amorphous water ice[7] (Prialnik and Bar-Nun, 1987; Prialnik, 1992) were

[7] A metastable and highly porous state of $H_2O$ ice, formed during the condensation of water at low pressure and temperature conditions. As implied by its name, it lacks the characteristic crystalline structure of hexagonal lattices of common water ice. It can survive for long periods of time in low temperature and pressure conditions, as those encountered in the outer Solar System. When it is heated above a certain temperature threshold, its structure readjusts into the well-known crystal form in an exothermic and irreversible procedure that follows an activation law (Schmitt et al., 1989). This transformation takes place in two different phases as before the formation of the typical hexagonal crystal, the ice passes from an intermediate cubic form. Its most intriguing quality, is its capacity to trap volatile species that can be released later on during the crystallization phase. It has been experimentally demonstrated that when ice condensates at very low pressure and temperature conditions, relevant to the formation of comets in the proto-

also introduced as a mean to explain outbursts of activity that could not be explained through typical sublimation. In parallel to these models and inspired by the discoveries on the composition and the physical properties of cometary nuclei, a considerable experimental work was carried out, in order to understand the behavior and the thermal properties of cometary dust and ices (Bar-Nun et al., 1985; Spohn et al., 1989; Spohn and Benkhoff, 1990; Steiner, 1990; Steiner and Kömle, 1991; Kossacki et al., 1994; Seiferlin et al., 1996).

While the majority of models in the following years focused their attention on comet 46P/Wirtanen, then target of the upcoming Rosetta space mission (before it changed to comet 67P/C-G) (e.g. Benkhoff and Boice, 1996; Capria et al., 1996; Kossacki et al., 1999b), some first steps towards more distant objects were taken. Fanale and Salvail (1997); Capria et al. (2000) and De Sanctis et al. (2000) modeled the activity of simulated objects in the orbits of Centaurs (2060) Chiron (or 95P/Chiron) and (5145) Pholus. They concluded that periodic CO-driven activity can be expected from gas escaping from 'pockets' close to the surface or being released from crystallizing amorphous ice. More studies followed up, focusing on individual objects on Centaur orbits: P/2004 A1 (LONEOS) (Capria et al., 2009), (10199) Chariklo (Guilbert-Lepoutre et al., 2011) or the Centaur population as a whole (Guilbert-Lepoutre, 2012; Davidsson, 2021). Their results, in line with the previous studies, highlighted the possibility of activity during that intermediate phase of chaotic orbital evolution far away from the Sun. They concluded that the main mechanism should be the crystallization of amorphous $H_2O$ ice starting around 10-12 au and lasting for short periods, implying sporadic activity, probably due to some abrupt change in their orbital elements (Guilbert-Lepoutre et al., 2011; Fernández et al., 2018). Davidsson (2021) suggested that crystallization is efficient only at distances up to 8-10 au and that the segregation of volatile elements (such as $CH_4$ (Luna et al., 2008), $N_2$ (Satorre et al., 2009) or CO (Simon et al., 2019)) from $CO_2$, in a process similar to the trapping and release of molecules during the crystallization of amorphous $H_2O$ ice, is a more relevant activity mechanism in the Centaur region.

Parallel to these studies, a small number of works have considered the possibility of processing during the earlier stages of cometary evolution, in

planetary disc, not only it ends up with this highly disordered structure but it entraps volatile species, such as CO, $CO_2$, Ar, $N_2$ in a similar, yet far more efficient, manner as the clathrate hydrates (Bar-Nun et al., 1985; Hudson and Donn, 1991; Notesco and Bar-Nun, 1996; Collings et al., 2003; Bar-Nun et al., 2007; Fayolle et al., 2011; Prialnik and Jewitt, 2022). These gases can be released later on during the consecutive phase transitions (to cubic and hexagonal ice) and can contribute in the cometary activity (Jewitt, 2009; Meech et al., 2009; Guilbert-Lepoutre, 2012). We should mention here, that this ability of gas trapping is not limited to the $H_2O$ molecule but concerns other molecules as well, such as $CO_2$ which can trap for example CO (Simon et al., 2019) or $N_2$ (Satorre et al., 2009).

the protoplanetary disk and the reservoirs. Their main assumption is that this activity is mainly driven by internal heating by radioactive elements (Prialnik et al., 1987). Haruyama's et al. (1993) model was probably the first model to study thermal processing during the reservoir phase and in particular at the Oort Cloud. By considering heating from radioactive elements and different configurations for the thermal conductivity, they concluded that low conductivity objects are bound to have their nucleus crystallized, while high conductivity objects should retain their amorphous ice content. Similar results were proposed by Prialnik and Podolak (1995), who suggested that large objects (R $>$ 20 km) in the reservoirs or at the protoplanetary disk are expected to have their nucleus crystallized as they are sufficiently large to allow the temperature to rise to sufficient levels for the crystallization of amorphous ice to take place. De Sanctis et al. (2001) examined the thermal evolution of objects in the Kuiper Belt by considering two energy sources: the Sun and internal heating from radioactive elements. They concluded that even at far away distances ($\sim$50 au), the combined effect of solar irradiation and radioactive heating can result in the depletion of the most volatile elements such as CO. Several studies followed under similar assumptions regarding the heat sources (Choi et al., 2002; Merk and Prialnik, 2003; Malamud and Prialnik, 2015; Kral et al., 2021; Lisse et al., 2021; Loveless et al., 2022; Malamud et al., 2022; Parhi and Prialnik, 2023) for objects in the Kuiper Belt, arriving at similar conclusions: a depletion of highly volatile species, affecting, if not the entire nucleus, at least a subsurface layer of a few kilometers. Merk and Prialnik (2006) and Prialnik and Merk (2008), considered accretion parallel to the thermal processing by solar irradiation and radioactive heating. They found that accretion can greatly diversify the possible outcomes for the objects interiors, where water ice is expected to melt or at least to crystallize close to the center. Their results, in agreement with Haruyama et al. (1993) and Prialnik and Podolak (1995), suggested that it is more probable to find pristine parts in the outermost layers of Kuiper Belt objects, rather than in the deep interiors.

Recently Davidsson (2021) and Golabek and Jutzi (2021) examined the thermal processing even earlier, just after the formation of the planetesimals on the protoplanetary disk and before their scattering towards their source reservoirs. Golabek and Jutzi (2021) considered only internal heating from radioactive elements during the planetesimals formation, while taking into account the possibility of collisional heating. They concluded that the preservation of highly and moderately volatile species such as CO and $CO_2$ is possible for planetesimals with radii smaller than 20 km that formed relatively late ($>$ 3.5 Myr) when radioactive heating becomes insignificant. Davidsson (2021) took into account both external (by solar irradiation) and internal (by radioactive elements) heating. He demonstrated that all objects sooner or later will lose all their free condensed highly volatile content on timescales ranging from a few thousand to 200 million years. In addition,

$CO_2$ ice is expected to sublimate from a thin, yet significant, subsurface layer ($\sim$30 m) and amorphous ice is expected to crystallize in a layer of 200 m below the surface.

## 1.5 Rationale for the Current Work

If we attempt to summarize the results from the thermal evolution models presented above into one principal conclusion, that would probably be that thermal processing is indeed conceivable at all stages of the orbital evolution of comets, resulting in significant alterations of their highly volatile components but also of their moderately volatile and amorphous water ice inventory. This conclusion, as mentioned previously, is putting a shadow over the primitive nature of comets, suggesting that their physical and chemical properties as we observe them today, have not been entirely preserved (Guilbert-Lepoutre et al., 2016). This processing is driven by different mechanisms at every stage of evolution with radioactive heating -if present (Malamud et al., 2022)- being the preferred choice for the early phases and crystallization of amorphous water ice for the intermediate phases bringing comets back to the inner Solar System.

However, as expected for studies spanning over three of four decades, some conflicting results and conclusions can be identified, leaving questions to be answered:

1. The predicted hyper-volatile depletion has been proposed to take place at different phases of comets' evolution. Most studies are indicating that it should occur during the reservoir phase, but some studies are suggesting an earlier depletion during their ejection from the protoplanetary disk, raising questions about the actual timeline of volatile depletion.

2. While this volatile depletion is reported by theoretical studies, an important number of recent observations suggest long-distance CO-driven activity. Although, some studies are suggesting alternative ways of storing hyper-volatile components, allowing their conservation, there are still some incompatibilities between the theoretical onset of this activity and the observations. Is there a possibility of retaining highly volatile species, even as free condensates during the scattering and reservoir phase of comets?

3. Although these thermal evolution studies acknowledge an evolutionary process indirectly, in practice they do not account for the actual dynamical evolution. Their results are usually obtained by placing their simulated objects at stable, circular or eccentric orbits for long periods of time. These orbits can be random, as long as they keep the object

in the area of interest, or chosen to coincide with the current orbit of a Centaur or Kuiper Belt object (e.g. Malamud and Prialnik, 2015). However, as presented in Section 1.3, the orbital evolution is rarely stable, with the exception of some populations at the Kuiper Belt (Kaib and Sheppard, 2016). Does this unstable, and often chaotic, evolution of the planetesimals moving outwards or the comets moving inwards plays a role in their thermal processing and if so in what way? Can we constrain in a statistically significant manner this processing, at least at the level of cometary populations, given that objects, even from the same population, are expected to evolve differently?

Motivated by these questions, we propose a novel approach, consisting in coupling an adapted thermal evolution model to dynamical trajectories obtained from $N$-body simulations, tracking the orbital evolution of simulated comets from the outer planetesimal disk to their source reservoirs and then back in the inner parts of the Solar System.

This approach allows the examination of the thermal processing of simulated particles from early on and with continuity, taking into account the effects of their orbital evolution. The use of $N$-body simulations provides a sufficient amount of particles and possible trajectories, permitting a statistically significant view of the thermal imprint among objects of the same population, but also a comparison between different populations, making a first step towards constraining the primitiveness of the cometary populations in our Solar System.

# Chapter 2

# An Initial Coupling Attempt

Our first order of business, before advancing with the development of our adapted thermal evolution model, was to run a set of 'diagnostic' simulations. These simulations had a double objective: on the one hand to test the requirements of the coupling between a thermal evolution model and dynamical trajectories obtained from $N$-body simulations and on the other hand to test our initial hypothesis that the long-term orbital evolution of cometary nuclei is intimately related to their physical evolution.

To do so, we used a simplified version of an existing thermal evolution model (Guilbert-Lepoutre et al., 2011) and a sample of particles leaving the scattered disk (hereafter SD) and scattered inwards towards Jupiter-crossing orbits, obtained by $N$-body simulations performed by Nesvorný et al. (2017). This initial coupling attempt quickly revealed a series of issues, both on the physical and the numerical nature of the project, that we needed to resolve in order to successfully couple the thermal to the dynamical evolution of comets.

*An extended version of this chapter has been published as an independent article in 'The Astrophysical Journal' (Gkotsinas et al., 2022). The original publication can be found on Appendix B.*

## 2.1 A First Coupling Attempt

### 2.1.1 Brief Description of the Thermal Evolution Model

The thermal evolution model that was used in this initial approach is detailed in Guilbert-Lepoutre et al. (2011). In its original version, the model solves the time-dependent differential equation for the heat transfer in a fully three-dimensional porous sphere, while accounting for processes such as the crystallization of amorphous water ice or internal heating by radioactive elements.

This time-dependent differential equation for the heat diffusion can be written as:

$$\rho_{bulk} c \frac{\partial T}{\partial t} + div(-\kappa \overrightarrow{grad}\, T) = \mathcal{S}, \tag{2.1}$$

where $\rho_{bulk}$ (kg m$^{-3}$) is the object's bulk density, $c$ (J kg$^{-1}$ K$^{-1}$) the material's heat capacity, $T$ (K) the temperature, $\kappa$ (W m$^{-1}$ K$^{-1}$) the material's effective thermal conductivity, and $\mathcal{S}$ the heat sources and sinks.

To numerically resolve this differential equation a set of initial and boundary conditions is necessary (Prialnik et al., 2004)[1]. These boundary conditions refer to the energy flux $F(r)$ on the interval $0 <$ r $<$ R, where at the lower end is the center of the nucleus and on the upper end its surface. At the center the common assumption is that the energy flux vanishes (i.e. $F(r) = 0$). At the surface the boundary condition at the sub-solar point is:

$$(1 - \mathcal{A}) \frac{L_\odot}{4\pi d_H^2} = \varepsilon \sigma T^4 + \kappa \frac{\partial T}{\partial z} \tag{2.2}$$

with the nucleus' insolation given as a function of $\mathcal{A}$ the Bond's albedo, $L_\odot$ the solar constant and $d_H$ (au) the heliocentric distance; the thermal emission given as a function of $\varepsilon$ the IR emissivity, $\sigma$ the Stefan-Boltzmann constant and T (K) the temperature; and the heat flux towards the interior given as a function of the surface's thermal conductivity $\kappa$ (W m$^{-1}$ K$^{-1}$).

It is through this boundary condition, and more precisely of its left-hand term describing the received solar radiation, that the coupling between the thermal evolution model and the orbital evolution is achieved. The $N$-body simulations can provide at specified intervals information on the orbital elements of a simulated comet, such as the semimajor axis, the eccentricity and the inclination. Using these orbital elements we can calculate the heliocentric distance of the comet and from Equation (2.2) estimate the amount of the received solar energy that is transported to the comet's interior, contributing to its thermal evolution. Although the above description seemingly describes a straightforward procedure, in reality this coupling is not so trivial as the underlying processes act on very different timescales.

### 2.1.2 The Timescale Issue and Numerical Considerations

Thermal evolution processes such as phase transitions (sublimation, recondensation, crystallization of amorphous ices and so on), heat or gas diffusion, operate usually in timescales ranging from a few minutes or hours to a few days or months, depending on the temperature conditions and the examined process (e.g. Prialnik et al., 2004). On the other hand, the $N$-body simulations used to study the orbital evolution of comets, describe billion-year processes, requiring long output frequencies, of the order of hundreds to thousands of years, to follow a comet's orbital changes (e.g. Nesvorný

[1] A detailed description of the numerical considerations regarding thermal evolution models is given in Chapter 4

et al., 2017). For example in the sample that we used for these initial simulations, orbital information was available at a cadence of 100 years. Given that it is the $N$-body simulations that dictate the timescales of the coupling, as they provide the boundary conditions for the thermal evolution model, a first major issue emerged: How can we resolve thermal processes taking place at such short timescales, without any information about the comet's position in the time between the output intervals? To answer this question a number of simplifying assumptions were employed, most of which were used later on for the adapted thermal evolution model (see Chapter 3).

Special attention was given to the numerical aspect of the coupling as well. As our intention was to cover a large period of a comet's lifetime, usually of the order of tenths of million years, during which the heat diffusion equation must be repeatedly resolved in a comet's interior, the calculation times can quickly become unmanageable, if not prohibitive. This issue demanded additional simplifying assumptions aiming at the reduction of the computational time and at keeping the problem at hand tractable.

### 2.1.3 Working Assumptions

A first working assumption was to reduce the model's dimensions. For such long timesteps, latitudinal effects at the surface due to the shape of a comet nucleus, its rotation (diurnal variations), or seasonal variations, cannot be resolved. In fact they need to be averaged out during each dynamical timestep, so there was no need to use a slow rotator approximation for the surface or a 2D/3D thermal evolution model for the interior (for more details see Section 4.1). Therefore, we considered that a 1D version of the thermal evolution model is adequate for this approach. In addition, we assumed that the incident solar energy is uniformly distributed over the surface of the nucleus, an approximation known as the 'fast rotator', providing a spherical average of the energy received by the nucleus (Huebner et al., 2006).

Two further assumptions were made to simplify the resolution of Equation (2.1). The first one concerned the effective thermal conductivity which can be written in the general form:

$$\kappa = h\ \phi\ \kappa_{solid} + \kappa_{rad} \tag{2.3}$$

where $\kappa_{solid}$ is the conductivity of the solid material of the nucleus and $\kappa_{rad}$ the radiative conductivity, accounting for the heat transfer through radiation through the pores:

$$\kappa_{rad} = 4 r_p \varepsilon \sigma T^3 \tag{2.4}$$

with $r_p$ (m) the average pore radius, usually set to be the same size as the grains of the medium (Huebner et al., 2006), $\varepsilon$ the material's emissivity, and $\sigma$ the Stefan-Boltzmann constant. Given that the grain size was set at $10^{-6}$ $\mu$m

following Huebner et al. (2006), the size of the pore radius was equally small, implying insignificant contributions to the resulting conductivity, allowed us to disregard this term.

The letters $h$ and $\phi$ denote two reduction factors. The factor $h$ is a dimensionless quantity, known as the Hertz correction factor. It describes the reduction of the effective cross section of the grains in a porous material (Gundlach and Blum, 2012) and may theoretically vary from $10^{-4}$ to 1, although values of the order of $10^{-2}$ are considered as the most plausible and commonly used (e.g Huebner et al., 2006). The factor $\phi$ is a correction factor applied to account for the effect of the porous structure of cometary material. Guilbert-Lepoutre et al. (2011) used the Russell's correction factor (Russell, 1935), calculated as:

$$\phi = \frac{\psi^{2/3} f + (1 - \psi^{2/3})}{\psi - \psi^{2/3} + 1 - \psi^{2/3}(\psi^{1/3} - 1) f} \tag{2.5}$$

where $\psi$ is the porosity of the nucleus (here set at a constant value of 0.8, following measurements from 67P/C-G (Kofman et al., 2015)) and $f$ the ratio between the solid and the radiative conductivity.

The second and admittedly most radical simplification was to neglect all the phase transitions we could not resolve in the provided timestep of 100 years. In Equation (2.1), this translates to $\mathcal{S}$=0, implying that the modified model does not describe faithfully the thermal processing during active stages of the orbital evolution, when phase transitions are at the origin of cometary activity. As a consequence no gas diffusion is accounted for, so that the mass is conserved, allowing the use of composition-independent thermo-physical properties for the cometary material, in particular for the heat capacity and the thermal conductivity.

Even with those assumptions and a simplified version of the thermal evolution model, the resolution of the heat diffusion in the interior of the nucleus required smaller timesteps of the order of the year (see Section 3.1.4 for a more detailed discussion). Intermediate timesteps could be easily created for each timestep provided by the dynamical simulation, however an additional assumption regarding the heliocentric distance at each and every intermediate timestep was required. A solution to this problem came from the use of an energy-averaged orbital distance. Prialnik and Rosenberg (2009) proposed a solution to replace eccentric orbits by circular ones that receive the same total amount of energy over an orbital period. The radius for these circular orbits or as we called it the 'equivalent semimajor axis' ($a_{eq}$) was calculated as: $a_{eq} = a(1 - e^2)$. Those circular orbits greatly simplified the coupling, as they provided an energy-based constant distance between subsequent timesteps of the dynamical simulation.

One could argue that further reductions of the dynamical timesteps could have been attempted allowing the resolution of other thermal processes as

well. However, reducing the timesteps to the order of minutes or hours for simulations spreading over millions of years would lead to a prohibitive amount of timesteps and calculation times[2].

## 2.2 Initial Applications

With the above considerations, the problem was reduced to the study of the thermal evolution of dusty spheres, evolving into Jupiter-crossing orbits following chaotic orbital trajectories due to the close encounters with the giant planets (see Section 1.3.3).

### 2.2.1 Processing of a Simulated JFC

In Figure 2.1 a representation of the thermal evolution of a simulated comet, obtained from the proposed coupling is given. This comet has a relatively short lifetime in the inner Solar System comparing to other particles in our sample. It gets scattered inwards by Neptune rather quickly, orbiting close to Saturn almost from the beginning of the simulation (at ∼300 kyr) and has three passages from the JFC area: two very close at ∼900 kyr after the beginning of the simulation and one at ∼1.2 Myr, before its ejection from the Solar System at ∼ 1.45 Myr.

This trend of multiple approaches to areas of particular thermal significance within Jupiter's orbit, where phase transitions such as water ice sublimation can be triggered was observed for the majority of our simulated JFCs. The number of approaches and the degree of the recorded heating intensity (depending on both their duration and the equivalent semimajor axis value) varied between the simulated comets. These two elements provided a first indication of the effects the long-term dynamical evolution has on the thermal processing of cometary nuclei. Moreover, they suggested that cometary nuclei observed in the inner Solar System may have been exposed to substantial heating in their past, allowing for thermally-induced alteration processes to take place deep below their surfaces.

We notice the strong influence of the thermal conductivity, expressed here through the Hertz correction factor, on the evolution of the temperature distributions. Using the 80 K isotherm as a rough indicator, we observe that as the Hertz factor is reduced, the heated subsurface area is reduced as well. Indeed, the maximum depth of the 80 K isotherm is ∼150 m for h=$10^{-2}$, ∼50 m for h=$10^{-3}$, and only ∼10 m for h=$10^{-4}$. This is a natural consequence of heat conduction, as the skin depth ($\delta$) – a rough estimate of how deep a surface temperature change can propagate below the surface – is

[2] As an indication the median lifetime of a particle leaving the SD, until the moment of its ejection was 54 million years

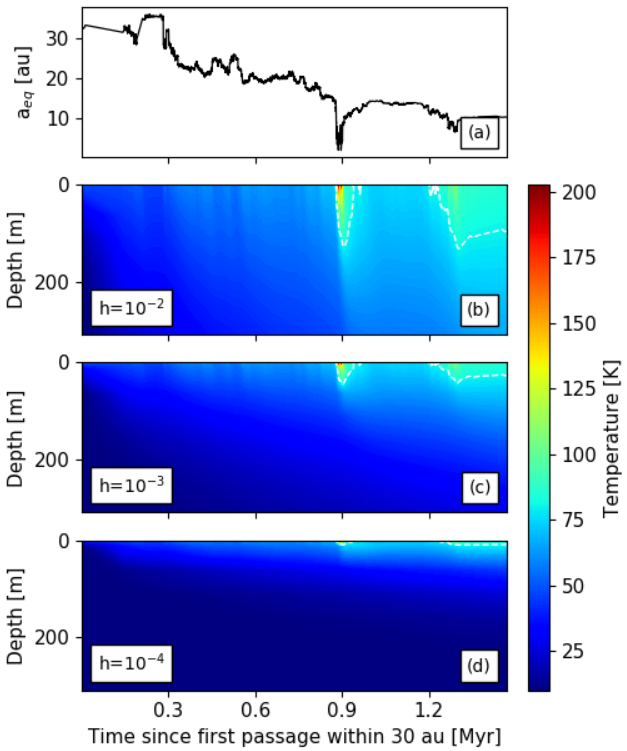


**Figure 2.1:** Temperature distributions in a subsurface layer of 200m for one of the simulated JFCs of our sample, and for three different values of the Hertz factor. Panels: (a): Evolution of the equivalent semimajor axis from the moment the object escapes the SD to the moment of its ejection from the Solar System, (b) Temperature distribution over time for h=$10^{-2}$, (c) Temperature distribution over time for h=$10^{-3}$, (d) Temperature distribution over time for h=$10^{-4}$. The white dashed line denotes the 80 K isotherm.

directly dependent on the value of the thermal conductivity ($\delta = \sqrt{\frac{P\kappa}{\pi\rho_{bulk}c}}$, with $P$ a reference period of time).

### 2.2.2 Overview of the Processing on the Entire Sample

To constrain the thermal processing in our JFC sample, and as no actual phase transitions were considered, we resolved in the tracking of the evolution of three isotherms:

- 25 K, for the sublimation temperatures for hyper-volatile species, such as CO ;

- 80 K, for the sublimation temperatures of moderately-volatile species, such as $CO_2$ ;
- 110 K, representative of the crystallization of amorphous water ice phase at timescales of the order of 100 yr, as the dynamical evolution output frequency.

We should remind that as no phase transitions are actually considered, no heating delay associated with the sublimation of volatile species, nor any recondensation are accounted for. In fact, when volatile species sublimate, their partial pressure peaks at the sublimation front. Molecules following pressure gradients, can recondense at any place of the nucleus sustaining the appropriate temperature and pressure conditions, above or below the sublimation front. As the temperature evolution is followed for timescales much longer than those of the sublimation and gas diffusion timescales (Prialnik et al., 2004), this indirect method of examining the thermal processing is only relevant to alterations on the primordial composition, and whether it can be maintained in near-surface layers. We assumed that volatile species, if initially present as pure condensate, can sublimate if their sublimation temperature is reached. For example free condensed CO would sublimate down to the level of the 25 K isotherm, and free condensed $CO_2$ down to the level of the 80 K isotherm. Whether the sublimating species escape the nucleus or recondense in its interior, the net result in our approach is an alteration of the primordial composition. When these layers subsequently contribute to the observed cometary activity, cannot be considered to reflect the primitive material incorporated in cometary nuclei.

We examined the maximum depths of these isotherms at two specific moments of their lifetime: (a) the moment objects transitioned to a JFC orbit for the first time, and (b) the last moment of the simulation, when the simulated JFCs were ejected from the Solar System. To define this transition moment and in general the JFC phase, we adopted Sarid's et al. (2019) proposed definition for JFCs, requiring orbits with perihelia $q < 5.2$ au (well within Jupiter's orbit) and aphelia $Q < 7$ au (decoupled of Saturn's gravitational influence).

For example the simulated JFC presented in Figure 2.1 at the moment of its transition to a JFC orbit for the first time, having previously spent $\sim$0.88 Myr on transient orbits in the giant planet region, has the three isotherms (25 K, 80 K, 110 K) located at $\sim$810 m, $\sim$60 m and $\sim$5 m respectively below the surface for $h = 10^{-2}$, and at $\sim$60 m, $\sim$3 m and $\sim$60 cm respectively for $h = 10^{-4}$. At the final moment of its JFC phase, having experienced intense processing, for $h = 10^{-2}$ the 25 K isotherm is located at the same depth ($\sim$810 m), whereas the 80 K isotherm advanced to $\sim$160 m, and the 110 K isotherm to $\sim$60 m. For $h = 10^{-4}$, the three isotherms are closer to the surface ($\sim$60 m, $\sim$9 m and $\sim$4 m respectively). With the above

considerations this simulated comet would have 'lost' these volatile species from an important subsurface layer while its amorphous water ice would have crystallized in a less important, yet not insignificant, subsurface layer before its first transition to a JFC. During the intense processing of the JFC phase it is the moderately-volatile species and the crystallization of amorphous water ice that advance further on, as the fate of its hyper-volatile content seems to have already been determined by the time spent in transient orbits at the Centaur area.

**Crystallization of amorphous water ice** We assumed that the crystallization of amorphous water ice, if at all present inside JFCs, would follow the 110 K isotherm. Figure 2.2 shows the depths of this isotherm, as a function of the Hertz factor, for the initial and final moments of the model JFCs. Before the first transition to JFC orbits, the three different values of the conductivity yield similar depth distributions: for nearly all simulated JFCs the 110 K isotherm remains within 40 m from the surface (up to 80 m for $h = 10^{-2}$). As expected the isotherm advances further during the JFC phase, remaining though quite close to the surface: for the bulk of the simulated JFCs, the isotherm is located in the top ∼80 m below the surface. In the case of $h = 10^{-2}$, we can find it in deeper layers, though rarely below ∼400 m.

These depths are compatible with results from Guilbert-Lepoutre (2012) who studied the survival of amorphous water ice in Centaurs, using fixed orbits in the giant planet region for 10 Myr. These initial results suggest that the survival of amorphous water ice is definitely conceivable in the interior of cometary nuclei, and is in agreement with the hypothesis that this phase transition could be a possible source of activity, for example in the form of outbursts in the Centaur area (e.g. Wierzchos and Womack, 2020).

**Volatile content following the 80 K isotherm** The distributions of depths reached by the 80 K isotherm are quite similar to those for the 110 K isotherm (see Figure 2.3). Not surprisingly, as the temperature of interest is smaller, it is generally found in deeper layers. The minimum processing involves the top ∼100 m regardless of the thermal conductivity value. For $h = 10^{-2}$, we note that almost all simulated JFCs are liable to lose their moderately volatile content from the first 40 m below the surface. Interestingly, this can happen before the first transition to JFC orbits when 69.5% of the simulated JFCs have the isotherm located between 40 and 80 m and 28% have it below 80 m. Only 2.5% (7 simulated JFCs) have the 80 K isotherm above 40 m. A similar trend is observed for $h = 10^{-3}$, albeit less pronounced as 62.3% simulated JFCs have the 80 K isotherm between 40 and 80 m. For $h = 10^{-4}$, the majority of the model JFCs (79%) have this isotherm located in the first 40 m (average depth of 17.2 m).

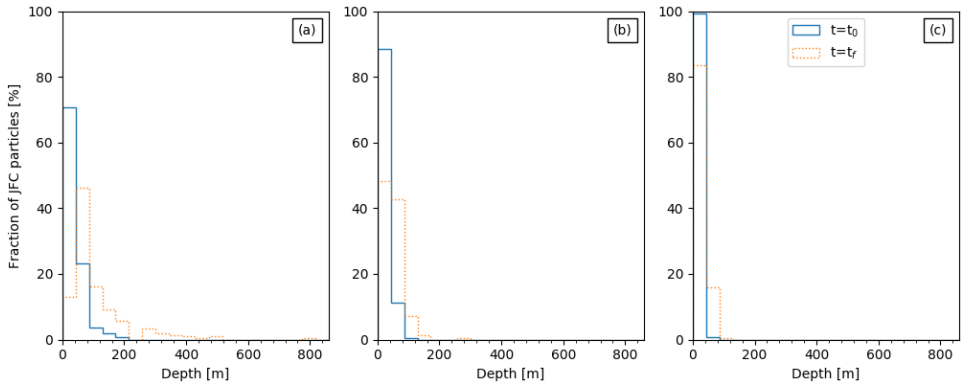


**Figure 2.2:** Location of the 110 K isotherm for the entire sample (276 simulated JFCs) at: $\mathbf{t}_0$ moment of first transition to JFC (blue solid line) and $\mathbf{t}_f$ final moment of the JFC phase (orange dashed line) for the three values of the Hertz factor considered : $h = 10^{-2}$ (panel a), $h = 10^{-3}$ (panel b), $h = 10^{-4}$ (panel c).

At the end of their JFC phase, the isotherm advanced on average ∼80 m below the surface when $h = 10^{-2}$, ∼70 m when $h = 10^{-3}$, and ∼9 m for $h = 10^{-4}$. This suggests that the main processing related to this particular isotherm occurs during their JFC phase, although the processing during the Centaur phase is not negligible, even for the least conductive scenario.

**Hyper-volatile species traced by the 25 K isotherm** The distribution of depths reached by the 25 K isotherm for the different values of the thermal conductivity is given in Figure 2.4. It is apparent that with respect to this particular isotherm, the thermal conductivity (through the choice of Hertz factor in this initial approach) is critical to assess the corresponding processing. The distributions obtained at the first transition and at the end of the JFC phase, are almost identical. For $h = 10^{-2}$ (and $10^{-3}$ to some degree), most simulated JFCs have already heated up to their center (located at 5000 m below the surface) before their first transition to a JFC orbit (77% and 33.3% respectively). For the least conductive scenario ($h = 10^{-4}$), only 27.9% of the model JFCs retain the 25 K isotherm in the top 250 m layer, the average depth for the overall sample being ∼650 m. At the final moment of their JFC lifetime we see that less than 10% of model JFCs are able to maintain the 25 K isotherm in the top 1 km (only 1 model JFC keeps the isotherm in the top 250 m) for $h = 10^{-2}$. For $h = 10^{-3}$, only 30% of the model JFCs keep the isotherm within 1 km below the surface (∼8% keep it within 250 m), whereas for $h = 10^{-4}$, 27% of the model JFCs have the 25 K isotherm within 250 m, and 50% within 500 m.

Following the processing assumptions, all simulated JFCs in our sam-

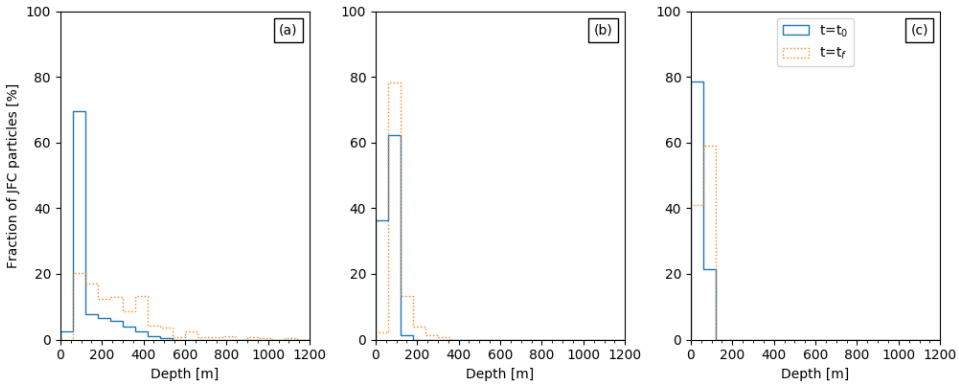


**Figure 2.3:** Location of the 80 K isotherm for the entire sample (276 simulated JFCs) at: $\mathbf{t}_0$ moment of first transition to JFC (blue solid line) and $\mathbf{t}_f$ final moment of the JFC phase (orange dashed line) for the three values of the Hertz factor considered: $h = 10^{-2}$ (panel a), $h = 10^{-3}$ (panel b), $h = 10^{-4}$ (panel c).

ple (except one) would have lost their free condensed CO in the top 250 m subsurface layer before their first arrival on JFC orbits. We could further argue that, given the extremely low sublimation temperature of hypervolatiles, these species would be lost as pure condensate even before their return to the giant-planet area, since isothermal surface temperatures in the Kuiper Belt range between 30 and 50 K. As the necessary temperature conditions for the loss of hyper-volatile species are omnipresent in the inner Solar System, the time spent in transient orbits can be crucial for the survival or depletion of these species. This is illustrated in Figure 2.5 where all the objects having prolonged stays on transient orbits are more susceptible to heating at greater depths. For $h = 10^{-2}$, objects with lifetimes over $\sim$8 Myr are prone to losing all free condensed hyper-volatiles from their entire nucleus. For $h = 10^{-3}$, simulated JFCs with lifetimes over $\sim$90 Myr would experience the same fate. In contrast, none is found to lose its hyper-volatile content below 2500 m for $h = 10^{-4}$.

## 2.3 Reviewing our Initial Approach

As described in Section 1.4.1, despite the uncertainties surrounding the structure and composition of cometary nuclei, the presence of ice species in comets is undeniable. With that in mind, neglecting their presence in this initial approach has been the most severe assumption with important consequences in our results. Ignoring their presence implies the absence of additional energy sources and sinks related to their phase transitions, such as the energy released during the crystallization of amorphous water ice

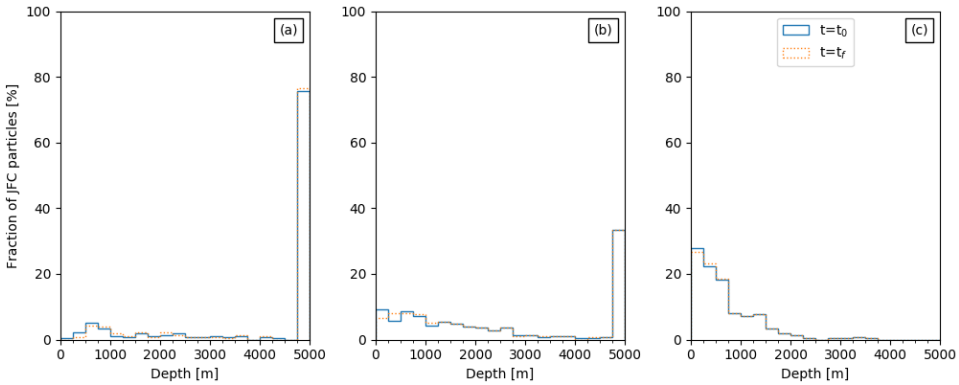


**Figure 2.4:** Location of the 25 K isotherm for the entire sample (276 simulated JFCs) at: $\mathbf{t}_0$ moment of first transition to JFC (blue solid line) and $\mathbf{t}_f$ final moment of the JFC phase (orange dashed line) for the three values of the Hertz factor considered : $h = 10^{-2}$ (panel a), $h = 10^{-3}$ (panel b), $h = 10^{-4}$ (panel c).

(Schmitt et al., 1989) and the energy consumption during ice sublimation (Prialnik et al., 2004). In fact, when sublimation and recondensation of volatile compounds take place, the heat transport via the vapor phase is very important, becoming even more effective than heat conduction by the solid matrix (Huebner et al., 2006). As a consequence, during the active phase, heat transfer by latent heat becomes the dominant heat mechanism. This can strongly influence the temperature profiles within the nucleus, something that it is not accounted for in this initial approach. While an icy compound is sublimating, the input energy is consumed by the phase transition so that the increase in the internal temperature is halted. This might limit the progress of successive heat waves observed in Figure 2.1, as the energy would be consumed to sublimate ices. In this regard, the depths estimated previously should be considered as upper limits to the actual processing of cometary nuclei, although the effects of this energy consumption for such long timescales are not easily constrained.

Furthermore ignoring the possibility of phase transitions implies that surface erosion cannot be considered either, as it is mainly associated with the sublimation of water ice. Estimates from the published literature indicate that the erosion rate can vary from tenths of cm up to approximately 2 m per yr for a JFC, depending on the thermal characteristics, the heliocentric distance, the inclination of the spin axis, and the cometocentric latitude of the nucleus. Huebner et al. (2006) estimated an erosion rate varying from 10 cm $\mathrm{yr}^{-1}$ to 2.1 m $\mathrm{yr}^{-1}$ for comet 46P/Wirtanen, while estimates for comet 67P/Churyumov-Gerasimenko give an average erosion rate of 0.67 to 2.9 m, depending on the thermo-physical parametrization of the surface

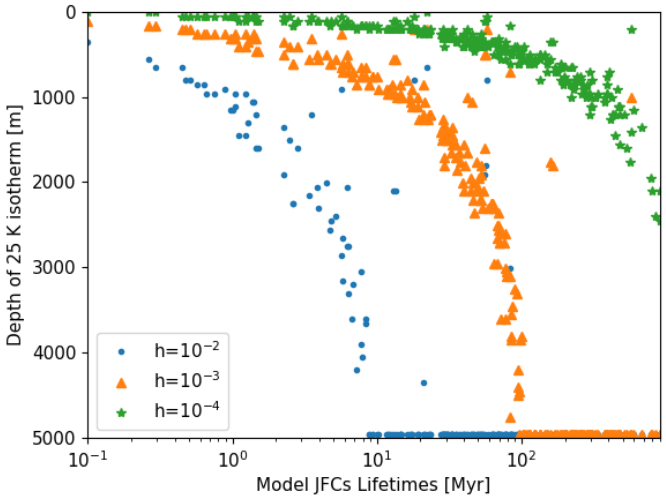


**Figure 2.5:** Maximum depths of the 25 K isotherm as a function of the inner Solar System lifetimes of the 276 simulated JFCs of our sample, for three different values of the Hertz factor.

(Keller et al., 2015). Accounting for the cumulative effect of erosion over long timescales becomes important during the active phase of JFCs, as a significant amount of processed surface material can be removed, revealing or bringing close to the surface unprocessed layers.

In Table 2.1 we present a statistical overview of the average status of an object in our sample, consisting of 276 simulated JFCs, at the moment of its first transition to JFC orbits and at the moment of its ejection from the Solar System, for the considered conductivity values. We notice that on average, a simulated JFC has already undergone sufficient heating for alteration processes to take place at considerable depths, regardless of the temperature examined and the conductivity scenario considered. This implies that a typically observed JFC should be significantly altered, with the primordial inventory of volatiles severely modified due to sublimation, gas diffusion, depletion and enrichment of internal volumes on long timescales. In particular, the processed layer is substantially larger than the estimated size of the layers involved in producing cometary activity observed for most JFCs (e.g. Huebner et al., 2006). In other words, cometary activity as it is observed today, should be produced from layers which have been substantially processed. Even if we were somehow able to observe an object transitioning to a JFC orbit – while actually knowing it is the first time this object undergoes this transition – our results imply that we would still observe an altered body. This realization highlights the importance of ac-

**Table 2.1:** Average depths [m] of the considered isotherms for three values of the Hertz factor, at distinct times of our sample of model JFCs' orbital evolution. In parentheses the standard deviations are for its value are given.

| T (K) | $h = 10^{-2}$ | $h = 10^{-3}$ | $h = 10^{-4}$ |
|---|---|---|---|
| **First transition to a JFC orbit** | | | |
| 25 | 4142.2 (1529.9) | 2561.5 (1894.0) | 651.7 (615.2) |
| 80 | 125.7 (92.3) | 50.1 (36.8) | 17.2 (23.0) |
| 110 | 27.1 (37.5) | 10.0 (19.4) | 2.1 (5.4) |
| **End of JFC phase** | | | |
| 25 | 4181.7 (1474.1) | 2575.1 (1882.8) | 656.2 (611.8) |
| 80 | 278.3 (177.6) | 99.7 (51.1) | 40.9 (28.1) |
| 110 | 107.9 (103.4) | 40.2 (39.0) | 13.4 (21.9) |

counting for the past history of each comet in order to better constrain its present thermal, physical and chemical state.

Important implications regarding cometary activity in the Centaur area can also be inferred. Recent studies have tried to link the activity of Centaurs to their orbital evolution. For example, Fernández et al. (2018) suggested that active Centaurs are prone to drastic drops in their perihelion distances unlike inactive Centaurs, for timescales of the order of $10^2$ to $10^3$ years. Guilbert-Lepoutre (2012), found that crystallization of amorphous water ice can be a source of activity, efficient at heliocentric distances up to 10-12 au, sustained though for a limited time (typically hundreds to thousands of years), implying that active Centaurs should have suffered a recent orbital change. Davidsson (2021) nuanced this result, by showing that crystallization would be efficient only up to 8-10 au, while the sublimation of $CO_2$ should be the only source of activity at distance between 10-12 au. Cabral et al. (2019); Li et al. (2020); Lilly et al. (2021) on the other hand did not detect any activity amongst various dynamically stable Centaurs. The results of these initial simulations are compatible with these predictions. Indeed, both the sublimation of moderate volatiles (such as $CO_2$) and the crystallization of amorphous water ice were triggered during the Centaur phase of our simulated JFCs, each time their perihelion distance dropped and the heat wave advanced at a layer previously unaltered. The objects examined were found to be active for a period of the order of $10^3$ yr of their $10^6$-$10^7$-year residence in the Centaur area. This activity period is not continuous, in fact the objects were recorded to be active at several shorter periods of time, on average $\sim$10 times during their Centaur lifetime, in agreement with the sporadic activity detected in Centaurs (e.g. Jewitt, 2009).

## 2.4 Next Steps Towards an Efficient Coupling

More importantly, this initial set of simulations fulfilled its primary objectives. First and foremost, these results consolidated the importance of examining the long-term orbital evolution to infer the physical and chemical characteristics of individual comets and cometary populations. The chaotic nature of their trajectories, can be the origin of substantial alterations on cometary nuclei, but can also explain, among other parameters, the compositional and activity divergences observed between cometary populations. With that in mind, we considered that it would be interesting to acquire larger samples and include in this work other cometary populations as well. This would allow direct comparisons between cometary populations (such as the JFCs and the LPCs), allowing more sophisticated conclusions on their primitive nature. Moreover it motivated us to go further back in time and examine the possibility of processing at earlier stages of their orbital evolution, during the dispersal of the planetesimal disk or their prolonged residence in their source reservoirs.

Secondly, these simulations motivated the development of a thermal evolution model, adapted to the needs of the long-term coupling to the orbital evolution of comets as this is determined by the $N$-body simulations. This adapted thermal evolution aimed at the resolution of some of the issues described in Section 2.1, prioritizing the inclusion of volatile species in the simulated comets, to better constrain their thermal processing. Special attention was given in the numerical aspects of the model seeking to resolve minor numerical issues related mainly to the grid and the intermediate timesteps, that could be a source of instabilities. Of course all these improvements, introduced specifically for this type of coupled simulations, were designed bearing in mind that the problem needs to remain manageable in terms of computational time, that in some cases in this initial approach exceeded the five days for a single simulated comet. In the following chapters, we describe all these considerations regarding our adapted thermal evolution model, both from a physics and a numerical point of view, and we review some of the methods used in this initial approach to improve the accuracy of the coupling.

# Chapter 3

# Thermal Evolution Model: Physical Processes & Parameters

In this chapter we describe the physical parametrization of our adapted thermal evolution model. We detail the thermal processes accounted for and the governing equations used to describe them. A comprehensive review of the employed parameters by other thermal evolution models is presented at every step, allowing to better justify our choices. We explain the reasons for neglecting or approximating a certain number of the aforementioned processes due to limitations imposed by the long-term nature of our simulations and the long time steps of the $N$-body simulations. Finally, we present an asynchronous ice evolution model designed for the study of the long-term evolution of volatile species in the simulated cometary nuclei.

## 3.1 Energy Conservation Equation

In order to describe the diffusion of the received solar energy from the surface towards the interior of a comet, we resolve a time-dependent, partial differential equation (PDE hereafter) expressing the energy conservation, that can be written in the general form (see also Chapter 2):

$$\rho_{bulk} c \frac{\partial T}{\partial t} + div(-\kappa \overrightarrow{grad}\, T) = \mathcal{S} \tag{3.1}$$

where $\rho_{bulk}$ (kg m$^{-3}$) is the nucleus bulk density , $c$ (J kg$^{-1}$K$^{-1}$) the nucleus' material heat capacity, $T$ (K) the temperature, $\kappa$ (W K$^{-1}$ m$^{-1}$) the nucleus effective thermal conductivity, and $\mathcal{S}$ a term incorporating the internal heat sources and sinks, related to a variety of phase transitions.

In the following subsections we provide a detailed description of all the terms appearing in Equation (3.1) for a nucleus that is modeled as a porous

aggregate of dust and ices. We use a typical composition in cometary thermal modeling (e.g. Espinasse et al., 1989; Benkhoff and Boice, 1996; Enzian et al., 1997; Coradini et al., 1997; De Sanctis et al., 2005; Marboeuf et al., 2012; Davidsson, 2021), consisting of a mixture of refractory and organic material representative of the dust component and a selection of the more abundant ice species observed on comets (e.g. Bockelée-Morvan and Biver, 2017): CO which can be considered representative of hyper-volatile species, $CO_2$ representative of moderate volatile species and $H_2O$ ice in -at least initially- amorphous phase, as indirect observational data (such as the amorphous structure of interstellar ice grains -the building blocks of comets- or its capacity of trapping and releasing volatile species far more efficiently than crystalline ice clathrates) suggest its presence in comets (Meech et al., 2009; Prialnik and Jewitt, 2022).

### 3.1.1 Bulk Density

The bulk density of the nucleus is calculated as a mass-weighted average of the compact densities of its dust and ice components, reduced by a factor expressing the porous nature of the nucleus:

$$\rho_{bulk} = (1 - \psi) \left( \sum^{i} \frac{X_i}{\rho_i^c} \right)^{-1} \tag{3.2}$$

where $\psi$ is the nucleus' porosity and $X_i$ and $\rho_i^c$ (kg m$^{-3}$) the mass fraction and compact density of the $i$-th component.

#### a) Compact Densities

For the components' compact densities we adopt common values from the published literature, wherever this is possible. Due to a lack of precise measurements on the dust composition, different assumptions on the dust nature lead to a variety of values, ranging from 1000 to 3500 kg m$^{-3}$ (e.g. Enzian et al., 1997; De Sanctis et al., 2001; Merk and Prialnik, 2003; Krause et al., 2011). In this work, we adopt the value from Enzian et al. (1997): 3000 kg m$^{-3}$, a slightly reduced estimate of the typical values (3250-3500 kg m$^{-3}$) used for silicates, which allows to account for the presence of organics. The compact density of CO ice is set at 890 kg m$^{-3}$, the density measured at the transition point between the crystalline phase $\alpha$ and $\beta$ ($\sim$61.55 K) (Clayton and Giauque, 1932; Tancredi et al., 1994). This value is in very good agreement with recent measurements by Luna et al. (2022) who measured the CO ice density at low temperatures (between 13 and 28 K) and found it to vary between 849 and 890 kg m$^{-3}$. For the compact density of $CO_2$ ice, we use a median value of 1500 kg m$^{-3}$, inferred from low temperature (between 10 and 90 K) density variations measurements by Satorre

**Table 3.1:** Compact densities of nucleus components

| Component | Value (kg $m^{-3}$) | Reference |
|---|---|---|
| $\rho_{CO}$ | 890 | Luna et al. (2022) |
| $\rho_{CO_2}$ | 1500 | Satorre et al. (2008) |
| $\rho_{H_2O_{cr}}$ | 917 | Eisenberg and Kauzmann (2005) |
| $\rho_{H_2O_{am}}$ | 940 | Ghormley and Hochanadel (1971) |
| $\rho_{dust}$ | 3000 | Enzian et al. (1997) |

et al. (2008). The compact density of crystalline $H_2O$ ice is set at 917 kg $m^{-3}$, measured at a temperature of 0 °C and standard atmospheric pressure (Eisenberg and Kauzmann, 2005). The amorphous $H_2O$ ice density is set to 940 kg $m^{-3}$, following Ghormley and Hochanadel (1971) measurements, which demonstrated that the density between the two phases is essentially the same, an observation confirmed recently by Gómez et al. (2020) who measured a density of approximately 900 kg $m^{-3}$. We summarize our choices in Table 3.1.

**b) Mass Fractions**

Internal characteristics, such as the composition and the components abundances, must be derived from activity patterns and observations of the coma (see Section 1.4.1). However such deductions are not straightforward, as many different parameters can compromise them. We can cite for example uncertainties related to the absence of uniformity in the composition, the relative abundances of volatile species (Bockelée-Morvan and Biver, 2017) or the dust to ice ratios (Choukroun et al., 2020).

Deductions from the physical characteristics of comet 67P/C-G, suggest an ice volume fraction ranging from 6% to 11% and a refractories volume fraction ranging from 16% to 21% (Choukroun et al., 2020) for a nucleus with a porosity ranging between 73% and 76% (Herique et al., 2016). For this composition, an elementary ice mixture was suggested with volume fractions of 71% for $H_2O$ ice, 14% of $CO_2$ and 15% of CO (Fulle et al., 2019), consistent with mass loss rates measured in the coma (Hassig et al., 2015; Bockelée-Morvan et al., 2016), although updated values suggest relative abundances to $H_2O$, 0.3-3% for CO and 7% for $CO_2$ (Biver et al., 2022). However, these fractions are not necessarily representative of all comets, as both individual observations (e.g. Bauer et al., 2021; Biver et al., 2021) and surveys (Ootsubo et al., 2012; Harrington Pinto et al., 2022) indicate lower CO abundances for example and a dominance of $CO_2$ over CO. In addition the relative abundances of these volatile ices to water, present a wide range of values on comets, affected also by the heliocentric distance of the observations: 0.3-26% for CO and 4-30% for $CO_2$ (Biver et al., 2022). Observations

of interstellar environments (Gerakines et al., 1999) and models on protoplanetary discs (Drozdovskaya et al., 2016), expected to shed light on the ices initially incorporated at cometary nuclei, suggest slightly higher abundances of $CO_2$ ice, with mass fractions as high as 23% and mass fractions ranging from 3% to 15% for CO ice, which signify a mass fraction of 70% for $H_2O$ ice, if minor molecules are ignored.

Given this broad spectrum of values and uncertainties, we choose a rather simplified initial composition. We set the refractories to ice ratio at one, slightly lower than the general predictions, starting our simulations with ice-rich planetesimals. The ice abundances relative to $H_2O$ ice are also generic, respecting the dominance of $H_2O$ over the other ices and the dominance of $CO_2$ over CO: $CO/H_2O$ = 5% and $CO_2/H_2O$ = 15%. This suggest an initial composition of 42% $H_2O$ ice, 6% $CO_2$ ice and 2% CO ice. We consider that all initial $H_2O$ ice is in the amorphous phase, so this initial composition does not contain any crystalline $H_2O$ ice.

**Table 3.2:** Interior composition

| Comp. | Relative Abundance | Fraction (total=1.00) |
|---|---|---|
| Dust | 1 | 0.50 |
| $H_2O$ | 1 | 0.42 |
| CO | 0.05 | 0.02 |
| $CO_2$ | 0.15 | 0.06 |

### c) Porosity

Rosetta measurements on comet 67P/C-G, indicate a highly porous nucleus, with a porosity ranging between 70 and 80% (Sierks et al., 2015; Preusker et al., 2015; Jorda et al., 2016). These measurements, providing the best constraints so far, are coming to confirm previous estimates for a low bulk density and a very high porosity on the nuclei of other visited comets (Lamy et al., 2015).

Two main approaches can be identified for establishing the porosity in thermal evolution models: (a) attempt to calculate it using a certain number of physical and geometrical assumptions for the structure of the nucleus and (b) set it at an initial fixed value.

An example of the first approach is to calculate the porosity as the empty space inside the nucleus, ensuing after the removal of all the space occupied by solid material, which for our elemental composition can be expressed as:

$$\psi = 1 - \frac{\rho_d}{\varrho_d} - \frac{\rho_{am} + \rho_{cr}}{\varrho_{H_2O}} - \sum \frac{\rho_i}{\varrho_i} \tag{3.3}$$

where $\varrho$ denotes the characteristic compact density of the non-porous solid-phase and $\rho$ the partial density, i.e. the mass per unit volume of cometary material of the different species of the nucleus (Prialnik et al., 2004; Huebner et al., 2006). Another approximation makes use of the hydrostatic equi-

librium equation and the gravitational pressure and assumes that below a certain porosity threshold, which can be calculated, the material will start compacting (Henke et al., 2012; Davidsson, 2021). The level of complexity can grow significantly if grain and pore size distributions are added, as they are important parameters for the characterization of a porous medium, although not very well constrained (Shoshany et al., 2002). Uncertainties regarding the distribution of the voids in a cometary nucleus might directly affect the calculation of the bulk density (and of the conductivity (Gundlach and Blum, 2012)), as different considerations should be made for big or smaller voids distributed between the grains. We refer the reader to Huebner et al. (2006) for a detailed review of the different calculation methods and considerations.

The most common practice, and the one we adopt in this model, is to simply preset the porosity on an initial value. Although less realistic than a calculation such as the one described by Equation (3.3), as porosity is expected to evolve with phase transitions, it has a certain number of advantages. Apart from its simplicity, it reduces the introduction of additional free parameters in the model (such as the partial densities appearing in Equation 3.3 or the grain and pore sizes distribution), related to geometrical assumptions or the behavior of refractories and ice mixtures. Moreover, it guarantees that the porosity remains always within an expected range, consistent for example with the aforementioned measurements on 67P/C-G. For our study we chose an average of these estimations (75%) as the initial and fixed value of the porosity.

### 3.1.2 Specific Heat Capacity

We calculate the specific heat capacity of the nucleus as a mass-weighted average of the specific heats of its components:

$$c = \sum^{i} X_i c_i \tag{3.4}$$

where $X_i$ is the mass fraction of the $i$-th component of the nucleus and $c_i$ (J $kg^{-1}$ $K^{-1}$) its specific heat capacity.

Regarding the specific heat capacity of the dust component, as with its density, many expressions and values can be found in the literature, depending on the assumptions on its nature and composition. It is a common practice to set it at as a constant with values ranging from 700 to 1400 J $kg^{-1}$ $K^{-1}$, with the values on the upper end being the most prevalent (e.g Ellsworth and Schubert, 1983; Prialnik et al., 2004; Huebner et al., 2006; Krause et al., 2011). Temperature dependent expressions exist as well: Haruyama et al. (1993) considered the specific heat capacity to be a linear function of the temperature with a slope of 2.5. Other works followed similar but more elaborate practices, by adopting arithmetic means for the specific heats of

silicates and organic refractories (Tancredi et al., 1994) or of terrestrial minerals (Enzian et al., 1997), setting the slope of their linear functions to 5 and 3 respectively. Malamud and Prialnik (2015) used an exponential function, obtained by fitting data of $Ni_2SiO_4$-olivine with the resulting heat capacity ranging from 0 to $\simeq$800 J $kg^{-1}$ $K^{-1}$. Recently, Davidsson (2021) fitted measurements on crystals of $Mg_2SiO_4$ (forsterite), which for temperatures from 6 to 380 K give a specific heat capacity between 0 and 965 J $kg^{-1}$ $K^{-1}$. Given this large amount of options, all within an accepted range of values we decided to adopt the temperature dependent expression of Enzian et al. (1997):

$$c_{dust} = 3T \tag{3.5}$$

which despite its simplicity is in very good agreement with more complex relations (e.g. Malamud and Prialnik, 2015) and has the advantage of being more realistic in the low temperatures area, when compared to constant values.

For the specific heat capacity of CO we employ an expression valid for temperatures up to 61.55 K from Clayton and Giauque (1932):

$$c_{CO} = 35.7T - 187 \tag{3.6}$$

Above this temperature a constant value may be applied (e.g. Tancredi et al., 1994), however in our model such a transition is not taken into account given the high rate of sublimation below this temperature (Meech and Svoren, 2004; Fray and Schmitt, 2009).

For the specific heat capacity of $CO_2$ ice, we adopt a linear fit on data taken from Giauque and Egan (1937), as suggested in Davidsson (2021), in order to obtain a similar expression as the one for CO:

$$c_{CO_2} = 6.34T + 167.8 \tag{3.7}$$

We note that although a linear fit is not necessarily the most adequate approximation, it is sufficient for the purposes of our model and is more consistent with the expressions for the other ices.

A similar expression is used for the crystalline $H_2O$ ice, taken from Klinger (1980), who fitted data from Giauque and Stout (1936):

$$c_{H_2O} = 7.49T + 90 \tag{3.8}$$

We should mention that Shulman (2004) studied the ratio $c_{H_2O}/T$, for the same data set and claimed that this empirical approximation is not valid for temperatures below 100 K (see Figure 1 in his paper). He proposed three different approximations of higher order ($T^4$-$T^6$), ensuring the asymptotic behavior of the heat capacity with the temperature. However, given that the differences between Klinger's (1980) and Shulman's (2004) approximations

**Table 3.3:** Specific heat capacities of nucleus components

| Component | Expression | Reference |
|---|---|---|
| $c_{CO}$ | $35.7T$ - 187 | Clayton and Giauque (1932) |
| $c_{CO2}$ | $6.34T$ + 167.8 | Giauque and Egan (1937) |
| $c_{H_2O}$ | $7.49T$ + 90 | Giauque and Stout (1936) |
| $c_{dust}$ | $3T$ | Enzian et al. (1997) |

are not very significant for the range of temperatures (>20 K) considered in our model, we decided to retain the expression of Klinger (1980), mainly for its simplicity. Similar objections can apparently be raised on the expressions for the other ices as well, but once again we chose to maintain the simple, yet sufficient in the current work's context, linear approximations.

Finally, due to the lack of direct measurements and thus of an expression for the specific heat capacity of amorphous $H_2O$ ice, we followed the common practice and used the crystalline $H_2O$ ice expression in order to predict its variation with the temperature. We summarize the expressions for the specific heat capacities presented previously on Table 3.3.

### 3.1.3 Effective Thermal Conductivity

In order to calculate the effective thermal conductivity we need to take into account the heat transport mechanisms at work in a porous medium such as a comet's nucleus. In Figure 3.1 a schematic representation of these mechanisms is given: (a) conductive heat transport through the solid material, (b) radiative heat transport and (c) diffusive heat transport due to gas movement within the pores. In this work, the heat transport due to the gas diffusion is neglected, as it is taking place in very short timescales that we are unable to resolve and we focus on the conductive and radiative transport mechanisms (see Figure 3.2 and Section 3.1.4 for more details).

The effectiveness of the conductive heat transport depends on the conductivity of the solid components on the one hand and on the porosity and the granular nature of the nucleus on the other. The conductivity of the solid, as in the case of the density and the specific heat capacity, is calculated as a mass-weighted average of the conductivities of the solid components:

$$\kappa_{solid} = \sum^{i} X_i \kappa_i \tag{3.9}$$

where $X_i$ and $\kappa_i$ (W $m^{-1}K^{-1}$) are the mass fraction and the conductivity of the $i$-th component respectively.

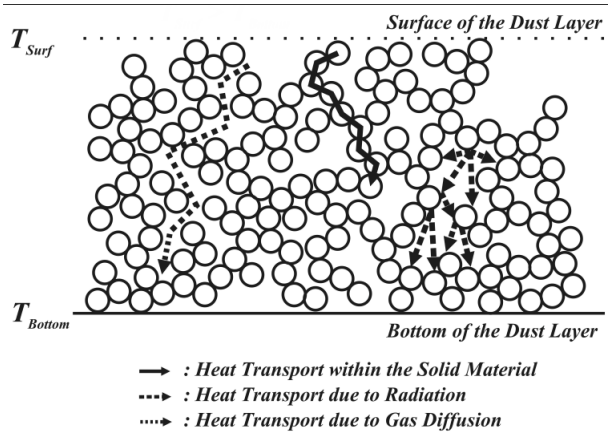


**Figure 3.1:** Mechanisms of heat transport in a porous medium (Figure adapted from Gundlach and Blum (2012)).

### a) Solid Components Conductivities

The conductivity of the dusty component, as is the common practice, is fixed at a constant value. A variety of different values have been used throughout the years, usually volumetric averages of different mixtures, representative of cometary materials: silicate (Ellsworth and Schubert, 1983), terrestrial minerals (Enzian et al., 1997), basalt (Tancredi et al., 1994), fused quartz (Haruyama et al., 1993). Despite the different considerations, a convergence in the range 2-5 W $m^{-1}K^{-1}$, with a preference for values on the high end of this range. In our model we use an average value (2.5 W $m^{-1}K^{-1}$), close to the lower end of this range, assuming that the dust component is a mixture of silicates with conductivity of 4.2 W $m^{-1}K^{-1}$ (Ellsworth and Schubert, 1983) and organic material, usually modeled with a conductivity an order of magnitude lower than silicates.

To our knowledge, an expression or measurements for the conductivity of CO ice have not been proposed so far. An expression for the amorphous $H_2O$ ice is often used instead, under the assumption that CO ice in very low temperatures ($<$20 K) is expected to be in an amorphous phase (Escribano et al., 2013; Cazaux et al., 2017) with a very low conductivity (e.g. Enzian et al., 1997; Orosei et al., 1999; Davidsson, 2021). The only actual measurements we could find in the literature come from the experimental studies of Muñoz Caro et al. (2016) and Sumarokov et al. (2019). They both measured high conductivities around 10 W $m^{-1}K^{-1}$ at 3 K, quickly dropping to 1 W $m^{-1}K^{-1}$ for temperatures between 7-20 K. Given these measurements, we set the CO conductivity at 0.1 W $m^{-1}K^{-1}$ following the decline trend demonstrated by Muñoz Caro et al. (2016) and the expected low conductivities for amorphous ices.

Finding measurements or a widely used expression for the $CO_2$ ice has

**Table 3.4:** Conductivities of nucleus components

| Component | Value/Expression | Reference |
|---|---|---|
| $\kappa_{CO}$ | 0.1 W $m^{-1}K^{-1}$ | Muñoz Caro et al. (2016) |
| $\kappa_{CO_2}$ | $93.4/T$ | Mellon (1996) |
| $\kappa_{H_2O_{am}}$ | $2.34{\cdot}10^{-3}$T $+2.8{\cdot}10^{-2}$ | Klinger (1980) |
| $\kappa_{H_2O_{cr}}$ | $567/T$ | Klinger (1980) |
| $\kappa_{Dust}$ | 2.5 W $m^{-1}K^{-1}$ | - |

been challenging as well. As in the case of CO ice, the amorphous $H_2O$ ice expression is used as well (e.g Orosei et al., 1999; Davidsson, 2021), based on the same assumption for low temperature ices. Mellon (1996) in a study of the $CO_2$ ice content in Martian polar deposits, used a temperature dependent expression:

$$\kappa_{CO_2} = 93.4/T \tag{3.10}$$

obtained from fitted data from Kravchenko and Krupskii (1986). We compared this expression to the only measurements we could lay hands on from Sumarokov et al. (2003) and we found a good match between the two data sets for temperatures above 10 K. We should note here, that Seiferlin et al. (1996) measured conductivities one or two orders of magnitude lower (0.01-0.08 W $m^{-1}K^{-1}$) for porous $CO_2$ ice in the range 90-130 K, which are compatible with interpolated data from Sumarokov et al. (2003).

For the conductivity of crystalline $H_2O$ ice we make use of the expression proposed by Klinger (1980):

$$\kappa_{H_2O_{cr}} = 567/T \tag{3.11}$$

and for the conductivity of the amorphous $H_2O$ ice we use a theoretical estimate from the same work (Klinger, 1980):

$$\kappa_{H_2O_{am}} = 2.34 \cdot 10^{-3}T + 2.8 \cdot 10^{-2} \tag{3.12}$$

as is the general practice in thermal evolution modeling of comets (e.g. Enzian et al., 1997; Guilbert-Lepoutre et al., 2011). We should mention that Kouchi et al. (1992) measured an amorphous $H_2O$ ice conductivity four orders of magnitude lower than Klinger (1980) in the range of 125-135 K. However, as the conductivities calculated by Equation (3.12) are already very low and as the amorphous ice is expected to crystallize in this range of temperatures, we decided that Equation (3.12) is sufficient for the purpose of this work. We sum up all the values and expressions for the components conductivities on Table 3.4.

### b) Corrections for the Porosity and the Granular Nature of the Material

The effects of the porosity and the granular nature of the medium to the effective thermal conductivity are introduced in the form of reduction factors, aiming to readjust the solid conductivity calculated in Equation (3.9).

To account for the reduced heat conduction due to porosity we can simply multiply the solid conductivity by a generic factor $\phi < 1$. A variety of geometrical considerations have been proposed for the calculation of this reduction factor, focusing on the microstructure of the material, the cross-section area of the pores and the volume of the void inside the nucleus (Prialnik et al., 2004). For a comprehensive review of the different approximations and their historical evolution we refer the reader to Prialnik et al. (2004) and Huebner et al. (2006). In our model we use the Russell's correction factor (Russell, 1935), an expression used extensively in models for the thermal evolution of comets (e.g. Espinasse et al., 1989; Rickman et al., 1990; Coradini et al., 1997; Orosei et al., 1999; Guilbert-Lepoutre et al., 2011; Marboeuf et al., 2012):

$$\phi = \frac{\psi^{2/3} f + (1 - \psi^{2/3})}{\psi - \psi^{2/3} + 1 - \psi^{2/3}(\psi^{1/3} - 1) f}, \tag{3.13}$$

where $f$ is the ratio of the solid to the radiative conductivity, which can be calculated as:

$$\kappa_{rad} = 4 \epsilon \sigma r_p T^3 \tag{3.14}$$

with $\epsilon$ the material's emissivity, $\sigma$ (W m$^{-2}$ K$^{-4}$) the Stefan-Boltzmann constant, $r_p$ (m) the radius of the pores and $T$ (K) the temperature of the matrix.

Considering that the solid matrix is composed of small icy dust grains, an additional reduction should be introduced to describe conduction only through a small fraction of the total surface area. This correction, known as the *Hertz factor*, introduced to comets' thermal modeling by Mendis and Brin (1977), can be calculated as the ratio of the contact area to the cross section of a spherical grain (Huebner et al., 1999; Kossacki et al., 1999a). Laboratory measurements give a wide variety of values, ranging from $10^{-1}$ to $10^{-4}$ (Huebner et al., 2006). However a consensus seems to have been established around values of the order of $10^{-2}$ (e.g. Huebner et al., 1999; Davidsson and Skorov, 2002; Shoshany et al., 2002; Lasue et al., 2008; Prialnik and Rosenberg, 2009; Gundlach and Blum, 2012), which is the value we use in our model.

Laboratory experiments demonstrate that the Hertz factor can change through a process known as *ice sintering* (Swinkels and Ashby, 1981; Kossacki et al., 2015). Ice sintering is a form of metamorphism that changes the

microstructure of an aggregate of grains, leading to the growth of the grains contact area (or *neck*), hence of the Hertz factor, as a result of a variety of temperature-driven diffusion mechanisms (Gundlach et al., 2018; Molaro et al., 2019). Aside from the expected modifications on the thermal conductivity, an increase in the cohesiveness of the loose material and the tensile strength was observed (Kossacki et al., 1994). In this work, this effect is not taken into account on the one hand because we lack the necessary resolution to integrate this type of short-time processes and on the other hand because at the temperatures that sintering is taking place, the radiative term becomes dominant, so no significant modifications are expected in the effective thermal conductivity (Kossacki et al., 1994).

Accounting for the above corrections and the contribution of the radiative transport through the pores given in Equation (3.14), the expression for the effective thermal conductivity used in this work is:

$$\kappa_{eff} = h\phi\kappa_{solid} + \kappa_{rad} \tag{3.15}$$

which is expected to be a few orders of magnitudes lower than the bulk conductivity of the compacted material. We note that the conductive term in Equation (3.15) dominates over the radiative term at low temperatures (T$<$100 K). Above this threshold the contribution of the radiative term becomes more significant and above 150 K dominant, as the heat is mainly transported by radiation through the pores (Huebner et al., 2006).

We should note that various suggestions for the calculation of the effective thermal conductivity can be found in the published literature. Some incorporate the Hertz factor directly in the porosity correction (e.g. Steiner and Kömle, 1991; Shoshany et al., 2002), while others impose directly an initial constant effective conductivity, within an expected range (after reduction), a solution that is certainly more numerically efficient (Prialnik et al., 1987; Kuhrt and Keller, 1994; Benkhoff and Huebner, 1995). However, as the conductivity is the key parameter in our model, we opted for a more complicated, yet realistic, solution. Our main concern was to respect the constraints suggested for comet 67P, which so far are the most reliable estimates on the effective thermal conductivity. Indeed, for a porosity of 75% and a Hertz factor $h = 10^{-2}$ our resulting thermal conductivity falls in the range of $10^{-3}$-$10^{-4}$, in good agreement with the 67P's estimates (Keller et al., 2015).

### 3.1.4 Internal Sources and Sinks

The last term appearing in Equation (3.1), denotes the internal heat sources and sinks. In most thermal evolution models the main contributions to this term come from the latent heat consumed or released during the sublimation and condensation of ices (e.g Benkhoff and Spohn, 1991; Huebner et al., 2006). Additional energy sources contributing to the total

energy budget have been considered such as heat transport by gas diffusion in the porous matrix (e.g Benkhoff and Huebner, 1995), internal heating by radioactive elements (e.g. Prialnik et al., 1987; Prialnik and Podolak, 1995; De Sanctis et al., 2001; Guilbert-Lepoutre et al., 2011) or energy released during the exothermic process of crystallization of amorphous water ice (e.g. Bar-Nun et al., 1985; Schmitt et al., 1989).

In our model this term is set to zero, implying that all phase transitions are neglected, at least in a classic direct way. As a consequence, our model does not describe faithfully the energy conservation during the active phases of the thermal evolution of a comet when phase transitions are at the origin of cometary activity. To explain this -admittedly- unconventional choice, it is essential to understand the timescales at which the main thermal processes (i.e. heat and gas diffusion, volatile sublimation and crystallization of amorphous water ice) operate in a comet's nucleus.

**a) Characteristic Timescales**

The timescale of the heat diffusion can be derived from Equation (3.1) without source or advection terms. Considering a layer of finite thickness $\Delta r$, at a specified temperature $T$, the thermal timescale can be written as:

$$\tau_{th} = \frac{\rho c (\Delta r)^2}{\kappa} \tag{3.16}$$

where all the symbols hold the same meaning as previously.

In a similar manner, the gas diffusion timescale can be deduced from the mass conservation equation (see Section 3.3) (Huebner et al., 2006):

$$\tau_{gas} = \frac{3}{8} \frac{(\Delta r)^2}{\psi r_p} \left( \frac{2\pi m}{\kappa T} \right)^{\frac{1}{2}} \tag{3.17}$$

with $m$ the molecular mass of a given volatile and the rest of the symbols as described previously.

To estimate the sublimation timescale we can use the surface mass release rate (Huebner et al., 2006):

$$Q = P_{sat}(T) \left( \frac{m}{2\pi k_B T} \right)^{\frac{1}{2}} \tag{3.18}$$

where $P_{sat}$ (Pa) is the saturation vapor pressure of a given volatile. Assuming that $Q = \rho / \tau_{sub}$, the timescale of sublimation of the $i$-th volatile species can be written as a function of the temperature as:

$$\tau_{sub} = \frac{\rho}{P_{sat} \sqrt{\frac{m}{2\pi k_B T}}} \tag{3.19}$$

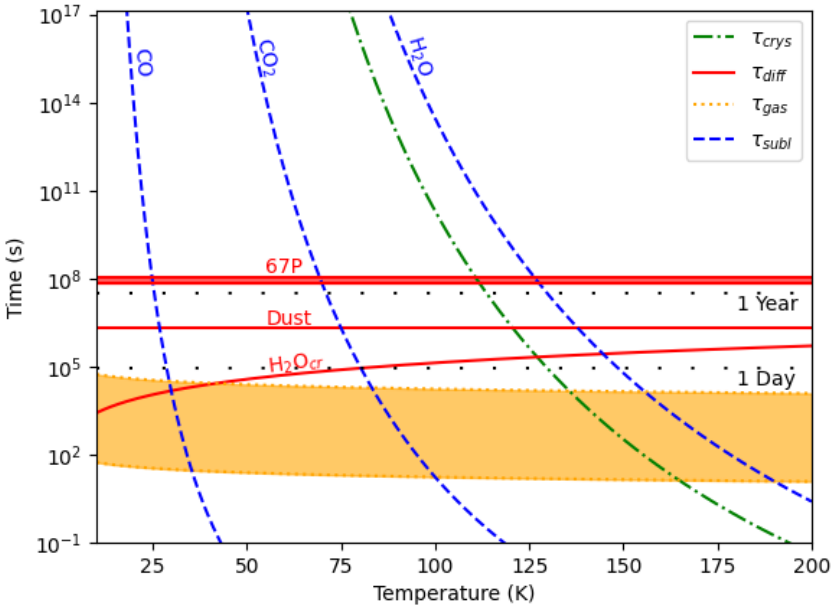


**Figure 3.2:** Characteristic timescales of the main physical processes taking place in a comet's nucleus: (a) Crystallization of amorphous $H_2O$ ice denoted by the green dashed dotted line, (b) Sublimation of different volatile species denoted by the blue dashed lines, (c) Gas diffusion within the pores for pores' radius between $10^{-3}$ and $10^{-6}$ denoted by the orange dotted lines and the orange shaded area, (d) Heat diffusion in nucleus of different compositions: pure dust, pure crystalline $H_2O$ ice and a nucleus with characteristics resembling those of comet 67P/Churyumov-Gerasimenko. The black loosely dotted lines serve as indicators for the timescales.

Finally, the timescale of the crystallization is given in the form of an activation law, relating the time of crystallization to the temperature, proposed by Schmitt et al. (1989) who measured the crystallization rate of pure $H_2O$ ice for temperatures in the range 125-150 K:

$$\tau = Ae^{-E_a/kT} \tag{3.20}$$

where $A = 9.54{\cdot}10^{-14}$ s and $E_a/k = 5370$ K, with $E_a$ the activation energy.

In Figure 3.2 these timescales are plotted as a function of the temperature, for a layer of thickness $\Delta r = 1$ m, in a nucleus with a porosity of 0.5 and for typical values of the bulk density, the heat capacity and the conductivity, as detailed in the previous sections. We notice that the considered thermal processes operate on very different timescales, with the differences reaching multiple orders of magnitude. For example, the thermal diffusion timescale

in a compact dusty layer is of the order of months ($10^6$ s), while the gas diffusion timescale, regardless of the pore size, is of the order of hours at best. The sublimation rates for the different ices considered accelerate considerably with the temperature, especially for $CO_2$ and $H_2O$ ices, which can sublimate in a matter of a few minutes provided high enough temperatures. The crystallization timescale is highly variable as well. For temperatures below 80 K it exceeds the Solar System's lifetime, setting a time threshold below of which the calculation of the crystallization rate becomes meaningless. However, for temperatures between 100 and 110 K it drops to the order of years and for temperatures in the range of 125-150 K to typical timescales of laboratory experiments (Jewitt, 2009). Coupling thermal processes with so diverse timescales was already a challenge and a source of instabilities on its own for thermal models in the past (e.g. Orosei et al., 1999; Prialnik et al., 2004), without adding comets' dynamical evolution which is a billion-year process.

To overcome this difficulty we do not take into consideration the thermal processes, the timescales of which are not resolvable during the time steps used in our model, as imposed by the output step of the $N$-body simulations. This choice entails that no gas diffusion and hence no heat transport within the pores is accounted for in our model. To do so, very small time steps of the order of minutes are necessary, which would render our simulation extremely lengthy, if not numerically prohibitive. Similarly, phase transitions and their contributions to the total thermal budget through the latent heat exchanged during sublimation or recondensation are not considered as well. On the contrary, the crystallization of amorphous $H_2O$ ice can be estimated, using Equation (3.20), but we cannot model the instantaneous trapped gases release during crystallization as other models do (e.g. Espinasse et al., 1989; Orosei et al., 1999; Davidsson, 2021). This leaves us with the heat diffusion, that can be resolved -provided an appropriate numerical grid- in timescales compatible with those of the dynamical evolution. Of course this demands a reduced time step as well, but reducing the time step in the order of the year is a far more reasonable and realistic choice numerically.

**b) Heating by Radioactive Elements**

As described in Section 1.4.2 several studies have tried to establish the effects of internal heating, following the decay of radioactive elements during the early stages of icy bodies' evolution (Prialnik et al., 1987; Haruyama et al., 1993; Prialnik and Podolak, 1995; De Sanctis et al., 2001; Choi et al., 2002; Merk and Prialnik, 2006; Guilbert-Lepoutre et al., 2011; Davidsson et al., 2016; Mousis et al., 2017; Davidsson, 2021; Golabek and Jutzi, 2021). A first remark that we have to make at this point is that although the consideration of radioactive elements in thermal evolution models is a standard practice, their actual presence in cometary nuclei is still debatable. For ex-

ample, isotopic analyses of cometary samples from comet 81P/Wild 2 did not find any traces of radioactive elements such as $^{26}$Al (Levasseur-Regourd et al., 2018; Malamud et al., 2022). The uncertainties surrounding the timing of the formation of planetesimals can also be an important factor for the inclusion or not of radioactive elements on cometary nuclei, as they are expected to extinct after a few million years. For example objects formed after 3.5 Myr after the CAI formation are not expected to be significantly affected by radioactive heating (Golabek and Jutzi, 2021). Without the intention to argue for or against the presence of radioactive elements on cometary nuclei, we should note that what these studies have highlighted is how much the outcome of early processing depends on poorly known characteristics such as the timescale of formation of cometary nuclei or their formation mechanism (e.g. Prialnik et al., 2004; Merk and Prialnik, 2006; Golabek and Jutzi, 2021), their initial size (e.g. Prialnik and Podolak, 1995; Davidsson, 2021), or their conductivity (e.g. Haruyama et al., 1993). With that in mind, we decided that accounting for radioactive heating would only add a layer of uncertainty and a number of free parameters, without contributing further to our current understanding of the early phases of cometary evolution. We therefore choose to exclude that source of heating and focus on a key aspect that has not been studied before: the influence of the early dynamical evolution and the effects of varying insolation on cometary nuclei.

## 3.2 Boundary Conditions

With the internal heat sources set to zero, the only source of energy we consider in our model is the solar irradiation, which is a function of the comet's heliocentric distance and thus of its dynamical evolution. It is accounted for through the surface boundary condition of Equation (3.1) where an energy balance is calculated, requiring that:

$$\rho_{bulk} c \frac{\partial T}{\partial r} + div(\Phi) = 0 \tag{3.21}$$

which in spherical coordinates, yields:

$$\rho_{bulk} c \frac{\partial T}{\partial r} + \left( \frac{2}{R} \Phi + \frac{1}{r^2} \frac{\partial \Phi}{\partial r} \right) = 0 \tag{3.22}$$

with $\Phi$ (W m$^{-2}$) the radial energy flux, describing all the energy exchanges between the surface and an infinitely thin subsurface layer. It can be calculated as an average of the energy balance in an infinitely thin subsurface layer. This flux is actually an average of the flux entering the layer and a flux including the solar irradiation and the thermal emission (Mekler et al., 1990; Prialnik, 1992):

$$\Phi = \frac{1}{2}\left(\sigma\epsilon T^4 - (1-\mathcal{A})\frac{F_\odot}{d_h^2}\cos\zeta - \kappa\frac{\partial T}{\partial r}\right) \tag{3.23}$$

where $\mathcal{A}$ is the Bond's albedo, $F_\odot$ (W m$^{-2}$) the solar constant, $d_h$ (au) the heliocentric distance, $\zeta$ (rad) the local zenith angle while the rest of the symbols have the same meaning as previously. The terms on the right hand side of Equation (3.23) describe, from left to right: (a) the thermal emission of the nucleus, (b) the incoming solar energy and (c) the heat transported towards the interior.

If $\Delta r$ is the layer's thickness, then the radial derivative of the flux for this layer is:

$$\frac{\partial\Phi}{\partial r} = \frac{1}{\Delta r}\left(\sigma\varepsilon T^4 - (1-\mathcal{A})\frac{F_\odot}{d_h^2}\cos\zeta + \kappa\frac{\partial T}{\Delta r}\right) \tag{3.24}$$

The root of Equation (3.22), with $\Phi$ and $\partial\Phi/\partial r$ given from Equations (3.23) and (3.24) is the nucleus' surface temperature at a given moment and position in the Solar System.

The local zenith angle is set to zero. This choice implies that we are always examining the thermal processing at the subsolar point, i.e. the surface area receiving the maximum of the solar energy. Obviously, this is not representative of the entire nucleus. However, given the long-term nature of our simulations, changes on the rotational characteristics of cometary nuclei, due to nongravitational forces for example (Yeomans et al., 2004), are very probable. These may change the local zenith angle of a given point in a cometary surface and by consequence the amount of the received energy. By fixing our model to the subsolar point we avoid the addition of an extra free parameter, such as the long-term changes of the rotational characteristics of cometary nuclei, which cannot be accounted for in a statistically significant manner anyway, and we make sure that we examine constantly the maximum effects of solar irradiation, although other values such as an average or a mean can be more realistic.

In the center of our objects we consider that the heat flux is vanishing, so that if at the center of the nucleus the radius is $r_0$ (Prialnik et al., 2004):

$$\Phi(r_0) = 0 \tag{3.25}$$

## 3.3 Asynchronous Coupling

As we explained in Section 3.1.4, the short timescales of gas diffusion and our obligation to use relatively large time steps, do not allow us to treat the motion of gas molecules inside the nucleus and hence the ice content evolution in a conventional way. Ideally, this question is answered by the resolution of the mass conservation equation (e.g. Espinasse et al., 1989; Benkhoff and

Boice, 1996; Coradini et al., 1997; Davidsson and Skorov, 2002), which can be written in the general form:

$$\frac{\partial \rho}{\partial t} + div(\overrightarrow{grad}\ \Phi) = Q \tag{3.26}$$

where $\rho$ (kg $m^{-3}$) is the density of the $i$-th component, $\Phi$ (molecules $m^{-2}$ $s^{-1}$) is the gas molecules flux and $Q$ is the gas source term, describing the associated processes taking place (sublimation, condensation, gas release). It is possible to resolve this equation for every component separately by assuming low gas densities inside the nucleus, implying more collisions between the gas particles and the pore walls, than between the gas particles themselves (Orosei et al., 1999).

As this direct approach is numerically challenging in the context of this work, but an estimation of the evolution of the ice content is necessary for the assessment of the thermal processing of a comet's nucleus, we turned to an alternative solution. We adopt the *asynchronous coupling* solution, proposed initially in Schorghofer (2008) and developed further in Schorghofer (2010) and Schorghofer (2016). It is based on the idea that we are dealing with temperature-driven processes, so if we can calculate averages of the temperature variations over a given time period, for example during a dynamical step, we can indirectly estimate the evolution of the otherwise inaccessible processes mentioned previously. To do so, a thermal evolution model is employed to calculate the temperature and vapor pressure variations in a small body's interior within a time step. With the internal temperature and pressure conditions established, an ice evolution model is employed to estimate the evolution of the ice components during the current dynamical time step. We followed the general principles of this method, with some necessary adjustments imposed by our orbit-averaging technique, which is based on equilibrium-temperature averages, suggesting a different way of calculating the temperature and vapor pressure averages.

### 3.3.1 Ice Evolution Modeling

Assuming a buried ice table inside the nucleus, we can calculate the developed vapor flux between the surface and the ice table as:

$$J = D_{eff} \frac{P_{surf} - P_{sat}(d)}{d} \tag{3.27}$$

where $D_{eff}$ (s) the effective diffusion coefficient, $P_{surf}$ (Pa) the surface pressure, here set to zero, $P_{sat}$ (Pa) the average saturation vapor pressure and $d$ (m) the depth of the ice table. The effective diffusion coefficient is a function of the local diffusion coefficient ($m^2 s^{-1}$), which can be written as:

$$D = \frac{\pi}{8+\pi} \frac{\psi}{1-\psi} \frac{v_{th}}{\xi} r_p \tag{3.28}$$

where $\psi$ is the nucleus' porosity, $v_{th} = \sqrt{8k_bT/\pi m}$ (ms$^{-1}$) the mean thermal speed, $\xi$ the tortuosity, an intrinsic property of the porous medium, defined as the ratio between the actual flow path to the straight distance between the two ends of this flow path (Bear, 1988) and $r_p$ (m) the pores' radius. We note that many expressions for the local diffusion coefficient exist, such as the Knudsen's formula (Espinasse et al., 1991), or the Clausing equation (Steiner, 1990). Here, for consistency reasons, we use Equation (3.28), proposed in Schorghofer (2016). Guilbert-Lepoutre (2014) reported that vapor fluxes calculated with different local coefficients are all in good agreement by a factor that does not exceed the order of unity.

With these considerations we calculate the effective diffusion coefficient from the surface to the ice table:

$$D_{eff} = d \left( \int_0^d \frac{d}{D} \right)^{-1} \tag{3.29}$$

The erosion rate of the ice table moving towards the interior, as ices sublimate and vapor escapes through the pores is evaluated as (Orosei et al., 1999; Huebner et al., 2006):

$$\frac{dr}{dt} = \frac{-J}{\rho} \tag{3.30}$$

with $\rho$ (kg m$^{-3}$) the compact density of the $i$-th ice component.

Replacing the vapor flux calculated in Equation (3.27) in the above expression and rearranging, yields:

$$d(r)\frac{dr}{dt} = D_{eff}\frac{P_{sat}(T)}{\rho} \tag{3.31}$$

which upon integration over a given time interval, here the dynamical time step $\Delta t$, gives the advancement of the ice table during this interval:

$$d(\Delta t) = \left( d(0) + 2D_{eff}\frac{P_{sat}}{\rho} \right)^{\frac{1}{2}} \tag{3.32}$$

We should note, that this analytical method does not explicitly account for internal processes such as gas flow or the re-condensation below and above the ice interfaces. As a consequence, we cannot consider explicitly internal heat sources or sinks such as energy released during ice re-condensation or crystallization of amorphous water ice. Instead we account for the two processes that dominate the thermally induced activity in comets, i.e. the heat and the gas diffusion. This allows a realistic first order estimate of a cometary nucleus evolution.

### 3.3.2 Saturated Vapor Pressure

The calculation of the saturated vapor pressure, appearing in Equation (3.32), plays a key role in the estimation of ice retreat and survival during a comet's lifetime. As with the other parameters, we tried to use the most representative and up to date values, while keeping the calculation as simple as possible wherever this was possible. For a comprehensive review of the empirical expressions for ice molecules present in cometary nuclei we refer the reader to Fray and Schmitt (2009).

For the needs of our study we tested expressions proposed by Clayton and Giauque (1932), Brown and Ziegler (1980), Fanale and Salvail (1984), Fanale and Salvail (1990), Orosei et al. (1999), Huebner et al. (2006), Feistel and Wagner (2007) and Fray and Schmitt (2009) for the ices considered in our model: CO, $CO_2$ and $H_2O$ .

We found more or less a good agreement between the different relations for $CO_2$ and $H_2O$ ices, the best documented molecules among the three considered here. Most of the discrepancies were observed at low temperatures, with the relation proposed by Huebner et al. (2006) being the least consistent, as expected given its limited domain of validity. For these two molecules we employ a simple empirical expression obtained from the Clausius-Clapeyron equation, proposed by Fanale and Salvail (1984) and Fanale and Salvail (1990):

$$P_{sat}(T) = Ae^{-B/T} \tag{3.33}$$

where the coefficients $A$ and $B$ for $CO_2$ are 107.9 $10^{10}$ Pa and 3148 K and for $H_2O$, 356 $10^{10}$ Pa and 6141.667 K respectively. This expression is in excellent agreement with more complex expressions like the ones proposed by Brown and Ziegler (1980) and Orosei et al. (1999), while using only two terms and coefficients. The expression for the $H_2O$ presented some important differences in low temperatures with the more accurate and complex relation proposed by Feistel and Wagner (2007). However, the calculated pressures are so low for both expressions, that no significant consequences are recorded in our model.

Important differencies were observed among the available expressions for CO ice, with severe implications regarding its survival during a comet's orbital evolution. In Figure 3.3, we notice that Equation (3.33) with coefficients proposed by Fanale and Salvail (1990) presents important differences compared to the other expressions by one or two orders of magnitude. Fray and Schmitt (2009) ex-

**Table 3.5:** CO vapor pressure polynomial coefficients

| Coefficient[1] | |
|---|---|
| $A_0$ | 1.80741183(+1) |
| $A_1$ | -7.69842078(+2) |
| $A_2$ | -1.21487759(+4) |
| $A_3$ | 2.73500950(+5) |
| $A_4$ | -2.90874670(+6) |
| $A_5$ | 1.20319418(+7) |

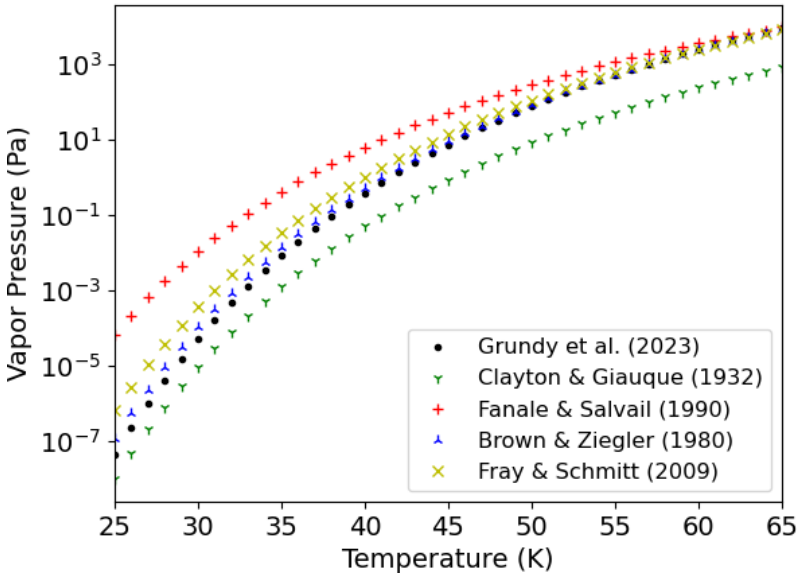


**Figure 3.3:** Saturation vapor pressures for CO ices over temperatures between 25-65 K, as proposed by different studies (see labels and text).

plained that this discrepancy is related to an overestimation by 10% of the triple point pressure and therefore the resulting relation is that of the liquid-gas equilibrium. Between the remaining expressions it is unclear which one is the more reliable. We selected the relation proposed by Brown and Ziegler (1980), which can be considered to be an average of them all, and which is in very good agreement with recent low-temperature vapor pressure measurements by Grundy et al. (private communication). This relation is a polynomial of the general form:

$$ln(P_{sat}) = A_0 + \sum_{i=1}^{5} A_i T^i \tag{3.34}$$

where the coefficients are given in Table 3.5. We note that the Huebner et al. (2006) proposed relation is not represented in Figure 3.3 due to its reduced domain of validity (50-70 K). Using this relation instead of the one proposed by Fanale and Salvail (1990), has important implications on the survival of CO ice, as an order of magnitude lower vapor pressure suggests lower sublimation rates for given temperatures and therefore longer retention time and therefore ice interfaces closer to the surface.

**Table 3.6:** Thermal model's physical parameters

| Parameter | Symbol | Value | Units |
|---|---|---|---|
| Bond's Albedo | $\mathcal{A}$ | 0.04 | - |
| IR Emissivity | $\varepsilon$ | 0.96 | - |
| Hertz factor | $h$ | 0.01 | - |
| Mean Pore Radius | $r_p$ | $10^{-6}$ | m |
| Tortuosity | $\xi$ | 1 | - |
| Local zenith angle | $\zeta$ | 0 | rad |
| Porosity | $\psi$ | 0.75 | - |
| Radius | R | 5000 | m |
| Initial Temperature | T | 10 | K |

## 3.4 Parameters of the Nominal Object

For the remaining key parameters we selected typical values from the published literature (Huebner et al., 2006). These choices are presented in Table 3.6. For example for the Bond's albedo and the emissivity we chose 0.04 and 0.96 respectively, which are the values used almost exclusively in thermal evolution models for more than three decades (Huebner et al., 2006) and those that have been measured by space missions on different comets (e.g. Keller et al., 1986; Brownlee et al., 2003; A'Hearn et al., 2005; Li et al., 2013).

The radius of our nominal object was arbitrarily set at 5 km. There is no particular argument to support this choice, except that it can be considered as a typical size for a JFC parent body (e.g. Knight et al., 2023) and that it allows a comprehensive view of the possible processing without being numerically compromising. By choosing a larger or smaller initial size, we would only allow for bigger or smaller chances for hyper-volatile retention at bigger depths (Davidsson, 2021; Kral et al., 2021; Parhi and Prialnik, 2023). However no significant changes in the physical parametrization of the model are expected. Of course larger initial size implies bigger grids (see Chapter 4) and therefore longer calculations and vice versa.

The initial temperature is set at 10 K, significantly lower than the sublimation temperatures of hyper-volatiles (Meech and Svoren, 2004; Fray and Schmitt, 2009). This choice allows the condensed CO ice to be present in its solid state initially, as the net sublimation rate at this temperature is very low (see also Figure 3.2).

[1] The number in parenthesis denotes the power of ten by which the preceding number is to be multiplied.

# Chapter 4

# Thermal model: Numerical Methods

The main objective of our model is to calculate, as accurately as possible, the temperature in the interior of our simulated comets at every time step provided by the $N$-body simulations. Unlike other models where the time step was freely chosen in order to achieve a stable solution, in our case it is limited by the dynamical time steps and the long-term nature of our simulations, which impose a slightly different approach on our resolution method.

Some general considerations regarding our thermal evolution model's dimensions are presented in Section 4.1. A detailed description of the numerical aspects of our model, starting from the discretization of the calculation domain, is given in Sections 4.2 and 4.3. In Sections 4.4 and 4.5 we describe the spatial and temporal discretization of Equation (3.1) in our model. In Section 4.6 we detail the treatment of the boundary conditions and in Section 4.7 we illustrate the resolution technique for the system of the discretized equations. Finally in Section 4.8, we present an outline of the execution scheme of our model.

## 4.1 A 1D Thermal Evolution Model

Although most of the comets that have been observed closely (e.g. 1P/ Halley, 19P/Borrelly, 81P/Wild, 9P/Tempel 1, 103P/Hartley, 67P/C-G) present irregularly shaped nuclei, the most convenient practice in their modeling is to consider a spherical symmetry, in order to keep the number of free parameters on a manageable level and render the solution of the problem feasible (Huebner et al., 2006).

Most of the thermal evolution models for cometary nuclei are restricted to one dimension -the radial- and consider a uniform distribution of the solar energy all over the surface providing a spherical average of the energy

received by the nucleus, an approximation commonly known as the 'fast rotator'. This approximation permits the adaptation of larger time steps and reduces drastically the computation time, but is inadequate for the resolution of seasonal and diurnal variations. To take them into account a 'slow rotator'approximation should be adopted, imposing smaller time steps, of the order of the spin period, prolonging the computation time greatly. Of the models adapting a 'slow rotator'approach, the simplest ones, known as 1.5-D models, consider a single cell/point, usually placed on the equator and follow its temperature variations as it rotates around the spin axis (e.g. Benkhoff and Boice, 1996; Capria et al., 1996).

An evolution of these 1.5-D models was to examine not only a single point on the equator, but a number of points spread out along a meridian, allowing the incorporation of latitudinal fluxes in the model (e.g. Enzian et al., 1997). These type of models are known as 2.5-D models. The next step was to consider both latitudinal and diurnal effects, in what is known as a quasi 3-D approach, as it did not account for latitudinal heat conduction (e.g. Gutiérrez et al., 2000; Julian et al., 2000; Lasue et al., 2008). These models followed the calculations of 1.5-D structure but used boundary conditions for the entire sphere (Rosenberg and Prialnik, 2007). Naturally, the next step were fully 3-D models, considering both meridional and azimuthal fluxes with boundary conditions for the entire sphere (Rosenberg and Prialnik, 2007; Guilbert-Lepoutre et al., 2011). It goes without saying that as the level of dimensions, grid complexity and considered fluxes rises, the computation time increases as well.

In the current work, our aim is to obtain a general appreciation of the long-term evolution of cometary nuclei. A relatively high computation time is already imposed by the dynamical simulations, so from the thermal modeling point of view, our goal is to keep this computation time to realistic levels, especially as we study populations and not individual objects. Diurnal and seasonal variations are already very difficult to be taken into account with the considered time steps, without mentioning of course our incapacity to account for the spin axis rotation in a statistically significant manner. The same argument extends to the study of irregular shapes which is only pertinent for individual and well constrained objects. Taking into account these considerations, we consider that a spherically symmetric, 1-D model fits well with the computational necessities, but also with the purpose of this work, which is to get a first-order assessment of the primitiveness of cometary populations.

## 4.2 Discretization Scheme

The first step to resolve numerically a PDE such as the Equation (3.1) is to change the continuous nature of the problem (expressed through the

domain of calculation) into a discrete and finite grid (Tannehill et al., 1997). Our goal is to transform the problem into a two-boundary one, consisting of a system of equations, one for each point of the grid (hereafter nodal points), that can be resolved numerically using iterative methods (Prialnik et al., 2004).

To achieve this transformation, a variety of discretization techniques exists. In the following paragraphs we give a brief description of the most commonly used, before justifying our choice.

- **Finite Differences Method (FDM):** In this method, the derivatives of the dependent variable of the PDE (i.e. the temperature in Equation (3.1)) are approximated usually by truncated Taylor series around the nodal points of the calculation domain. It assumes that the variation of the dependent variable follows the behavior of a polynomial in a given direction and that the derivatives of higher orders are not significant. The substitution of the truncated Taylor series in the PDE leads to the Finite Differences form of the PDE which can be resolved numerically (Patankar, 1980).

- **Finite Volumes Method (FVM):** In this method, the calculation domain is divided into non-overlapping, discrete elementary cells commonly known as control volumes, usually surrounding the nodal points. The PDE is integrated directly over each control volume, while appropriate profiles are employed to describe the variation of the dependent variable between nodal points and to evaluate the corresponding integrals. The numerical resolution of the resulting discretized equation gives the values of the dependent variable at the nodal points (Patankar, 1980).

- **Finite Elements Method (FEM):** In this method, the calculation domain is divided into elementary structures -the finite elements- connected through a series of nodes, similarly to the Finite Volume Methods. For each finite element, a specific variable or quantity is calculated by interpolating the values of this variable at the adjacent nodes. When reconnecting the finite elements, this variable will be interpolated in the whole calculation domain in a piecewise manner, which explains why this method is often described as a piecewise polynomial interpolation method. The key to this method is the selection of the most adequate values at the nodes which seek to minimize a relevant function like the total energy. This minimization process will create a set of algebraic equations for all the variables at the nodes that can be resolved numerically (Cook, 1995).

Each of the above methods presents a number of advantages and disadvantages in the discretization of PDEs. In our model we used the Finite

Volume Method (hereafter FVM). This choice was based mainly on two considerations, that take into account both the technical and the physical aspect of the problem:

1. **Simplicity of implementation:** Although not the most straightforward method among the three, the FVM has a quite easy and rather standard implementation both from an algebraic and a conceptual point of view, especially for relatively simple calculation domains, such as the radial component of a sphere (Patankar, 1980; Cook, 1995).

2. **Inherent conservation property:** The FVM is a strictly conservative method, in the sense that it guarantees the automatic conservation of all the dependent variables (e.g. energy, mass, momentum). This is due to the fact that it solves directly the integral form of the equations, i.e. the conservative form, implying an overall conservation over the calculation domain (Patankar, 1980; Tannehill et al., 1997).

## 4.3 Grid Considerations

The grid construction holds a key role in our model as it affects not only the accuracy of our results, but also the feasibility of our simulations. The latter was one of our main concerns throughout this work, as our intention was to examine the thermal processing of cometary populations during the entire, or at least an important part of their lifetime, implying long-term numerical simulations. This highlights the necessity for a grid that has a sufficient resolution to accurately resolve the Equation (3.1), while keeping the computational time at acceptable levels.

### 4.3.1 Grid Generation

From a practical point of view we can distinguish two main practices for generating a grid using the FVM. The difference between them is strictly conceptual, but it entails a great deal of changes in the resulting discretized equation (Patankar, 1980).

The first practice focuses on the nodal points on which the dependent variable is calculated. It divides the calculation domain by placing accordingly the nodal points and then it places the control volumes around them in a way that their faces are positioned midway through two adjacent nodal points. On the contrary, the second practice focuses on the control volumes themselves. The initial step is to divide the domain using the control volumes (of equal or variable size) and then proceeds in the placement of the nodal points in their geometrical center.

As noted by Patankar (1980), the first practice provides a better accuracy on the calculation of the fluxes at the interfaces, thanks to their equidistant

placement from the nodal points where the variables are calculated. This is one of the key elements in the FVM, in order to assure an overall conservation over the calculation domain (see also Section 4.4.1). However, this practice in the case of non-uniform grids, such as ours, leads to nodal points at positions that differ from the geometrical center of their respective control volumes. As the FVM calculates all the different quantities at the nodal points this can be a source of inaccuracies as the values computed will not be necessarily representative of the conditions in the control volume. Moreover, this practice often requires special considerations for the discretization equation at the boundaries where we end up having half control volumes. These two problems can be immediately resolved by the implementation of the second practice which places the nodal points always in the center of the control volumes and on which the calculation domain can be divided in such a way that the boundaries of the first and the last control volume, coincide with its boundaries.

For this work we selected to build our grid using the second practice, mainly for the convenience it provides in the discretization process and considering that the accuracy in the calculation of the fluxes at the interfaces can be achieved through a careful, although more costly computationally-wise, implementation. We should note here that the above discussion becomes senseless in the case of uniform grids, which is not our case, as the resulting grids will be identical.

### 4.3.2 Control Volume Size

We build our grid using gradually growing blocks of control volumes. This implies uniformity within each block, breaking only at their boundaries where control volumes of different size are placed. This selection allows for a finer grid close to the surface where higher resolution is necessary to resolve acute temperature changes and a smaller spatial accuracy for the deeper parts of the nucleus where these changes are expected to be much smoother. This is an essential step towards the minimization of the computational time, as it reduces the number of control volumes on which the discretized equation is resolved, in places where high resolution is not necessary.

The size of the nominal control volume is decided after taking into account the characteristic timescale of the heat diffusion and the dynamical time step. As briefly discussed in Chapter 2 and as will be described in the next chapter, the dynamical simulations that we used in this work were designed to output data every 100 to 1000 years, depending on the adopted parametrization. In order to ensure the convergence of the simulated temperature distribution, allow the internal structure to adjust and avoid abrupt and unrealistic temperature changes within a time step we created smaller time steps within the predefined dynamical output step, usually of the order of a year. Comparing the length of the time step to the timescale of heat

diffusion (see Figure 3.2) imposes a nominal size (here of 0.5 to 1 m) for the control volumes, below which any calculation becomes meaningless as we lack the necessary resolution.

### 4.3.3 Grid Indexing

Last but not least, we discuss briefly the details concerning the indexing in our discretization scheme, necessary in order to better understand the demonstration that follows. As we are working on a two-boundary problem, on a finite spherical domain with a radius bounded by the following conditions: $0 \leq r \leq R$, we can, once again, identify two main practices for indexing our grid. In the first one we start from the center and move towards the surface (known as the direct convention) and in the second one we start from the surface and move towards the center (opposed convention). If we consider that the total radius of a nucleus is the sum of all the radii of the control volumes (or the nodal points):

$$R = \sum_{i=0}^{n} r_i \tag{4.1}$$

then in the case of the direct convention, $i = 0$ at the center and $i = n$ at the surface. Conversely in the case of the opposed convention $i = n$ at the center and $i = 0$ at the surface.

In our model, we adopt the opposed convention which we consider to be more suitable in a scenario where the heat source is external (i.e. at the surface boundary) and where the indexing allows to follow the propagation of the heat wave towards the inner parts of the nucleus in a more intuitive way.

In Figure 4.1 we give a schematic representation of three random control volumes in our grid, to illustrate the previous discussion and to guide the spatial discretization presented in Section 4.4. The general idea is to divide the calculation domain into $n$ control volumes. This selection implies that at each iteration we calculate the temperature at $n + 2$ nodal points, as we account for the nodal points at the center of every control volume plus the two at the boundaries of the domain. We note as well that the radial distance of the control volumes from the center of the nucleus, denoted with the letter $r$, is counted from the left-hand interface of the control volume.

## 4.4 Spatial Discretization of the PDE

We focus on the $i$-th control volume, as presented in Figure 4.1, to illustrate the spatial discretization process detailed below. We follow a very standard implementation of the FVM, as described in Patankar (1980) unless otherwise noted.

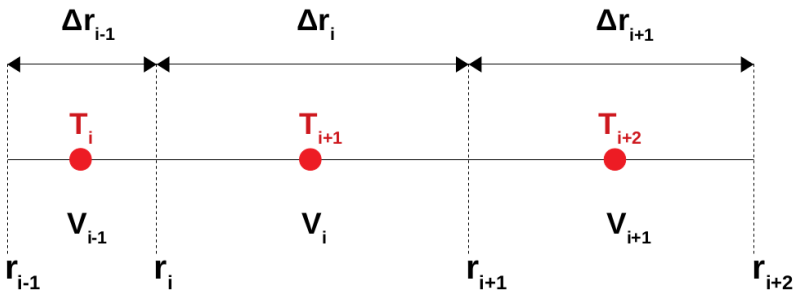


**Figure 4.1:** Schematic representation of the $i$-th control volume ($V_i$) alongside the surrounding control volumes ($V_{i-1}$ and $V_{i+1}$) and their corresponding nodal points where the temperatures ($T$) are calculated, denoted with red dots. The dotted lines mark the boundaries of each control volume but also their radial distance ($r$) from the center of the nucleus. Their sizes, the distance between two boundaries, is denoted as $\Delta r$.

As described briefly in Section 4.2, we start by integrating directly Equation (3.1) on the $i$-th control volume:

$$\int_{V_i} \rho c \frac{\partial T}{\partial t} dV = \int_{V_i} \nabla \left( \kappa \frac{\partial T}{\partial r} \right) dV \tag{4.2}$$

Given that we are working on a one-dimensional, spherical calculation domain, the transformation in spherical coordinates yields:

$$\iiint \rho c \frac{\partial T}{\partial t} r^2 \sin\phi dr d\theta d\phi = \iiint \frac{1}{r^2} \frac{\partial}{\partial r} \left( r^2 \kappa \frac{\partial T}{\partial r} \right) r^2 \sin\phi dr d\theta d\phi \tag{4.3}$$

which gives:

$$\rho c \frac{\partial T}{\partial t} V_i = 4\pi \left( r_{i+1}^2 \kappa_{i+1} \left. \frac{\partial T}{\partial r} \right|_{i+1} - r_i^2 \kappa_i \left. \frac{\partial T}{\partial r} \right|_i \right) \tag{4.4}$$

where $r_i$ and $r_{i+1}$ mark the position of the interfaces of the $i$-th control volume (see Figure 4.1) and $\kappa_i$ and $\kappa_{i+1}$ the effective thermal conductivity at these interfaces.

To evaluate the spatial derivatives of Equation (4.4) we need a profile assumption for the variation of the temperature on the interfaces as explained in Section 4.2. We employ one of the simplest assumptions available: a piecewise profile, using linear interpolation functions between the nodal points, which give the slope $\partial T/\partial r$ on the interfaces as:

$$\left. \frac{\partial T}{\partial r} \right|_{i+1} = 2 \frac{T_{i+2} - T_{i+1}}{\Delta r_i + \Delta r_{i+1}} \quad \text{and} \quad \left. \frac{\partial T}{\partial r} \right|_i = 2 \frac{T_{i+1} - T_i}{\Delta r_i + \Delta r_{i-1}} \tag{4.5}$$

### 4.4.1 Treatment of the Conductivity at the Interfaces

As we noted earlier, the FVM guarantees an overall conservation of the dependent variables over the calculation domain. However, special attention is needed when calculating the fluxes at the interfaces, as they can become a factor of inconsistencies. If we assume, for example, that the conductivity at an interface is that of the adjacent nodal points, in order to estimate the flux at this position, we will end up with two different expressions for the same flux. This assumption violates a basic principle of the FVM, which imposes that a flux leaving a control volume must be equal to the flux entering the adjacent control volume, suggesting that the interface fluxes and therefore the interface conductivities must be treated independently.

Let us consider the case of the interface at the position $r_{i+1}$ of the Figure 4.1. The flux at this position can be written as:

$$q_{r+1} = 2\kappa_{i+1}\frac{T_{i+1} - T_{i+2}}{\Delta r_i + \Delta r_{i+1}} \tag{4.6}$$

If we consider that the conductivity at the center of the control volume $V_i$ is $\kappa_p$ [1] and at the center of the control volume $V_{i+1}$, $\kappa_e$ [2] and the temperature at the interface is $T_{r+1}$, then the flux leaving the control volume $V_i$ and the flux entering the control volume $V_{i+1}$ are:

$$q_p = 2\kappa_p\frac{T_{i+1} - T_{r+1}}{\Delta r_i} \tag{4.7}$$

$$q_e = 2\kappa_e\frac{T_{r+1} - T_{i+2}}{\Delta r_{i+1}} \tag{4.8}$$

As those fluxes should be equal at the interface we can assume that:

$$q_p = q_e = q_{r+1} \tag{4.9}$$

Solving Equations (4.7) and (4.8) for the temperature at the interface $T_{r+1}$ and replacing the resulting expression in Equation (4.6) we get after rearranging a new expression for the flux at the interface:

$$q_{r+1} = \frac{T_{i+1} - T_{i+2}}{\frac{\Delta r_i}{2\kappa_p} + \frac{\Delta r_{i+1}}{2\kappa_e}} \tag{4.10}$$

The comparison between Equation (4.6) and Equation (4.10) yields an expression for the conductivity at the interface:

[1] This conductivity is derived from the temperature at the center of the control volume, i.e. $\kappa(T_{i+1})$. We use this annotation for this particular demonstration in order to avoid any confusion with the conductivity at the interface $(r+1)$.

[2] Which is derived by the temperature $T_{i+2}$.

$$\kappa_{r+1} = \frac{\Delta r_i + \Delta r_{i+1}}{\frac{\Delta r_i}{\kappa_p} + \frac{\Delta r_{i+1}}{\kappa_e}} \tag{4.11}$$

As noted in Patankar (1980), this conductivity is not merely an arithmetic mean of the adjacent control volume conductivities as one would have expected, but rather their harmonic mean, which is a much more effective formulation.

### 4.4.2 Spatially Discretized Equation

Having calculated the slope $\partial T/\partial r$ (Equations (4.5)) and the conductivity at the interfaces (Equations (4.11)), we can substitute them to Equation (3.1) to obtain the final form of the spatially discretized equation:

$$\frac{\partial T}{\partial t} = \frac{8\pi}{\rho c V_i}\left(r_{i+1}^2 \kappa_{i+1} \frac{T_{i+2} - T_{i+1}}{\Delta r_i - \Delta r_{i+1}} - r_i^2 \kappa_i \frac{T_{i+1} - T_i}{\Delta r_i - \Delta r_{i-1}}\right) \tag{4.12}$$

with:

$$\kappa_{i+1} = \frac{\Delta r_i + \Delta r_{i+1}}{\frac{\Delta r_i}{K_{i+1}} + \frac{\Delta r_{i+1}}{K_{i+2}}} \quad \text{and} \quad \kappa_i = \frac{\Delta r_{i-1} + \Delta r_i}{\frac{\Delta r_{i-1}}{K_i} + \frac{\Delta r_i}{K_{i+1}}} \tag{4.13}$$

where with $\kappa$ we represent the conductivity at the interfaces and with $K$ the conductivity calculated at the center of the control volumes.

## 4.5 Time Discretization of the PDE

The next step in the discretization process is to treat the unsteady term appearing on the left-hand side of Equation (4.12). The goal is to establish the temperatures on the nodal points at the end of a defined time step ($\Delta t$), departing from the values at a moment $t$. We integrate Equation (4.12) over this time step:

$$\int_t^{t+\Delta t} \frac{\partial T}{\partial r} dt = \frac{8\pi}{\rho c V_i} \int_t^{t+\Delta t} \left(r_{i+1}^2 \kappa_{i+1} \frac{T_{i+2} - T_{i+1}}{\Delta r_i + \Delta r_{i+1}} - r_i^2 \kappa_i \frac{T_{i+1} - T_i}{\Delta r_i + \Delta r_{i-1}}\right) \tag{4.14}$$

Once again, an assumption is needed in order to evaluate the variation of the temperature from the moment $t$ to the moment $t + \Delta t$. From the different possibilities we employ a generalized form, which will allow us a certain versatility in our choice for the final resolution scheme:

$$\int_t^{t+\Delta t} T_{i+1} dt = [f T_{i+1}^{t+\Delta t} + (1-f) T_{i+1}^t] \Delta t \tag{4.15}$$

with $f$ a weighing factor that ranges from 0 to 1.

Depending on the value of the factor $f$, the discretized equation takes the form of some of the well-known resolution schemes for PDEs. In particular:

- For $f = 0$ we resolve an explicit scheme, where the dependent variables (in this case the temperature) are obtained in terms of already known quantities from the previous time step (Tannehill et al., 1997; Moukalled et al., 2015).
- For $f = 1$ we resolve an implicit scheme, where the calculation of the dependent variables requires the simultaneous resolution of a set of equations, involving information from the current status of the system and the future one (Tannehill et al., 1997; Moukalled et al., 2015).
- For intermediate values we resolve semi-implicit schemes. For example, for $f = 0.5$ we are reduced to what is known as a Crank-Nicolson scheme (Crank and Nicolson, 1947), which assumes a linear variation for the dependent variable within the time step (Patankar, 1980).

Using Equation (4.15) we can rewrite Equation (4.14) on its final form, where the values of the dependent variable at the moment $t + \Delta t$ are on the left-hand side of the equation and the values at the moment $t$ at the right-hand side of it:

$$\begin{aligned}
&\left(-r_i K_i \frac{f}{\Delta r_{i-1} + \Delta r_i}\right) T_i^{t+\Delta t} \\
&+ \left(\frac{\rho c V_i}{8\pi \Delta t} + r_{i+1}^2 K_{i+1} \frac{f}{\Delta r_i + \Delta r_{i+1}} + r_i^2 K_i \frac{f}{\Delta r_i + \Delta r_{i+1}}\right) T_{i+1}^{t+\Delta t} \\
&+ \left(-r_{i+1} K_{i+1} \frac{f}{\Delta r_i + \Delta r_{i+1}}\right) T_{i+2}^{t+\Delta t} \\
&= \left(r_i^2 K_i \frac{1-f}{\Delta r_{i-1} + \Delta r_i}\right) T_i^t \\
&+ \left(\frac{\rho c V_i}{8\pi \Delta t} - r_{i+1}^2 K_{i+1} \frac{(1-f)}{\Delta r_i + \Delta r_{i+1}} - r_i^2 K_i \frac{(1-f)}{\Delta r_i + \Delta r_{i+1}}\right) T_{i+1}^t \\
&+ \left(r_{i+1} K_{i+1} \frac{(1-f)}{\Delta r_i + \Delta r_{i+1}}\right) T_{i+2}^t
\end{aligned} \tag{4.16}$$

This final equation can be also written in the generalized form:

$$a_i T_i^{t+\Delta t} + b_i T_{i+1}^{t+\Delta t} + c_i T_{i+2}^{t+\Delta t} = \alpha_i T_i^t + \beta_i T_{i+1}^t + \gamma_i T_{i+2}^t \tag{4.17}$$

where the coefficients $a_i, b_i, c_i, \alpha_i, \beta_i, \gamma_i$ are determined for the resolution scheme selected in this work in Sections 4.5.2 and 4.5.3.

### 4.5.1 Time Scheme Selection

The more intuitive and straightforward option, as we depart from the current state of the system to calculate a future state, is to use an explicit scheme. It has the advantage of a simplified implementation, as we can easily observe if we set the factor $f$ to zero. The final expression for the temperature $T_{i+1}^{t+\Delta t}$ is reduced to its most simple form, depending only from the values at the current moment $t$. However, this scheme has very low numerical stability and convergence, implying that if the selection of the time steps and the control volumes is not the appropriate, unrealistic results could emerge. In the resolution presented above, if we assume uniform conductivity and equal control volumes, the typical stability criterion can be expressed as (Patankar, 1980):

$$\Delta t < \frac{\rho c (\Delta r)^2}{2\kappa} \tag{4.18}$$

This implies that for a specified grid with relatively small control volumes, allowing for a better spatial precision, the number of time steps can increase significantly, rendering this scheme prohibitive from a computational point of view, especially in the case of long-term simulations as in the case of this work. A simple application using values for the effective thermal conductivity, the bulk density and the specific heat capacity as presented in the previous chapter and for control volume of 1 m in size, indicates that we would need a time step of the order of the month ($2.5 \times 10^6$ s), which would decrease significantly for smaller control volumes. This time step is not prohibitive for typical simulations, but in our case, where the orbital evolution is monitored over millions to billions of years can increase the computational time significantly.

Semi-implicit schemes, such as the Crank-Nicolson, provide a better physical representation thanks to their more realistic variation of the dependent variable between two time moments, while being more accurate than the explicit scheme as well. They are often described as unconditionally stable, implying stability even for very large time steps, but Patankar and Baliga (1978) and Patankar (1980) demonstrated that oscillatory solutions can appear, leading to unrealistic results, even though these oscillations will decrease and eventually die out as the system advances over time, implying that a careful implementation is still necessary to avoid divergence. This augmented precision and better physical representation comes however with an additional cost. If we set $f$=0.5 we note that in the calculation of $T_{i+1}^{t+\Delta t}$, temperatures from the future state are also involved. The resolution of such a system is not straightforward as an explicit one, but requires the resolution of a set of simultaneous equations, which is bound to have an effect to the computational time of a simulation.

The fully implicit scheme ($f$=1) is the only truly unconditionally stable

scheme, guaranteeing physically plausible results without specific stability conditions (Patankar, 1980). As in the case of the semi-implicit schemes it has the downside of a complicated implementation, unlike the explicit scheme as it also requires the resolution of a set of simultaneous equations, again with an increased computational cost. On the other hand, this disadvantage can be balanced out by the ability of the scheme to handle larger time steps and control volume sizes.

In this work we decided to use a resolution technique that combines the advantage of better physical representation of the Crank-Nicolson scheme to the unconditional stability of the fully implicit scheme. We used the predictor-corrector method proposed by Douglas and Jones (Douglas and Jones, 1963) which is a two-step iterative procedure requiring the inversion of tridiagonal matrix at every step (Prialnik et al., 2004). The evolution of the dependent variable from a time $t$ to a time $t + \Delta t$ passes through an intermediate step at time $t+\Delta t/2$. At this intermediate step, a fully implicit *predictor* calculates a solution from the designated coefficients at time $t$ by resolving a set of linear equation by means of a tridiagonal matrix inversion (see Section 4.7). At the next step, a semi-implicit *corrector*, calculates the values of the dependent variable at $t + \Delta t$ using the coefficients calculated at the predictor step, again by means of tridiagonal matrix inversion. It was selected for its high stability, resulting from the combination of an implicit (predictor) and a semi-implicit method (corrector), and high accuracy, enhanced by the use of an extra step (i.e. the predictor) in exchange for the small computational load of adding an intermediate calculation at every step (Douglas and Jones, 1963). This method has been widely used in models studying the thermal evolution of cometary nuclei over the last three decades (e.g. Espinasse et al., 1989; Orosei et al., 1999; Guilbert-Lepoutre et al., 2011), with different selection of schemes for the predictor and the corrector.

### 4.5.2 Predictor

With the above considerations the Equation (4.17) changes slightly for the predictor to:

$$a_i T_i^{t+\Delta t/2} + b_i T_{i+1}^{t+\Delta t/2} + c_i T_{i+2}^{t+\Delta t/2} = \alpha_i T_i^t + \beta_i T_{i+1}^t + \gamma_i T_{i+2}^t \tag{4.19}$$

which can also be written in matrix form as:

$$M[T^{t+\Delta t/2}] = N[T^t] + P \tag{4.20}$$

where $M$, $N$ and $P$ are diagonal matrices having as elements the coefficients of Equation (4.19):

$$M = \begin{pmatrix} b_0 & c_0 & 0 & \cdots & \cdots & \cdots & \cdots & \cdots & \cdots & 0 \\ a_1 & b_1 & c_1 & 0 & \cdots & \cdots & \cdots & \cdots & \cdots & \vdots \\ 0 & a_2 & b_2 & c_2 & \ddots & & & & & \vdots \\ \vdots & \ddots & \ddots & \ddots & \ddots & \ddots & & & & \vdots \\ \vdots & & \ddots & \ddots & \ddots & \ddots & \ddots & & & \vdots \\ \vdots & & & \ddots & a_i & b_i & c_i & \ddots & & \vdots \\ \vdots & & & & \ddots & \ddots & \ddots & \ddots & \ddots & \vdots \\ \vdots & & & & & \ddots & \ddots & \ddots & \ddots & 0 \\ \vdots & & & & & & \ddots & a_{n-1} & b_{n-1} & c_{n-1} \\ 0 & \cdots & \cdots & \cdots & \cdots & \cdots & \cdots & 0 & a_n & b_n \end{pmatrix} \tag{4.21}$$

$$N = \begin{pmatrix} \beta_0 & \gamma_0 & 0 & \cdots & \cdots & \cdots & \cdots & \cdots & \cdots & 0 \\ \alpha_1 & \beta_1 & \gamma_1 & 0 & \cdots & \cdots & \cdots & \cdots & \cdots & \vdots \\ 0 & \alpha_2 & \beta_2 & \gamma_2 & \ddots & & & & & \vdots \\ \vdots & \ddots & \ddots & \ddots & \ddots & \ddots & & & & \vdots \\ \vdots & & \ddots & \ddots & \ddots & \ddots & \ddots & & & \vdots \\ \vdots & & & \ddots & \alpha_i & \beta_i & \gamma_i & \ddots & & \vdots \\ \vdots & & & & \ddots & \ddots & \ddots & \ddots & \ddots & \vdots \\ \vdots & & & & & \ddots & \ddots & \ddots & \ddots & 0 \\ \vdots & & & & & & \ddots & \alpha_{n-1} & \beta_{n-1} & \gamma_{n-1} \\ 0 & \cdots & \cdots & \cdots & \cdots & \cdots & \cdots & 0 & \alpha_n & \beta_n \end{pmatrix} \tag{4.22}$$

$$P = \begin{pmatrix} \delta_0 \\ \delta_1 \\ \delta_2 \\ \vdots \\ \delta_{n-1} \\ \delta_n \end{pmatrix} \tag{4.23}$$

The elements for the above matrices are calculated from Equation (4.16) if we set $f$=1 for a fully implicit scheme:

$$a_i = -r_{i-1}^2 \frac{1}{\frac{\Delta r_{i-1}}{K_{i-1}} - \frac{\Delta r_{i-2}}{K_{i-2}}} \tag{4.24}$$

$$c_i = -r_i^2 \frac{1}{\frac{\Delta r_{i-1}}{K_{i-1}} - \frac{\Delta r_{i-2}}{K_{i-2}}} \tag{4.25}$$

$$b_i = \frac{\rho c V_{i-1}}{4\pi \Delta t} - c_i - a_i \tag{4.26}$$

$$\alpha_i = 0 \tag{4.27}$$

$$\gamma_i = 0 \tag{4.28}$$

$$\beta_i = \frac{\rho c V_{i-1}}{4\pi \Delta t} \tag{4.29}$$

$$\delta_i = 0 \tag{4.30}$$

### 4.5.3 Corrector

In a similar manner, the Equation (4.17) for the corrector is:

$$a'_i T_i^{t+\Delta t} + b'_i T_{i+1}^{t+\Delta t} + c'_i T_{i+2}^{t+\Delta t} = \alpha'_i T_i^{t+\Delta t/2} + \beta'_i T_{i+1}^{t+\Delta t/2} + \gamma'_i T_{i+2}^{t+\Delta t/2} \tag{4.31}$$

which, as previously, can be written in matrix form:

$$M'[T^{t+\Delta t}] = N'[T^{t+\Delta t/2}] + P' \tag{4.32}$$

where $M'$, $N'$ and $P'$ are the following matrices:

$$M' = \begin{pmatrix} b'_0 & c'_0 & 0 & \cdots & \cdots & \cdots & \cdots & \cdots & \cdots & 0 \\ a'_1 & b'_1 & c'_1 & 0 & \cdots & \cdots & \cdots & \cdots & \cdots & \vdots \\ 0 & a'_2 & b'_2 & c'_2 & \ddots & & & & & \vdots \\ \vdots & \ddots & \ddots & \ddots & \ddots & \ddots & & & & \vdots \\ \vdots & & \ddots & \ddots & \ddots & \ddots & \ddots & & & \vdots \\ \vdots & & & \ddots & a'_i & b'_i & c'_i & \ddots & & \vdots \\ \vdots & & & & \ddots & \ddots & \ddots & \ddots & \ddots & \vdots \\ \vdots & & & & & \ddots & \ddots & \ddots & \ddots & 0 \\ \vdots & & & & & & \ddots & a'_{n-1} & b'_{n-1} & c'_{n-1} \\ 0 & \cdots & \cdots & \cdots & \cdots & \cdots & \cdots & 0 & a'_n & b'_n \end{pmatrix} \tag{4.33}$$

$$N' = \begin{pmatrix} \beta'_0 & \gamma'_0 & 0 & \cdots & \cdots & \cdots & \cdots & \cdots & \cdots & 0 \\ \alpha'_1 & \beta'_1 & \gamma'_1 & 0 & \cdots & \cdots & \cdots & \cdots & \cdots & \vdots \\ 0 & \alpha'_2 & \beta'_2 & \gamma'_2 & \ddots & & & & & \vdots \\ \vdots & \ddots & \ddots & \ddots & \ddots & \ddots & & & & \vdots \\ \vdots & & \ddots & \ddots & \ddots & \ddots & \ddots & & & \vdots \\ \vdots & & & \ddots & \alpha'_i & \beta'_i & \gamma'_i & \ddots & & \vdots \\ \vdots & & & & \ddots & \ddots & \ddots & \ddots & \ddots & \vdots \\ \vdots & & & & & \ddots & \ddots & \ddots & \ddots & 0 \\ \vdots & & & & & & \ddots & \alpha'_{n-1} & \beta'_{n-1} & \gamma'_{n-1} \\ 0 & \cdots & \cdots & \cdots & \cdots & \cdots & \cdots & 0 & \alpha'_n & \beta'_n \end{pmatrix} \tag{4.34}$$

$$P' = \begin{pmatrix} \delta'_0 \\ \delta'_1 \\ \delta'_2 \\ \vdots \\ \delta'_{n-1} \\ \delta'_n \end{pmatrix} \tag{4.35}$$

As in the case of the predictor, the coefficients for the above matrices are calculated from Equation (4.16) if we set $f$=0.5, for a semi-implicit Crank-Nicolson scheme:

$$a'_i = -\frac{r_{i-1}^2}{2} \frac{1}{\frac{\Delta r_{i-1}}{K_{i-1}} - \frac{\Delta r_{i-2}}{K_{i-2}}} \tag{4.36}$$

$$c'_i = -\frac{r_i^2}{2} \frac{1}{\frac{\Delta r_{i-1}}{K_{i-1}} - \frac{\Delta r_{i-2}}{K_{i-2}}} \tag{4.37}$$

$$b'_i = \frac{\rho c V_{i-1}}{4\pi \Delta t} - c_i - a_i \tag{4.38}$$

$$\alpha'_i = \frac{r_{i-1}^2}{2} \frac{1}{\frac{\Delta r_{i-1}}{K_{i-1}} - \frac{\Delta r_{i-2}}{K_{i-2}}} \tag{4.39}$$

$$\gamma'_i = \frac{r_i^2}{2} \frac{1}{\frac{\Delta r_{i-1}}{K_{i-1}} - \frac{\Delta r_{i-2}}{K_{i-2}}} \tag{4.40}$$

$$\beta'_i = \frac{\rho c V_{i-1}}{4\pi \Delta t} - \gamma_i - \alpha_i \tag{4.41}$$

$$\delta'_i = 0 \tag{4.42}$$

## 4.6 Boundary Conditions

The next step in the discretization process is to define the discretized equation at the boundaries of our calculation domain, where the general discretized Equation (4.17) will be slightly different. To do this, we need to define the conditions at these points of discontinuity. We consider that at the center of our objects, the heat flux is equal to zero. This condition where the flux is specified at the boundary is known as a Neumann boundary condition (Moukalled et al., 2015) and the evaluation of the temperature derivative results in:

$$T_{n+1} = T_n \tag{4.43}$$

With the above consideration, we can compute the coefficients for the predictor (Equation (4.20)) and the corrector (Equation (4.32)) at the center of the nucleus:

$$a_n = a'_n = 1 \tag{4.44}$$
$$b_n = b'_n = -1 \tag{4.45}$$
$$c_n = c'_n = 0 \tag{4.46}$$
$$\alpha_n = \alpha'_n = 0 \tag{4.47}$$
$$\beta_n = \beta'_n = 0 \tag{4.48}$$
$$\gamma_n = \gamma'_n = 0 \tag{4.49}$$
$$\delta_n = \delta'_n = 0 \tag{4.50}$$

At the surface a thermal balance equation (see Equation 3.22) is used in order to estimate the surface temperature. This type of condition where the value at the boundary is specified explicitly is known as Dirichlet boundary condition (Moukalled et al., 2015) and imposes the following matrix coefficients for the predictor (Equation (4.20)) and the corrector (Equation (4.32)):

$$a_0 = a'_0 = 0 \tag{4.51}$$
$$b_0 = b'_0 = 1 \tag{4.52}$$
$$c_0 = c'_0 = 0 \tag{4.53}$$
$$\alpha_0 = \alpha'_0 = 0 \tag{4.54}$$
$$\beta_0 = \beta'_0 = 0 \tag{4.55}$$
$$\gamma_0 = \gamma'_0 = 0 \tag{4.56}$$
$$\delta_0 = \delta'_0 = T_{surface} \tag{4.57}$$

### 4.6.1 Considerations for the Flux at the First Control Volume

As noted in Guillot and McCool (2015), special consideration should be given to the flux entering the first control volume in order to assure a second-order spatial convergence. The FVM method that we used for the spatial discretization of Equation (3.1) is a method of second-order accuracy, regarding the rate of convergence of the numerical solution. However the approximation for the flux derivative at the control volume adjacent to the surface, used in the literature (e.g. Patankar, 1980; Versteeg and Malalasekera, 2007), is very often of first-order accuracy, which can only display second-order spatial convergence under certain conditions, mainly when the time step decreases significantly. In order to avoid any inconsistencies, it is better to approximate it with a second-order expression. In this work we follow Guillot and McCool (2015)'s second-order boundary approximation, which is derived from a Taylor expansion applied on the first two control volumes of our grid, which are presented in Figure 4.2.

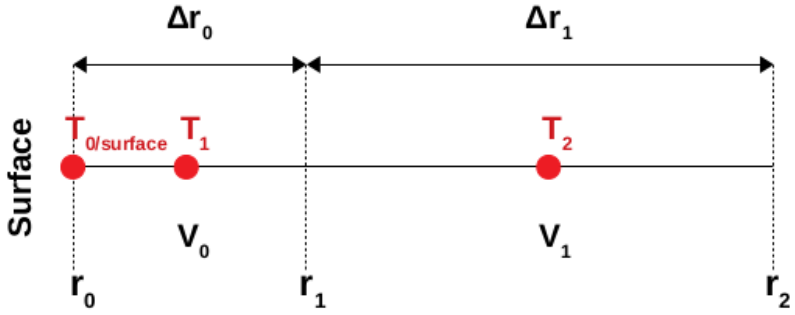


**Figure 4.2:** Schematic representation of the first two control volumes at the upper boundary (surface) in our grid. The nodal points, where the temperatures are calculated, are denoted with red dots. The dashed lines mark the boundaries of the control volumes with the first one coinciding with the beginning of our domain. The size of the control volumes is denoted as $\Delta r$, and by design $\Delta r_1 = 2\Delta r_0$.

Taking into account that in our grid setup $\Delta r_1 = 2\Delta r_0$, we can write the following Taylor expansions for the temperatures at the center of the first two control volumes:

$$T_1 = T_0 + \frac{\Delta r_0}{2}\frac{\partial T}{\partial r}\bigg|_{r=r_0} + \frac{\Delta r_0^2}{4}\frac{\partial^2 T}{\partial r^2}\bigg|_{r=r_0} + \mathcal{O}(\Delta x^2) \tag{4.58}$$

$$T_2 = T_0 + 2\Delta r_0\frac{\partial T}{\partial r}\bigg|_{r=r_0} + 4\Delta r_0^2\frac{\partial^2 T}{\partial r^2}\bigg|_{r=r_0} + \mathcal{O}(\Delta x^2) \tag{4.59}$$

Solving the above system of equations for the first derivative of the temperature while eliminating the second, leads to:

$$\left.\frac{\partial T}{\partial r}\right|_{r=r_0} = \frac{4T_1 - \frac{1}{4}T_2 - \frac{15}{4}T_0}{\frac{3}{2}\Delta r_0} \tag{4.60}$$

Using this expression for the temperature derivative and following the spatial and temporal discretization presented in Sections 4.4 and 4.5, we obtain the discretized equation for the first control volume:

$$\begin{aligned}
\left(-f\frac{5}{4}\frac{r_0^2 k_0}{\Delta r_0}\right) T_0^{t+\Delta t} \\
+\left(\frac{\rho c V_0}{8\pi\Delta t} + f\frac{r_1^2 k_1}{\Delta r_0 + \Delta r_1} + f\frac{4r_0^2 k_0}{3\Delta r_0}\right) T_1^{t+\Delta t} \\
+\left(-f\frac{r_1^2 k_1}{\Delta r_0 + \Delta r_1} - f\frac{r_0^2 k_0}{12\Delta r_0}\right) T_2^{t+\Delta t} \\
= \left((1-f)\frac{5}{4}\frac{r_0^2 k_0}{\Delta r_0}\right) T_0^t \\
+\left(\frac{\rho c V_0}{8\pi\Delta t} + (1-f)\frac{r_1^2 k_1}{\Delta r_0 + \Delta r_1} + (1-f)\frac{4r_0^2 k_0}{3\Delta r_0}\right) T_1^t \\
+\left((1-f)\frac{r_1^2 k_1}{\Delta r_0 + \Delta r_1} + (1-f)\frac{r_0^2 k_0}{12\Delta r_0}\right) T_2^t
\end{aligned} \tag{4.61}$$

which yields the following matrix coefficients for the predictor ($f$=1) and the corrector ($f$=0.5) respectively:

$$a_1 = -\frac{5}{4}\frac{r_0^2 k_0}{\Delta r_0}, \qquad a_1' = -\frac{5}{8}\frac{r_0^2 k_0}{\Delta r_0} \tag{4.62}$$

$$b_1 = \frac{\rho c V_0}{8\pi\Delta t} + \frac{r_1^2 k_1}{\Delta r_0 + \Delta r_1} + \frac{4 r_0^2 k_0}{3\Delta r_0}, \quad b_1' = \frac{\rho c V_0}{8\pi\Delta t} + \frac{r_1^2 k_1}{2(\Delta r_0 + \Delta r_1)} + \frac{2 r_0^2 k_0}{3\Delta r_0} \tag{4.63}$$

$$c_1 = -\frac{r_1^2 k_1}{\Delta r_0 + \Delta r_1} - \frac{r_0^2 k_0}{12\Delta r_0}, \qquad c_i' = -\frac{r_1^2 k_1}{2(\Delta r_0 + \Delta r_1)} - \frac{r_0^2 k_0}{24\Delta r_0} \tag{4.64}$$

$$\alpha_1 = 0, \qquad \alpha_1' = \frac{5}{8}\frac{r_0^2 k_0}{\Delta r_0} \tag{4.65}$$

$$\beta_1 = \frac{\rho c V_0}{4\pi\Delta t}, \qquad \beta_1' = \frac{\rho c V_0}{8\pi\Delta t} - \frac{r_1^2 k_1}{2(\Delta r_0 + \Delta r_1)} - \frac{2 r_0^2 k_0}{3\Delta r_0} \tag{4.66}$$

$$\gamma_1 = 0, \qquad \gamma_1' = \frac{r_1^2 k_1}{2(\Delta r_0 + \Delta r_1)} + \frac{r_0^2 k_0}{24\Delta r_0} \tag{4.67}$$

$$\delta_1 = 0, \qquad \delta_1' = 0 \tag{4.68}$$

We remind that these coefficients are valid only for a specific configuration of the grid. If this configuration changes, for example, the size of the second control volume is equal to the size of the first control volume, the coefficients will change accordingly, but the procedure will remain the same.

## 4.7 Resolution of the Tridiagonal System of Equations

In the final step of this procedure, having created our system of discretized equations, we seek to resolve them simultaneously in order to obtain the temperature at the designated nodal points. For the resolution of this tridiagonal system of equations for the predictor and the corrector (Equations 4.20 and 4.32 respectively) we use the Thomas Algorithm (Thomas, 1949) which is a simplified, yet efficient, variation of the Gaussian elimination method. The main idea of the algorithm is to transform these equations in the form:

$$U[T_{n+1}] = Q \tag{4.69}$$

where $U$ is an upper triangular matrix of the form:

$$U = \begin{pmatrix} 1 & u_0 & 0 & \cdots & \cdots & \cdots & \cdots & \cdots & 0 \\ 0 & 1 & u_1 & 0 & & & & & \vdots \\ \vdots & 0 & 1 & u_2 & 0 & & & & \vdots \\ \vdots & & \ddots & \ddots & \ddots & 0 & & & \vdots \\ \vdots & & & 0 & 1 & u_i & 0 & & \vdots \\ \vdots & & & & \ddots & \ddots & \ddots & 0 & \vdots \\ \vdots & & & & & 0 & 1 & u_{n-2} & 0 \\ \vdots & & & & & & 0 & 1 & u_{n-1} \\ 0 & \cdots & \cdots & \cdots & \cdots & \cdots & \cdots & 0 & 1 \end{pmatrix} \tag{4.70}$$

and $Q$ a one-dimensional matrix of the form:

$$Q = \begin{pmatrix} q_1 \\ q_2 \\ \vdots \\ q_i \\ \vdots \\ q_{n-1} \\ q_n \end{pmatrix} \tag{4.71}$$

of which the coefficients are calculated as:

$$u_i = \frac{c_i}{b_i - a_i u_{i-1}} \tag{4.72}$$

$$q_i = \frac{d_i - a_i q_{i-1}}{b_i - a_i u_{i-1}} \tag{4.73}$$

where $a_i, b_i, c_i$ are the elements of the matrix M (or M$'$ in the case of the corrector) and $d_i$ are the elements of a 1-D matrix created from the summation of the N and P (or N$'$ and P$'$ for the corrector) matrices.

After transforming equations 4.20 and 4.32 in the form:

$$M[T_{n+1}] = D \tag{4.74}$$

or:

$$a_i T_i + b_i T_{i+1} + c_i T_{i+2} = d_i \tag{4.75}$$

we proceed in the transformation of the M matrix into an upper triangular matrix using a method known as forward substitution which implies the transformation of the D matrix to the Q matrix as well. The solution for

the system of equations for $T$ described by the equation 4.69 becomes then trivial as $T_{n+1} = q_n$ and then moving backwards (backward substitution) we can obtain the remaining $T$ values as:

$$T_i = q_i - u_i T_{i-1} \tag{4.76}$$

## 4.8 Execution Scheme

Having establish the main numerical methods used for the calculation of the temperature in the interior of our simulated comets, we give an outline of the model's execution scheme.

### 4.8.1 First Part: Initialization of Nucleus Parameters

In the first part of the execution we have the initialization of the basic geometrical and physical parameters of the nucleus. An analytic discussion on the parametrization was made in Chapter 3. Here we list briefly the basic properties to be initialized in the first part of the execution:

1. Set the size of the object's nucleus, by declaring an initial radius.
2. Initialization of nucleus properties (albedo, emissivity, porosity, pore radius etc.)
3. Initialization of the nucleus' material properties (dust and ices fractions, dust and ices properties such as density, conductivity, heat capacity etc).
4. Grid generation, by setting a nominal control volume size, based on the assumptions presented in Section 4.3.
5. Set initial temperature at 10 K, a very low value allowing for any type of temperature increase or decrease related to the orbital evolution. Set initial position of the different ice interfaces in the nucleus, at depths of 0.25 m below the surface.

### 4.8.2 Second Part: Orbital Elements Treatment

In the second part, the orbital parameters, obtained by the $N$-body simulations, describing the comet's trajectory are introduced to the model. An analytical description of the dynamical aspects of our simulations and our treatment of the orbital elements will be given in Chapter 5. Here we describe the steps taken in the model when this information is provided by the user:

1. Read time and orbital elements (semimajor axis, eccentricity etc) from the designated file.
2. Time initialization.
3. Creation of the dynamical time steps.
4. Calculation of equivalent orbits (see Section 5.5) or create the appropriate stepping by sub-sampling the orbits at every time using the eccentric anomaly.

### 4.8.3 Third Part: Calculation of the Internal Temperature and Ice Species Evolution

This is the main part of the model where the thermal evolution of the nucleus is calculated over its dynamical lifetime. We iterate on the dynamical time steps as those are introduced in the previous phase. For every time step the model performs the following calculations:

1. Creation of smaller time steps for the temperature calculations (for more details see Section 4.3).
2. For each of these smaller time steps the code:
   (a) Calculates the solar input at the surface.
   (b) Finds the position of the different interfaces.
   (c) Calculates the physical properties of the nucleus at every layer (conductivity, density, heat capacity), as those are defined by the ice interfaces.
   (d) Using a bisection method and the thermal balance at the surface, calculates the surface temperature at the upper boundary of our discretization scheme.
   (e) Calculates the coefficients for the matrices $M, N$ and $P$ for the discretized equation at the predictor.
   (f) Calculates the temperature at the predictor.
   (g) If an equivalent orbit is used it moves to the temperature calculation at the corrector, if not, it re-calculates the surface temperature, at the new position at a time equal to $\Delta t/2$.
   (h) Calculates the coefficients for the matrices $M, N$ and $P$ for the discretized equation at the corrector.
   (i) Calculates the temperature at the corrector.
3. Having calculated an average temperature over the dynamical time step, the thermal evolution of the ice species during this dynamical time step is calculated, as follows:

(a) Calculates the progress of the crystallization of the amorphous water ice by examining the fraction between the time step and the crystallization timescale for the temperature profile at a given time step. If the fraction is above one, then we consider that no amorphous ice exists in a given control volume and we advance the crystallization front accordingly. No partial crystallization is considered in the model.

(b) Calculates the developed vapor pressures for each component.

(c) Calculates the effective gas diffusion coefficient for every gas component.

(d) Calculates the advancement of the ice interfaces in the nucleus.

(e) Calculates the surface erosion -if any- of the comet.

4. Saves the temperature profile of the nucleus at every dynamical time step, alongside the position of every interface.

5. Moves back to point (2) of this third part and repeat the subsequent steps based on the updated temperatures and interface positions.

This part is iterating over all the dynamical steps until the end of the dynamical lifetime of the comet, which also marks the end of the simulation.

# Chapter 5

# *N*-body Simulations

As already mentioned in the previous chapters, the second ingredient of our approach is the use of $N$-body simulations, tracking the orbital evolution of a large number of planetesimals originating in the outer parts of the protoplanetary disk.

Their use presents three main advantages, that we consider to be this work's greatest assets. First and foremost, they provide realistic dynamical trajectories at every evolutionary phase, especially during phases of abrupt and frequent orbital changes due to planetary perturbations. Second, they guarantee a continuity in the thermal study of our simulated comets, even if we want to examine some phase of their evolution independently. Third, as the dynamical pathway of each particle is unique, due to the stochastic nature of the events that form it (planetary perturbations, passing stars, galactic tides and so on), the fact that we can obtain a multitude of particles and pathways allows for a statistically significant view of the resulting thermal processing.

In the present work, our main focus were the Short-period or (according to Levison's (1996) classification) Ecliptic Comets, encompassing planetesimals evolving towards the Kuiper Belt and the scattered disk, from where they return to become Jupiter-family Comets, by passing through the intermediate stage of Centaurs (see also Figure 1.8). We also examined the early processing of two other populations of planetesimals: those that are scattered outwards to form the Oort Cloud, from where they are expected to return as Long-period Comets and those planetesimals that did not survive the planetary migration and were ejected early on from the planetesimal disk.

A general overview of the $N$-body simulations that provided the different samples is presented in Section 5.1. A detailed description of each sample and their particular considerations is given in Sections 5.2, 5.3 and 5.4 for the JFC, LPC and ejected samples respectively. In Section 5.5 we develop an orbit averaging technique that was employed for the coupling of the dynamical

trajectories with the thermal evolution model.

## 5.1 Overview of the *N*-body simulations

We used two sets of $N$-body simulations to produce our working samples. They both follow the same principles, but have some minor differences in their initial setups. The first set of simulations, which is described in detail in Nesvorný et al. (2017) and Vokrouhlický et al. (2019), provided the JFC and LPC samples and the second, detailed in Raymond et al. (2020b), provided the sample for the ejected planetesimals.

Both sets of $N$-body simulations track the orbital evolution of the four giant planets, placed initially in a multi-resonant setup (Levison et al., 2011) and an additional ice giant, to increase the probability of reproducing the Solar System's current orbital architecture (Nesvorný and Morbidelli, 2012). In both sets of simulations the giant planet instability is triggered immediately, at t=0. None of the simulations included the terrestrial planets, the formation of which is still unclear if it was completed at the time of the giant planet instability (Morbidelli et al., 2018; Clement et al., 2018; Liu et al., 2022). Nongravitational forces were not considered in either simulation.

In the first set of simulations, one million massless planetesimals are placed in an outer planetesimal disk, beyond Neptune's initial orbit at distances between 24 and 30 au. Moderate timescales were used to describe the implantation at the source reservoirs, assuming a two-stage migration for Neptune: 10 Myr for the first stage, before the instability, and 30 Myr for the second stage after the instability. The orbital evolution is followed throughout the planetesimals' lifetime, starting from their ejection and implantation in their reservoirs as the planets migrate and the planetesimal disk is dispersed and up until their return in the inner Solar System after a prolonged stay in the reservoirs and their definitive ejection from it. These simulations were performed by David Nesvorný at the Department of Space Studies of the Southwest Research Institute (SwRI), using the `swift_rmvs4` code, part of the Swift $N$-body integration package (Levison and Duncan, 1994), on NASA's Pleiades supercomputer.

The second set of simulations had a slightly different initial setup. The inner edge of the planetesimal disk is placed at 21.4 au instead of 24 au and the number of the initial particles is one thousand, three orders of magnitude smaller than the first set of simulations. Given the low implantation efficiency at the outer Solar System reservoirs (see Sections 1.3.2 and 1.3.2), this simulation did not have a sufficient amount of particles to form the reservoirs. However, the orbital elements for a large number of particles that got ejected were available, which we were able to use for the study of the ejected population. These simulations were performed by Nathan A. Kaib at the Department of Physics and Astronomy of the University of Oklahoma, using

a modified version of the *Mercury* hybrid integrator in order to include the Galactic tidal field and perturbations from passing stars, on the OU Supercomputing Center for Education & Research (OSCER) at the University of Oklahoma (OU).

## 5.2 JFC Sample

Our JFC sample consists of 383 particles, evolving from the planetesimal disk to the Trans-Neptunian area and then back to the inner Solar System, where they successfully reproduce the orbital distribution of the observed JFCs, as this was obtained from the JPL Small-Body Database Search Engine[1] in January 2017 (Nesvorný et al., 2017). This orbital distribution considers only "*active*" JFCs with perihelion distances within 2.5 au, at least once in their lifetime, and a known total absolute magnitude ($H_t$) smaller than 10.9. This subset was selected as it is better characterized by observations, although a small bias might be introduced by this magnitude filter (Nesvorný et al., 2017).

As we mentioned previously the particles were followed throughout their entire lifetimes. However, for purely numerical reasons (computational and storage limitations), a choice on the phases of evolution to be recorded and the optimal output frequency had to be made. We aimed our attention at the phases marked by planetary perturbations by the giant planets, where solar irradiation is more important and alterations more likely to occur: (a) the outwards scattering phase and (b) the return phase until their final ejection from the Solar System. Orbital elements during the reservoir phase were not outputted, as no intense, solar-driven processing, at least compared to the two other phases, was expected. We remind here, that the majority, if not all, of the previous studies, agrees that in this stage of evolution, any thermal processing should be driven by the decay of radioactive elements, if those are present in cometary nuclei (see Sections 1.4.2). Our choice can be further corroborated by rough estimates of the ambient temperatures[2] in the scattered disk which are $\simeq$37 K at 50 au and $\simeq$25 K at 100 au, which is close to the sublimation temperatures of the more volatile species (such as CO, $N_2$, $CH_4$) observed on comets (Meech and Svoren, 2004).

The first phase was considered to last 200 Myr, starting at the beginning of the simulation. This cut was selected in order to ensure that all the planetesimals were placed in relatively stable orbits in the Kuiper Belt and the scattered disk and that these reservoirs were properly formed. The nominal output frequency was 1000 yr, with an increased cadence of 100 yr whenever

[1] `http://ssd.jpl.nasa.gov/sbdb_query.cgi`

[2] An estimation can be made by considering a black body temperature for an isothermal spherical body, following for example the relation: $T_{BB} = 278 r_h^{-1/2}$, where $r_h$ is the heliocentric distance.

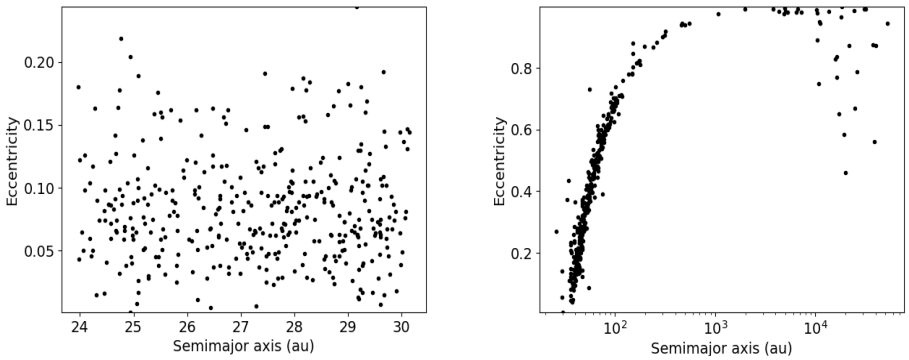


**Figure 5.1:** Initial (left-hand panel) and final (right-hand panel) distributions of the semimajor axis and eccentricities of the particles in our sample during the ejection phase from the outer planetesimal disk.

a planetesimal was detected at heliocentric distances within 23 au, where increased thermal processing was anticipated.

For the second phase, where the particles are moving towards Jupiter-crossing orbits, the output frequency was set directly to 100 yr, but was recorded only if a particle was detected at heliocentric distances within 30 au. The timescale of this last phase varied between particles as it depended on a unique trajectory leading each particle to its ejection from the Solar System. The maximum value recorded is of the order of one billion years (999.96 Myr) and the minimum of the order of tens of thousand years (0.0995 Myr). On average the particles of our sample took $\simeq$155 Myr to get ejected from the moment they are first detected to be within Neptune's orbit, with the median value being $\simeq$64 Myr.

The nominal output step of 1000 yr, enhanced by an order of magnitude when a particle approached the giant-planet region, is 5 to 6 orders of magnitude shorter than the phases of dynamical evolution examined. This was considered to be a good compromise between numerical constraints and the necessity to record frequently the orbital changes with a satisfactory resolution. Of course, for the majority of thermal processes these time steps are still too large (see Section 3.1.4), demanding further assumptions as we discuss later in this chapter.

In Figure 5.1, the initial (left panel) and final (right panel) distributions of the semimajor axis and eccentricities are presented. We note that no preference for a specific semimajor axis value exists. The eccentricities, following a Rayleigh distribution (Nesvorný et al., 2017), are generally very low, as the majority of the particles ($\simeq$71%) have initial eccentricities below 0.1. On the right panel, we can see the formation of the Kuiper Belt and the scattered disk (SD) after 200 Myr in the simulation. We note that the majority of the particles ($\simeq$47%) populates the inner part of the SD that is defined by

orbits with $50 < a < 200$ au. 41% of the particles are on stable orbits in the classical Kuiper Belt ($a < 50$ au), and only a small percentage ends up at the outer SD ($200 < a < 1000$ au).

The fact that from the initial one million particles, only 383 made it to our JFC sample, confirms the low implantation efficiency that was mentioned earlier and in Chapter 1. If we consider the losses occuring at the Centaur area (Di Sisto and Brunini, 2007; Bailey and Malhotra, 2009; Fraser et al., 2022) we realize that only a small fraction manages to reach Jupiter-crossing orbits. As there was a necessity to improve these statistics in the inner Solar System in order to obtain a satisfactory JFC sample and the use of a larger number of initial planetesimals was numerically challenging, Nesvorný et al. (2017) used cloning for the particles reaching Saturn's orbit. If $r_h < 9$ au, 100 new orbits were produced from the original, by imposing a small random perturbation on the velocity vector.

In Figure 5.2 an example of the orbital evolution of a single particle during the two examined phases is presented. During the outwards scattering and implantation phase (upper panel), the particle is scattered slowly outwards, following orbits with perihelia in the area of $\simeq$30 au, after a series of encounters with Neptune, as described in Section 1.3.2. The particle ends up after $\simeq$80 Myr, in more stable orbits in the SD, known as fossilized orbits, where its semimajor axis remains relatively stable, with small changes of no more than 1.5 au (Kaib and Sheppard, 2016; Nesvorný and Vokrouhlický, 2016; Nesvorný et al., 2017). Its return to the inner solar system, is presented on the lower panel of Figure 5.2, from the moment it is first detected within Neptune's orbit and until its ejection. This particle has a moderate lifetime of $\sim$19 Myr in the inner Solar System. The particle is scattered inwards from one planet to the planet interior to it, until it reaches Jupiter-crossing orbits (Levison and Duncan, 1997). At this point its semimajor axis is reduced so that it passes within 2.5 au and becomes an observable JFC (Brasser and Wang, 2015; Roberts and Muñoz-Gutiérrez, 2021). It is clear from the density of points that most of its lifetime ($\sim$16 Myr) is spent beyond 10 au, with orbits between those of Neptune and Saturn in the Centaur area. Once under the dynamical control of Jupiter, the ejection phase begins and the particle is scattered outwards and leaves the solar system quickly ($\sim$3 Myr).

Figure 5.3 gives a statistical representation of the orbits frequented by the 383 particles of our sample, during their return to the inner Solar System. Most particles tend to remain on transient orbits between those of Saturn and Neptune in the Centaur area, for most of their lifetimes, which explains the relatively long timescales of this phase (Di Sisto and Brunini, 2007). Of course, there is a diversity of outcomes governed by the stochastic nature of close gravitational encounters with the giant planets and the existence of particles with shorter dynamical lifetimes, scattered quickly inward by Neptune, Uranus or Saturn is not so rare. Once a particle becomes a JFC its dynamical lifetime decreases significantly as it is ejected by Jupiter quickly

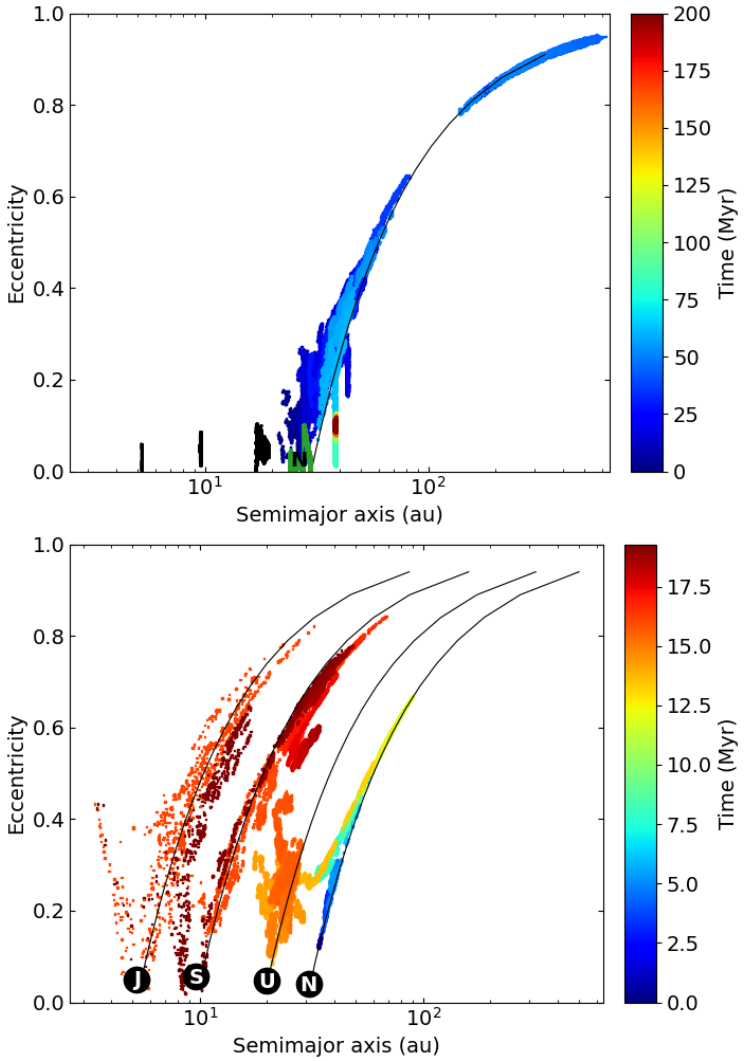


**Figure 5.2:** Example of a particle's orbital evolution during the ejection and implantation on the scattered disk phase on the first 200 Myr of the simulation (upper panel) and during its return to the inner solar system (lower panel), from the first time it crosses Neptune's orbit, until its ejection after approximately 19 Myr. The red and green clusters on the upper panel mark Uranus' and Neptune's orbits during migration. Giant planets are designated by black dots on the lower panel. The black curves represent orbits with perihelia close to the current position of each giant planet. The color code denotes the time evolution.

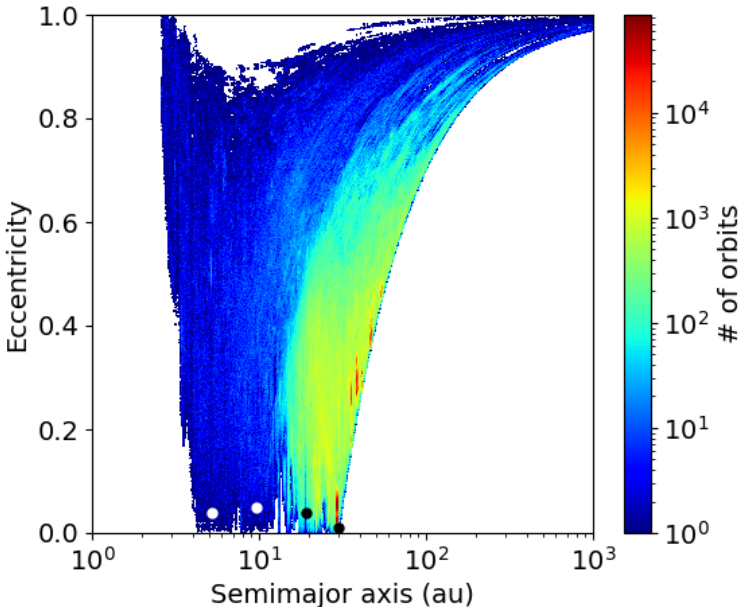


**Figure 5.3:** Density histogram of the orbits for the entire sample in the semimajor axis – eccentricity plane. Orbits of the giant planets are highlighted with white and black dots. The color code represents the number of orbits per bin.

(Dones et al., 1996; Di Sisto et al., 2009; Nesvorný et al., 2017). From the distribution in Figure 5.3, we note that there is no clear limit in eccentricity values, although values substantially cluster between 0.1 and 0.5.

## 5.3 LPC Sample

Our LPC or Oort Cloud comets sample consists of 360 particles, evolving from the same area of the protoplanetary disk towards the Oort Cloud, before coming back inwards to become LPCs.

As noted in Vokrouhlický et al. (2019), an accurate and comprehensive survey for this cometary population that can provide the necessary information for its orbital distribution does not exist. With that in mind, our objective was to build a sample of LPCs, with a size comparable to our JFC sample, with perihelia within 10 au, and a cumulative distribution of their minimum perihelion distance that would be linear. The first condition was purely arbitrary. Our motivation was to obtain some trajectories with perihelion distances that allow some processing to take place, although a lack of large-perihelion orbits ($q > 5$ au) is observed (Vokrouhlický et al., 2019).

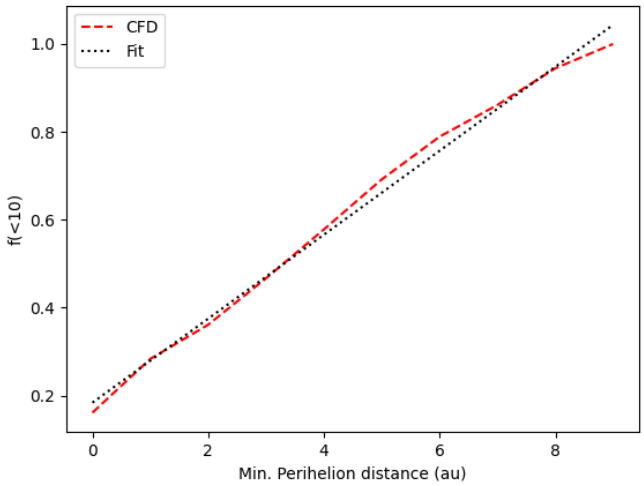


**Figure 5.4:** Cumulative distribution function of the minimum perihelion distance (q < 10) during the return phase for the 360 particles of our sample (red dashed line) compared to a linear fit (black dotted line).

For the second condition we had two arguments: on the one hand our desire to examine equally all possible orbits, without biasing our selection. On the other hand this linear fit is observed for the low perihelia (q < 5 au) (Vokrouhlický et al., 2019), where the activity allows a better characterization and is also expected for larger perihelia (Fernández, 2005), despite the current observational deficiency. This cumulative distribution of perihelion distances, which determined the particles on our sample, is presented in Figure 5.4, compared to a linear fit.

We examined the thermal processing of LPCs during their first phase of orbital evolution, that of the outwards scattering and implantation on the Oort Cloud. As with the JFC sample, this phase lasted for 200 Myr, a time period which guarantees the formation of the reservoir and the dispersal of the planetesimal disk. Their initial and final distributions in the semimajor axis-eccentricity parameter space is given in Figure 5.5, superimposed on the distribution of the JFC sample for comparison. We note that as in the case of the JFCs, no particular preference on the initial semimajor axis exists and that the majority of particles (∼62%) start with eccentricity below 0.1. At the last output at t = 200 Myr, we observe the Oort Cloud formation, despite the small number of particles in our sample. If we consider that the inner edge of the OC is at 1000 au (for consistency with the previous definition of the SD), we can see that the majority of particles is already placed in the OC (61%), populating for the most part (75%) the area beyond the Oort peak at 10000 au, from where dynamically new objects are expected, while

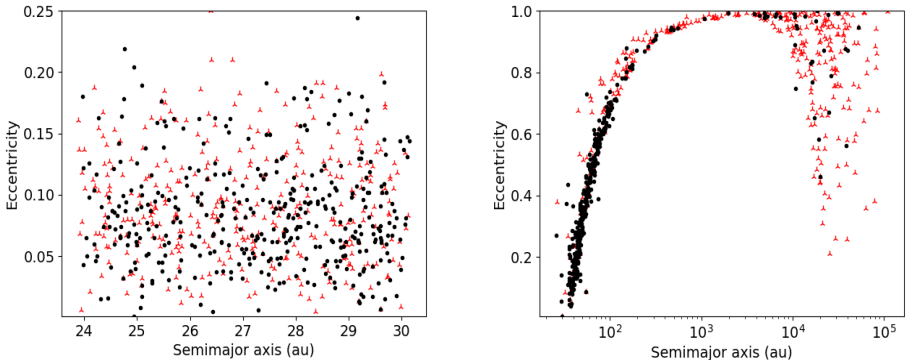


**Figure 5.5:** Initial (left-hand panel) and final (right-hand panel) distributions of the semimajor axis and eccentricities of the particles in our LPC sample (red triangles), plotted over the initial and final distributions of the JFC sample (black dots) for comparison, during the ejection phase from the outer planetesimal disk.

the rest (25%) are expected to become returning LPCs. Regarding the 39% that did not end up in the OC at the last recorded output, we can see that a few have not finished their implantation, having semimajor axis a $>$ 600 au and high eccentricities, while some of them remain in the area where a $<$ 1000 au, from where they are expected to return to the inner Solar System as HTCs.

Their orbital elements where recorded following the same strategy that was used for the JFC sample: a nominal output frequency of 1000 yr, enhanced to 100 yr cadence whenever the object was within 23 au. In Figure 5.6 we present an example of the orbital evolution of a particle from the LPC sample as it is scattered towards the OC. This particle was scattered outwards by Saturn, after spending almost 50 Myr in the protoplanetary region. It reached the OC after $\sim$75 Myr, passing the Oort peak for a small period of time, before it finds a stable orbit in the inner OC. As it was mentioned earlier we did not examine the return phase in this work for reasons that are explained in Chapter 7, so we do not demonstrate a return trajectory as we did for the particle presented in Figure 5.2 or a density histogram of the dynamical pathways of the return phase as we did for the JFC phase (Figure 5.3).

## 5.4 Ejected Sample

Our ejected sample consists of 675 particles, originating from a protoplanetary disk slightly bigger than in the previous simulations, as it starts at 21.4 au, 2 Hill radii outside of Neptune's initial orbit (Raymond et al., 2020b). As previously, the initial distribution of semimajor axis is isotropic and the

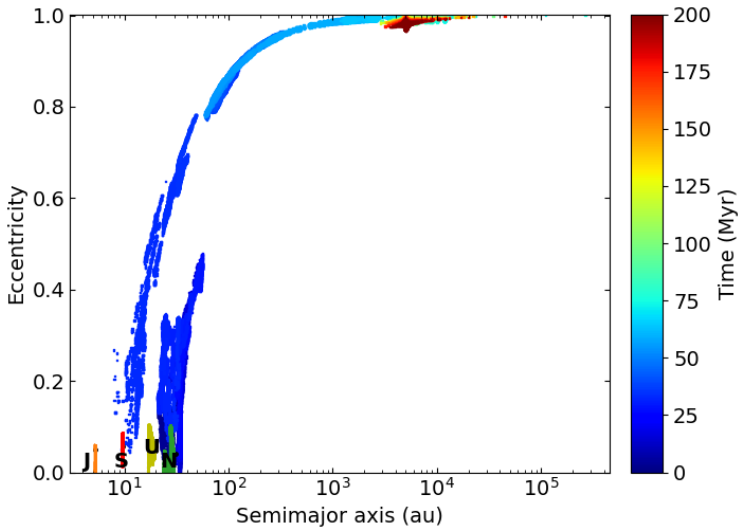


**Figure 5.6:** Example of a particle's orbital evolution during outwards scattering and implantation on the Oort Cloud phase on the first 200 Myr of the simulation. The orange, red, yellow and green clusters mark Jupiter's, Saturn's, Uranus' and Neptune's orbits respectively during migration as designated by their initials.

initial eccentricities very low ($e < 0.01$). These planetesimals interact with the giant planets after the disk disperses and are eventually ejected from the Solar System without reaching one of the source reservoirs. The ejection is considered to occur when they attain distances larger than 1 pc (206,265 au). The timescale of the ejection varies between particles, as each particle's trajectory is unique, determined by the stochastic nature of the its encounters with the giant planets. This point becomes evident by looking at the dispersion of the ejection's time: the average value is ∼32 Myr and the median ∼17 Myr after the beginning of the simulation, indicating a relatively quick ejection, with the shortest ejection time recorded at ∼1 Myr. The possibility of particles spending considerable time in the planetary area is not so rare though, with the longest ejection recorded at ∼186 Myr.

The output frequency was set at 1 Myr. This step, although ideal for the initial purpose of these simulations, was very large for the coupling with the thermal evolution model (see previous discussion in Section 5.2). To reduce this time step at values that were better handled by the thermal evolution model, we took advantage of an extra feature of the simulation: a track record of every time a planetesimal underwent a close gravitational encounter with a giant planet, or passed within 2.5 au of the Sun. The treatment of the encounters with the giant planets was relatively straightforward as all the orbital elements were already calculated, but the consideration of close passages required a certain number of assumptions to obtain all the or-

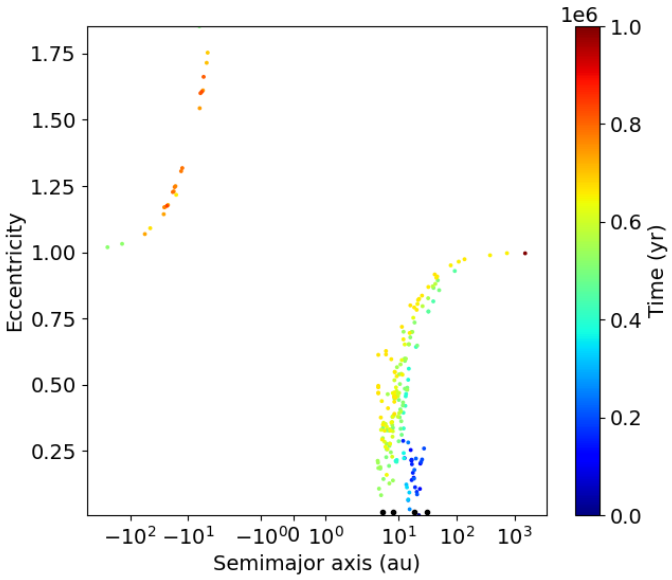


**Figure 5.7:** Example of ejection trajectory in the semimajor axis - eccentricity parameter space. The color code marks the time evolution since the beginning of the simulation. The black dots denote the position of the giant planets at the time of the ejection.

bital elements, which were not readily available. The available information was the time of the passage and the distance at perihelion. Using the time value we were able to place these passages in the chronology of the orbital evolution of each particle, as this was reconstructed by the standard outputs and the encounters with the planets. We assumed that between close encounters the semimajor axis of the orbit remained stable, based on a theoretical calculation by Milani et al. (1987), and that any orbital change is due to small modifications of the eccentricity which we were able to calculate with the other two quantities (i.e. the semimajor axis and the perihelion distance). These two considerations, allowed us to reconstruct the pathways leading to ejection, with a more dense, but non-constant, time step, that had the quality of providing a very good resolution on the periods of major orbital changes.

In Figure 5.7, an example of one of these reconstructed trajectories, leading to a rather quick ejection after only 1 Myr, is given. We notice how the particle initially drifts slightly inwards, where it encounters Jupiter. The gravitational interactions with the planet provoke the excitation of its orbital energy (i.e. semimajor axis and eccentricity) leading eventually to hyperbolic orbits as the particle gradually becomes unbound from the Solar System and heads towards the interstellar space. We should note here, that

in the universal variable approach the semimajor axis of a hyperbolic orbit is considered to be negative so that the energy equation takes the same form as for any type of orbit (Curtis, 2014).

## 5.5 Averaging Elliptic Orbits

*An extended version of this section has been published as an independent article in 'The Astronomical Journal' (Gkotsinas et al., 2023). The original publication can be found on Appendix D.*

### 5.5.1 Motivation and Context

The coupling of cometary trajectories to the thermal evolution model requires smaller time steps than those provided by the $N$-body simulations, to resolve thermal processes taking place on significantly shorter timescales (see Section 3.1.4). Given that no further information was available from the dynamical simulations, a new strategy was necessary to split these time steps sufficiently enough for the resolution of the heat diffusion equation.

A typical approach would be to consider elliptic orbits between consecutive outputs, parametrized by the provided orbital elements of these outputs. Then smaller time steps could be created using constant increments of the eccentric anomaly. This strategy is often employed in cometary thermal evolution models, as it provides finer sampling close to perihelion, where intense activity is expected (Meech and Svoren, 2004). Such an approach, seemingly ideal, can however come with some flaws in our case.

A first issue was some observed positional disparities. Aside from the orbital elements $(a, e, i)$ the $N$-body simulations monitored also the heliocentric distance. Applying the elliptic orbits approach, implies that the orbits should normally position the particles from the first to the next heliocentric distance output, or at least very close. However, this was not necessarily true, suggesting that some intermediate orbital changes could occur during the time steps.

A second issue was noted in Safrit et al. (2021), where a similar sample was used. They suggested that an ambiguity is introduced by the lack of information on the direction of the comet, i.e. if it is on the inbound (towards perihelion) or the outbound (towards aphelion) arc of its trajectory. This may be less important for orbits with orbital periods smaller than the output frequency (P $<$ 100 yr), which are expected to complete at least one revolution within the time step. However, it becomes an issue for orbits with longer orbital periods (P $>$ 100 yr), which are not completed within this output step.

To alleviate these issues, and avoid the introduction of biases and additional free parameters in our simulations, we opted for a different solution.

We replaced the elliptic orbits with averaging circular ones, assuring the conservation of key quantities (such as the energy) over an orbital period. The use of circular orbits solves by definition some of the aforementioned issues as the role of the direction and the orbital period becomes meaningless. In addition, a small, yet not negligible, improvement in numerical efficiency is achieved. For example, the calculation of the received energy for an object on a circular orbit, always on the same distance from the Sun, is less costly than on an elliptic orbit where the distance changes constantly.

Energy-averaged circular orbits have already been used in studies of the thermal evolution of small bodies (Prialnik and Rosenberg, 2009; Guilbert-Lepoutre, 2012; Snodgrass et al., 2017). A similar technique has also been used in climate modeling of putative Earth-like planets on eccentric orbits, where the controlling factor determining whether a planet may retain liquid water is the total energy received over a planet's orbit (Williams and Pollard, 2002; Bolmont et al., 2016). For the purposes of this work, we examined and compared different methods for averaging elliptic orbits in the context of comets' thermal evolution, to select the most appropriate for our model.

### 5.5.2 Brief Presentation of the Main Averaging Schemes

Among the existing approaches for averaging elliptic orbits, the most intuitive one is to estimate an average distance between the object and the focal point. The orbit equation for an elliptic orbit can be written as (Curtis, 2014):

$$r = a\frac{1-e^2}{1+e\cos\theta} \tag{5.1}$$

where $a$ (au) is the semimajor axis, $e$ the eccentricity and $\theta$ (rad) the true anomaly. By integrating Equation (5.1) over the true anomaly over an orbital period we obtain a first expression for an average distance which we can call true-anomaly-averaged radius (Curtis, 2014):

$$\bar{r}_\theta = a\sqrt{1-e^2} \tag{5.2}$$

An alternative approach is to integrate Equation (5.1) over the average angular velocity ($2\pi$/P), where $P$ is the orbital period, of an object in an elliptic orbit over the course of an orbital period. This approach results in the second expression for an average distance, which we call time-averaged radius (Curtis, 2014):

$$\bar{r}_t = a\left(1+\frac{e^2}{2}\right) \tag{5.3}$$

The most common method though is to integrate over a physical quantity, such as the flux or the energy received by an object over an orbital period.

This is the most physically-plausible way to approach the problem, as it ensures that the total energy intercepted by an object, often the most crucial parameter, is not modified over an orbit. Using Equations (5.2) and (5.3) we can calculate a true-anomaly-averaged and a time-averaged flux from which a new set of radii can be deduced (Mendez and Rivera-Valentin, 2017):

$$\bar{r}_{\theta F} = \frac{a(1-e^2)}{\sqrt{2+e^2}} \tag{5.4}$$

$$\bar{r}_{tF} = a(1-e^2)^{\frac{1}{4}} \tag{5.5}$$

the second of which is commonly used on planetary habitability studies (e.g. Bolmont et al., 2016).

In the same spirit, Mendez and Rivera-Valentin (2017) proposed an alternative radius calculated from the equilibrium temperature ($T_{eq}$), guaranteeing an average equilibrium temperature over an orbital period. By integrating the equilibrium temperature over an orbital period they deduced an effective thermal radius:

$$r_T = a\left[\frac{2\sqrt{1+e}}{\pi}\boldsymbol{E}\sqrt{\frac{2e}{1+e}}\right]^{-2} \tag{5.6}$$

$$\approx a(1+\frac{1}{8}e^2+\frac{21}{512}e^4+\mathcal{O}(e^6)) \tag{5.7}$$

where $E$ is the complete elliptic integral of the second order.

We notice that all of the proposed expressions are simple functions of the semimajor axis ($a$) and the eccentricity ($e$). In practice, this means that for any elliptic orbit, using just these two parameters, we can create an 'equivalent' circular orbit using the radii calculated in Equations (5.2, 5.3, 5.4, 5.5 and 5.7). Surprisingly enough, averaging over different quantities results in quite different expressions and distances from the focal point. In general for any given $(a, e)$ couple we can order the resulting expressions as: $\bar{r}_{\theta F} < \bar{r}_{\theta} < \bar{r}_{tF} < r_T < \bar{r}_t$. This means that for a specific orbit, averaging the flux over the true anomaly ($\bar{r}_{\theta F}$) will always place an object closer to the Sun than for example a time-average calculation of the radius ($\bar{r}_t$).

### 5.5.3 Comparative Study

To decide on the most suitable expression for our simulations, we used a thermal evolution model (Guilbert-Lepoutre et al., 2011) with a simplified setup, to compare the internal temperature distributions on a number of simulated objects orbiting on elliptical orbits and their equivalent circular orbits. To test the validity limits of each expression we performed our tests in a range of orbital parameter space relevant to the inner Solar System

(i.e. $\simeq$3-30 au). We placed the simulated comets on 110 different orbits, defined by an equal number of $(a, e)$ couples. We sample the semimajor axis logarithmically ($10^x$, with $x$ ranging between 0.5 and 1.5 with a step of 0.1) suggesting more orbits close to the Sun, where the heating is more important, and the eccentricity linearly between 0 to 0.9 at increments of 0.1.

We run a total of 660 simulations: 110 reference simulations for all the $(a, e)$ couples with objects on elliptic orbits that served as the basis for the comparisons with the remaining 550 simulations where the objects were placed on their equivalent circular orbits created using Equations 5.2 to 5.7. The simulations' time was arbitrarily set at $\simeq$1 Myr, to allow the heat to diffuse sufficiently deep in the objects' interior. This allowed us to examine the temperature differences between the elliptic and their equivalent orbits in their interiors and look for any cumulative or propagation effects that might be introduced during long-term simulations.

In Figure 5.8 an example of the internal temperature distributions produced for an object on an elliptic orbit with $a$=10 au and $e$=0.5 and its equivalent circular orbits is presented. For clarity only the first 1000 yr of the 1 Myr simulation are presented, but this is sufficient to notice the averaging effects. Clearly, none of the averaged orbits reproduce the heating cycle of the elliptic orbit as the object moves between the apsides (i.e. the seasons). Instead, as the distance from the Sun is constant, the heat diffusion follows a steady rhythm and is uniform throughout an orbital period. However, it is evident that some averaging schemes work better than the others. For example, the true-anomaly-averaged flux ($\bar{r}_{\theta F}$, panel (c) in Figure 5.8), although it captures the high temperatures of the perihelion passage, presents excessively high temperatures at the interior. The other solutions seem to give a good representation of the interior distribution, but fail to capture the perihelion passage. To identify the more efficient schemes and to evaluate the level of divergence from the elliptic orbit, we compared individual temperature profiles. These profiles where chosen to be near the end of the simulations ($\simeq$1 Myr), where the differences are expected to be more important.

In Figure 5.9 an example of this comparison is presented for three types of elliptic orbits: (a) a highly eccentric and relatively short orbit with $a$=7.94 au and $e$=0.7, (b) a longer, moderately eccentric orbit with $a$=10 au and $e$=0.5 and (c) a long ($a$=25.11 au) low eccentricity ($e$ = 0.2) orbit. Temperature profiles from the reference elliptic orbit at perihelion, aphelion and two points halfway in between at times coinciding with a quarter of its orbital period, both on its way inwards (from aphelion to perihelion) and outwards (from perihelion to aphelion) are used for the comparison with the circular profiles. The latter, as expected, are nearly-vertical as constant illumination is implied.

This comparison confirmed some of the previous remarks and allowed us

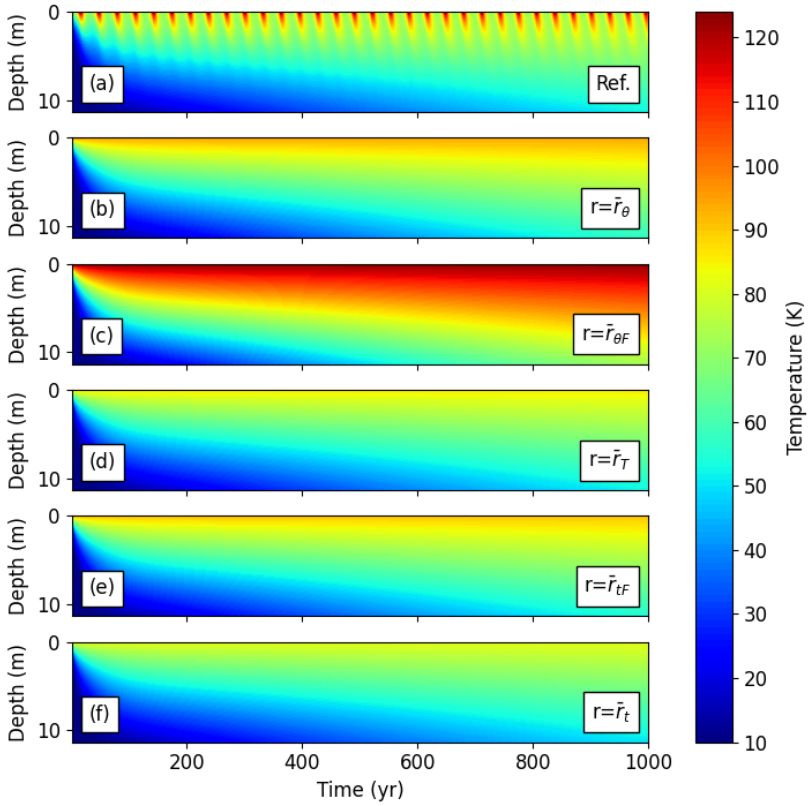


**Figure 5.8:** Subsurface temperature distributions for a layer of 10 m over a period of 1000 years for: (a) an elliptic orbit with $a$=10 au and $e$=0.5, (b) true-anomaly-averaged radius ($\bar{r}_\theta$), (c) true-anomaly-averaged flux ($\bar{r}_{\theta F}$), (d) effective thermal radius ($r_T$), (e) time-averaged flux ($\bar{r}_{tF}$) and (f) time-averaged radius ($\bar{r}_t$) equivalent circular orbits.

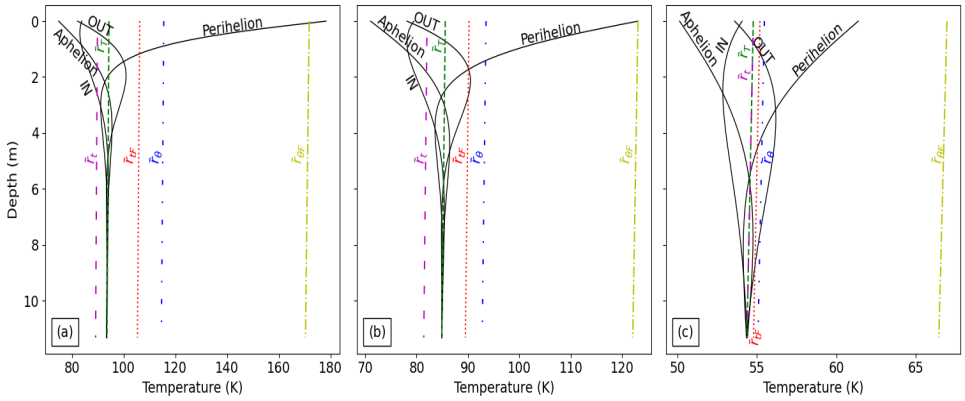


**Figure 5.9:** Temperature profiles for a subsurface layer of 10 m, ∼1 Myr after the start of the simulations, for three $a, e$ couples: (a) $a$=7.94 au and $e$=0.7, (b) $a$=10.0 au and $e$=0.5, (c) $a$=25.11 and $e$=0.2. The solid black lines give the temperature profiles of elliptic orbits at perihelion, aphelion and halfway through -time-wise- both inwards and outwards. The temperatures profiles for the equivalent orbits are: true-anomaly-averaged radius ($\bar{r}_\theta$) (blue loosely dashed-dotted line), true-anomaly-averaged flux ($\bar{r}_{\theta F}$) (yellow dashed-dotted line), time-averaged radius ($\bar{r}_t$) (purple loosely dashed line), time-averaged flux ($\bar{r}_{tF}$) (red dotted line) and effective thermal radius ($r_T$) (green dashed line).

to distinguish the most efficient averaging scheme:

- The true-anomaly-averaged flux ($\bar{r}_{\theta F}$) is capturing the effect of the perihelion passage better than the other schemes, even for the less eccentric orbit (panel (c) of Figure 5.9), where the temperature difference at the surface is ≃6 K. Nevertheless, it fails completely on the other positions both on the surface and the subsurface: Divergences range from ≃11 K in the least eccentric to ∼80 K in the most eccentric orbit.

- The true-anomaly-averaged radius ($\bar{r}_\theta$) works slightly better, with calculated surface temperatures between those of the two apsides and subsurface profiles closer to the reference ones. The temperature differences range from ≃20 K in the most eccentric, to almost complete convergence in the least eccentric orbits.

- Overall, the time-averaged expressions (Equations 5.3, 5.5 and 5.7) performed better. Despite their failure to reproduce the high surface temperatures encountered at perihelion, especially for the most eccentric orbits, these schemes reproduce much better the cooling effect of the aphelion passage, leading to internal temperature distributions reaching convergence with those of the reference orbit in all the examples of Figure 5.9.

- The effective thermal radius ($r_T$) stands out as it produced produced an internal temperature distribution converging almost perfectly to the reference one, with complete convergence very close to the surface: below 5-6 m in the first two examples and 10 m in the last.

### 5.5.4 Efficiency in the Orbital Parameter Space

Having established that true-anomaly-averaged (or spatial) expressions are the least consistent with the reference simulations, we focused our attention to the time-averaged schemes and their efficiency on the whole orbital parameter space. To do so, we examined temperature differences between the averaging schemes and the reference elliptic orbits at three depths of our simulated comets: the surface and 1 and 10 meters below it at the four instances of orbital revolution described previously.

In Figure 5.10 we present the temperature differences ($\Delta T$) between the three time-averaged formulas ($\bar{r}_t$, $\bar{r}_{tF}$, $r_T$) and the elliptic orbits at perihelion. All schemes underestimate the surface temperatures during the perihelion passage. The time-averaged radius ($\bar{r}_t$) deviates the most from the reference orbits (maximum $\Delta T$ of $\simeq$358 K or in terms of relative difference by 73%), especially for very eccentric ($e$ >0.5) and short orbits ($a$ <10 au). It is followed by the effective thermal radius ($r_T$) with maximum divergence of $\simeq$343 K (relative difference of 70%). The time-averaged flux ($\bar{r}_{tF}$) presents a maximum $\Delta T$ of $\simeq$298 K (or relative difference of 61%). These relative differences at the surface rise with the eccentricity, becoming important ($\simeq$20%) above $e$=0.3, and really significant for high eccentricities (50% for $e$=0.7 and $\simeq$70% for $e$=0.9) for the time-averaged and the effective thermal radius. The time-averaged flux ($\bar{r}_{tF}$) has slightly smaller relative deviations especially above $e$ >0.4 where it is constantly lower than the other time-averaged schemes by $\simeq$4-9%.

All three schemes are more robust in the objects' interiors (middle- and right-hand panels of Figure 5.10). At 1 m below the surface the time-averaged radius ($\bar{r}_t$) differences converge quickly for all orbits (maximum $\Delta T$ of $\simeq$26 K) except for distant ($a$ >10 au) and highly eccentric ($e$ >0.5) orbits for which the maximum $\Delta T$ is $\simeq$49 K. The same stands for the effective thermal radius ($r_T$) only with better convergence for short ($a$ <10 au) and low-eccentric orbits ($e$ <0.5). For distant ($a$ >10 au) and highly eccentric ($e$ >0.5) orbits the problem remains but is slightly less pronounced (with maximum $\Delta T$ of $\simeq$44 K). Long period orbits with prolonged excursions into warm areas around perihelion allow the heatwave to advance deeper in the interior and extend the temperature differences well below the surface. In these cases underestimating the perihelion temperature remains problematic, unlike the cases of short orbits ($a$ <10 au) where the heating, although more intense, takes place in a short period of time that is not sufficient for its diffusion in the interior (panel (a) versus panel (b) in Figure 5.9 for exam-

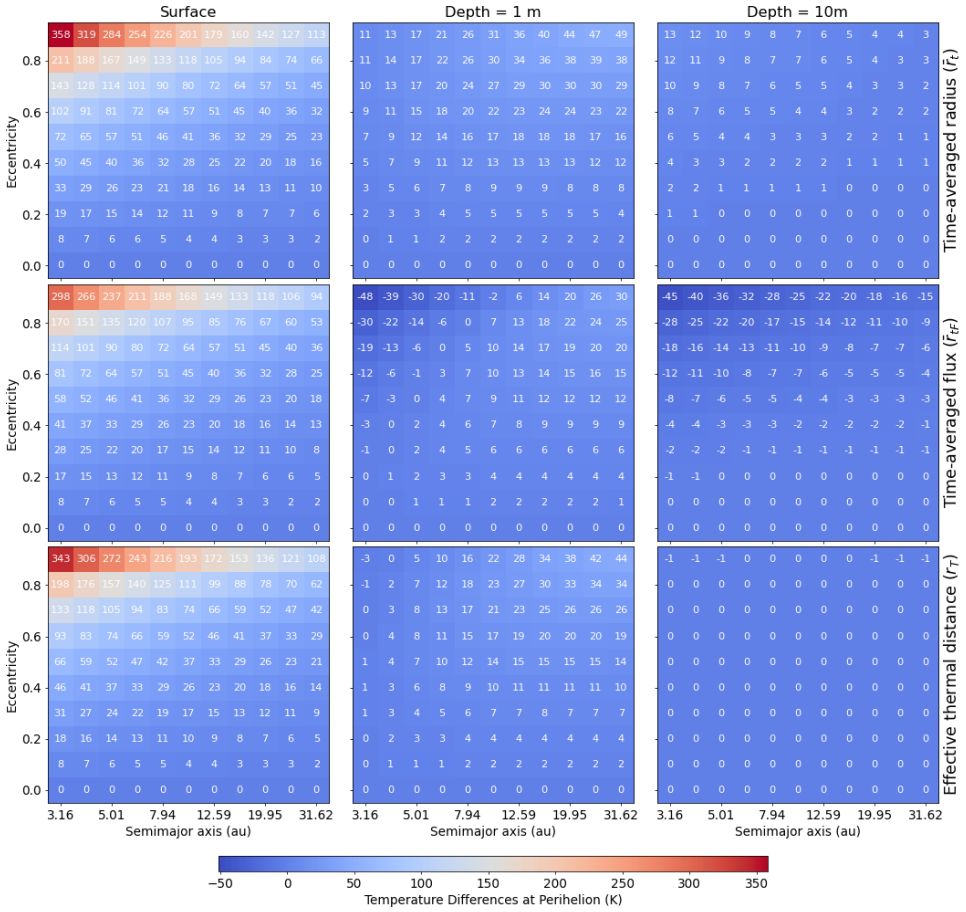


**Figure 5.10:** Temperature differences between the elliptic orbits at perihelion and the time-averaged radius ($\bar{r}_t$) (top row), the time-averaged flux ($\bar{r}_{tF}$) (middle row) and the effective thermal radius ($r_T$) equivalent orbits (bottom row) for three depths: surface (left panels), 1 m (middle panels) and 10 m (right panels) for all the $a, e$ couples.

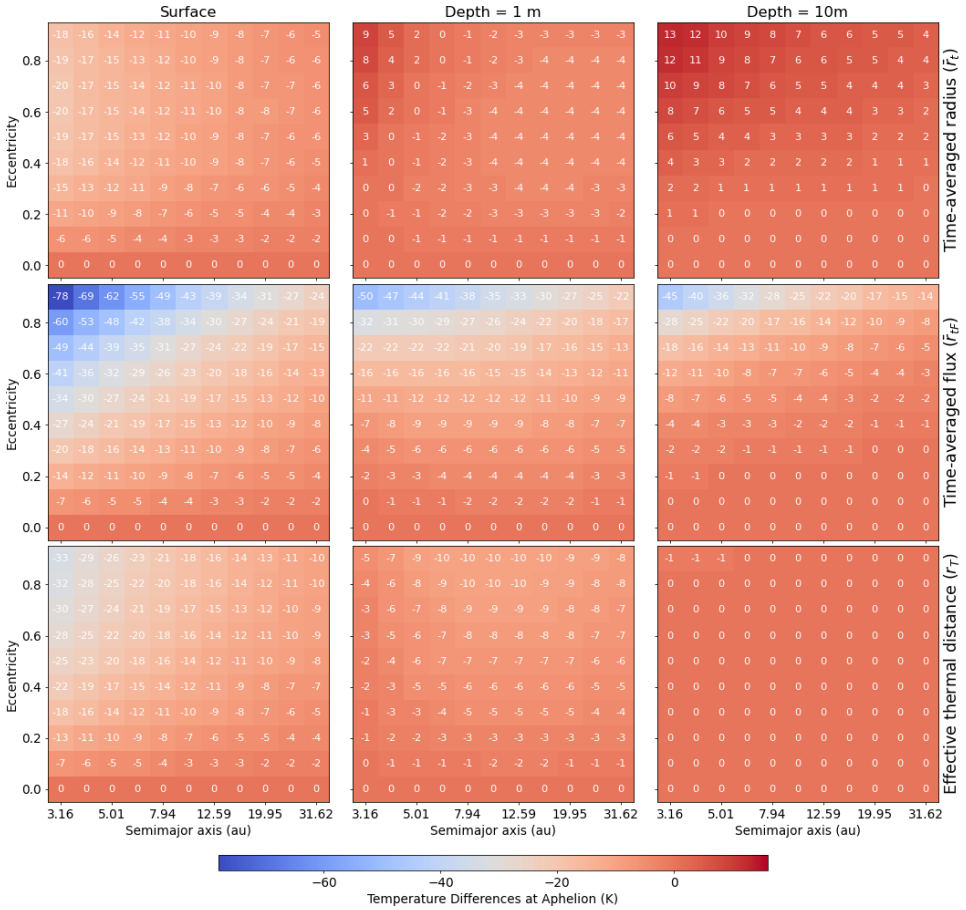


**Figure 5.11:** Temperature differences between the elliptic orbits at aphelion and the time-averaged radius ($\bar{r}_t$) (top row), the time-averaged flux ($\bar{r}_{tF}$) (middle row) and the effective thermal radius ($r_T$) equivalent orbits (bottom row) for three depths: surface (left panels), 1 m (middle panels) and 10 m (right panels) for all the $a, e$ couples.

ple). These differences almost completely disappear 10 m below the surface in the case of the effective thermal radius ($r_T$) ($\Delta T_{max}$=-1 K for $e$ =0.9, lower right panel in Figure 5.10) and the time-averaged radius ($\bar{r}_t$) (with the exception of very short ($a$ <10 au ) and highly eccentric orbits ($e$ >0.7)). On the contrary, the time-averaged flux ($\bar{r}_{tF}$) differences at the interior (middle panels in Figure 5.10) fail to achieve convergence in high eccentricities ($e$ ≥0.5), whether it is a short or a long orbit. In addition these deviations persist at larger depths (middle right panel of Figure 5.10), as there is still no convergence for highly eccentric orbits ($e$ ≥0.5) and the differences on low eccentricity orbits are higher than those of the effective thermal radius and the time-averaged radius.

At aphelion we notice a reversal on the averaging behavior: the temperatures, as expected, are overestimated (Figure 5.11). The time-averaged radius ($\bar{r}_t$) works better than the other methods in the surface and the close subsurface area ($\Delta T_{max}$=20 K versus $\Delta T_{max}$=-78 K for the $\bar{r}_{tF}$ and $\Delta T_{max}$=33 K for the $r_T$ at the surface and $\Delta T_{max}$=9 K versus $\Delta T_{max}$=50 K and $\Delta T_{max}$=10 K respectively, 1 m below the surface). However, at 10 m below the surface the convergence for the effective thermal radius is almost complete ($\Delta T_{max}$=-1 K in only three short and eccentric orbits) unlike for the time-averaged radius and the time-averaged flux where there is still no convergence.

As expected the temperature differences are less pronounced at the two halfway points inwards and outwards (see Figures A.1 and A.2 in the Appendix), when compared to those of the two apsides (Figures 5.10 and 5.11). However, the efficiency of the time-averaged schemes for averaging elliptic orbits is confirmed furthermore and the distinction of the effective thermal radius among the time-averaged schemes is established. Indeed the calculated temperatures reproduce better the average temperatures on elliptic orbits and they achieve convergence very quickly in the interior.

### 5.5.5 Present Work Selection

Overall the time-averaged schemes work better than the true-anomaly or spatial-averaged ones. This is because the true-anomaly formulas are restricted to the calculation of an average distance from the focal point. Although this seems to be a sufficient assumption, it ignores a crucial piece of information: the different time spent by an object at different distances from the focal point. Indeed an object on an elliptic orbit will move much faster close to perihelion than close to aphelion, implying -in our case- more time in colder regions. This information is integrated in temporal expressions rendering them more appropriate in the approximation of elliptic orbits. With that in mind, the 'weighted'surface temperatures obtained from the time-averaged schemes, which are generally closer to the aphelion temperatures of an elliptic orbit, are more appropriate than an average of the perihelion-aphelion temperatures as proposed by the spatial-averaged schemes.

As mentioned earlier the time-averaged ($\bar{r}_t$) and the effective thermal radius ($r_T$) better approximate the temperature distributions of elliptic orbits with the exception of the surface temperatures at perihelion. These two distances are increasing functions of the eccentricity whereas the time-averaged flux ($\bar{r}_{tF}$) is a decreasing one (Mendez and Rivera-Valentin, 2017). This implies that for a given $(a, e)$ couple, the time-averaged flux will place an object closer to the perihelion, leading to a systematic overestimation of the surface temperature. On the other hand, the time-averaged and the effective thermal radius, (very close by definition, see Equations (5.3) and (5.7)) place the object closer to the aphelion accounting better for the lower temperatures

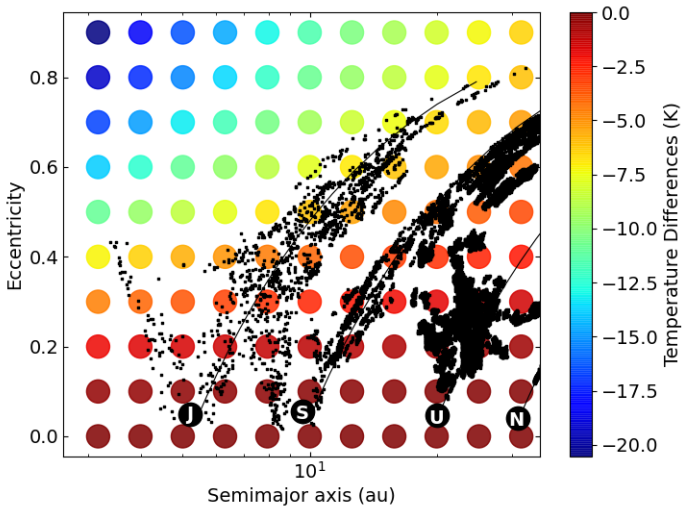


**Figure 5.12:** An average of the effective thermal radius ($r_T$) inwards and outwards for all the $a, e$ couples. Each circle represents a point in our orbital parameter space sampling. The color code gives the scale of the temperature difference.

reigning during the biggest part of an orbit (especially for highly eccentric ones), managing better to represent the internal temperature distribution. Interestingly, there is no clear distinction on the efficiency between these two formulas, as the time-average radius works better at aphelion and halfway through both inwards and outwards at the surface and 1 m below, but fails to convergence as quickly as the effective thermal radius which manages to converge in all cases at maximum 10 m below the surface.

For complementary reasons we also tested the equivalent semimajor axis ($a_c = a(1 - e^2)$) proposed in Prialnik and Rosenberg (2009), deriving also from a time-averaging integral and used in our initial approach (see Chapter 2). As this average distance provides the same energy per orbit as the real eccentric one, it is reliable only when orbital periods are very close. Otherwise significant deviations were observed (for very eccentric orbits for instance), with a systematic overestimation of the surface and internal temperatures. Its validity thus remains limited to low eccentricity orbits ($e$ <0.3) or very limited timescales, as done in Guilbert-Lepoutre (2012); Snodgrass et al. (2017).

To test the use of averaged circular orbits in practice, we compared the orbital changes of the particle in Figure 5.1 as it moves inwards to an average of the inwards and outwards surface temperature differences for the effective thermal radius ($r_T$). Figure 5.12 points out that with the exception of short

and highly eccentric orbits ($a$ <10 au and $e$ >0.5), which are rarely visited by particles in our sample (sew also Figure 5.3), the differences between the averaged circular orbits and the reference elliptic ones are very small (usually between 1 and 7 K) in the more frequented areas of the orbital parameter space. Even in the area of long and highly eccentric orbits ($a$ >10 au and $e$ >0.5), the temperature divergences are not higher than ∼10 K.

Of course the use of averaged orbits, despite the conceptual and numerical advantages described earlier, is not flawless. Their inability to capture the high temperatures around perihelion, as highlighted in Figure 5.10, may lead to a significant loss of information, as high-temperature thermal processes like the sublimation of water ice, associated with nucleus erosion, are poorly described. This of course, is not the case for low-temperature thermal processes, such as the sublimation of hyper and moderately volatile species (Meech and Svoren, 2004). From this point of view, averaging orbits can be a very effective and useful with a large area of validity, suitable for tracing the long-term and long-distant activity (well beyond Jupiter's orbit), driven by volatile species other than water, which is the main purpose of our model and this work.

# Chapter 6

# Applications of the Thermal Evolution Model

## 6.1 Early Thermal Processing

We ran a total of 1418 simulations to examine the early thermal processing on simulated planetesimals during the dispersion of the planetesimal disk. The simulated planetesimals examined are part of the samples described in Sections 5.2, 5.3 and 5.4. All the particles had the same initial characteristics (composition, porosity etc., see Chapter 3), as they are considered to have formed in the same area of the protoplanetary disk. We remind that for the KB/SD and OC populations the $N$-body simulations recorded their orbital evolution for a period of 200 Myr from the beginning of the simulation. The tracking of the orbital evolution for the ejected population varied as each particle has its own orbital pathway, with the slowest ejection taking place after $\sim$186 Myr from the beginning of the simulation.

### 6.1.1 Ending Conditions

Besides the working assumptions inherited by the $N$-body simulations, such as the output frequency and the different flags increasing the output cadence, three additional conditions were added in the final simulations, after a series of diagnostic tests. These conditions aimed at improving the efficiency of the simulations, by forcing their completion before their 'dynamical' ending, if no thermal processing was expected to take place in the simulated planetesimals.

The first condition called for the ending of the simulation when the thermal evolution became stagnant after a certain number of iterations. This condition was added to avoid meaningless integrations that did not contribute to an object's thermal status. In practice, if after 100 iterations no advancement in the ice interfaces was recorded the simulation was stopped,

regardless if the 200 Myr limit has been reached. Planetesimals that consumed rather quickly their hyper-volatile content and did not record any significant changes in the other volatile species were mainly affected.

The second condition was introduced as a complementary tool to the first one. It aimed at particles that maintained a part of their hyper-volatile content at some subsurface layer without any significant evolution. In fact, we observed that for these type of particles, the first condition failed to identify the stagnancy of the thermal evolution due to small changes in the float precision. These changes occurred at large heliocentric distances ($>$ 70 au) where low ambient temperatures are expected. We therefore set the second ending flag at a $>$ 100 au. At that distances an estimation of the ambient temperature yields $\sim$27 K. Considering that at such distances the particles were on their way out and no significant drop of their orbital elements is expected, provoking an increase in temperature, this condition allowed for a significant improvement in computation time, without any loss of information.

A specific ending condition was used for the ejected population, where the orbital evolution was quite different. In the case of ejected planetesimals as we saw in Section 5.4 the orbits will eventually become hyperbolic as the orbital elements are excited and the planetesimals become unbound from the Solar System. Given that our orbit averaging technique has been validated only in the case of elliptic orbits, the simulations were ended when the orbit of an ejected particle became hyperbolic, flagged by eccentricity values, e $>$ 1.0. From a thermal evolution point of view, this was a harmless condition, as the passage from eccentric to hyperbolic orbits occurs usually at large values of the semimajor axis (a $>$ 100 au), where no significant alterations were expected.

### 6.1.2 Examples of Early Processing for Individual Particles

In Figures 6.1, 6.2 and 6.3 we present examples for the evolution of the temperature distributions at the interior of simulated planetesimals from the three studied populations: KB/SD, OC and ejected planetesimals respectively. The evolution of the ice species, wherever visible; is plotted over the temperature distributions. We note this specifically to avoid any confusion with the technique employed in our initial simulations (see Chapter 2). Here, the evolution is calculated using the ice evolution model described in Section 3.3.

Although the dynamical pathway of each particle is unique and its thermal evolution not necessarily representative of the population, this allow to get some first impressions of some general tendencies of their thermal processing and how the aforementioned conditions are applied. We remind that for every output of the orbital evolution, represented here by the effective thermal radius ($r_T$), a temperature profile is calculated, allowing the

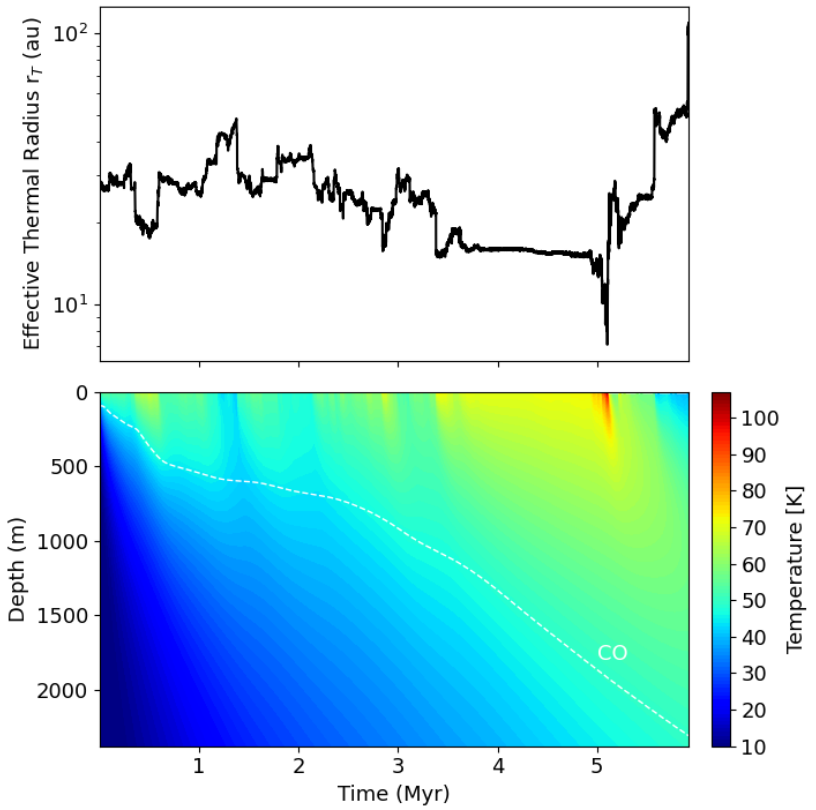


**Figure 6.1:** Example of thermal processing for a planetesimal scattered outwards to the Kuiper Belt/Scattered Disk. Upper panel: Evolution of the effective thermal radius ($r_T$). Lower panel: Temperature distribution in the planetesimal's interior for a subsurface layer of ∼2500 m. The color code denotes the temperature. The dashed white line represents the advancement of the CO ice interface. The $CO_2$ and amorphous $H_2O$ ice interfaces are not visible in this scale, as they remained very close to the surface.

.

subsequent calculation of the advancement of the ice interfaces. For these examples particles with relatively short simulation timescales were chosen, permitting a better visibility of the internal evolution.

**KB/SD Particle:** The thermal evolution for this particle was simulated for ∼6 Myr, before the simulation ended as the object moved at large heliocentric distances beyond 100 au and started cooling (see Figure 6.1). The particle roams the planetary area for ∼5 Myr, where it interacts gravitationally with the giant planets. These encounters provoke changes in its orbital elements, bringing it from colder to warmer areas and vice versa, resulting in subsequent heating and cooling periods for its interior. A sudden drop of

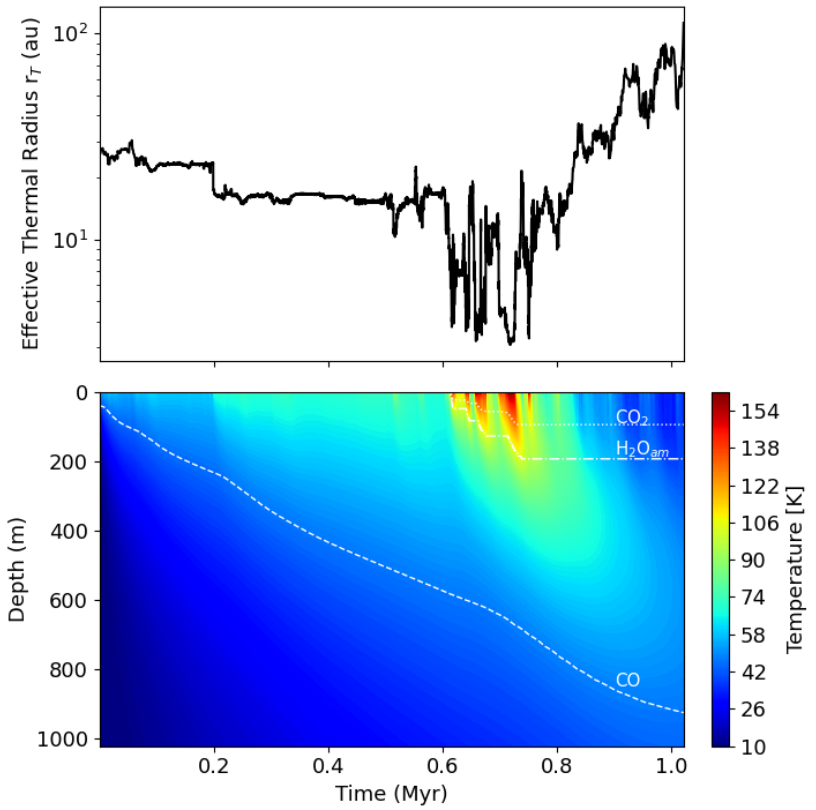


**Figure 6.2:** Example of thermal processing for a planetesimal scattered outwards to the Oort Cloud. Upper panel: Evolution of the effective thermal radius ($r_T$). Lower panel: Temperature distribution in the planetesimal's interior for a subsurface layer of ∼1000 m. The color code denotes the temperature. The dashed, dotted and dashed-dotted white lines represent the advancement of the CO, $CO_2$ and amorphous $H_2O$ ice interfaces respectively.

.

its orbital elements will bring it close to Jupiter and Saturn resulting on the one hand in an intense heating period and on the other hand in the beginning of its scattering towards the Trans-Neptunian area. The CO interface is constantly advancing towards deeper layers, while the other species are only slightly affected during the intense heating period: the $CO_2$ interface advances ∼1.2 m and the crystallization front ∼6 m, (not visible in this scale). From that point on, no significant processing was recorded.

**OC Particle:** This particle despite spending less time in the planetary area (∼1 Myr) is submitted to a more intense heating as it orbits close to Jupiter for a period of ∼200 kyr (upper panel of Figure 6.2). It is interesting to observe the heating pattern in this case. The surface temperatures are

higher and the heating more intense than in the particle presented previously, provoking the sublimation of $CO_2$ ices and the crystallization of amorphous $H_2O$ ice deeper in the planetesimal's interior. However as the residence times are much shorter, there was not enough time for the heat wave to further propagate in the particle's interior, leaving the deepest parts of the object at low temperatures. After this intense heating period, during which several heating episodes can be identified, the object is scattered towards the OC where no significant alterations are recorded in its interior. The comparison between the orbital evolution and the induced thermal processing of these two particles provides a first hint on the different processing outcomes of these two populations.

**Ejected Particle:** This particle although submitted to the least intensive heating in terms of intensity (see the temperature scale in the lower panel of Figure 6.3), reflects a general trend observed in the ejected population: Prolonged residence time in the planetary area. This particle spends the bulk of its Solar System lifetime ($\sim$1.6 Myr) between the orbits of Saturn and Neptune, until the former provokes its ejection. Although compared to other particles of the ejected population this is a generally short time, compared to the particles of the other populations we can say that it is bigger by a factor of $\sim$5 at least. This tendency to spend larger periods of times at smaller heliocentric distances is characteristic of the ejected population, hinting for more processed interiors.

Before advancing with the population analysis we would like to remind that these drops in the effective thermal radius and the resulting intense thermal periods, are not to be confused with typical perihelion passages. Every point in the upper panels of the Figures 6.1, 6.2 and 6.3 represents an averaged orbit, created by the orbital elements of the particle at this particular moment of its orbital evolution. With that in mind, we can say that these drops are the result of an object's tendency to orbit closer to the Sun.

### 6.1.3 Early Thermal Processing of Cometary Populations

As we mentioned earlier, examining individual objects can reveal some of the characteristics of the induced thermal processing, but not necessarily of all the planetesimals of a population. To this end, the use of $N$-body simulations proved to be indispensable. As they provided a large number of particles and trajectories, they allowed a statistically significant examination of the thermal processing of the three studied populations. This processing is quantified by the evolution of the ice and crystallization interfaces, as in our initial approach, although this time this advancement is not inferred by the developing temperatures in the cometary interiors but calculated by an ice evolution model.

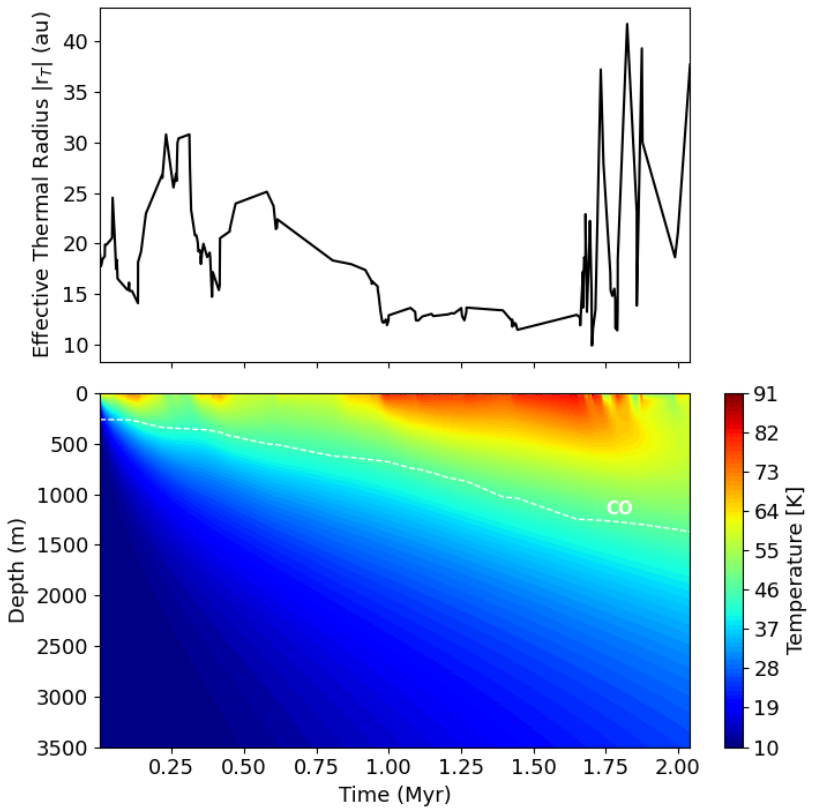


**Figure 6.3:** Example of thermal processing for a planetesimal as it gets ejected from the Solar System. Upper panel: Evolution of the absolute value of the effective thermal radius ($r_T$). Lower panel: Temperature distribution in the planetesimal's interior for a subsurface layer of ∼3500 m. The color code denotes the temperature. The dashed white line represents the advancement of the CO ice interface. The $CO_2$ and amorphous $H_2O$ ice interfaces are very shallow (∼1 m below the surface) and thus not visible in this scale.

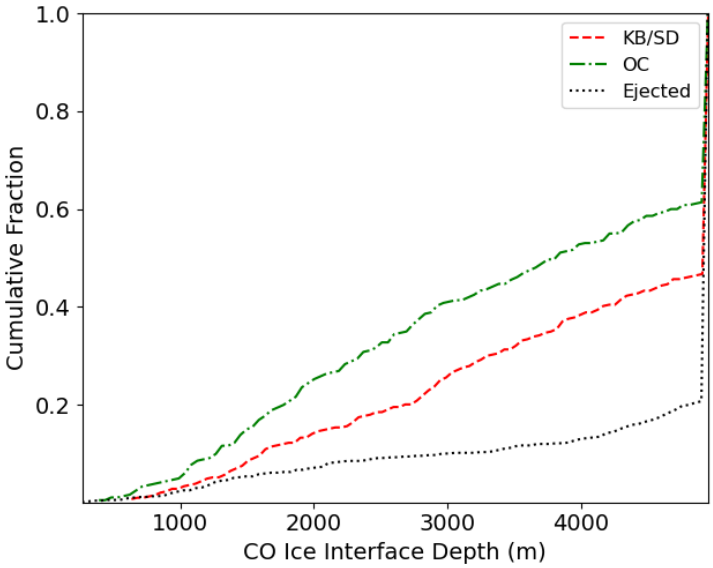


**Figure 6.4:** Cumulative distribution of the CO ice interface depths for the members of the three studied populations: KB/SD (red dashed line), OC (green dashed-dotted line) and ejected (black dotted line) planetesimals, at the end of their outwards scattering and ejection respectively.

In Figure 6.4, the cumulative distribution of the depths of the CO ice interface for all the particles in the three studied populations at the end of the simulations is presented. We remind that the end differs between particles, even for the KB/SD and OC populations, as additional ending conditions were added to the one imposed by the $N$-body simulations, where the output was halted at 200 Myr. As an indication the mean and median simulation times for the KB/SD population changed to ∼80 and ∼36 Myr after the application of the ending conditions. The shortest outward scattering was recorded at ∼1.4 Myr. Of course several particles did not meet any of the ending conditions and their thermal evolution was tracked for the whole 200 Myr. For the OC population, the corresponding numbers are considerably lower, ∼31 and ∼16 Myr for the mean and the median simulation times respectively and ∼640 kyr for the shortest simulation. These numbers show that OC particles are not just scattered farther out, but they are scattered out much quicker. For the ejected population, the eccentricity limit shortens as well as the initial lifetimes calculated by the $N$-body simulation: on average we follow the thermal evolution for ∼16 Myr, with the median being ∼10 Myr and the shortest thermal simulation lasting ∼1000 yr.

We note a clear distinction in the processing of the three populations, directly related to their orbital evolution. The ejected population, although studied for much shorter timescales, is the most processed population, for the reasons described in Section 6.1.2. Indeed, 78% of its members have exhausted their CO content. The possibility of CO ice surviving close to the surface is rather weak as only 9% of the ejected planetesimals preserved their CO content in the upper half of the nucleus. These numbers confirm previous estimations (Raymond et al., 2020b) for intense processing of this population, compared to the particles surviving the ejection and ending up in the source reservoirs.

Planetesimals ending up in the KB/SD experienced important processing as well. Approximately 53% of the members of this population have lost their CO content down to their core. However, retaining hyper-volatiles close to the surface is not inconceivable with 17% of the particles maintaining CO in the upper half of their nuclei.

The least processed population, and the one with the more chances of preserving hyper-volatiles is the OC population, the progenitors of LPCs. Although two out of five particles (∼39%) were not able to retain CO ice at all, the chances of its survival, even close to the surface, are significantly higher: 36% of its members maintained CO ice above 2500 m below the surface at the end of the simulations.

These processing estimations based on the CO ice, are in general confirmed by the study of the evolution of the $CO_2$ ice and crystallization interfaces, although an interesting difference appears between the KB/SD and OC populations. Figures 6.5 and 6.6 confirm that the ejected population is the most processed among the three, as both the $CO_2$ and crystalliza-

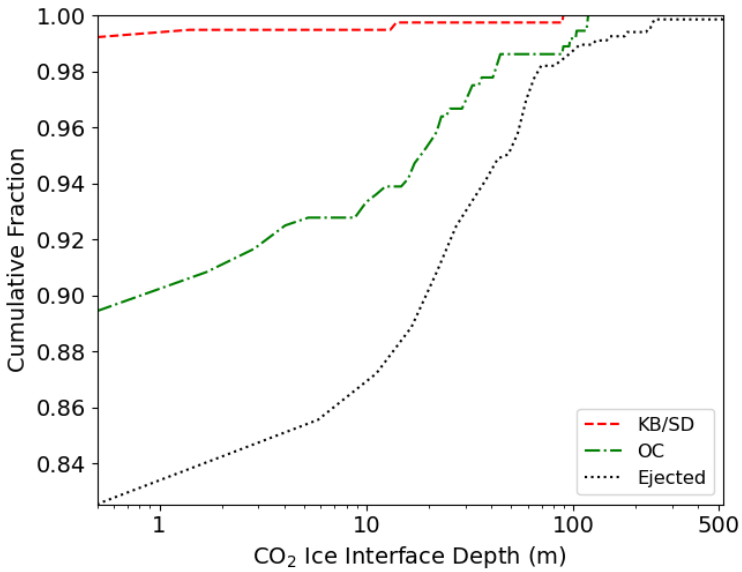


**Figure 6.5:** Cumulative distribution of the $CO_2$ ice interface depths for the members of the three studied populations: KB/SD (red dashed line), OC (green dashed-dotted line) and ejected (black dotted line) planetesimals, at the end of their outwards scattering and ejection respectively.

.

tion interfaces have advanced deeper in a larger amount of its members. As these processes operate on higher temperatures, harder to attain in the outer parts of the planetesimal disk, the number of processed planetesimals is significantly reduced compared to the CO estimation. Approximately 18% of the members of this population have lost part of their $CO_2$ content, and 27% had an upper layer crystallized. This processing is generally constrained in the first 100 m below the surface, although in a small percentage ($< 2\%$ for both molecules) more significant processing, reaching the first 1000 m below the surface was recorded. These percentages are significantly lower in the other two populations: $\sim$10% in the case of the OC (for both $CO_2$ and amorphous $H_2O$ ice) and just $\sim$1.3% for the KB/SD particles.

The interesting observation is that if we use the $CO_2$ ice and crystallization interfaces as processing indicators, the KB/SD population appears to be less processed than the OC population, contrary to the CO estimations. This indicates that the survival of hyper-volatiles, as it can takes place in a wide range of distances, depends on the residence time at these distances where the sublimation is possible. As the KB/SD objects are usually scattered outwards by Neptune in longer timescales and they often remain in the KB and inner parts of the SD ($a < 100$ au) where temperatures can sus-

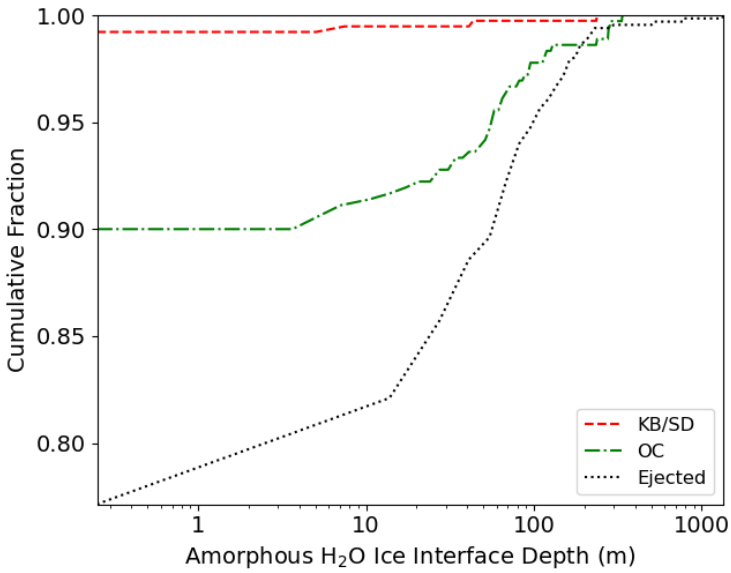


**Figure 6.6:** Cumulative distribution of the depths of the amorphous $H_2O$ ice crystallization front for all the particles of the three studied populations: KB/SD (red dashed line), OC (green dashed-dotted line) and ejected (black dotted line) planetesimals, at the end of their outwards scattering and ejection respectively.

tain CO sublimation, they are expected to lose more of their hyper-volatile content. This also implies that they rarely roam the planetary area, where the sublimation of $CO_2$ and the crystallization of amorphous $H_2O$ ice can take place. On the contrary, planetesimals ending up in the OC, can have short passages from the planetary area as it is more likely to get scattered outwards by one of the other planets. As in the example of Figure 6.2 this is expected to provoke intense but short heating episodes that can affect most of the icy components, but on a thinner subsurface layer.

The relation between the timescale of the outwards scattering and the possibility of retaining hyper-volatiles in these two populations is presented in Figure 6.7. We can clearly see that planetesimals ending up at distances within 40 au (denoted with blue dots), no matter the timescale of their ejection, cannot retain hyper-volatiles. Planetesimals scattered quickly ($t < 100$ Myr) and at larger distances ($a > 40$ au) are those with the higher chances of preserving their hyper-volatile content. Of course, exceptions to these observations exist, proving once again the stochastic nature of the outwards scattering. However, some distance and time limits can still be identified and some Trans-Neptunian areas and populations such as the classical KB

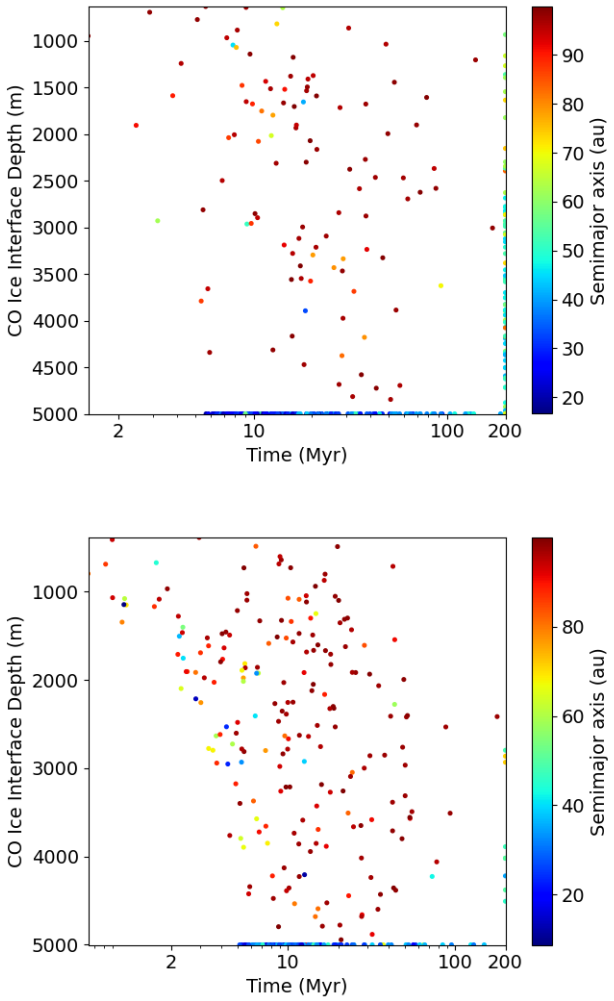


**Figure 6.7:** Timescales of the outwards scattering vs the depth of the CO ice interface at the end of the simulations for all the particles in the KB/SD population (upper panel) and the OC population (lower panel). The color code denotes the final value of the semimajor axis for each particle.

and the resonant populations seem unlikely to retain hyper-volatile species. Moreover this time-distance relation confirms our initial hypothesis that the orbital trajectory can be a decisive factor of the thermal processing of comets even from the early phases of their existence. It can also explain some of the compositional differences observed between the two populations.

Analytical statistics on the thermal processing of the three studied populations, confirming the above observations regarding their thermal processing are given in Table 6.3.

**Table 6.1:** Depths (m) of the interfaces for the examined ice species in our model: CO, $CO_2$ and amorphous $H_2O$ ice, at the end of the scattering or ejection phase, for the three populations: KB/SD, OC and Ejected comets.

| Ice Species | Max. | Min. | Median | Mean | $\sigma$ |
|---|---|---|---|---|---|
| **Kuiper-Belt/Scattered Disk** | | | | | |
| CO | 5000.0 | 631.7 | 5000.0 | 3986.8 | 1341.9 |
| $CO_2$ | 90.1 | 0.5 | 0.5 | 0.8 | 4.6 |
| $H_2O_{am}$ | 240.5 | 0.3 | 0.3 | 1.0 | 12.5 |
| **Oort Cloud** | | | | | |
| CO | 5000.0 | 388.0 | 3850.8 | 3494.1 | 1513.3 |
| $CO_2$ | 119.0 | 0.5 | 0.5 | 3.5 | 13.7 |
| $H_2O_{am}$ | 340.5 | 0.3 | 0.3 | 8.9 | 37.9 |
| **Ejected** | | | | | |
| CO | 5000.0 | 261.0 | 5000.0 | 4575.1 | 1063.6 |
| $CO_2$ | 533.7 | 0.5 | 0.5 | 8.8 | 31.8 |
| $H_2O_{am}$ | 1366.5 | 0.3 | 0.3 | 21.1 | 75.3 |

### 6.1.4 Planetesimal Disk Origin

As an important number of particles from the KB/SD and OC populations was identified to be less processed, the possibility of a common origin from a particular area of the planetesimal disk had to be explored. Using the median values for the depths of the CO interface (see Table 6.1) we divided the populations to less and more processed and included the ejected population to the query as well. We did not find any preference for a particular area of origin in the planetesimal disk for any of the three populations. This proved that the initial distance distribution does not play any role in the thermal processing of the planetesimals and that their fate is purely the result of a completely random sequence of events.

## 6.2 Return to the Inner Solar System

We examined the thermal processing of the KB/SD objects as they returned to the inner Solar System to become 'active' JFCs (see Section 5.2), as in our initial approach (see Chapter 2), though this time the methodology and the sample has evolved. Our goal was to examine the possibility of long-distance activity mainly in the Centaur area (see Section 1.4.2), and obtain a first-order assessment of the thermal processing of an object as it transitions to Jupiter-crossing orbits. As in our initial approach, we used the Sarid et al. (2019) definition to describe the transition to JFCs, requiring orbits with perihelia within Jupiter's orbit ($q < 5.2$ au) and aphelia $Q < 7.0$ au, guaranteeing that the particles are under the gravitational influence

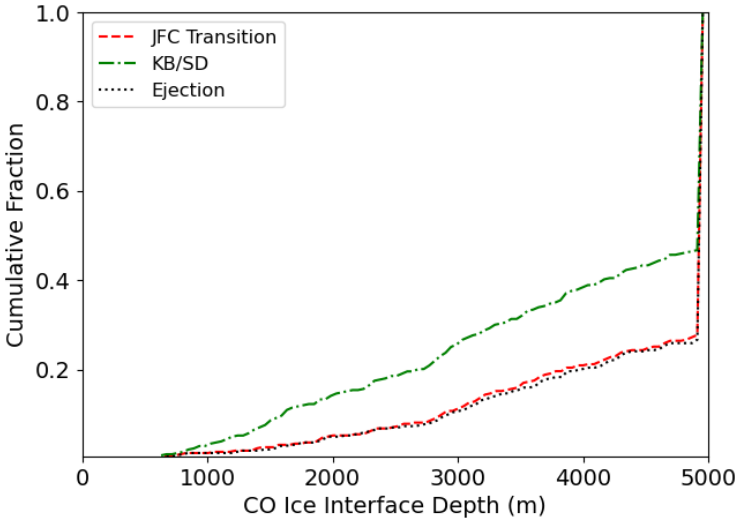


**Figure 6.8:** Cumulative distribution of the CO ice interface depths for returning KB/SD objects, evolving to Jupiter-crossing orbits. Three distributions are compared: the distribution at the KB/SD (green dashed-dotted line) (the same as in Figure 6.4), the distribution at the end of the Centaur phase and as the objects transition to JFCs (red dashed line) and the distribution at the end of the JFC phase as the comets are ejected from the Solar System (black dotted line).

.

of Jupiter. The evolution of the CO, $CO_2$ and crystallization interfaces is used to evaluate the thermal processing at two distinct evolutionary phases: (a) the Centaur phase and (b) the JFC phase itself until the ejection of a comet from the Solar System, similarly to our initial approach.

In Figures 6.8, 6.9 and 6.10, the cumulative distributions for the depths of these interfaces at the end of these two evolutionary phases are presented, in comparison to the distributions at the KB/SD presented in Figures 6.4, 6.5 and 6.6. We remind that the particles have already undergone an initial phase of processing, during their outwards scattering and were assumed to have remained relatively stable at their source reservoirs. The results of these simulations are summarized in the Table 6.2.

**Hyper-volatile Content:** From the evolution of the cumulative distribution between the KB/SD and the Centaur phase (green dashed dotted line and red dashed line in Figure 6.8 respectively), we notice that during the chaotic evolution in the planetary area an important number of particles is expected to be further depleted of its CO ice. Indeed CO depleted objects pass from 53% in the source reservoir to 75% at the time of the transition to

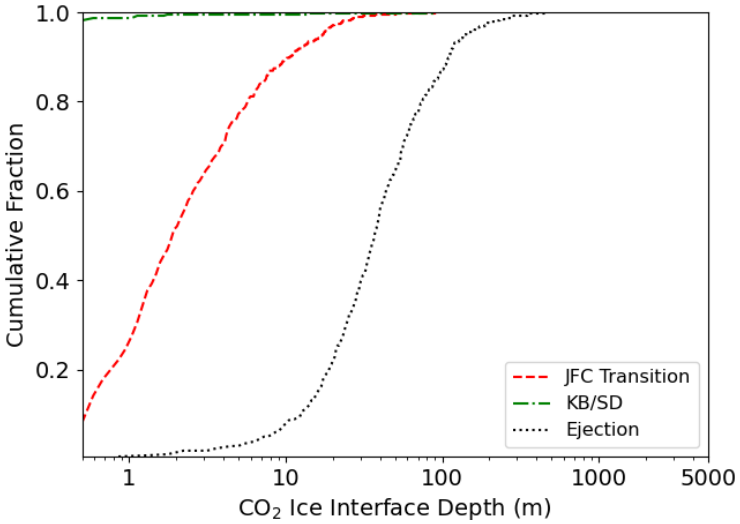


**Figure 6.9:** Cumulative distribution of the $CO_2$ ice interface depths for returning KB/SD objects, evolving to Jupiter-crossing orbits. Three distributions are compared: the distribution at the KB/SD (green dashed-dotted line) (the same as in Figure 6.5), the distribution at the end of the Centaur phase and as the objects transition to JFCs (red dashed line) and the distribution at the end of the JFC phase as the comets are ejected from the Solar System (black dotted line).

JFCs. Meanwhile all objects seem to lose part of their CO during the Centaur phase, although ∼8% seem able to retain some CO in a subsurface layer between 500 and 2500 m. The possibility of CO activity in the Centaur area and slightly beyond it[1] is compatible with recent predictions for long-distance activity, starting in the Kuiper Belt (Jewitt et al., 2021). We note that this activity was recorded mainly at large distances, so it is rather unlikely to be able to explain the detections of CO-driven activity on Centaurs (60558) 174P/Echeclus (Wierzchos et al., 2017) and 29P/Schwassmann-Wachmann (Wierzchos and Womack, 2020; Bockelée-Morvan et al., 2022), for which another mechanism like the crystallization of amorphous water ice must be at work. However it is interesting that there is a small fraction of particles able to maintain CO in the first 1000 m below their surface.

Interestingly, no significant evolution of the CO content is recorded during the JFC phase, as indicated by the almost exact superposition of the distribution at the transition (red dashed line in Figure 6.8) to the distribu-

[1] We remind here that our flag for the inwards scattering is the detection of a particle within 30 au (see Section 1.4.2), a condition that can be satisfied by long and highly eccentric orbits in the SD.

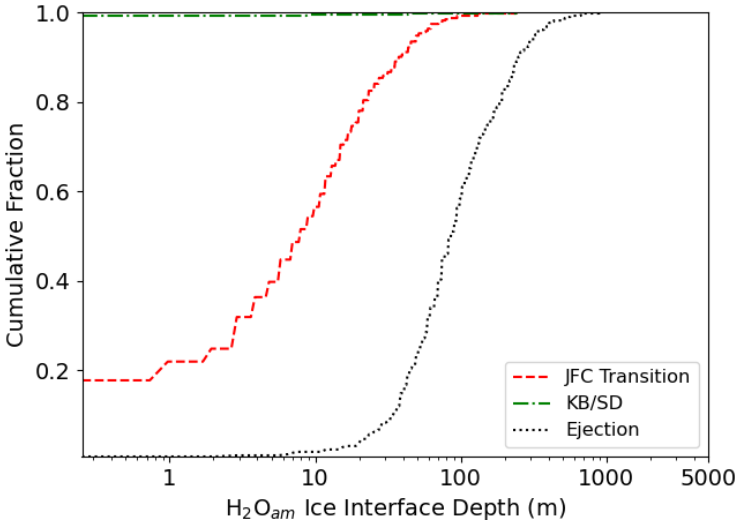


**Figure 6.10:** Cumulative distribution of the depths of the amorphous $H_2O$ ice crystallization front for returning KB/SD objects, evolving to Jupiter-crossing orbits. Three distributions are compared: the distribution at the KB/SD (green dashed-dotted line) (the same as in Figure 6.6), the distribution at the end of the Centaur phase and as the objects transition to JFCs (red dashed line) and the distribution at the end of the JFC phase as the comets are ejected from the Solar System (black dotted line).

.

tion at the ejection (black dotted line in Figure 6.8). We interpret this as a consequence of the nature of the heating during this phase. As described previously, intense heating does not necessarily imply deep penetration in the nucleus interior, a condition that is fulfilled by prolonged stays in warm areas. Given that the interface has already advanced significantly, and the JFC phase is very short (of the order of thousands of years), this condition is rarely satisfied, explaining the insignificant variations ( 1%) in the distributions.

**Moderately Volatile Content** As observed by the advancement of the distribution of the $CO_2$ ice interface, the sublimation of $CO_2$ can be one of the main sources of activity in the planetary area. Almost all of the returning particles (∼98%) lost part of their $CO_2$ content through sublimation from a subsurface area of ∼10 m, with a smaller percentage (∼12%) losing its $CO_2$ content from even deeper layers reaching at a maximum depths of ∼70 m. Of course, for almost 15% of the returning particles this interface did not advance signifcantly and remained within 1 m from the surface. Naturally, this sublimation is expected to intensify during the JFC phase, where high

temperatures are developing in such shallow subsurface layers. The activity during this evolutionary phase is already very well characterized by ground-based and *in situ* observations (e.g. Bockelée-Morvan et al., 2015), so our contributions here are less significant. We note that these results are compatible with Davidsson's (2021) suggested activity by segregation of $CO_2$ ice, a mechanism similar to the release of trapped molecules from the amorphous $H_2O$ ice structure as it crystallizes. However we showed that net sublimation of $CO_2$ is also possible at the Centaur area and should not neglected as an activity mechanism.

**Crystallization of Amorphous $H_2O$ Ice** As with the $CO_2$, the crystallization of amorphous $H_2O$ ice seems to be omnipresent in the Centaur area. Although not effective during the outwards scattering, with only 1.3% of the particles having a small subsurface area crystallized, in the Centaur area, a little more than 4 out of 5 particles (83%) in our sample have undergone crystallization in a part of their nucleus[2]. For 38% of these particles, the crystallization occurs at a layer expanding at a maximum of 10 m below the surface. For the rest of them the crystallization has advanced deeper at layers $\sim$100 m below the surface. Interestingly, we note that the crystallization front advances deeper compared to the $CO_2$ ice interface, contrary to what was suggested in our initial approach where the estimation was based purely on the subsurface temperatures. Using an ice evolution model this time, we note that this prediction has inverted. This is explained by the exponential increase of the crystallization rate as the temperature rises, which results in increased pace of the crystallization which overtakes the $CO_2$ sublimation interface (see also Table 6.2). These results are compatible with numerous studies suggesting the crystallization of amorphous $H_2O$ ice as a possible activity mechanism in the Centaur area (e.g Jewitt, 2009; Guilbert-Lepoutre, 2012).

## 6.3 A Short Comparison to our Initial Approach

As a sanity check, a set of additional simulations was launched, in which the objects returning from the KB/SD were considered to be completely unaltered. In other words, the early processing during the outwards scattering and the implantation phase was ignored. This allowed us to mimic our initial set of simulations and compare the two different methods of measuring the thermal processing of JFCs.

The results from this set of simulations are presented on Table 6.3, in which we added in parenthesis the relevant mean values from our initial simulations (see Table 2.1). The values compared are the ones obtained with a Hertz factor $h$=$10^{-2}$, the value used in our adapted model.

[2]We note here that the initial position of the ice front was 25 cm below the surface

**Table 6.2:** Depths (m) of the interfaces for the examined ice species in our model: CO, $CO_2$ and amorphous $H_2O$ ice, at the moment of their transition to Jupiter crossing orbits and at the end of their JFC lifetime.

| Ice Species | Max. | Min. | Median | Mean | Std ($\sigma$) |
|---|---|---|---|---|---|
| **First Transition to a JFC Orbit** | | | | | |
| CO | 5000.0 | 658.4 | 5000.0 | 4493.6 | 997.0 |
| $CO_2$ | 90.1 | 0.5 | 2.0 | 4.4 | 7.3 |
| $H_2O_{am}$ | 240.5 | 0.3 | 8.0 | 15.0 | 22.0 |
| **End of the JFC Phase** | | | | | |
| CO | 5000.0 | 673.8 | 5000.0 | 4515.1 | 976.7 |
| $CO_2$ | 459.0 | 0.9 | 37.4 | 53.0 | 53.2 |
| $H_2O_{am}$ | 892.5 | 0.3 | 86.5 | 122.4 | 111.0 |

We notice that our initial assumptions for the estimation of the thermal processing overestimated for the most part the affected subsurface areas. The only exception is the average position of the crystallization front at the end of the JFC phase, which in our initial calculations is closer to the surface. The most striking difference is on the average position of the $CO_2$ interface which is overestimated by a factor of $\sim$30 in the Centaur area and by a factor of $\sim$9 at the end of the JFC phase. Of course, these initial results were considered to be upper limits of the thermal processing (see Section 2.3 and Gkotsinas et al., 2022) and in that sense they gave a satisfactory depiction of the thermal processing of JFCs. However, our current results indicate that the processes involved, although temperature-driven, are a little bit more complicated than that. For example, the rates of sublimation or crystallization evolve with the temperature and can be less effective when the temperatures are low, even close to the sublimation temperatures. Selecting a threshold temperature can therefore be a good approximation, but might not be representative of the actual evolution of the process. We also showed that the timescale of the process, especially in the case of crystallization, is a crucial parameter (see Section 3.1.4), which cannot be taken into account by the threshold temperatures in our initial approach.

In addition, a certain number of physical and numerical parameters should be considered when this comparison is made. First and foremost, the orbital averaging technique used in the initial simulations. For that work an expression proposed by Prialnik and Rosenberg (2009) was employed. This expression, among others, has been revised in a follow-up work (see 5.5 and Gkotsinas et al., 2023), which suggested the use of a different expression, which can be characterized as much more conservative. This change is greatly affecting the heating outcomes, as the amount of received energy at the surface is much different in the two scenarios especially for moderate- and high-eccentricity orbits ($e > 0.3$). The fact that in our ther-

**Table 6.3:** Depths (m) of the interfaces for the examined ice species in our model: CO, $CO_2$ and amorphous $H_2O$ ice, at the moment of their transition to Jupiter crossing orbits and at the end of their JFC lifetime. In parenthesis the estimation of the initial simulations (see Chapter 2 and Table 2.1) are given for comparison.

| Ice Species | Max. | Min. | Median | Mean | Std ($\sigma$) |
|---|---|---|---|---|---|
| **First Transition to a JFC Orbit** | | | | | |
| CO | 5000.0 | 10.2 | 4735.3 | 3549.1 (4142.2) | 1773.5 |
| $CO_2$ | 56.8 | 0.5 | 2.0 | 4.4 ( 125.7) | 6.4 |
| $H_2O_{am}$ | 184.5 | 0.3 | 11.0 | 19.7 ( 27.1) | 25.6 |
| **End of the JFC Phase** | | | | | |
| CO | 5000.0 | 224.4 | 5000.0 | 3780.3 (4181.7) | 1591.7 |
| $CO_2$ | 587.9 | 0.9 | 43.7 | 63.4 (278.3) | 67.0 |
| $H_2O_{am}$ | 1356.5 | 0.3 | 118.5 | 171.5 (107.9) | 161.3 |

mal evolution model the advancement of the interfaces is calculated instead of being estimated as in our initial approach, should have an impact as well, although further work is necessary to establish the role of each parameter in the observed differences. Smaller discrepancies related to minor conceptual differences between the models can also be identified. For example the grid in our adapted model is better suited for long-term simulations, having a better resolution in the inner parts of the nucleus, allowing for better accuracy than in our initial approach.

# Chapter 7

# On the Primitive Nature of Cometary Populations

## 7.1 Early Processing in the Planetesimal Disk and the Source Reservoirs

We examined the thermal processing of 1418 planetesimals as they were scattered out during the dispersal of the protoplanetary disk by the migrating planets. Of them, 383 particles populated the Kuiper Belt and the scattered disk, 360 the Oort Cloud and 675 were ejected from the Solar System.

Our simulations recorded alterations primarily on the hyper-volatile content of all three populations. The moderately volatile and amorphous water ice content were also affected but to a lesser extent in the surviving populations (i.e. the KB/SD and OC planetesimals), whereas considerable modifications were reported for the ejected planetesimals.

### 7.1.1 Ejected Planetesimals

We demonstrated that the ejected planetesimals should be the most processed among the planetesimals examined in this study. With 78% of the particles having lost their CO content entirely and only 9% preserving CO in the first 2000 m below the surface, it is fair to say that the survival of pure condensed CO in the ejected population seems highly unlikely. The primordial $CO_2$ content has been affected in a relatively small number of planetesimals ($\sim$18%), affecting only shallow subsurface layers, in most cases within the first 100 m from the surface. The crystallization of amorphous water ice advanced in almost one out of four planetesimals ($\sim$23%), but as in the case of $CO_2$, this procedure was constrained to a subsurface layer of 100 m for the majority of the concerned planetesimals.

These results, described in detail in Chapter 6, indicate a processed population more so than the population that remains in the solar system. The

extent of this processing reflects the orbital evolution of these planetesimals, usually ejected by Jupiter or Saturn. The ejection by the two gas giants implies an increased number of passages from warmer areas, resulting in a more intense processing than in the other populations. The original study by Raymond et al. (2020b) reached a similar conclusion, by estimating the time a planetesimal spends in the giant planet region by the number of its close encounters with Saturn. Here, we made a step forward as we were able to quantify the processing and confirm these initial estimations in a more robust way.

As these planetesimals leave our Solar System, never to return, less attention has been paid to them so far. This is a natural consequence of our inability to examine these type of comets in the current time, unlike the surviving comets, eventually returning to the inner Solar System as JFCs and LPCs. Nevertheless, a growing interest for these objects has been developed lately after the detection of the first interstellar comets 1I/'Oumuamua (Meech et al., 2017a) and 2I/Borisov (Guzik et al., 2020; Jewitt et al., 2020). These interstellar visitors, aside from their 'exotic' provenance, attracted a lot of attention for a series of peculiar features. Among them is the apparent absence of observed activity of 1I/'Oumuamua ('Oumuamua ISSI Team et al., 2019) and the presence of CO, in unexpectedly high abundances, in the coma of 2I/Borisov (Bodewits et al., 2020; Cordiner et al., 2020).

To reconcile the observed nongravitational acceleration of 1I/'Oumuamua with this lack of observed activity, Seligman and Laughlin (2020) and Bergner and Seligman (2023) proposed the sublimation of molecular hydrogen or its production from radiolysis from $H_2O$ ice. Raymond et al. (2018a) and Raymond et al. (2018b) suggested that 1I/'Oumuamua could be an extinct fragment of a disrupted planetesimal, ejected from a solar system similar to ours, to explain the lack of visible outgassing. Supposing that 1I/'Oumuamua originated from a solar system resembling ours, although our Solar System seems to be quite exceptional (Raymond et al., 2020a), our simulations indicate that the scenario of an extinct ejected planetesimal is highly possible. The rather quick passage of 1I/'Oumuamua from our Solar System, resulted in the heating of a thin subsurface layer (Seligman and Moro-Martin, 2023), which if combined with an already processed nucleus can explain the lack of outgassing. Of course, given the nucleus stratification of an average ejected planetesimal (see Figures 6.4, 6.5 and 6.6), one would expect water ice outgassing. However no sensitive enough detections for water ice activity were made ('Oumuamua ISSI Team et al., 2019).

Explaining the CO-rich nature of 2I/Borisov seems a little bit more difficult. Bodewits et al. (2020) suggested an origin from a chemically distinct solar system, enriched in CO, whereas Price et al. (2021) proposed a formation scenario based on drifiting of ice-coated pebbles that can greatly enhance the $CO/H_2O$ ratio of the planetesimals. Seligman et al. (2022) advocated for different formation locations, inside and outside of the CO snow

line, to explain the peculiarities of the C/O ratios for the two interstellar objects. From our simulations, the possibility of CO-rich ejected planetesimals, although rare, exists. Supposing that 2I/Borisov could be one of the few objects that managed to maintain CO within the first 500 m below their surface, then the ejection time from its Solar System should not exceed the 10 Myr, with most probable values around ∼6 Myr, implying reduced visits in the giant planet area. A similar, yet not quantified, scenario has been recently proposed by Lisse et al. (2022), as a mean of maintaining the CO content in comets like 2I/Borisov.

### 7.1.2 Kuiper Belt/Scattered Disk Planetesimals

Planetesimals ending up in the KB/SD are the second most processed population, if we use their ability to retain CO ice as a processing criterion. We showed that 53% of these planetesimals lost entirely their free condensed CO ice, while another 30% maintained CO in their deep interior, below 2500 m. However, the chances of CO survival are higher compared to the ejected planetesimals as ∼17% managed to preserve CO in the first 2000 m below the surface. For that to happen, planetesimals have to be scattered outwards in short timescales ($<$ 100 Myr) at distances larger than 40 au. Indeed, planetesimals scattered outwards quickly, reaching distance higher than 70-80 au are those that managed to maintain their CO to their surface.

This possibility of CO survival in KB/SD objects is one of the most interesting findings of our work, as almost all of the previous studies suggested a complete depletion of hyper-volatiles. De Sanctis et al. (2001) examined the thermal evolution of large KBOs (R = 40 km), orbiting at distances between 39 and 43 au in nearly circular orbits (e = 0.05) and one in a more eccentric orbit (e = 0.2). Their simulations followed the evolution of these objects until they reached a quasi-steady state that allowed them to interpolate their future evolution. They considered heating from solar irradiation and radioactive elements. They found that the subsurface layers were completely depleted of CO, which survived only in a few cases in the innermost parts of their nuclei, as ice molecules moving inwards recondensed in deeper layers where temperature and pressure conditions were favorable. Choi et al. (2002) examined the evolution of KBOs, by considering the same heat sources and a variety of conductivity configurations. Their objects evolved on circular orbits with radii of 30, 90 and 120 au. They concluded that if KBOs have undergone radioactive heating then stratification and alterations in the composition are expected, with the hyper-volatile content being in most cases entirely lost. This led them to the conclusion that the survival of CO in KBOs should be possible only within the amorphous water ice structure.

More recent works from Kral et al. (2021), Lisse et al. (2021), Prialnik (2021), Steckloff et al. (2021) and Parhi and Prialnik (2023) reached similar conclusions. A complete depletion of CO ice is expected in KBOs

orbiting at distances of the order of ∼40-45 au. Their simulations were somehow closer to ours as the effect of radioactive decay was either not considered (Kral et al., 2021) or found to be negligible (Prialnik, 2021; Parhi and Prialnik, 2023), as the sizes of their objects were relatively small (R = 4-10 km). Prialnik (2021) and Parhi and Prialnik (2023) tested the possibility of survival at larger distances as well: 100 and 220 au. At 100 au their simulated objects lost their CO ice content entirely, although no mention of the timescale the depletion was made. At 220 au their objects managed to retain their CO content almost intact, as only a shallow subsurface layer was affected.

Attempting a comparison of our results to these studies is not trivial, given the variety of configurations between the underlying models. However we think that it is worthwhile, as it demonstrates the advantages of our method. In general, our results are in agreement with all the studies examining objects at distances up to 45 au, where we find a complete depletion of CO as well. However, objects at these distances are not necessarily characteristic of the cometary populations as they are not expected to return to the inner parts of the Solar System, as SDOs do (Nesvorný et al., 2017). It is this SD population that managed to retain a significant amount of its CO content in our simulations, with most of its members reaching these far-away distances at timescales sufficiently short for the retention of hyper-volatiles. Studying this effect is only possible by the use of $N$-body simulations, accounting for the movement from warmer to colder areas (and not always in that order). This movement can change significantly the outcomes of the processing as it allows the objects to cool down during their trajectories, a crucial parameter in the behavior of thermal evolution models, as it can act as a hyper-volatile protection mechanism. With this consideration, objects heated up sufficiently during their outwards journey reaching distances of 100 au, are not expected to go through any further significant alterations, as Prialnik (2021) and (Parhi and Prialnik, 2023) predicted.

As other works have previously demonstrated, no important alterations on lower volatility elements were recorded with only a few exceptions. The studies that predicted alterations on the entire icy primordial inventory (De Sanctis et al., 2001; Choi et al., 2002) found out that it was solely due to radioactive heating which is not accounted for in our model.

### 7.1.3 Oort Cloud Planetesimals

The planetesimals that populated the Oort Cloud were found out to be the least processed of all, based always on their ability to retain CO. As demonstrated in the previous chapter, although ∼39% of the particles lost their primordial CO content, an important fraction managed to maintain it relatively close to the surface (∼35% within the first 2500 m below the surface). As in the case of the KB/SD objects the survival of CO ices is

clearly the result of quick scattering towards the OC. As they managed to reach quickly long-distance orbits within the OC, their CO content was less affected, despite their exposure to intense, but short, heating during their short residence in the inner parts of the planetary area.

Obviously, most of the studies that examined the possibility of thermal processing in the OC, focused on the effects of radioactive heating (Haruyama et al., 1993; Prialnik and Podolak, 1995). These studies considered an initial composition of amorphous water ice (Haruyama et al., 1993) or amorphous water ice and dust (Prialnik and Podolak, 1995) with no other volatiles. Comparing our results to these works does not seem very pertinent from that point of view as we depart from a completely different set of initial assumptions. A more recent study from Lisse et al. (2022) predicted the dearth of hyper-volatile species in Oort Cloud Comets. This prediction was based on estimation of the residence times in the giant planet region and the Kuiper Belt. Their estimations predicted prolonged stays in those area of the order of hundreds of Myr. We showed that this is only partly true. In fact this outwards scattering can take place at different timescales, due to the stochastic nature of the close encounters of each planetesimal with the giant planets. Indeed, it might be a slow procedure as much as it can be a quick one, leading to different outcomes concerning the presence of CO in OC comets and making its survival a definite possibility.

The possibility of OC objects to maintain part of their primordial CO content during the implantation is consistent with the growing number of observations of suspected CO-driven activity on inbound LPCs, such as C/2017 K2 (PANSTARRS) (Jewitt et al., 2017; Meech et al., 2017b; Jewitt et al., 2021; Yang et al., 2021), C/2010 U3 (Boattini) (Hui et al., 2019) and C/2014 UN271 Bernardinelli-Bernstein (Farnham et al., 2021; Kelley et al., 2022). Although the return of the OC comets as LPCs was not modeled in this work (see Section 7.3), we can predict a similar activity to that of the returning KB/SD objects (see Sections 6.2 and 7.2), where CO sublimates from subsurface layers as the objects cross warmer areas. On the other hand the possibility of CO depletion, or at least very low CO abundance ratios as observed for example on comet C/2021 A1 (Leonard) (Faggi et al., 2023) is not excluded at all by our results. If only, they provide an additional explanation to the observed differences in the abundances on LPCs (e.g Ootsubo et al., 2012).

Alterations on the $CO_2$ and the amorphous water ice content were observed on a small number of planetesimals ($\sim$10%) populating the OC. This might be considered to be consistent with the observed variabilities in the $CO/CO_2$ and $CO_2/H_2O$ ratios observed by Ootsubo et al. (2012) on LPCs, although their sample is small and the observing distances short enough for recent thermal processing to act and alter their chemical composition and stratification.

### 7.1.4 The Possibility of Earlier Processing in the Primordial Disk

In a recent study, Davidsson (2021) examined the possibility of thermal processing on primordial disk objects, before their outwards scattering and the migration of the giant planets, which takes place at time zero in our simulations. Following Davidsson's (2021) scenario, our time zero should be in fact be set at ∼15 Myr. Indeed, the instability in the employed $N$-body simulations takes place approximately after 10 Myr (Nesvorný et al., 2017). Davidsson (2021) predicts that small objects of 2 km radius regardless of their scattering fate, are bound to lose their CO ices in a few thousand years (70-170 kyr). Their $CO_2$ ice should be lost at depths within 30 m from the surface and a subsurface layer of 200 m should have crystallized. Larger objects (R = 35-100 km) should also lose their CO content on larger timescales of 200 Myr, although this result is challenged by our findings as the outwards scattering is set in motion at these timescales and can radically increase the chances of CO survival. Obviously Davidsson's (2021) results, as they reset the time zero, can also reset our initial estimations, although changes on the timing of the instability can be crucial for the estimation of the initial processing of planetesimals on the planetesimal disk. We remind for example that several recent studies indicate the possibility of a very early instability during the gas disk dissipation and while the rocky planets were still forming (Clement et al., 2018; Liu et al., 2022).

## 7.2 Long-Distance Processing in the Planetary Region

For the KB/SD population, its return phase from the source reservoir was studied as well. We showed that before these particles transition to JFCs, important processing takes place in the giant-planet area during their time as Centaurs. This activity concerns the surviving CO content, but also the $CO_2$ and the amorphous $H_2O$ ice inventory as well, which have remained almost intact during the outwards scattering phase. In almost 4 out of 5 Centaurs (∼83%), the crystallization front advanced at least a few meters below the surface (∼10 m) with some objects crystallizing as deep as 100 m. The number of particles having lost part of their $CO_2$ ices is even bigger (98%), although for almost 20% this advancement was limited to half a meter below the surface.

These results are consistent with previous studies suggesting the crystallization of amorphous water ice (Guilbert-Lepoutre, 2012) and the segregation of $CO_2$ ice (Davidsson, 2021) as probable activity mechanisms in the Centaur area. What is more interesting to see here is the pattern of this activity, which was found to be sporadic, following some abrupt change

in the particles' orbital elements (Fernández et al., 2018). On the contrary, when the particles spend time on orbits that did not present any considerable orbital changes, no significant activity due to the sublimation of $CO_2$ ice and the crystallization of amorphous $H_2O$ ice was recorded. This is in agreement with observations that highlighted the lack of activity on Centaurs on dynamically stable orbits (Cabral et al., 2019; Li et al., 2020; Lilly et al., 2021). CO activity has also been observed on Centaurs: with certainty on 29P/Schwassmann–Wachmann (Bockelée-Morvan et al., 2022) but is also suspected to be responsible for transient or outbursting activity on Centaurs 95P/Chiron (Womack et al., 2017) and 174P/Echelus (Wierzchos et al., 2017). These observations are not incompatible with our results, as CO sublimation was also recorded during the Centaur phase.

As expected, important activity related to $CO_2$ sublimation and extensive crystallization of amorphous water ice is recorded during the JFC phase. Interestingly, in this phase, the CO content -if any- remains largely intact. This is explained by the previous advancement of the CO interface deep in the nuclei interior, making it 'unreachable' by the intense but short heating of the JFC phase. Our results for this evolutionary phase are of a lesser significance, as this phase is already described with a variety of far more adequate tools (ground-based observations, space missions but also better suited evolutionary models). Our orbital averaging technique is also less adequate in this phase where short perihelia are expected as important information will be lost (see below). In addition, the output frequency is inadequate for the resolution of the sharp and frequent orbital changes taking place close to Jupiter and Saturn (Seligman et al., 2021). This implies that intense heating periods might go unnoticed in our simulations (Guilbert-Lepoutre et al., 2023). Regardless of these issues, our results indicate that a typically observed JFC, has most probably undergone significant processing, capable to affect its primordial volatile inventory. This realization, for which we do not claim all merit, can have important consequences on the way current observations are interpreted and points to the necessity of accounting for the evolution history of JFCs.

### 7.2.1 A Conclusive Comment on our Results

At this point, we would like to clarify that the above interpretations should not be viewed as an attempt to provide conclusive or definite answers to such a diverse body of observations (see Section 1.5). They can however provide some very likely explanations for a variety of contradictory results, such as the predictions for CO depletion (Davidsson, 2021; Lisse et al., 2022) and the observations of long-distance CO-driven activity (see above). A lot of these different issues regarding cometary activity can be explained by the stochastic nature of cometary trajectories, whether it is on their way out or in the inner Solar System. We showed that this aspect of cometary

evolution is crucial, yet disregarded so far, and should be an important part of future considerations for the evolution of cometary populations. Of course not everything is decided by the orbital evolution of comets, as a series of other effects, such as shape, rotation, form, size (e.g. Vincent et al., 2019; Benseguane et al., 2022) or even collisions (e.g. Steckloff et al., 2023) not accounted for in this work, are also expected to have important effects on the thermal evolution of cometary nuclei.

## 7.3 A Critical Review of our Results

As briefly mentioned in previous chapters (see for example Sections 3.3 and 5.5.5) our choices and assumptions, whether they regarded the thermal evolution model, the averaging orbital method or the limitations imposed by the $N$-body simulations, come with important consequences, which should be mentioned in order to better evaluate the results presented previously.

### 7.3.1 Implications of Orbital Averaging

The use of temperature-averaged circular orbits replacing the actual elliptic ones proved to be a powerful tool, allowing the resolution of several issues arising by the large time steps of the $N$-body simulations, while improving significantly the performances of our simulations. However, their use comes with an important disadvantage: poor representation of high-temperature processes such as the sublimation of crystalline water ice.

As can be easily observed by the expression for the equivalent thermal radius (Equation 5.7), the employed circular orbits were systematically placing the simulated comets at distances closer to their aphelion. Although these distances presented the best matching for the developing internal temperatures between elliptic and circular orbits, it is obvious that they were constantly underestimating the surface temperatures, an effect that penalized the onset of water ice sublimation. In our best case scenario, the crystalline water ice interface was found to advance just a few millimeters, even during the JFC phase. Obviously, this is far from being representative of the actual activity in the JFC phase where high rates of sublimation are calculated (e.g Biver et al., 2002). As a consequence, no erosion was calculated either although important erosion rates are expected especially during the JFC phase (e.g Huebner et al., 2006; Keller et al., 2015).

This failure to describe the water ice sublimation has two main consequences on our results. On the one hand, no estimates on the rate of nucleus size changes were possible. On the other hand, the activity enhancement due to erosion was also neglected. Indeed, removing material from a comet's surface will result in the reduction of its radius, which consequently should bring closer to the surface the buried ice interfaces. This implies a sublimation enhancement as the penetrating heat wave can reach them more

easily. In that sense, our estimations on the resulting thermal processing are rather conservative. On the bright side, this intense water ice sublimation is expected to take place at small heliocentric distances rarely visited by the majority of our particles, with the exception of the JFC phase, that as already explained was not the main focus of this work. Of course, given the intense thermal processing of the ejected populations and to some extent of the OC population, this poor representation might also affect the early phases of evolution as well. Nevertheless, this poor description of the water ice sublimation, although it does not severely affect our primary results, should certainly be one of the issues to be reviewed on future long-term simulations of the thermal evolution of comets.

**The LPC Population** More importantly, this orbital averaging technique did not allow the study of LPCs. In fact, this technique was initially designed for the returning phase of JFCs, where a high number of orbital changes is recorded due to the close encounters with the giant planets. Given the mechanisms of the outwards scattering and of the ejection and their resemblance to that of the return towards the inner Solar System, we were able to apply it at this early processing phase as well. However this was not the case for the returning LPCs, which often passed through the Solar System only once (*jumpers*) at orbits with very large semimajor axis. Indeed in our selected sample 44% (157) of the particles were recorded to have only one passage through the planetary region. The rest of them recorded more passages through the planetary area although their orbits were often near-parabolic, which are not well described by our averaging orbital technique. This is also one of the subjects that needs to be reviewed in future studies of the long-distance processing of LPCs, a very promising field in our quest for the least processed and thus most primitive comets in our Solar System.

### 7.3.2 Implications of the Thermal Modeling Assumptions

As we described in Chapter 3 the coupling between the thermal evolution model and the $N$-body simulations required a number of simplifying assumptions. These assumptions have direct implications on our results and although they have been briefly mentioned at different chapters, it is useful to summarize them here and remind their effects.

Our thermal evolution model works in two steps: on the first step it resolves a simplified version of the heat diffusion equation over large time steps and on the second step an ice evolution model calculates the evolution of the ice content through estimates of the gas diffusion over these time steps. This approach differs significantly from the typical thermal evolution models that resolve the energy and mass conservation equations as a couple (e.g. Orosei et al., 1999). The consequence of this choice is that our thermal evolution model does not account explicitly for a number of secondary internal pro-

cesses and internal heat sources or sinks such as the latent heat consumed or released during the sublimation and recondensation of volatile species inside the nucleus. So if for example gas molecules can recondense above or below the ice interface, it will not be recorded in our model. However, given the timescales of our simulations, we expect that this short-term gas movement that is not accounted for in our model, will eventually be smoothed out, especially in the case of hyper-volatile species that sublimate at very low temperatures.

For reasons that were described in Section 3.1.4 we did not consider the presence of radioactive heating in our simulations. We can estimate that their contribution -if present- will most probably result in a further processing of the cometary nuclei, affecting mainly the hyper-volatile content, as for such small objects as the ones considered here, the developing internal heating will most probably escape, before affecting species of higher volatility (Haruyama et al., 1993; Prialnik and Podolak, 1995).

Another simplifying assumption was made on the distribution of the received solar energy on the nucleus of the simulated comets. We considered a spherical average based on the energy received at the sub-solar point of our objects, resulting in a uniform distribution of the energy on the surface. This assumption, allowed the use of larger steps and greatly simplified our simulations, but its clearly not realistic. Its use omits any diurnal and shape effects that are expected to act in favor of the preservation of the ice species, either because they would allow recondensation at different levels, or because they are expected to protect certain areas of the nucleus from the solar irradiation. Their inclusion in long-term simulations such as the ones presented during this work, would be numerically challenging, but should provide interesting insights on the actual thermal evolution of comets. Of course, aside from the use of more sophisticated models (2D, 3D), they would require additional information and/or assumptions regarding the long-term evolution of the rotational periods and of the shapes of cometary nuclei.

Last but not least, we would like to highlight the importance of the physical parametrization of our thermal evolution model. Given the significant level of uncertainties surrounding the bulk properties of cometary nuclei, but also the individual parameters of their constituting components, some of them had to be assumed. This will naturally affects the outcome of our results. The example of the saturation vapor pressure of CO is one of the most striking. In Section 3.3.2, we showed how the use of one expression can result in a quick depletion of CO in almost all of our simulated comets, and how another can reduce the sublimation rate significantly, resulting in increased survival probabilities. In our version of the thermal evolution model, constraining the thermal conductivity and the saturation vapor pressure is the most crucial steps towards the assessment of the thermal processing of cometary populations. Over the course of this work, we tried using the most up to date and accepted values available in the literature, but the devel-

opment of these parameters is still ongoing, so naturally a small change in those parameters is very likely to change the outcomes.

### 7.3.3 Towards a better assessment of the thermal processing of cometary populations

It is quite clear that the first major step towards a better assessment of the thermal processing of cometary populations would come from the adaptation of actual eccentric orbits instead of the circular averaged that were used in this work.

Although this choice was -in our opinion- sufficiently justified in the current context (see Section 5.5), it is undeniable that the use of eccentric orbits will 'unlock' a large number of additional information. This information is related mainly to the perihelion passage and the associated possibility of activity driven by low volatility species such as the water ice, which can also allow an estimation of the long-term erosion. In other words, this change will give us access to the evolution of the entire ice inventory but also to the size evolution of cometary nuclei. Of course for this to happen an improvement of the $N$-body simulations' resolution is required as well. More specifically, an increased cadence allowing for a better characterization of the orbital behavior of cometary nuclei, reducing the uncertainties between subsequent outputs is necessary.

Considering that throughout this work a rather simplified evolution model was proposed, a number of secondary improvements can be suggested as well that are expected to provide a more accurate description of the thermal evolution of comets, especially during the active phases. A first improvement would be to account for the gas movement within the porous matrix. This would allow the incorporation of processes like the recondensation (above or below an ice interface) of gas molecules. This feature which was not explored in our model can result in an enrichment of subsurface layers, creating secondary interfaces (or 'pockets' as Capria et al. (2000) andDe Sanctis et al. (2000) called them) of ices above the main interface, changing the stratification and allowing sublimation from layers closer to the surface. We have to note here, that this scenario does not change our conclusions regarding the alternation of these subsurface layers, as the fact that they might be replenished by ices originating from deeper layers does not mean that there is no change in the primordial composition of these layers.

A second improvement would be to include the omitted heat sources and sinks. This will allow a more accurate description of the energy balance and conservation during the active phases, as it would include the energy consumed or released during phase transitions. In the same context, the liberation of occluded species from the amorphous $H_2O$ or $CO_2$ ice structures during the crystallization or the segregation can be modeled as well in order to examine their contributions to the total gas production. Moreover,

the consideration of radioactive heating (although the incorporation of radioactive elements on cometary nuclei remains purely theoretical (Levasseur-Regourd et al., 2018)) can be included for completeness to study its effects in a parallel way to those of the solar energy.

We should however remind here that as more processes are added we move further away from the logic of an adapted and efficient model as the one proposed in this work and approach the more classic models for thermal evolution that are usually designed for short-term evolutionary studies. This conceptual choice will have a significant cost in the efficiency and the computational cost of the simulations without necessarily a considerable change in the results. With that in mind we would prioritize the use of elliptic orbits instead of circular ones as the number one issue towards an improvement of the current model, leaving aside for the moment the addition of excluded processes.

## 7.4 Final Conclusions

Returning to our initial inquiries presented in Section 1.5 of the Introduction, we can now attempt some answers, based on the results presented in the previous chapter and summarized above.

1. Our simulations revealed sublimation and depletion of the primordial free condensed CO at different evolutionary phases of our simulated comets' lifetimes. In other words and contrary to some of the previous predictions, although depletion is clearly one of the possible outcomes for CO, its fate is not necessarily decided in the protoplanetary disk or the source reservoirs. This conclusion might explain the observed long-distance CO-driven activity of inbound LPCs, which is not easily explained if for example LPCs are completed depleted of CO. We should note, that this result does not exclude the possibility of trapping CO (or any other hyper-volatile for that matter) in the amorphous water or $CO_2$ ice structures as many studies are suggesting.

2. The above conclusion provides an answer to our second inquiry as well. Indeed, as we showed in the previous chapter, the diversity of dynamical pathways leading comets in and out of the Solar System, renders the conservation of hyper-volatiles possible. A conservation condition in which planetesimals scattered outwards at timescales within 100 Myr, at large distances in the SD ($a > 50$-60 au), was established, although other possibilities for the retention of CO exist. We also observed that planetesimals scattered towards the KB at distances within 40-45 au, regardless of the timescale of the scattering, were not able to retain their CO, establishing that way a depletion criterion.

3. These remarks lead naturally to the main conclusion of this work, that the thermal processing and consequently the level of primitiveness of cometary nuclei is inextricably related to their orbital evolution. We demonstrated that among the three studied populations, KB/SD, OC and ejected objects, different average levels of processing are recorded, with the ejected population being the most and the OC population the least processed one. These results indicate that in our quest for the most primitive cometary population future space missions should target the LPC population, as is the case of the upcoming Comet Interceptor mission (Snodgrass and Jones, 2019).

Expanding a little more these conclusions, we would like to add that:

4. JFCs seem to have undergone significant alterations, modifying their primordial volatile inventory, before they reach typical observation distances in the inner parts of the Solar System. These alterations imply that the observed activity is very likely triggered from thermally processed layers, pointing to the necessity of accounting for the past evolutionary history when interpreting the current observations.

5. We note that the method proposed in this work, although initially designed for the study of cometary populations, can have interesting applications on individual objects as well. Examples of such applications can be found in Guilbert-Lepoutre et al. (2023), where the long-term thermal evolution of proxies of the Centaurs 29P/Schwassmann-Wachmann 1, P/2019 LD2 (ATLAS), and P/2008 CL94 (Lemmon) is examined. These type of simulations open a new window in thermal evolution studies that can find interesting applications on preliminary studies of targets for upcoming space missions or observational campaigns.

# Appendix A

# Supplementary Figures

## A.1 Averaging Schemes Supplementary Figures

In Figures A.1 and A.2 we present, for completeness the temperatures differences, as presented in Figures 5.10 and 5.11 of the main text for the halfway points inwards and outwards, respectively.

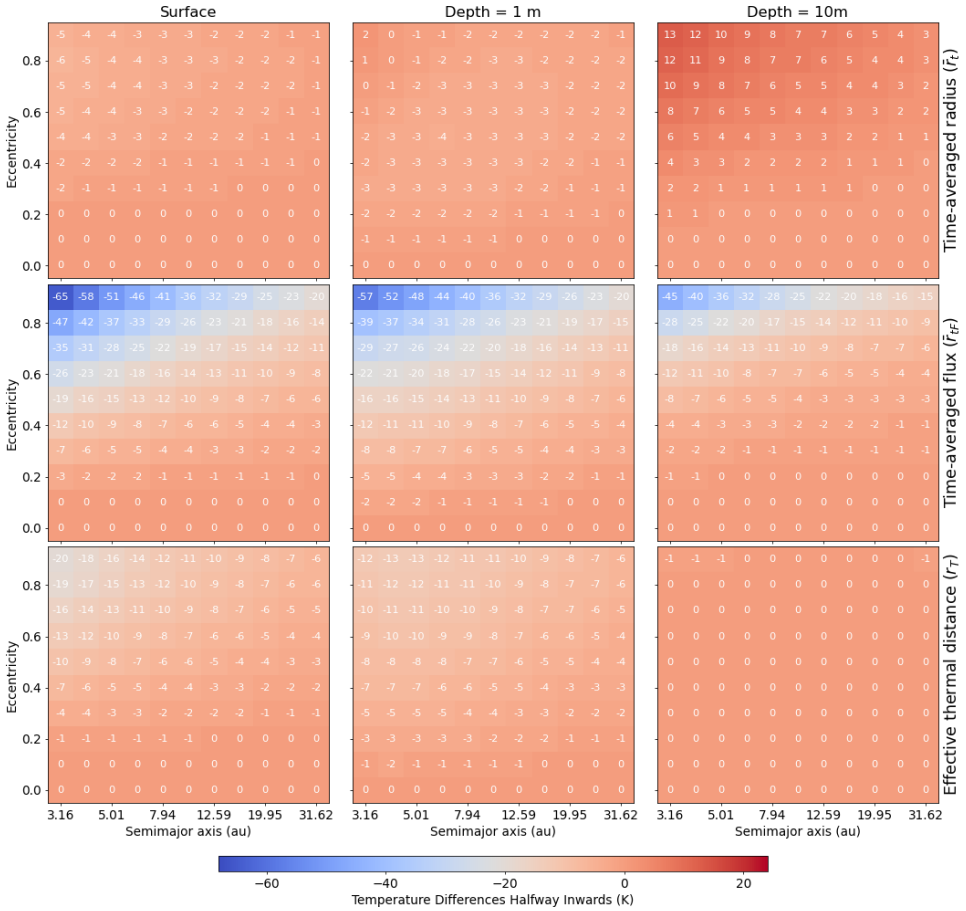


**Figure A.1:** Temperature differences between the elliptic orbits halfway through inwards (time-wise) and the time-averaged radius ($\bar{r}_t$) (top row), the time-averaged flux ($\bar{r}_{tF}$) (middle row) and the effective thermal radius ($r_T$) equivalent orbits (bottom row) for three depths: surface (left panels), 1 m (middle panels) and 10 m (right panels) for all the $a, e$ couples.

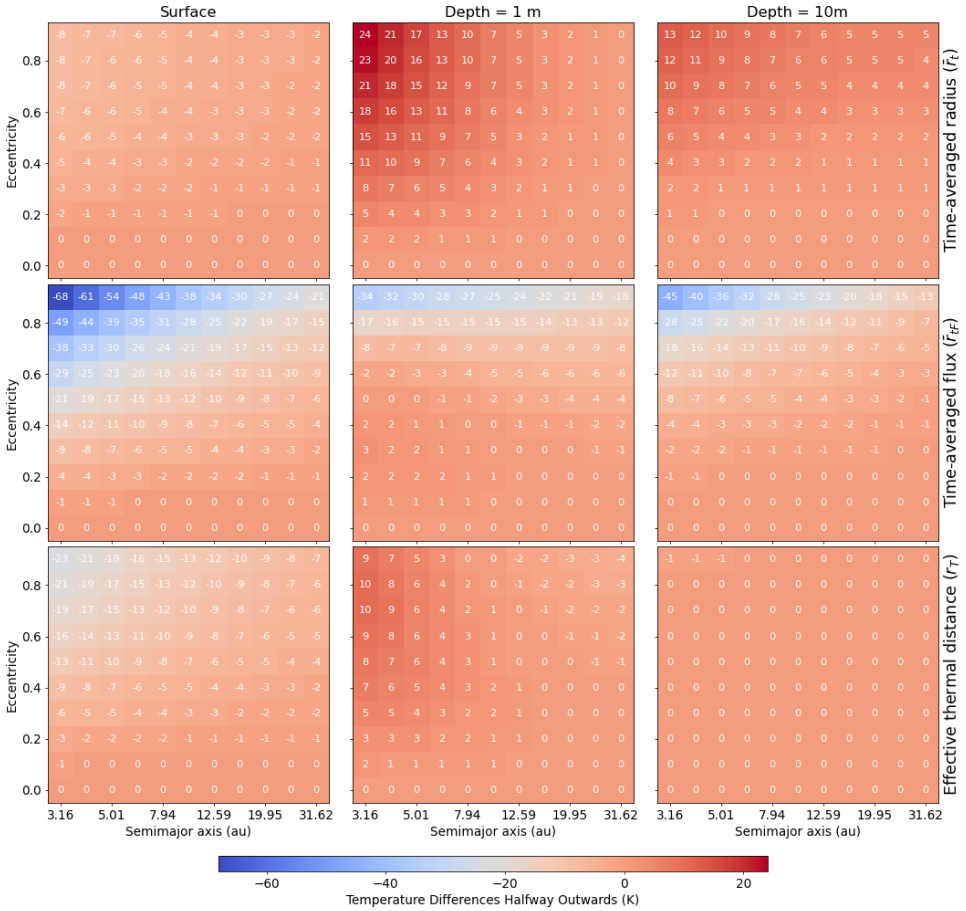


**Figure A.2:** Temperature differences between the elliptic orbits halfway through outwards (time-wise) and the time-averaged radius ($\bar{r}_t$) (top row), the time-averaged flux ($\bar{r}_{tF}$) (middle row) and the effective thermal radius ($r_T$) equivalent orbits (bottom row) for three depths: surface (left panels), 1 m (middle panels) and 10 m (right panels) for all the $a, e$ couples.

# Appendix B

# Article ApJ (2022)

Article published on the journal *The Astrophysical Journal*: Gkotsinas et al., (2022), ApJ, 928, 43, 12 pp.

The Astrophysical Journal, 928:43 (12pp), 2022 March 20 https://doi.org/10.3847/1538-4357/ac54ac


# Thermal Processing of Jupiter-family Comets during Their Chaotic Orbital Evolution

Anastasios Gkotsinas[1], Aurélie Guilbert-Lepoutre[1], Sean N. Raymond[2], and David Nesvorny[3]
[1] Laboratoire de Géologie de Lyon: Terre, Planètes, Environnnement, CNRS, UCBL, ENSL, F-69622, Villeurbanne, France; anastasios.gkotsinas@univ-lyon1.fr
[2] Laboratoire d'Astrophysique de Bordeaux, Univ. Bordeaux, CNRS, F-33615 Pessac, France
[3] Department of Space Studies, Southwest Research Institute, 1050 Walnut Street, Suite 300, Boulder, CO 80302, USA
*Received 2021 December 20; revised 2022 February 8; accepted 2022 February 10; published 2022 March 25*

## Abstract

Evidence for cometary activity beyond Jupiter's and Saturn's orbits—such as that observed for Centaurs and long-period comets—suggests that the thermal processing of comet nuclei starts long before they enter the inner solar system, where they are typically observed and monitored. Such observations raise questions as to the depth of unprocessed material and whether the activity of Jupiter-family comets (JFCs) can be representative of any primitive material. Here we model the coupled thermal and dynamical evolution of JFCs, from the moment they leave their outer solar system reservoirs until their ejection into interstellar space. We apply a thermal evolution model to a sample of simulated JFCs obtained from dynamical simulations that successfully reproduce the orbital distribution of observed JFCs. We show that due to the stochastic nature of comet trajectories toward the inner solar system, all simulated JFCs undergo multiple heating episodes resulting in significant modifications of their initial volatile contents. A statistical analysis constrains the extent of such processing. We suggest that primordial condensed hypervolatile ices should be entirely lost from the layers that contribute to cometary activity observed today. Our results demonstrate that understanding the orbital (and thus, heating) history of JFCs is essential when putting observations in a broader context.

*Unified Astronomy Thesaurus concepts:* Comets (280); Short period comets (1452); Comet nuclei (2160); Comet dynamics (2213); Comet volatiles (2162); Computational methods (1965)

## 1. Introduction

Jupiter-family comets (JFCs) represent a population of icy objects whose orbits are primarily determined by the gravitational influence of Jupiter. JFCs are characterized by short orbital periods ($\leqslant 20$ yr) and low inclinations ($\lesssim 30°$) (Di Sisto et al. 2009; Nesvorný et al. 2017). They are thought to originate from the Kuiper Belt and scattered disk (Brasser & Morbidelli 2013) and evolve through the giant-planet region on unstable orbits, before reaching the inner solar system after a close encounter with Jupiter (Levison & Duncan 1997; Di Sisto et al. 2009; Nesvorný et al. 2017; Fernández et al. 2018; Steckloff et al. 2020).

The thermally induced processing of JFCs' physical and chemical properties can be divided into four distinct phases (e.g., Meech & Svoren 2004; Prialnik et al. 2004):

1. An initial stage that encompasses the formation of cometary nuclei themselves and their processing prior to their displacement in the outer solar system reservoirs;
2. A "reservoir" phase, lasting several billion years, where nuclei are thought to remain relatively unaltered;
3. An intermediate phase of orbital perturbations bringing comet nuclei from their reservoirs to the inner solar system;
4. A short-lived phase of intense processing known as the "active phase," where cometary activity is mostly driven by water-ice sublimation at distances within Jupiter's orbit ($\sim$3 au).



Although the active phase is considered to drive the most intense and rapid evolution, multiple lines of evidence suggest that accounting for that stage of processing alone does not provide the full picture of the comets' thermal processing. Considerable modeling efforts have examined the possibility of thermal processing and activity even from the earlier stages of evolution. Such studies propose that alterations start as early as the formation of comet nuclei, and before their displacement in outer solar system reservoirs (e.g Prialnik & Merk 2008; Raymond et al. 2020; Davidsson 2021), but also during the prolonged storage phase, where surface temperatures between 30 and 50 K can be attained (e.g., Capria et al. 2000; De Sanctis et al. 2000, 2001; Choi et al. 2002). The existence of active Centaurs (e.g., Jewitt 2009; Lin et al. 2014; Mazzotta Epifani et al. 2017, 2018; Steckloff et al. 2020; de la Fuente Marcos et al. 2021), alongside the recent observations of the long-distant activity of comets (e.g., Meech et al. 2017; Jewitt et al. 2017; Hui et al. 2018, 2019; Yang et al. 2021; Farnham et al. 2021), provide direct evidence that cometary activity starts beyond the orbit of Neptune.

In this paper, we investigate the thermal processing of JFCs during their complete orbital evolution. We start from the time that cometary nuclei leave their reservoirs and follow their dynamical evolution until they are ejected from the solar system. We apply a thermal evolution model to a sample of model JFCs from the dynamical simulations of Nesvorný et al. (2017). In this sample, model JFCs evolve from Neptune- to Jupiter-crossing orbits with perihelion distances $q < 2.5$ au, reproducing the orbital distribution of currently observed JFCs. We perform thermal evolution calculations coupled to the dynamical evolution of 276 model JFCs in order to obtain the internal temperature distribution and its evolution. This enables us to assess the degree of thermal processing among JFCs in a statistically significant manner.

In Section 2, we describe our thermal evolution model and our model JFC sample, along with considerations necessary for their coupling. In Section 3, we present the results of our simulations for both individual simulated JFCs and the whole sample. In Section 4, we discuss the limitations of our approach and their consequences on the results, while in Section 5 we present our conclusions.

## 2. Methods

Coupling the thermal and orbital evolution of comet nuclei is not a trivial procedure, as the underlying processes act on very different timescales. On the one hand, the orbital evolution spreads over millions of years or more, demanding large calculation time steps, usually of the order of years (for instance, our sample of model JFCs has a fixed output frequency of 1 per 100 yr). On the other hand, typical timescales for processes at the origin of cometary activity can vary from a few hours or days (e.g., sublimation of volatile species; De Sanctis et al. 2015), to months or years (e.g., crystallization of amorphous water ice in the giant-planet region; Guilbert-Lepoutre 2012). Solving the time-dependent equations of heat transfer and gas flow in a porous medium, while accounting for multiple phase transitions (e.g., crystallization, sublimation), during an orbital evolution spanning on million years, leads to a prohibitive amount of calculation time. As a consequence, a number of simplifying assumptions are adopted in order to keep the problem at hand tractable.

### 2.1. Thermal Evolution Model

First, a driving assumption comes from the 1 per 100 yr dynamical output frequency. For such a long time step, latitudinal effects at the surface, due to the shape of a comet nucleus, its rotation (diurnal variations), or seasonal variations, cannot be resolved. Because they need to be averaged out during this dynamical time step, there is no critical need to use a slow-rotator approximation for the surface (Huebner et al. 2006) or a 2D/3D thermal evolution model for the interior. Besides, in our sample, the vast majority of clones spend a substantial fraction of their lifetime at large heliocentric distances, on transition orbits between Saturn and Neptune (e.g., Figure 3), where diurnal and seasonal temperature variations are less significant. Therefore, we can consider that a 1D approximation is adequate for this study. We thus use a 1D version of the 3D thermal evolution model described by Guilbert-Lepoutre et al. (2011) to solve the heat diffusion equation:

$$\rho_{\rm bulk}\, c\, \frac{\partial T}{\partial t} + \mathrm{div}(-\kappa\, \overrightarrow{\mathrm{grad}}\, T) = \mathcal{S}, \tag{1}$$

where $\rho_{\rm bulk}$ (kg m$^{-3}$) is the object's bulk density, $c$ (J kg$^{-1}$ K$^{-1}$) the material's heat capacity, $T$ (K) the temperature, $\kappa$ (W m$^{-1}$ K$^{-1}$) the material's effective thermal conductivity, and $\mathcal{S}$ the heat sources and sinks.

Second, we apply simplifying assumptions to the thermophysical properties of cometary material. The effective thermal conductivity of cometary material can be written as

$$\kappa = h\, \phi\, \kappa_{\rm solid} + \kappa_{\rm rad}, \tag{2}$$

where $h$ and $\phi$ are reduction factors for which various expressions exist (e.g., Shoshany et al. 2002; Gundlach & Blum 2012; Ferrari & Lucas 2016; see Figure (1) for comparison). The factor $h$ is a dimensionless quantity, known as the Hertz correction factor. It

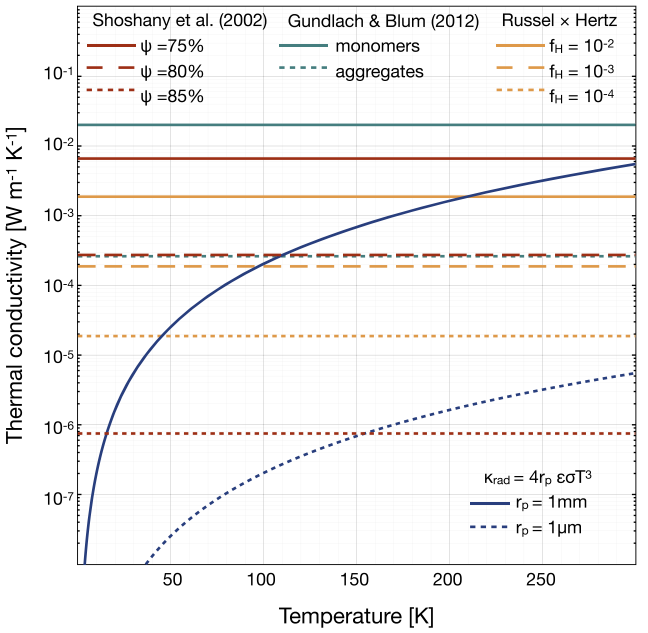


**Figure 1.** Values of the thermal conductivity $\kappa = h\, \phi\, \kappa_{\rm solid}$, with $\kappa_{\rm solid} = 4.2$ (W m$^{-1}$ K$^{-1}$), and correction factors computed with various formulae available in the literature.

describes the reduction of the effective cross section of the grains in a porous material (Gundlach & Blum 2012) and may theoretically vary from $10^{-4}$ to 1, although values of the order of $10^{-2}$ are considered the most plausible and commonly used (see Huebner et al. 2006 for a review). The factor $\phi$ is a correction factor applied to account for the effect of the porous structure of cometary material: Here we use Russell's correction factor (Russell 1935), calculated as

$$\phi = \frac{\psi^{2/3} f + (1 - \psi^{2/3})}{\psi - \psi^{2/3} + 1 - \psi^{2/3}(\psi^{1/3} - 1) f}, \tag{3}$$

where $\psi$ is the porosity and $f$ is the ratio between the solid conductivity and the radiative conductivity $\kappa_{\rm rad}$, which accounts for the transfer of heat through radiation in the pores:

$$\kappa_{\rm rad} = 4 r_p \varepsilon \sigma T^3, \tag{4}$$

with $r_p$ (m) the average pore radius, usually set to be the same size as the grains of the medium (Huebner et al. 2006; so $\sim$1 $\mu$m in our case), $\varepsilon$ the material's emissivity, and $\sigma$ the Stefan–Boltzmann constant.

In Figure 1, we can see that the various expressions for the thermal conductivity found in the literature produce significantly different values, varying by several orders of magnitude, depending on the porosity or value for the Hertz factor. We note that heat transport by radiation inside the pores becomes significant only for large values of the pore size and at temperatures higher than 100–150 K (higher than 200 K for the largest values of thermal conductivity). We thus ignore $\kappa_{\rm rad}$ in Equation (2) and use Russell's equation, further corrected by the Hertz factor. Three values—$10^{-2}$, $10^{-3}$, and $10^{-4}$— are considered for this factor in order to assess the influence of thermal conductivity on the simulation outcomes.

Finally, the most crucial simplification is to ignore phase transitions. In Equation (1), this translates to $\mathcal{S} = 0$. This

**Table 1**
Thermal Model's Physical Parameters

| Parameter | Symbol | Value | Unit | Reference |
|---|---|---|---|---|
| Radius | $R$ | 5000 | m | |
| Initial temperature | $T$ | 10 | K | |
| Porosity | $\psi$ | 0.8 | | Kofman et al. (2015) |
| Bulk density | $\rho_{\rm bulk}$ | 525 | kg m$^{-3}$ | |
| Dust density | $\rho_{\rm dust}$ | 3500 | kg m$^{-3}$ | Huebner et al. (2006) |
| Heat capacity | $c_{\rm dust}$ | 1000 | J kg$^{-1}$ K$^{-1}$ | Kömle et al. (2017) |
| Effective conductivity | $\kappa$ | 4.2 | W m$^{-1}$ K$^{-1}$ | Ellsworth & Schubert (1983) |
| Mean pore radius | $r_p$ | $10^{-6}$ | m | Huebner et al. (2006) |
| Bond albedo | $\mathcal{A}$ | 0.04 | | Huebner et al. (2006) |
| Emissivity | $\epsilon$ | 0.9 | | Huebner et al. (2006) |
| Hertz factor | $h$ | $10^{-2}$–$10^{-4}$ | | Huebner et al. (2006) |

means that our model does not faithfully describe the thermal processing during active stages of the orbital evolution when phase transitions are at the origin of cometary activity. It also entails that no gas diffusion is accounted for, such that the mass is conserved, allowing the use of composition-independent thermophysical properties for the cometary material, in particular for the heat capacity and the thermal conductivity.

Each simulated JFC is thus modeled as a highly porous sphere with a radius of 5 km. Thermophysical parameters are chosen to be averages in the published literature (see Table 1). The initial temperature is set at 10 K, allowing for any type of temperature increase or decrease related to the orbital evolution, and significantly lower than the sublimation temperatures of hypervolatiles. This aspect is important for examining the relative depths where conditions for the loss of such free condensed species are present.

The boundary condition at the surface for Equation (1) is

$$(1 - \mathcal{A})\frac{L_\odot}{4\pi d_H^2} = \varepsilon\sigma T^4 + \kappa\frac{\partial T}{\partial z} \quad (5)$$

with the nucleus' insolation given as a function of $\mathcal{A}$ the Bond's albedo, $L_\odot$ the solar constant and $d_H$ (au) the heliocentric distance; the thermal emission given as a function of $\varepsilon$ the emissivity, $\sigma$ the Stefan–Boltzmann constant and T (K) the temperature; and the heat flux toward the interior given as a function of the surface's thermal conductivity $\kappa$ (W m$^{-1}$ K$^{-1}$). We assume that the incident solar energy is uniformly distributed over the surface of the nucleus, an approximation known as "fast rotator," providing a spherical average of the energy received by the nucleus (Huebner et al. 2006).

### 2.2. Model JFCs Sample

Our sample of model JFCs was produced from a simulation by Nesvorný et al. (2017) of the long-term dynamical evolution of outer solar system bodies. It includes 276 model JFCs chosen from a run that successfully reproduced the orbital distribution of observed JFCs. This run was part of a simulation performed with moderate timescales describing the implantation of the Kuiper Belt and scattered disk, assuming a two-stage migration for Neptune: 10 Myr for the first stage, before the instability, and 30 Myr for the second stage after the instability (see Section 3 in Nesvorný et al. (2017), for a detailed description). The sample of model JFCs was produced during the last segment of the integration, from $t \approx 3.5$ Gyr until the current epoch. Just like actual JFCs, the simulated ones start in their source reservoir, mainly the scattered disk, and gradually evolve inward during the simulation. All selected model JFCs were active and observable, having at some point in their lifetime perihelion distances within 2.5 au. For each model JFC, the orbital evolution starts to be recorded from the first time its heliocentric distance is within 30 au and continues until its ejection from the solar system. The dynamical lifetimes of our model JFCs range from a few thousand years (minimum value ∼0.1 Myr) to almost a billion years (maximum value ∼908 Myr), with a median of ∼54 Myr. The evolution of orbital elements (heliocentric distance, semimajor axis, eccentricity, and inclination) is recorded every 100 yr.

Figure 2 presents an example of the orbital evolution for a model JFC, from the moment it is first detected within Neptune's orbit, until its ejection. This model JFC has a relatively long lifetime of ∼19 Myr. Figure 2 demonstrates the hand-off process through which a comet is scattered inwards from one planet to the planet interior to it until it reaches Jupiter-crossing orbits (Levison & Duncan 1997). At this point the comet's semimajor axis is reduced such that it passes within 2.5 au and becomes an observable JFC (Brasser & Wang 2015; Roberts & Muñoz-Gutiérrez 2021). It is clear from the density of points in Figure 2 that the model JFC spends most of its lifetime (∼16 Myr) beyond 10 au, with orbits between those of Neptune and Saturn. During this time, it would be classified as a Centaur, defined by Jewitt (2009) as an object with $a_J < a$, $q < a_N$. Once under the dynamical control of Jupiter, the ejection phase begins, and the model JFC is scattered outwards and quickly leaves the solar system (∼3 Myr).

Figure 3 shows where in the orbital parameter space our 276 model JFCs statistically spend their time. As was the case for the model JFC from Figure 2, most model JFCs tend to spend the bulk of their lifetimes, once within 30 au, on transient orbits between those of Saturn and Neptune in the Centaur area. Of course, there is a diversity of outcomes governed by the stochastic nature of close gravitational encounters with the giant planets. JFCs scattered quickly inward by Neptune, Uranus, and Saturn tend to have shorter dynamical lifetimes. Indeed, every model JFC's dynamical lifetime is short once it becomes a true JFC with $q < 2.5$ au (Di Sisto et al. 2009; Nesvorný et al. 2017). From the distribution in Figure 3, we note that there is no clear limit in eccentricity values, although values substantially cluster between 0.1 and 0.5.

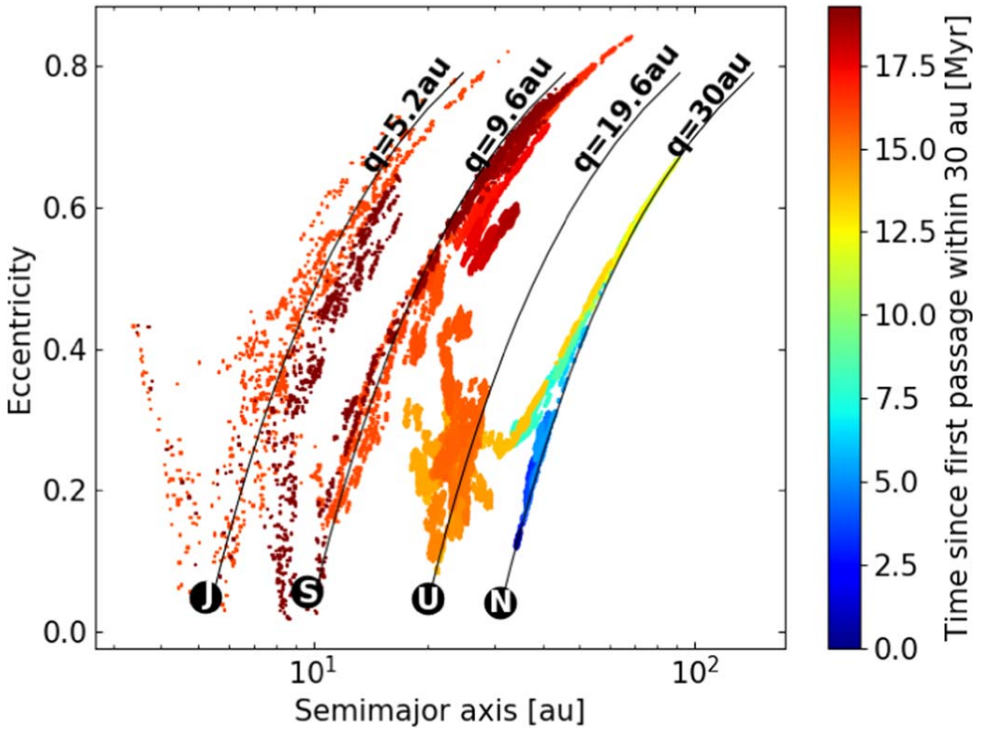


**Figure 2.** Example of a model JFC's orbital evolution from the first time it crosses Neptune's orbit, until its ejection from the solar system after approximately 19 Myr. The orbits of the giant planets are given by the black dots. Black curves show the locus of orbits with perihelia corresponding to the distance of each giant planet. The color code provides the time evolution.

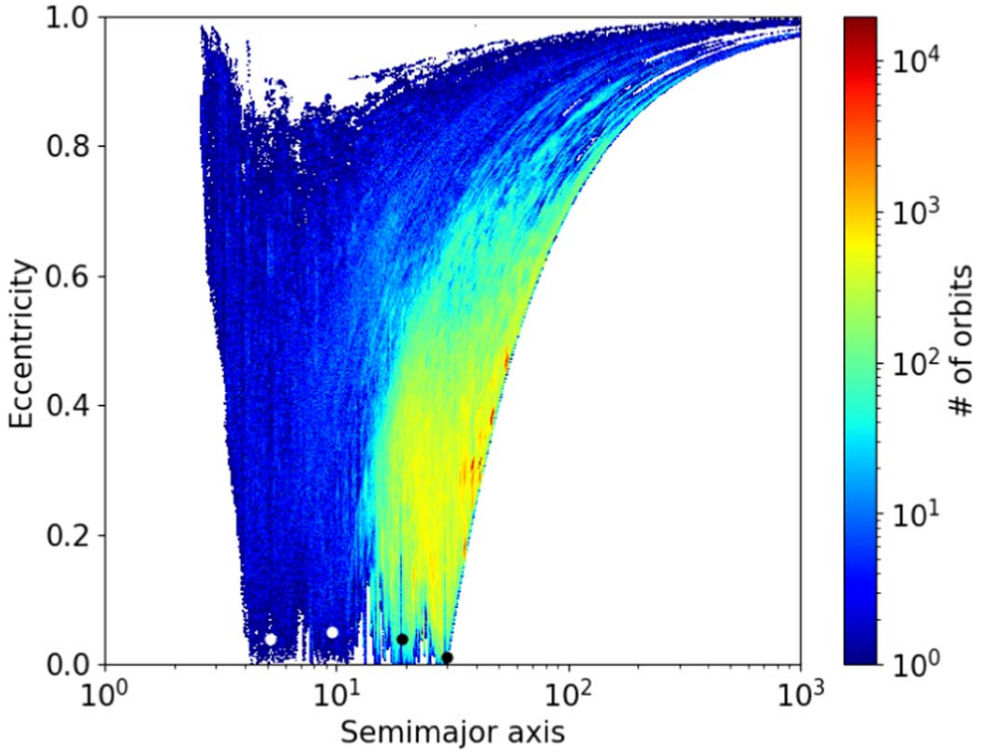


**Figure 3.** Density histogram of the orbits for the entire sample in the semimajor axis–eccentricity plane. Orbits of the giant planets are highlighted with white and black dots. The color code represents the number of orbits per bin width.

### *2.3. Coupling the Thermal and Dynamical Evolution*

In practice, the thermal and dynamical evolution of each model JFC are coupled via the boundary condition of the thermal evolution model (Equation (5)), where the heliocentric distance is required to compute the energy balance at the surface. Figure 4 shows an example of the evolution for a model JFC's fully recorded orbital evolution. We note that the orbits explored span a wide range of orbital periods, sometimes

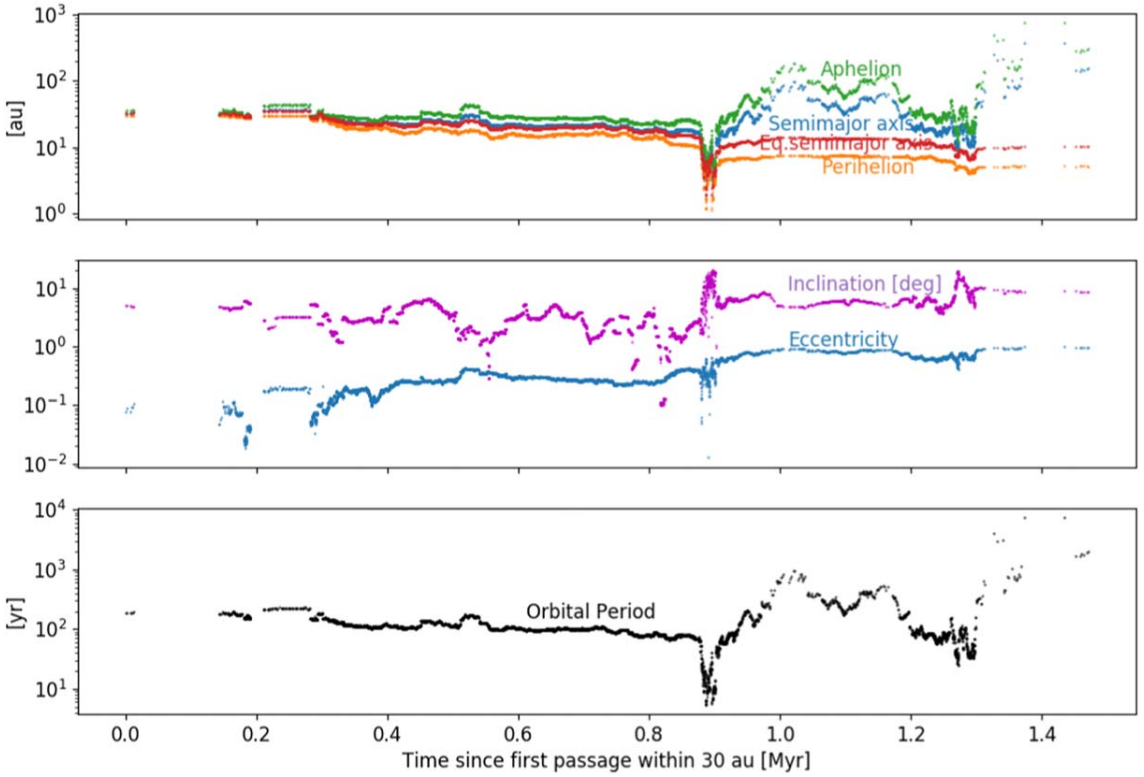


**Figure 4.** Evolution of orbital parameters for a model JFC. Upper panel: semimajor axis, perihelion and aphelion distances, and equivalent semimajor axis. Middle panel: eccentricity and inclination of the model JFC. Lower panel: orbital period of the model JFC.

larger than the dynamical time step (100 yr), sometimes much smaller (Figure 4, bottom panel). Hence, only a fraction of the orbit is explored (or in the case of orbits with small orbital periods, several orbits are explored during the dynamical time step, plus a fraction): From a thermal point of view, large differences can arise whenever this fraction is close to perihelion or aphelion. To alleviate this problem, and in order to treat all orbits in the same fashion, we use an energy-averaged orbital distance. Prialnik & Rosenberg (2009) showed that for simulations on long timescales, eccentric orbits can be modeled as circular ones receiving the same total energy over an orbital period. The equivalent semimajor axis $a_{\rm eq}$ is simply $a_{\rm eq} = a(1-e^2)$ with $a$ the semimajor axis and $e$ the orbital eccentricity. The evolution of $a_{\rm eq}$ is shown in red in Figure 4, upper panel, between the semimajor axis and perihelion. In our thermal simulations, we recalculate $a_{\rm eq}$ every 100 yr, when orbital elements change. For the duration of the dynamical output, this equivalent circular orbit is subsampled in order to perform thermal calculations on a smaller, more appropriate thermal time step.

## 3. Results

### 3.1. Processing of Individual Model JFCs

Figure 5 shows the evolution of the temperature distribution for the same model JFC as in Figure 4. It is a relatively short-lived one within our sample: Quickly scattered inwards by Neptune, such that it orbits close to Saturn almost from the beginning of the dynamical run (at ∼3500 Myr), it is ejected from the solar system after ∼1.45 Myr. We note that the evolution of the temperature distributions depends on the thermal conductivity, depicted here via the Hertz correction factor (Figure 5). Using the 80 K isotherm as a rough indicator for the sublimation of moderately volatile species (such as $CO_2$; white dashed line in Figure 5), we observe that the lower the Hertz factor, the lesser the extent of internal heating: The 80 K isotherm is located at ∼150 m for $h = 10^{-2}$, at ∼50 m for $h = 10^{-3}$, and at ∼10 m for $h = 10^{-4}$. This is a natural consequence of heat conduction, as the skin depth $\delta$—a rough estimate of how deep a surface temperature change can propagate below the surface—is directly dependent on the value of the thermal conductivity ($\delta = \sqrt{\frac{P\kappa}{\pi \rho_{\rm bulk} c}}$, with $P$ a reference period of time).

Figure 5 also shows how the chaotic orbital evolution of a comet nucleus is imprinted on its thermal evolution. This particular model JFC enters (and then leaves) regions of thermal significance in the inner solar system (e.g., where critical phase transitions such as water-ice sublimation can be triggered) more than once during its lifetime. Three main approaches can be identified in this case, associated with individual heating episodes (most clearly visible in panel (b) of Figure 5: two at $t \sim 3502.85$ Myr and one at $t \sim 3503.3$ Myr). This trend of multiple heating episodes, observed for all model JFCs in our sample, with a varying number of approaches and varying degrees of heating intensity (depending on both their duration and the associated equivalent semimajor axis value), suggests that actual comet nuclei observed in the inner solar system may have been exposed to substantial heating in their past, allowing for thermally induced alteration processes to occur in deep layers below their surface.

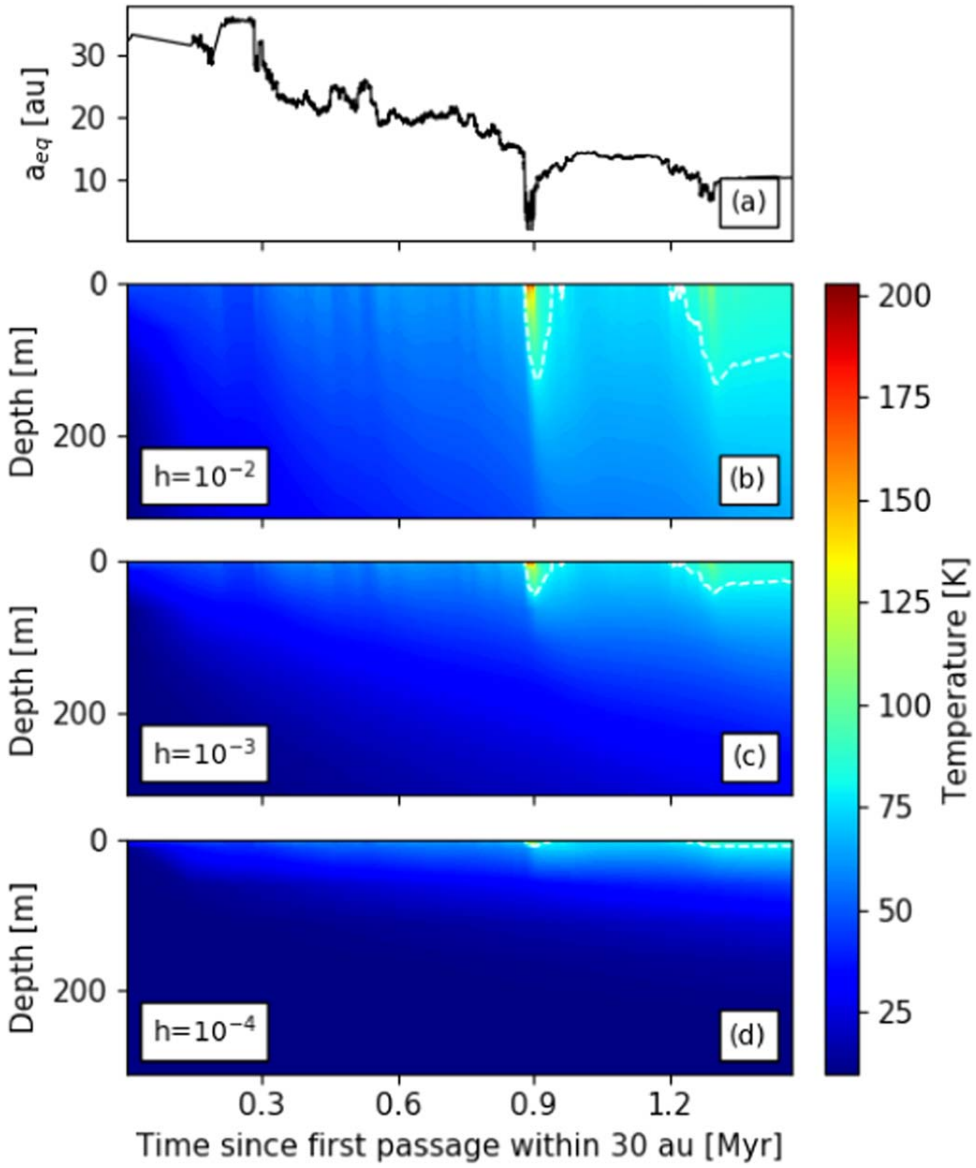


**Figure 5.** Temperature distributions in a subsurface layer of 200 m for the model JFC of Figure 4, and for three different values of the Hertz factor. Panels: (a) Evolution of the equivalent semimajor axis (see Section 2.2), (b) temperature profile evolution over time for $h = 10^{-2}$, (c) temperature profile evolution over time for $h = 10^{-3}$, and (d) temperature profile evolution over time for $h = 10^{-4}$.

### *3.2. Processing in the Sample of Model JFCs*

To constrain statistically the thermal processing of the model JFCs in our sample, we track the depths of three isotherms, at two specific moments of their dynamical lifetime: (a) the moment a model JFC transitions to a JFC orbit, allowing us to examine the initial conditions for JFCs, and (b) the last moment of their JFC phase, in order to study the degree of total processing.

For each phase transition, a characteristic timescale can be computed (see Prialnik et al. 2004 for sublimation timescales), such as $\tau_{cr} = 9.54 \times 10^{-14} \exp\left(\frac{5370}{T}\right)$ for the crystallization of amorphous water ice (Schmitt et al. 1989). In our case, we assume a characteristic timescale of the order of 100 yr (the dynamical time step), which provides a corresponding temperature associated with these common alteration processes:

1. 25 K, representative of sublimation temperatures of hypervolatile species (such as CO);
2. 80 K, representative of sublimation temperatures for moderately volatile species (such as $CO_2$);
3. 110 K, representative of the amorphous to the crystalline water-ice phase transition, a relevant process as indirect observational data suggest the presence of amorphous ice both in comets (Meech et al. 2009) and Centaurs (Jewitt 2009; Guilbert-Lepoutre 2012).

We adopt the Sarid et al. (2019) classification, where JFCs are defined as objects with $q < 5.2$ au and $Q < 7$ au. We avoid classifications using the Tisserand parameter with respect to Jupiter (Levison 1996): Although more accurate, they ignore the presence of the other planets. In our sample, some model JFCs ($\sim$11%) do not satisfy the Sarid et al. (2019) criterion for JFCs. For those, we consider that the transition to a JFC occurs the first time at $q < 2.5$ au.

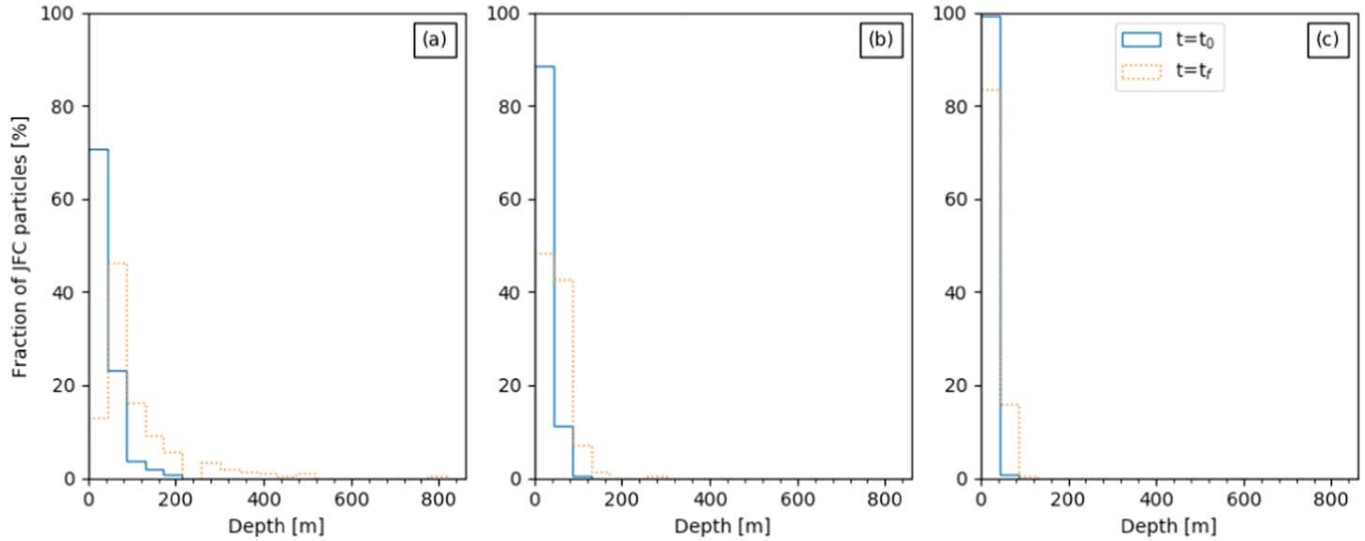


**Figure 6.** Location of the 110 K isotherm for the entire sample at $t_0$, the moment of transition to JFC (blue solid line), and $t_f$, the final moment of the JFC phase (orange dashed line) for the three values of the Hertz factor considered: $h = 10^{-2}$ (panel a), $h = 10^{-3}$ (panel b), and $h = 10^{-4}$ (panel c).

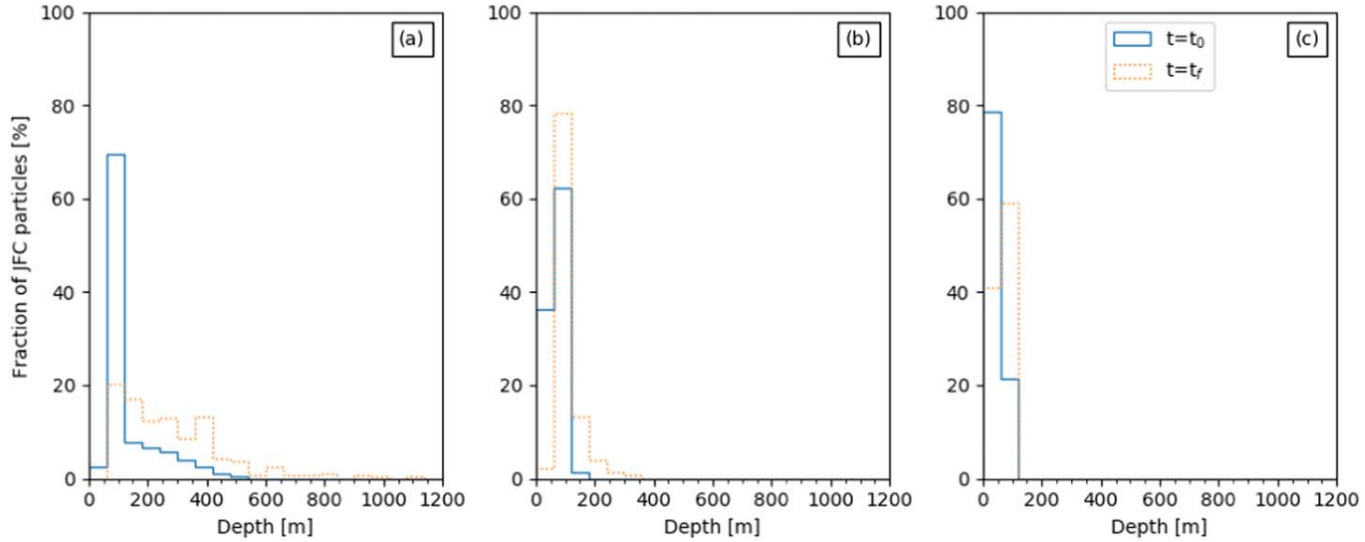


**Figure 7.** Location of the 80 K isotherm for the entire sample at $t_0$, the moment of transition to JFC (blue solid line), and $t_f$, the final moment of JFC phase (orange dashed line) for the three values of the Hertz factor considered: $h = 10^{-2}$ (panel a), $h = 10^{-3}$ (panel b), and $h = 10^{-4}$ (panel c).

For the sake of illustration, we use the model JFC presented in Figure 5. Following the Sarid et al. (2019) criterion, it transitions to a JFC orbit for the first time at $t$ =3502.8687 Myr, having previously spent ∼0.88 Myr on transient orbits in the giant-planet region. At the moment of this first transition, the three isotherms (25 K, 80 K, 110 K) are located at ∼810 m, ∼60 m, and ∼5 m, respectively, below the surface for $h = 10^{-2}$, and at ∼60 m, ∼3 m, and ∼60 cm, respectively, for $h = 10^{-4}$. At the final moment of its JFC phase, having experienced intense processing, for $h = 10^{-2}$, the 25 K isotherm is located at the same depth (∼810 m), whereas the 80 K isotherm advanced at ∼160 m and the 110 K isotherm at ∼60 m. For $h = 10^{-4}$, the three isotherms are closer to the surface (at ∼60 m, ∼9 m, and ∼4 m, respectively). We emphasize that because no phase transition is actually computed, there is no heating delay associated with the sublimation of volatile species nor any recondensation. Indeed, when volatile species sublimate, their partial pressure peaks at the phase transition front. Molecules then follow pressure gradients and recondense in any volume that sustains the appropriate temperature and pressure conditions, either toward the surface or deeper in the interior. We track the temperature evolution for timescales so long that both sublimation and gas diffusion timescales are shorter than the lifetime of our model JFCs. As such, the results presented here and below are significant with respect to the primordial composition, and whether it can be maintained in near-surface layers. We thus assume that volatile species, initially present as pure condensate, can sublimate if their sublimation temperature is reached: free condensed CO would sublimate down to the level of the 25 K isotherm, and free condensed $CO_2$ down to the level of the 80 K isotherm. Whether molecules escape the nucleus or recondense in the interior, where conditions allow it, the net result is an alteration of the primordial composition. When these layers subsequently contribute to the cometary activity that we observe, they are no longer pristine, thus they

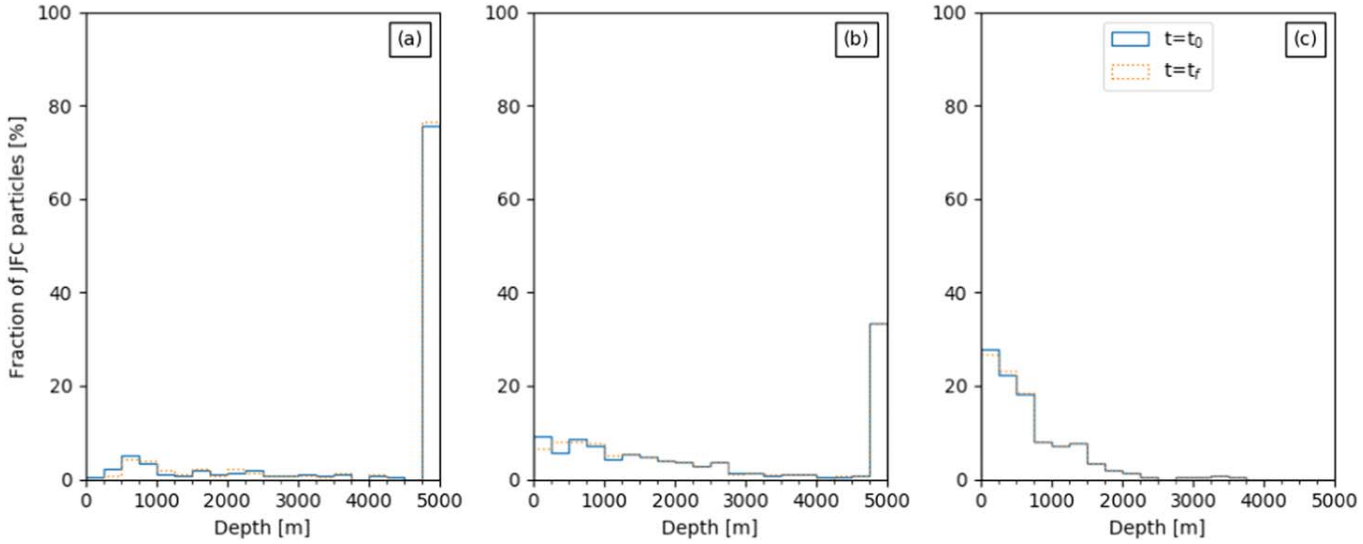


**Figure 8.** Location of the 25 K isotherm for the entire sample at $t_0$, the moment of transition to JFC (blue solid line), and $t_f$, the final moment of the JFC phase (orange dashed line) for the three values of the Hertz factor considered: $h = 10^{-2}$ (panel a), $h = 10^{-3}$ (panel b), and $h = 10^{-4}$ (panel c).

do not reflect the primitive material incorporated in comet nuclei. For simplicity, we refer to the "loss" of respective volatile species hereafter: The reader should keep in mind that it is the primordial inventory of volatile species, which is lost.

With the above assumptions, the above model JFC would have "lost" these volatile species from a substantial subsurface layer before its transition to JFC. During the intense processing of the JFC phase, we note that it is the moderately volatile species and the crystallization of amorphous water ice that are mostly considered, as the fate of its hypervolatile content has already been determined by the time spent in transient orbits at the Centaur area. We present below the potential processing for the whole sample.

#### 3.2.1. Crystallization of Amorphous Water Ice

We assume here that the crystallization of amorphous water ice, if at all present inside JFCs, would follow the 110 K isotherm. Figure 6 shows the depths of this isotherm, as a function of the Hertz factor, for the initial and final moments of the model JFCs. Before transitioning to a JFC orbit for the first time, the three different values of the conductivity yield similar depth distributions: For nearly all model JFCs in the sample, the 110 K isotherm remains located within 40 m below the surface (up to 80 m for $h = 10^{-2}$). As can be expected from the conduction of heat with time, the isotherm propagates below the surface during the JFC phase (for all values of the effective thermal conductivity), remaining, however, quite close to the surface: For the bulk of the model JFCs, the isotherm is located in the top ~80 m below the surface. In the case of $h = 10^{-2}$, we can find it in deeper layers, though rarely below ~400 m. These depths are compatible with the results from Guilbert-Lepoutre (2012), who studied the survival of amorphous water ice in Centaurs, using fixed orbits in the giant-planet region for 10 Myr. Our results suggest that the survival of amorphous water ice is definitely conceivable in the interior of comet nuclei and do not challenge the hypothesis that this phase transition to crystalline water ice could be a possible source for activity among Centaurs or possible outbursts (e.g., Wierzchos & Womack 2020).

#### 3.2.2. Volatile Content Following the 80K Isotherm

The distributions of depths reached by the 80 K isotherm are quite similar to those for the 110 K isotherm (see Figure 7), although because the temperature of interest is smaller, it is generally found deeper below the surface. The minimum processing of model JFCs in our sample involves the top ~100 m for most objects and all values of thermal conductivity. For $h = 10^{-2}$, we note, however, that almost all model JFCs are liable to lose their moderately volatile content in the top 40 m below the surface, as the 80 K isotherm has progressed below that limit even before the model JFCs transition to JFC orbits: 69.5% of the model JFCs in the sample have the isotherm located between 40 and 80 m, 28% have it below 80 m. Only 2.5% (seven model JFCs) have the 80 K isotherm above 40 m. A similar trend is observed for $h = 10^{-3}$, albeit less pronounced: 62.3% of model JFCs have the 80 K isotherm between 40 and 80 m in this case. For $h = 10^{-4}$, the majority of the model JFCs (79%) have this isotherm located in the first 40 m (average depth of 17.2 m).

At the end of their JFC phase, the isotherm is found ~80 m below the surface on average for $h = 10^{-2}$, ~70 m for $h = 10^{-3}$, and ~9 m for $h = 10^{-4}$. This suggests that the dominant heating phase related to this particular isotherm occurs during their JFC phase, although the processing during the Centaur phase is not negligible at all, even for the least conductive scenario. Accounting for the sublimation of the corresponding volatile species on long timescales will therefore be of particular importance for future works.

#### 3.2.3. Hypervolatile Content Traced by the 25K Isotherm

The distribution of depths reached by the 25 K isotherm for the different values of the thermal conductivity is given in Figure 8. It is apparent that with respect to this particular isotherm, the thermal conductivity (through the choice of Hertz factor in our study) is critical to assess the corresponding processing, while the time at which the processing is examined plays no significant role. Indeed, the distributions obtained at the first time of transition and at the end of the JFC phase are almost identical (especially in the case $h = 10^{-2}$). For $h = 10^{-2}$

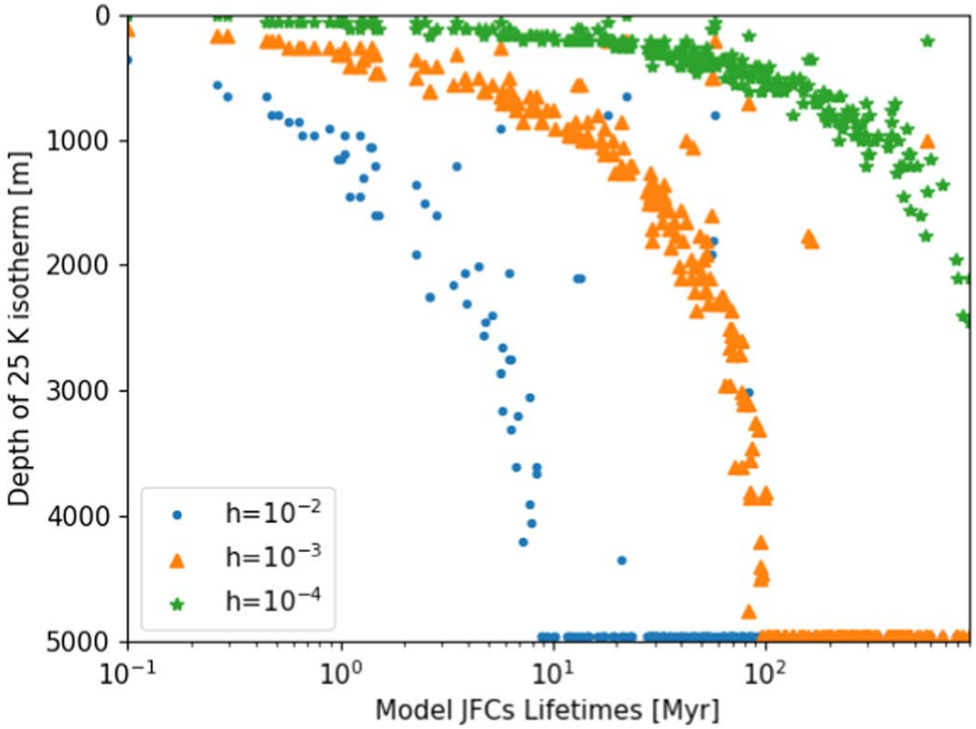


**Figure 9.** Maximum depths of the 25 K isotherm as a function of the lifetimes of the 276 model JFCs of our sample for three different values of the Hertz factor.

(and $10^{-3}$ to some degree), most model JFCs have already heated up down to their cores before their first transition to a JFC orbit (77% and 33.3%, respectively). For the least conductive scenario ($h = 10^{-4}$), only 27.9% of model JFCs retain the 25 K isotherm in the top 250 m layer, the average depth for the overall sample being ∼650 m. At the final moment of their JFC lifetime, we see that less than 10% of model JFCs are able to maintain the 25 K isotherm in the top 1 km (only one model JFC keeps the isotherm in the top 250 m) for $h = 10^{-2}$. For $h = 10^{-3}$, only 30% of model JFCs keep the isotherm within 1 km below the surface (∼8% keep it within 250m), whereas for $h = 10^{-4}$, 27% of model JFCs have the 25 K isotherm within 250 m, and 50% within 500 m.

Assuming that the 25 K isotherm is indicative of the loss of CO, for example, all model JFCs in our sample (except one) would have lost free condensed CO in the top 250 m subsurface layer before their first arrival on JFC orbits. We could further argue that, given the extremely low sublimation temperature of hypervolatiles, these species would be lost as pure condensate even before the model JFCs enter the giant-planet region because isothermal surface temperatures in the Kuiper Belt range between 30 and 50 K. Because the parameter controlling the outcomes of thermal simulations with respect to the 25 K isotherm is the thermal conductivity, the time spent in transient orbits is also critical. We illustrate this effect in Figure 9: Model JFCs spending long periods of time on transient orbits (i.e., model JFCs with longer lifetimes) are more susceptible to being heated up at greater depths. For $h = 10^{-2}$, model JFCs with lifetimes over ∼8 Myr are prone to losing all free condensed hypervolatiles down to their core. For $h = 10^{-3}$, model JFCs with lifetimes above ∼90 Myr would experience the same fate. In contrast, no model JFC is found to lose free condensed hypervolatiles below 2500 m for $h = 10^{-4}$. The exact depth will need to be confirmed by including the relevant phase transition, with appropriate diurnal and seasonal approximations, in further modeling work.

### 3.3. Relation to the Observed JFC Population

We use a random number generator to select a moment during the JFC phase of all model JFCs in order to examine the thermal processing of typically observed JFCs. The depth distributions for the different temperatures and Hertz factors considered are presented in Figure 10. We find that the depth distributions for the 25 K isotherm are almost identical to the distributions during the transition to JFCs and the JFC end states, with only slight differences of the order of 2%–3% for model JFCs having the isotherm close to the surface. This confirms our previous argument that for pure condensed hypervolatiles, the key factor is the time spent prior to the JFC phase in the Centaur area or before and the thermal characteristics of the cometary material controlling the amount of heat transferred toward the interior of comet nuclei.

As expected, the 80 K isotherm is located slightly deeper below the surface (for all thermal conductivities) when compared to the moment of transition and slightly shallower when compared to the final states of JFCs. For instance, in the case of $h = 10^{-2}$, although in 38% of the model JFCs the isotherm is retained between 40 and 80 m, in the remaining 62% it is located significantly deeper, as far as ∼750 m, whereas no model JFC has the isotherm in the first 40 m below the surface. Similar behavior is observed for $h = 10^{-3}$ and $h = 10^{-4}$, as witnessed by the increase in the average depths presented in Table 2. Similar results are drawn for the 110 K isotherm: For a randomly selected moment of the JFC phase, it is located between the initial and the final positions shown in Figure 6. Taking for example the case of $h = 10^{-2}$, we see that at a random moment, the fraction of model JFCs having this isotherm beyond the first 80 m below the surface is ∼30%, whereas in the moment of transition, this fraction was

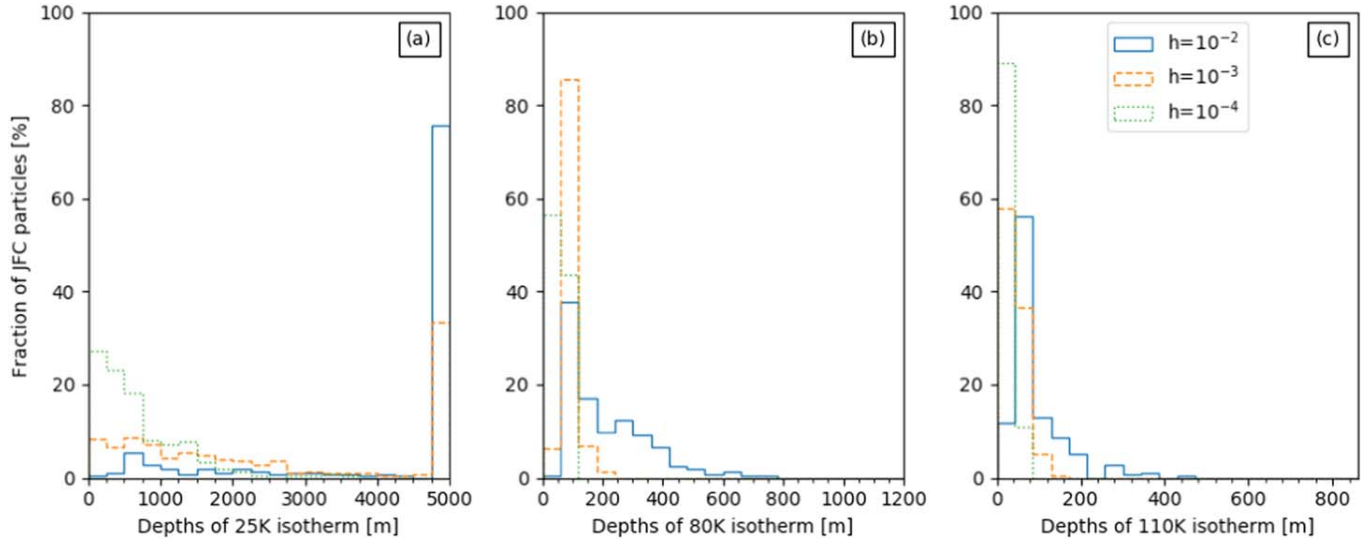


**Figure 10.** Temperature distributions for the entire sample at a random moment of their JFC phase for the different values of the Hertz factor considered: $h = 10^{-2}$ (blue solid line), $h = 10^{-3}$ (orange dashed line), and $h = 10^{-4}$: (a) 25 K and (b) 80 K (110 K).

less than 10% and at the final moment of the JFC phase mounts to ∼40%.

## 4. Discussion

### 4.1. Composition Effects and Latent Heat Transfer

To simplify our study, we have assumed that our model JFCs are made of a porous structure of refractories, with no ices included so as to avoid phase transitions. Despite the uncertainties regarding their structure and composition, actual comets clearly contain a number of icy species. Ignoring their presence removes the energy sources and sinks related to their phase transitions, such as the energy released during the crystallization of amorphous water ice (Schmitt et al. 1989) and the energy consumption during ice sublimation (Prialnik et al. 2004). In fact, when sublimation and recondensation of volatile compounds do occur inside comet nuclei, heat transport via the vapor phase is very important, sometimes more effective than heat conduction by the solid matrix (see Huebner et al. 2006 for a review). As such, during the active phase, the dominant heat transport mechanism is the transfer of latent heat: This strongly influences the temperature profile within actual comet nuclei and is not accounted for in our model JFCs. The direct consequence is that while an icy compound is sublimating, the input energy is used for the phase transition so that the internal temperature will stop increasing. This would limit the penetration of successive heat waves observed in Figure 5, as the heat would be consumed to sublimate ices, rather than propagating inward. In this regard, the depths achieved in our study could be considered as upper limits to the actual processing of comet nuclei.

Ignoring phase transitions also makes it impossible to account for surface erosion, which is associated with water-ice sublimation. Estimates from the literature indicate that the erosion rate can vary from tenths of centimeters up to approximately 2 m per year, depending on thermal characteristics, the heliocentric distance, the inclination of the spin axis, and the cometocentric latitude examined. Huebner et al. (2006) estimate an erosion rate varying from 10 cm $yr^{-1}$ to 2.1 m $yr^{-1}$ for 46P/Wirtanen, while estimates for 67P/Churyumov-Gerasimenko give an average erosion rate ranging from 0.67 to 2.9 m, depending on the thermophysical parameters considered for the surface (Keller et al. 2015). Accounting for the cumulative effect of erosion over long timescales becomes important during the active phase of JFCs, as a significant amount of processed surface material can be removed, revealing unprocessed layers (or bringing them closer to the surface) and changing the internal stratigraphy. A more sophisticated model, including carefully developed approximations for diurnal and seasonal variations of the temperature and activity, is clearly required for quantitative calculations of the actual internal stratification or the cumulative erosion with time.

Finally, we have seen how the thermal conductivity is instrumental in constraining the extent of subsurface thermally induced processing. Arguments summarized in Huebner et al. (2006) are in favor of a Hertz factor of the order of $10^{-2}$ (based on laboratory experiments, observations, and theoretical considerations), which in our simulations corresponds to the maximum processing considered. We have also ignored heat transport through radiation within the porous structure. For the lowest values of the Hertz factor, accounting for $\kappa_{rad}$ would

**Table 2**
Average Depth (m) of Three Isotherms for Three Values of the Hertz Factor, at Distinct Times of Our Sample of Model JFCs' Orbital Evolution

| $T$ (K) | $h = 10^{-2}$ | $h = 10^{-3}$ | $h = 10^{-4}$ |
|---|---|---|---|
| First Transition to a JFC Orbit | | | |
| 25 | 4142.2 ± 1529.9 | 2561.5 ± 1894.0 | 651.7 ± 615.2 |
| 80 | 125.7 ± 92.3 | 50.1 ± 36.8 | 17.2 ± 23.0 |
| 110 | 27.1 ± 37.5 | 10.0 ± 19.4 | 2.1 ± 5.4 |
| Random Time in the JFC Phase | | | |
| 25 | 4156.3 ± 1502.9 | 2566.60 ± 1889.8 | 654.1 ± 613.5 |
| 80 | 209.2 ± 130.1 | 81.0 ± 38.4 | 31.2 ± 26.9 |
| 110 | 89.9 ± 39.9 | 32.3 ± 32.8 | 10.1 ± 18.0 |
| End of the JFC Phase | | | |
| 25 | 4181.7 ± 1474.1 | 2575.1 ± 1882.8 | 656.2 ± 611.8 |
| 80 | 278.3 ± 177.6 | 99.7 ± 51.1 | 40.9 ± 28.1 |
| 110 | 107.9 ± 103.4 | 40.2 ± 39.0 | 13.4 ± 21.9 |

actually increase the effective thermal conductivity, even at low temperatures ($\kappa_{\rm solid}$ and $\kappa_{\rm rad}$ are of the same order of magnitude around 40–50 K for the lowest values of the Hertz factor; Huebner et al. 2006). This makes our results for $h = 10^{-4}$ unrealistic and favors evolution outcomes given for $h = 10^{-2}$ or $h = 10^{-3}$, albeit still limited by the lack of icy components in the material.

### 4.2. Limitations of the Orbital Approximation

To couple the thermal model to dynamical simulations, we effectively placed each model JFC on a circular orbit receiving the same total energy as its true, eccentric orbit (see Section 2.2). In practice, this averaging means that a model JFC receives a constant amount of solar energy for every thermal time step, regardless of its true orbit. The input flux and, therefore, the calculated surface temperature (Equation (5)) are both underestimated when actual heliocentric distances are smaller than the equivalent semimajor axis (typically close to the perihelion where the most intensive heating takes place) and overestimated when they are larger, especially close to the aphelion. In this regard, the effects of cumulative perihelion passages are always underestimated in our study. On the other hand, one could argue the model JFCs are not allowed to cool down when they are close to aphelion. After further analysis using real orbits, we find that this approximation is valid for relatively low eccentricities (e.g., $e < 0.5$), where deviations from circular orbits are small, as well as for orbits with a large semimajor axis because temperature variations across the orbit are less significant. This is the case for the majority of the orbits in our sample (see Figure 3). If improvements are required in this study, they need to address the key points identified above, i.e., accounting for phase transition or better constraints on the thermophysical parameters, rather than on the orbital approximations.

### 4.3. On the Activity of Centaurs and JFCs

With the aforementioned limits in mind, our results have several inferences regarding the activity of Centaurs and JFCs. Before our model JFCs go through their first transition to a JFC orbit, we consider them as Centaurs. Recent studies have tried to link the activity of Centaurs to their orbital evolution. Indeed, Guilbert-Lepoutre (2012) found that crystallization of amorphous water ice can be a source of activity, efficient at heliocentric distances up to 10–12 au, sustained though for a limited time (typically hundreds to thousands of years). This implies that active Centaurs should have suffered a recent orbital change. Davidsson (2021) nuanced this result by showing that crystallization would be efficient only up to 8–10 au, while the sublimation of $CO_2$ would be the only source of activity in the 10–12 au region. The study by Fernández et al. (2018) is compatible with a link between thermal and orbital evolution as the origin of active Centaurs. They find that active Centaurs are more prone to drastic drops in their perihelion distances than inactive Centaurs, with timescales of the order of $10^2$–$10^3$ yr. Finally, Cabral et al. (2019), Li et al. (2020), and Lilly et al. (2021) found no activity among various Centaur detections: The corresponding objects are dynamically stable on long timescales.

Our study shows that the 25 K isotherm reaches deep layers below the surface of most model comets early in the Centaur phase. Indeed, heating subsurface layers above this 25K temperature starts at large heliocentric distances and is relevant throughout the entire orbital evolution. Both the sublimation of moderately volatiles (such as $CO_2$) and the crystallization of amorphous water ice would be triggered during this Centaur phase, each time their perihelion distance drops and the heat wave reaches an internal layer that was not previously depleted during its past orbital evolution. Our sample suggests that on average, our objects could be active for a $10^3$ period during their $10^6$–$10^7$ yr life as Centaurs. This period is not continuous: Following chaotic evolution in the giant-planet region, we see that our model JFCs are active for several shorter periods of time, typically ∼10 times. We emphasize nonetheless that our results cannot be directly compared to the observed Centaur population because both the latter and our dynamical sample are biased. On the one hand, there has not been any systematic survey targeting the Centaur population (e.g., Cabral et al. 2019), so the typical ∼10% fraction of active Centaurs is meant to evolve. Besides, active Centaurs are more easily observable, typically being closer to the Sun, and displaying cometary activity. On the other hand, all our model Centaurs/JFCs do become JFCs at one point of their lifetime, which is not the case for all actual Centaurs, as some may be directly ejected before reaching Jupiter-crossing orbits.

### 4.4. Considerations on Observed JFCs

Following the thermal processing during the Centaur phase, once our model JFCs transition to actual JFC orbits, their subsurface layers can be already considerably altered. Our results suggest that at a random moment of their JFC phase, regardless of the temperature examined and the conductivity scenario considered, all model JFCs have already undergone sufficient heating for alteration processes to take place at considerable depths. We can thus infer that a typical observed JFC can be significantly altered, with the primordial inventory of volatiles lost due to sublimation, gas diffusion, depletion, and enrichment of internal volumes on long timescales. In particular, the processed layer is substantially larger than the estimated size of the layers involved in producing cometary activity observed for most JFCs (e.g., Huebner et al. 2006). In other words, cometary activity as it is observed today should be produced from layers that have been substantially processed. Our results suggest nonetheless that if these layers may be able to retain some amorphous water ice on the one hand, they should on the other hand have lost all pure primitive condensed hypervolatiles and a fraction of their primitive moderately volatile content. Even if we were able to observe an object transitioning to a JFC orbit—while actually knowing it is the first time the object experiences this transition—our results imply that we would be observing an altered body, in particular one with severe modifications of its hypervolatile content. This highlights the importance of accounting for the past history of each comet in order to better constrain its present thermal, physical, and chemical state.

### 4.5. Implications for Future Cryogenic Sample Return Missions

Our study, despite being a first-order approximation of the thermal processing of JFCs, can have direct implications for future cryogenic sample return missions. We observed that the expected loss of hypervolatile ices should be severe from a substantial subsurface area expanding several thousand meters. The same can be said for moderately volatile species, although the subsurface volume concerned is greatly reduced (see also

Table 2). Sample return missions aiming at depths of 3 m below the surface (e.g., Bockelée-Morvan et al. 2021) would likely not be able to access a primitive layer containing pure hypervolatile or moderately volatile ices. As a consequence, cryogenic temperatures lower than 80 K should not be a critical constraint for such missions.

## 5. Summary

We present the results of a first-order study of the coupled thermal and dynamical evolution of JFCs on their path inward from the Kuiper Belt and scattered disk. We applied a simplified thermal evolution model to a sample of 276 model JFCs, taken from a dynamical simulation that successfully reproduces their observed orbital distribution (Nesvorný et al. 2017). Our simulations show that:

1. Comet nuclei undergo multiple heating episodes, spread randomly across their dynamical lifetimes. These heating episodes are prolonged long-lasting periods, with a large number of orbital changes, each orbit being further characterized by seasonal cycles between their perihelion–aphelion passages. This pattern is observed for all model JFCs during their chaotic transition toward the inner solar system.
2. As a consequence, a substantial subsurface layer is heated, providing the necessary conditions for extensive thermal processing to occur. Processed layers can extend as deep as ∼4100 m on average for temperatures allowing the sublimation of hypervolatile species, ∼125 m for temperatures permitting the sublimation of moderately volatile species, and ∼27 m for temperatures allowing the crystallization of amorphous water ice (considering the most plausible scenario for thermal conductivity). These results have direct implications for the drilling depths of any cryogenic sample return mission, although a more detailed model would be required to confidently conclude limiting depths and temperatures.
3. Despite the limitations of our approach, the fate of hypervolatiles is so extreme that we can infer that all primordial condensed hypervolatiles should be lost from layers that subsequently contribute to any observed cometary activity.
4. For any typical observed JFC, activity is very likely triggered from layers that have been thermally processed and lost their primitive inventory of volatiles. This indicates that JFCs are probably inadequate targets for cryogenic sample return missions. It also points to the necessity of taking into consideration their entire evolutionary history, both thermal and dynamical, when interpreting current observations in a broader context.

We would like to thank the referee for a careful and thorough report on our manuscript. This study is part of a project that has received funding from the European Research Council (ERC) under the European Union's Horizon 2020 research and innovation program (grant agreement No. 802699). We gratefully acknowledge support from the PSMN (Pôle Scientifique de Modélisation Numérique) of the ENS de Lyon for the computing resources. S.N.R. is grateful to the CNRS's PNP program (*Programme National de Planétologie*).

*Facilities:* PSMN, ENS de Lyon.

## ORCID iDs

Anastasios Gkotsinas https://orcid.org/0000-0002-1611-0381
Aurélie Guilbert-Lepoutre https://orcid.org/0000-0003-2354-0766
Sean N. Raymond https://orcid.org/0000-0001-8974-0758
David Nesvorny https://orcid.org/0000-0002-4547-4301

## References

Bockelée-Morvan, D., Filacchione, G., Altwegg, K., et al. 2021, ExA, in press
Brasser, R., & Morbidelli, A. 2013, Icar, 225, 40
Brasser, R., & Wang, J. H. 2015, A&A, 573, A102
Cabral, N., Guilbert-Lepoutre, A., Fraser, W. C., et al. 2019, A&A, 621, A102
Capria, M. T., Coradini, A., De Sanctis, M. C., & Orosei, R. 2000, AJ, 119, 3112
Choi, Y.-J., Cohen, M., Merk, R., & Prialnik, D. 2002, Icar, 160, 300
Davidsson, B. J. R. 2021, MNRAS, 505, 5654
de la Fuente Marcos, C., de la Fuente Marcos, R., Licandro, J., et al. 2021, A&A, 649, A85
De Sanctis, M. C., Capaccioni, F., Ciarniello, M., et al. 2015, Natur, 525, 500
De Sanctis, M. C., Capria, M. T., & Coradini, A. 2001, AJ, 121, 2792
De Sanctis, M. C., Capria, M. T., Coradini, A., & Orosei, R. 2000, AJ, 120, 1571
Di Sisto, R. P., Fernández, J. A., & Brunini, A. 2009, Icar, 203, 140
Ellsworth, K., & Schubert, G. 1983, Icar, 54, 490
Farnham, T. L., Kelley, M. S. P., & Bauer, J. M. 2021, PSJ, 2, 236
Fernández, J. A., Helal, M., & Gallardo, T. 2018, P&SS, 158, 6
Ferrari, C., & Lucas, A. 2016, A&A, 588, A133
Guilbert-Lepoutre, A. 2012, AJ, 144, 97
Guilbert-Lepoutre, A., Lasue, J., Federico, C., et al. 2011, A&A, 529, A71
Gundlach, B., & Blum, J. 2012, Icar, 219, 618
Huebner, W. F., Benkhoff, J., Capria, M.-T., et al. 2006, Heat and Gas Diffusion in Comet Nuclei (Bern: International Space Science Institute)
Hui, M.-T., Farnocchia, D., & Micheli, M. 2019, AJ, 157, 162
Hui, M.-T., Jewitt, D., & Clark, D. 2018, AJ, 155, 25
Jewitt, D. 2009, AJ, 137, 4296
Jewitt, D., Hui, M.-T., Mutchler, M., et al. 2017, ApJL, 847, L19
Keller, H. U., Mottola, S., Davidsson, B., et al. 2015, A&A, 583, A34
Kofman, W., Herique, A., Barbin, Y., et al. 2015, Sci, 349, 2.639
Kömle, N. I., Macher, W., Tiefenbacher, P., et al. 2017, MNRAS, 469, S2
Levison, H. F. 1996, in ASP Conf. Ser., 107, Completing the Inventory of the Solar System, ed. T. Rettig & J. M. Hahn (San Francisco, CA: ASP), 173
Levison, H. F., & Duncan, M. J. 1997, Icar, 127, 13
Li, J., Jewitt, D., Mutchler, M., Agarwal, J., & Weaver, H. 2020, AJ, 159, 209
Lilly, E., Hsieh, H., Bauer, J., et al. 2021, PSJ, 2, 155
Lin, H. W., Chen, Y. T., Lacerda, P., et al. 2014, AJ, 147, 114
Mazzotta Epifani, E., Dotto, E., Ieva, S., et al. 2018, A&A, 620, A93
Mazzotta Epifani, E., Perna, D., Dotto, E., et al. 2017, A&A, 597, A59
Meech, K. J., Kleyna, J. T., Hainaut, O., et al. 2017, ApJL, 849, L8
Meech, K. J., Pittichová, J., Bar-Nun, A., et al. 2009, Icar, 201, 719
Meech, K. J., & Svoren, J. 2004, in Using Cometary Activity to Trace the Physical and Chemical Evolution of Cometary Nuclei, ed. M. C. Festou, H. U. Keller, & H. A. Weaver (Tuscon, AZ: Univ. Arizona Press), 317
Nesvorný, D., Vokrouhlický, D., Dones, L., et al. 2017, ApJ, 845, 27
Prialnik, D., Benkhoff, J., & Podolak, M. 2004, Modeling the Structure and Activity of Comet Nuclei (Tuscon, AZ: Univ. of Arizona Press), 359
Prialnik, D., & Merk, R. 2008, Icar, 197, 211
Prialnik, D., & Rosenberg, E. D. 2009, MNRAS, 399, L79
Raymond, S. N., Kaib, N. A., Armitage, P. J., & Fortney, J. J. 2020, ApJL, 904, L4
Roberts, A. C., & Muñoz-Gutiérrez, M. A. 2021, Icar, 358, 114201
Russell, H. 1935, J. Am. Ceram. Soc., 18, 1
Sarid, G., Volk, K., Steckloff, J. K., et al. 2019, ApJL, 883, L25
Schmitt, B., Espinasse, S., Grim, R. J. A., Greenberg, J. M., & Klinger, J. 1989, in Physics and Mechanics of Cometary Materials, ed. J. J. Hunt & T. D. Guyenne, Vol. 302 (Paris: European Space Agency), 65
Shoshany, Y., Prialnik, D., & Podolak, M. 2002, Icar, 157, 219
Steckloff, J. K., Sarid, G., Volk, K., et al. 2020, ApJL, 904, L20
Wierzchos, K., & Womack, M. 2020, AJ, 159, 136
Yang, B., Jewitt, D., Zhao, Y., et al. 2021, ApJL, 914, L17

# Appendix C

# Article ApJ (2023)

Article published on the journal *The Astrophysical Journal*: Guilbert-Lepoutre et al., (2023), ApJ, 942, 92, 14 pp.

The Astrophysical Journal, 942:92 (14pp), 2023 January 10 https://doi.org/10.3847/1538-4357/acaa3a


# The Gateway from Centaurs to Jupiter-family Comets: Thermal and Dynamical Evolution

Aurélie Guilbert-Lepoutre[1], Anastasios Gkotsinas[1], Sean N. Raymond[2], and David Nesvorny[3]
[1] Laboratoire de Géologie de Lyon; Terre, Planètes, Environnnement, CNRS, UCBL, ENSL, F-69622, Villeurbanne, France; aurelie.guilbert-lepoutre@univ-lyon1.fr
[2] Laboratoire d'Astrophysique de Bordeaux, Univ. Bordeaux, CNRS, F-33615 Pessac, France
[3] Department of Space Studies, Southwest Research Institute, 1050 Walnut Street, Suite 300, Boulder, CO 80302, USA
*Received 2022 July 18; revised 2022 November 28; accepted 2022 December 7; published 2023 January 17*

## Abstract

It was recently proposed that there exists a "gateway" in the orbital parameter space through which Centaurs transition to Jupiter-family comets (JFCs). Further studies have implied that the majority of objects that eventually evolve into JFCs should leave the Centaur population through this gateway. This may be naively interpreted as gateway Centaurs being pristine progenitors of JFCs. This is the point we want to address in this work. We show that the opposite is true: gateway Centaurs are, on average, *more* thermally processed than the rest of the population of Centaurs crossing Jupiter's orbit. Using a dynamically validated JFC population, we find that only ∼20% of Centaurs pass through the gateway *prior* to becoming JFCs, in accordance with previous studies. We show that more than half of JFC dynamical clones entering the gateway for the first time have already been JFCs—they simply avoided the gateway on their first pass into the inner solar system. By coupling a thermal evolution model to the orbital evolution of JFC dynamical clones, we find a higher than 50% chance that the layer currently contributing to the observed activity of gateway objects has been physically and chemically altered, due to previously sustained thermal processing. We further illustrate this effect by examining dynamical clones that match the present-day orbits of 29P/Schwassmann-Wachmann 1, P/2019 LD2 (ATLAS), and P/2008 CL94 (Lemmon).

*Unified Astronomy Thesaurus concepts:* Comets (280); Comet volatiles (2162); Comet nuclei (2160); Short period comets (1452); Comet dynamics (2213); Computational methods (1965)

## 1. Introduction

Jupiter-family comets (JFCs) are continuously replenished from their outer solar system reservoirs, the Kuiper Belt and the scattered disk (Fernandez 1980; Duncan et al. 1988; see distributions in Figure 1). Before JFCs enter the inner solar system, where they are typically observed on short period orbits with perihelion distances close to the Sun, they spend a significant amount of time as Centaurs (Levison & Duncan 1997; Tiscareno & Malhotra 2003). This dynamical cascade between populations, and the individual orbital tracks that these icy objects follow, can entail extensive modifications of their internal structure and composition (e.g., Gkotsinas et al. 2022, and references therein). In this context, the transient population of Centaurs is a key target for understanding progenitors of JFCs.

Recently, Sarid et al. (2019) reported that the transition from the Centaur to the JFC region involves a passage through a restricted area in the orbital elements space, described by orbits with a perihelion distance of $q > 5.4$ au and an aphelion distance of $Q < 7.8$ au, which translates into orbits with a semimajor axis of $5.2 < a < 7.8$ au and an eccentricity of $e < 0.2$. This "gateway" region has a heliocentric distance range that coincides with that where cometary nuclei are observed to be increasingly active within the giant-planet region (see the active Centaurs displayed with orange stars in Figure 1). Their dynamical models suggest that the majority of objects which eventually become JFCs transition from the Centaur population through this gateway. Subsequent work have emphasized the importance of studying the activity pattern of so-called gateway Centaurs, as they will likely transition to JFCs in relatively short timescales, becoming ideal targets to investigate how dynamical and thermal evolution alters comet nuclei before becoming JFCs (e.g., Steckloff et al. 2020; Kareta et al. 2021).

In this work, we examine the thermal processing of objects transitioning from the Centaur to the JFC region, with an emphasis on the gateway region. We use a sample of simulated JFCs (hereafter "dynamical clones"), successfully reproducing the current orbital distribution of JFCs, taken from a *N*-body simulation tracking the orbital evolution of the giant planets, and a large number of small bodies of the outer planetesimal disk (Nesvorný et al. 2017). We apply a thermal evolution model (Guilbert-Lepoutre et al. 2011) to the resulting orbital evolution tracks, in order to constrain the internal thermal structure—a method developed by Gkotsinas et al. (2022). Our goal is to assess the significance of this region for the physical properties of active Centaurs, as they evolve from the outer solar system to Jupiter-crossing orbits.

## 2. Coupled Thermal and Dynamical Evolution Study

### 2.1. Dynamical Clones

We consider in this study a sample of JFC dynamical clones generated from simulations performed by Nesvorný et al. (2017). The goal of their work was: (a) to model the formation of cometary reservoirs early in the solar system history; (b) follow their evolution up to the present time; and (c) assess how current observations of well-characterized JFCs could be used to constrain the orbital structure of the trans-Neptunian region. In order to do so, they performed end-to-end simulations, forming cometary reservoirs and letting them

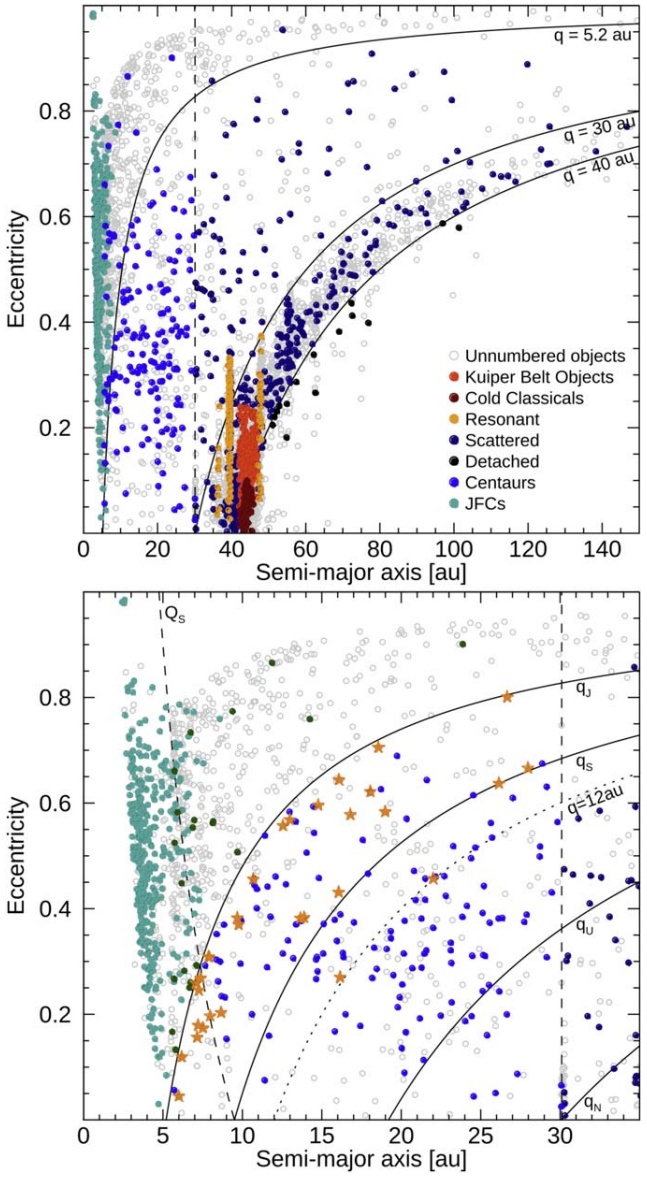


**Figure 1.** Distribution of icy objects in the solar system, from the trans-Neptunian to the JFC populations, in the semimajor axis (in au) vs. eccentricity plane. Neptune's orbit is marked by a vertical dashed line. Other lines of interest are displayed: on the top panel, the locus of perihelion distances at 5.2, 30, 40 au; on the bottom panel, the locus of perihelion distances at the giant planets and 12 au, and the locus of aphelion distance at Saturn. Orbital elements come from the JPL Solar System Dynamics database (https://ssd.jpl.nasa.gov). Active Centaurs are marked with orange stars on the bottom panel.

evolve for 4.5 Gyr. These simulations rely on a dynamical framework for the early evolution of the solar system, including the planetary migrations and instabilities which lead to the solar system as we know it now. They used the model described by Nesvorný & Morbidelli (2012), for which self-consistent simulations were performed and tested against various constraints from small body populations (e.g., asteroids, Kuiper Belt, Jupiter Trojans, and regular and irregular moons of the giant planets; Nesvorný 2018).

Nesvorný et al. (2017) calibrated their model by confronting the characteristics of their JFC dynamical clones (e.g., number and orbital element distributions) to observed comets. The observable JFCs, with a perihelion distance below 2.5 au, amount to 350–380 objects currently known and well-enough characterized to be used to perform such calibration (see also Seligman et al. 2021). For each resulting dynamical clone, they record the dynamical pathway from the time it leaves the reservoir until it is ejected out of the solar system. These trajectories can thus be used to study the dynamical and physical evolution of JFCs in a statistically significant manner. We note that non-gravitational forces were ignored. The time step for the simulations is 0.5 yr, however the trajectories themselves are recorded every 100 yr from the first time the clones reach 30 au on their way inward, out of the outer solar system's reservoirs.

### 2.2. Coupled Thermal and Orbital Evolution

For this study, we consider a total of 350 JFC dynamical clones, all of which have a perihelion distance within 2.5 au at some point in their lifetime. Coupling the thermal evolution of these clones to their orbital evolution requires making a number of assumptions to constrain their effective long-term thermal processing, which we describe below.

*Heat equation*—we use a 1D thermal evolution model derived from Guilbert-Lepoutre et al. (2011), which solves the heat diffusion equation:

$$\rho_{\rm bulk} c \frac{\partial T}{\partial t} + \mathrm{div}(-\kappa \overrightarrow{\mathrm{grad}}\, T) = \mathcal{S}, \quad (1)$$

with $\rho_{\rm bulk}$ (kg m$^{-3}$) the clone's bulk density, $c$ (J kg$^{-1}$ K$^{-1}$) the material's heat capacity, $T$ (K) the temperature, $\kappa$ (W m$^{-1}$ K$^{-1}$) the material's effective thermal conductivity, and $\mathcal{S}$ the heat sources and sinks. First, we exclude phase transitions, which we cannot track properly because they occur on timescales much smaller than the dynamical time step (Gkotsinas et al. 2022). Moreover, our thermal evolution model would require a prohibitive calculation time to solve time-dependent equations of heat transfer and gas flow in a porous medium, while accounting for multiple phase transitions, during the millions of years achieved by dynamical simulations. In Equation (1), this leads to $\mathcal{S} = 0$.

*Physical properties*—each dynamical clone is considered as a sphere with a 5 km-radius. This parameter has no influence on our results, as the only source of heating we consider is insolation of the surface. The size of clones ($R$, in m) would affect the conduction timescale $\tau = R^2 \rho_{\rm bulk} c/\kappa$ (s), which informs the time required to heat an object down to the core, and which is much longer than the orbital evolution timescale (for kilometer-sized objects). Essentially, we are interested in the processing of the subsurface layer which contributes to any activity observed today, i.e., a few hundred meters at most. All physical characteristics are assumed to remain constant through the dynamical evolution. For each parameter, we select a reference value extensively used in the literature (e.g., Prialnik et al. 2004; Huebner et al. 2006). The most critical of those is the thermal conductivity $\kappa$ (W m$^{-1}$ K$^{-1}$), which defines the fraction of heat diffusing toward the interior (see Gkotsinas et al. 2022 for the influence on the long-term processing of JFCs). Different values of the thermal conductivity ultimately result in different depths at which heat waves can penetrate below the surface, e.g., a lower conductivity induces the processing of a shallower subsurface layer. This effect does not modify the heating patterns that we describe though, nor the general conclusion, as subsequent activity generated from the

subsurface layers is also scaled with the thermal conductivity. Therefore, in the following, we only show results obtained with a thermal conductivity of $5 \times 10^{-3}\,\mathrm{W\,m^{-1}\,K^{-1}}$, a realistic value in agreement with laboratory experiments on cometary material (i.e., $0.002 < \kappa < 0.02\,\mathrm{W\,m^{-1}\,K^{-1}}$; Krause et al. 2011).

*Energy balance at the surface*—further simplifications are adopted regarding the calculation of the energy balance at the surface over the 100 yr dynamical time step. An averaged energy flux is computed at every time step, based on analytical solutions for the time-averaged energy flux received by objects in eccentric orbits (Williams & Pollard 2002; Méndez & Rivera-Valentín 2017). This averaged energy flux defines an averaged orbital distance computed as $a_{\mathrm{eq}} = a(1-e^2)$ (au), which is used in the surface boundary condition of Equation (1):

$$\frac{(1-\mathcal{A})L_{\odot}}{4\pi a_{\mathrm{eq}}^2} = \varepsilon\sigma_{\mathrm{SB}}T^4 + \kappa\frac{\partial T}{\partial r}, \tag{2}$$

with $\mathcal{A}$ the Bond's albedo, $L_{\odot}$ the solar constant, $\varepsilon$ the emissivity, and $\sigma_{\mathrm{SB}}$ the Stefan–Boltzmann constant. Diurnal and seasonal variations are not considered in our thermal simulations, as they are simply not resolved in such long-term dynamical simulations. Additional limitations arise when it comes to sharp orbital changes taking place mainly in the inner parts of the solar system, close to Jupiter and Saturn (Seligman et al. 2021): these are not resolved by the 100 yr time step in the dynamical simulation outputs. This implies that some short-scale heating episodes will go unnoticed in our thermal simulations. However, internal heating on such short timescales is likely limited to a shallow subsurface layer. Indeed, an intense but quick passage close to the Sun has a limited effect on a comet's interior than a lengthier exposure to a lesser amount of averaged energy received at the surface. Our averaging strategy over a 100 yr time step thus mitigates the effects of both short and long exposures to insolation.

## 3. Transition of Clones Between Centaurs and JFCs

### 3.1. Definition of Populations

To investigate the transition of icy objects between the Centaur and JFC populations, we first need to define the contours of these populations. To do so, we put labels on these bodies, based on cuts and thresholds in the distribution of their orbital elements, despite the clear continuity between populations (see Figure 1 for instance). In other words, these definitions do not inform, nor alter, the nature of these objects. Many definitions can be found in the literature, as recently reviewed by Seligman et al. (2021). In this study, we based our definitions for Centaurs and JFCs on the definition of the gateway as given in Sarid et al. (2019). We remind that it is introduced as orbits which do not cross the orbit of Jupiter, i.e., with a perihelion distance of $q > 5.4$ au. Objects in the gateway should also be well separated from the orbit of Saturn, i.e., they should have an aphelion distance of $Q < 7.8$ au. We thus define the Centaur population as having $5.4 < q < 30.1$ au and $5.4 < a < 30.1$ au, which is relatively similar to the comprehensive definition of Jewitt (2009). Consequently, Centaurs which are not in the gateway have $q > 5.4$ au, and $Q > 7.8$ au, and JFCs are objects with $q < 5.4$ au and $Q < 7.8$ au. With these definitions, a number of objects (or rather, orbits explored by clones) do not find any "host" population, because their orbital elements do not satisfy the thresholds to receive the corresponding label. Indeed, a number of clones transition to the JFC population from regions in the orbital space that do not fit the above cuts, due mainly to them having an $e > 0.3$ eccentricity, allowing clones with a large semimajor axis to reach Jupiter-crossing orbits. Hence, to achieve a complete description of the distribution, we define a population of Jupiter-crossers, with $q < 5.4$ au and $7.8 < Q < 14.5$ au. This 14.5 au threshold is based on the consideration that $a$ should be smaller than the semimajor axis of Saturn (so that the orbital evolution is dominated by interactions with Jupiter). We note that this category is relevant in particular for objects which never go through the gateway region during their lifetime.

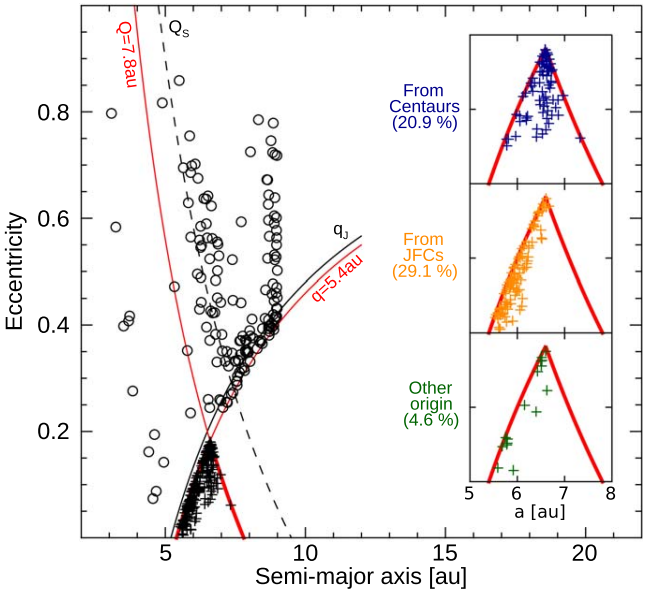


**Figure 2.** Distribution of dynamical clones in the semimajor axis vs. eccentricity plane on the first time they enter the gateway or cross Jupiter's orbit. Crosses correspond to clones (191 objects, 54.6% of the population) entering the gateway for the first time. Distributions as a function of their origin are given on the right panels (Centaurs in blue, JFCs in orange, and Jupiter-crossers in green). Circles correspond to the 159 clones (45.4%) which never go through the gateway: their distribution is given on the first time they become Jupiter-crossers before becoming JFCs.

### 3.2. To Go or Not Go Through the Gateway

With these thresholds in mind, we investigate the population of dynamical clones from Nesvorný et al. (2017) as they transition from Centaurs to JFCs. Among the 350 clones, we find that 191 objects reach the gateway region at least once in their lifetime (54.6%). Of those, 73 were Centaurs prior to entering the gateway (i.e., 20.9% of the overall clone population), while 102 objects (29.1%) were previously JFCs. In other words, these clones had already transitioned from Centaurs to JFCs without going through the gateway, which they entered then later during their lifetime. The remainder 16 clones (4.6%) entered the gateway from Jupiter-crossing orbits. The distribution of these objects is given in Figure 2.

Overall, we find that, strictly speaking, our population has only 20.9% of Centaurs which actually go through the gateway prior to becoming JFCs for the first time. Since 159 clones (45.4%) never go through the gateway at any point of their lifetime, we find that most Centaurs (79.1%) make their first

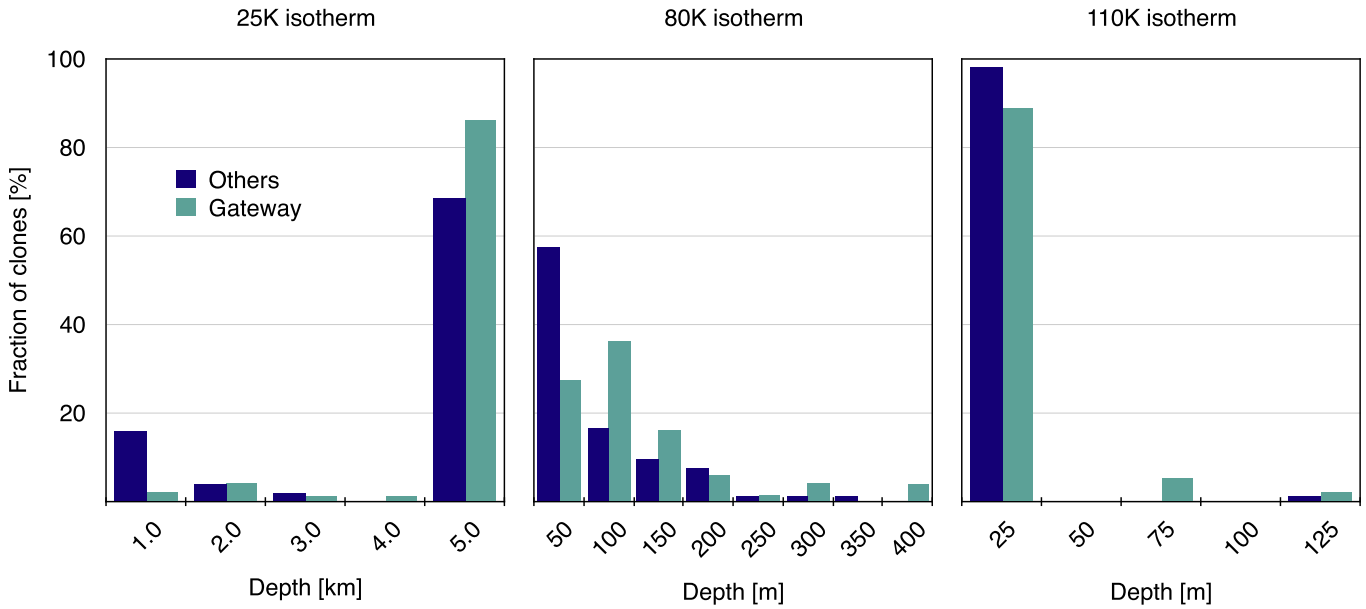


**Figure 3.** Temperature distributions for clones when they enter the gateway for the first time (teal), and clones when they first cross Jupiter prior to reaching JFC orbits (dark blue).

transition to the JFC population outside of the gateway region. As reported by Sarid et al. (2019), we find that an object—of those reaching the gateway region—can enter and exit the gateway more than once during its lifetime: the mean number of entrance is 7 to 8 times, the median is at 4 entrances though.

### *3.3. Thermal Processing of Clones in the Gateway*

In the same way as Gkotsinas et al. (2022), we assess the thermal processing of our dynamical clones in a statistical manner, by tracking the depth of three isotherms representative of key phase transitions: (a) 25 K, for the sublimation of hypervolatile species such as CO; (b) 80 K, for the sublimation of moderately volatile species such as $CO_2$; and (c) 110 K, for the crystallization of amorphous water ice. For clones which go through the gateway at some point of their lifetime, we record the depth of those isotherms the first time they enter this region: their corresponding orbital elements are shown in Figure 2. For clones which never go through the gateway, we record these depths the first time they cross the orbit of Jupiter, i.e., the first time their orbit satisfies $q < 5.4$ au and $7.8 < Q < 14.5$ au. The distribution of orbital elements of these clones in the semimajor axis versus eccentricity plane is given in Figure 2. We show the corresponding internal temperature distributions in Figure 3. We find some differences in the thermal processing of the two sub-populations, i.e., clones passing through the gateway versus clones reaching JFC orbits without ever entering the gateway in their lifetime.

Indeed, objects are statistically more processed on their first entrance in the gateway than the rest of the Centaurs when they transition to JFC orbits outside of the gateway. We applied a Mann–Whitney U non-parametric test for each isotherm: this test can be used for non-normal distributions of populations with different variances, to test the null hypothesis that two samples come from the same population. Each test confirms that the two groups are statistically different (null hypothesis rejected with a $p$-value of $10^{-6}$ for 25 K, and $10^{-8}$ for 80 and 110 K). This is mainly due to the fact that more than half of these objects (102 clones, or 53.4% of objects going through the gateway) have already been close to the Sun on JFC orbits, prior to reaching the gateway. In contrast, objects which never go through the gateway (which we call the "no-gateway" objects) are considered on their first time of crossing the orbit of Jupiter, prior to becoming JFCs in this comparison. The gateway clones are thus more processed on average than those of Centaur origin: their internal structure and composition are affected by the cumulative effect of experiencing higher temperatures in JFC orbits, and having spent more time (on average) close to the Sun. This effect was accounted for by Sarid et al. (2019) through a fading activity law.

If most dynamical clones are heated above 25 K down to the core, the no-gateway population has the largest fraction of objects able to maintain some hypervolatiles (as pure condensates) within the 1 km-subsurface layer (see Figure 3 and Table 1). Similarly, the 80 K isotherm is located on average ∼60 m below the surface for the no-gateway clones (median around 10 m), while the gateway population is heated above that temperature for more than 100 m on average (median at 60 m). The crystallization front (represented by the 110 K

**Table 1**
Depth of the 25, 80, and 110 K Isotherms for the Gateway and No-gateway Centaurs

| Gateway Centaurs (191 Objects) | | |
|---|---|---|
| Isotherm | Average depth (m) | Median depth (m) |
| 25 K | 4760 | 5000 |
| 80 K | 110 | 61 |
| 110 K | 20 | 4.4 |
| **No-gateway Centaurs (159 objects)** | | |
| Isotherm | Average depth (m) | Median depth (m) |
| 25 K | 3810 | 5000 |
| 80 K | 62 | 11 |
| 110 K | 4.2 | 0.25 |

**Note.** The averages and medians are computed from the temperature distributions shown in Figure 3.

isotherm) remains close to the surface for both sub-populations, although more objects in the gateway experience crystallization below 50–100 m than the no-gateway objects.

## 4. Implication for Individual Objects

### 4.1. Context of Active Centaurs

As of today, the origin of Centaurs' activity has not been definitively identified, and different processes may be involved for different individual objects (e.g., Prialnik et al. 1995; Capria et al. 2000; De Sanctis et al. 2000). Crystallization of amorphous water ice appears as a phase transition of choice to trigger activity, given the physical and orbital properties of active Centaurs (Jewitt 2009; see also Figure 1): indeed, currently known active Centaurs are too cold for water ice to sublimate, while the sublimation of other species such as CO or $CO_2$ would imply that activity should be observed even further out in the giant-planet region. Overall, Guilbert-Lepoutre (2012) suggested that the activity of Centaurs seems tightly linked to their orbit: as amorphous water ice crystallization progresses inward below the surface, sustained cometary activity fades with time. A change in surface energy balance (e.g., due to a drop in perihelion distance) is thus required to trigger a subsequent new spurt of activity. Davidsson (2021) argued that the sublimation and segregation of $CO_2$ may additionally play some role to explain the level of activity observed in the 10–12 au region.

Fernández et al. (2018) studied the dynamical evolution of both active and inactive Centaurs. They found that active Centaurs are prone to drastic drops in their perihelion distances, with a timescale of $10^2$–$10^3$ yr. The thermal results of Guilbert-Lepoutre (2012) are consistent with these timescales, as they suggested that a change in orbital elements might be required to trigger phase transitions, ensuing the adjustment to new thermal conditions. We note that searches for activity among recently discovered Centaurs have failed (e.g., Cabral et al. 2019; Li et al. 2020; Lilly et al. 2021), however, targeted objects are found on relatively stable orbits beyond Saturn, where no significant activity would be expected from the aforementioned processes.

With these considerations in mind, we find it relevant to study the coupled thermal and dynamical evolution of individual objects before they evolve to the orbit in which they are currently observed, to inform their possible past history and activity. We put an emphasis on the 80 and 110 K isotherms, representative of $CO_2$ sublimation and amorphous to crystalline phase transitions, respectively.

### 4.2. Selecting Clones for Centaurs of Interest

The study of gateway Centaurs has focused so far on two specific objects, 29P/Schwassmann-Wachmann 1 and P/2019 LD2 (ATLAS) (hereafter 29P and LD2, respectively; Sarid et al. 2019; Steckloff et al. 2020; Hsieh et al. 2021; Kareta et al. 2021; Seligman et al. 2021). In light of the results presented above, we provide some insight on the coupled thermal and dynamical evolution of the clones of these two bodies. We have added P/2008 CL94 (Lemmon) in this work (hereafter CL94), since it is an active Centaur currently located in the gateway (Kulyk et al. 2016). Clones of a specific object can be selected from the whole population by defining "boxes" around the values of the currently observed semimajor axis $a$, eccentricity $e$, and inclination $i$. For each orbital element, we define an acceptable range of tolerance where our dynamical clones can fall: the larger the acceptable range, the larger the number of clones that will satisfy the conditions at some point of their orbital evolution. We typically allow $\pm 0.05$ au for the semimajor axis, $\pm 0.05$ for the eccentricity, and $\pm 1°$ for the inclination. For each of the three objects mentioned above, we thus define the following "boxes":

29P $5.95 < a < 6.05$ au
$0.01 < e < 0.09$
$8.73 < i < 10.^{\circ}73$

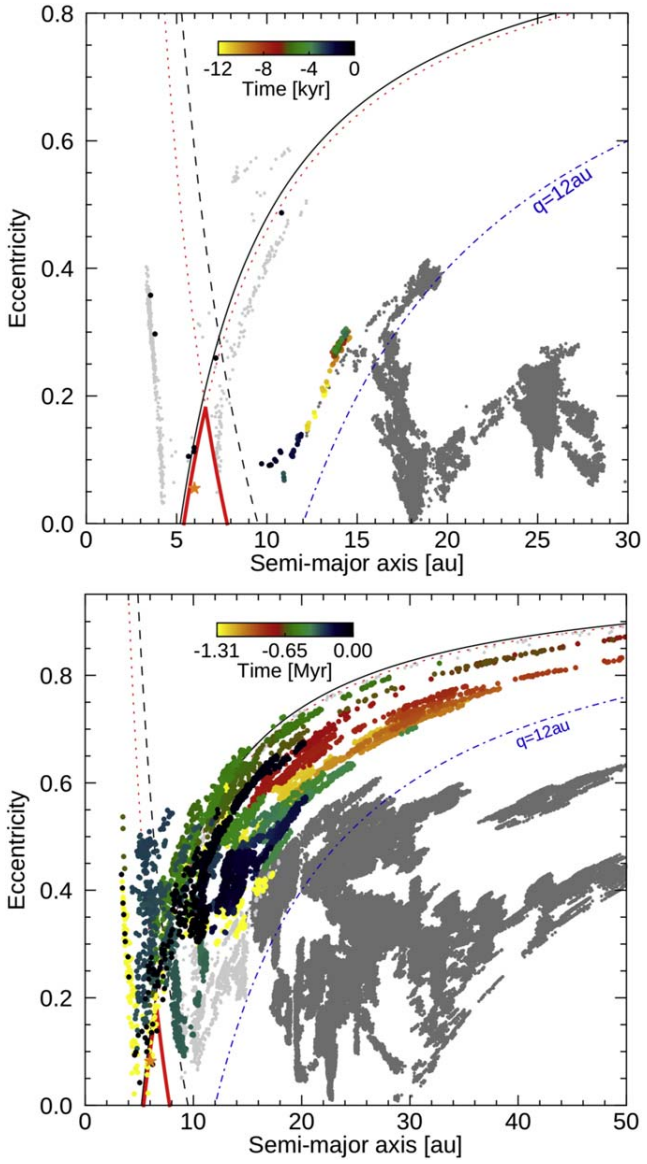


**Figure 4.** Orbital evolution of two clones of comet 29P in the eccentricity–semimajor axis plane. The clone from the top panel underwent relatively little heating before approaching the orbit of comet 29P, whereas the clone from the bottom panel was strongly heated during close passages to the Sun. One data point is given every 100 yr of dynamical evolution: the color code provides the time evolution for the duration subsequently displayed in Figure 8. The orbital evolution prior and after this time subset is shown in dark and light gray, respectively. The black solid line shows orbits with a perihelion distance of 5.2 au, the black dashed line shows orbits with an aphelion distance of 9.4 au, and the red lines provide the limits of the gateway. The blue dotted–dashed line shows orbits with a perihelion distance of 12 au.

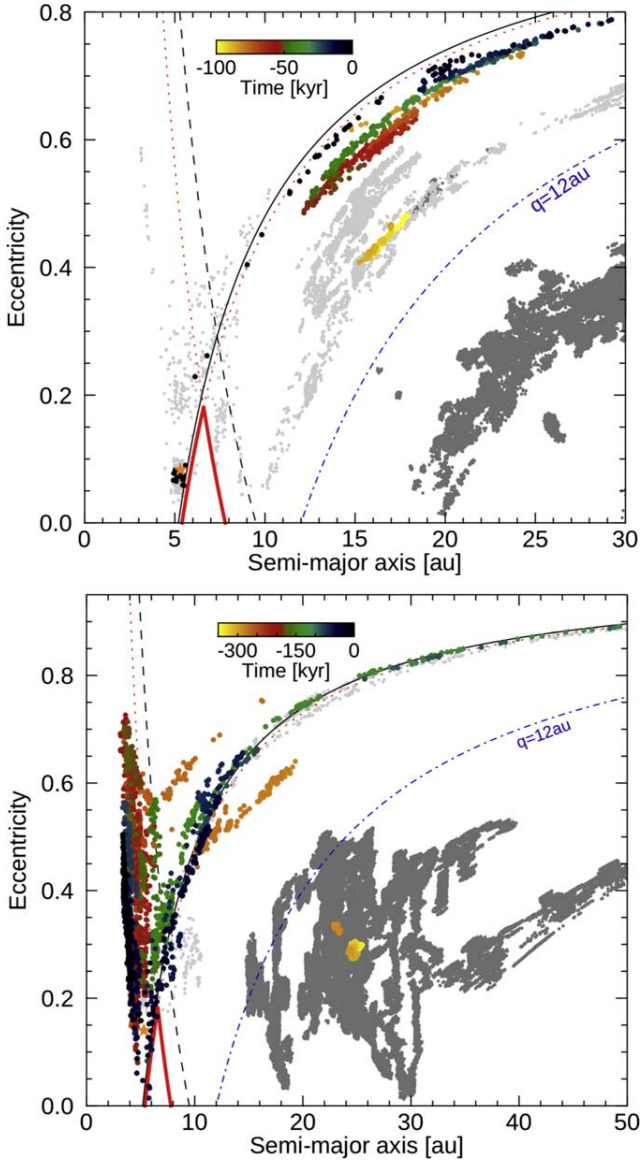


**Figure 5.** Orbital evolution of two clones of comet LD2 in the eccentricity–semimajor axis plane. As in Figure 4, the clone from the top panel underwent relatively little heating before approaching the orbit of comet LD2, whereas the clone from the bottom panel was strongly heated during close passages to the Sun. One data point is given every 100 yr of dynamical evolution: the color code provides the time evolution for the duration subsequently displayed in Figure 9. The orbital evolution prior and after this time subset is shown in dark and light gray, respectively. The black solid line shows orbits with a perihelion distance of 5.2 au, the black dashed line shows orbits with an aphelion distance of 9.4 au, and the red lines provide the limits of the gateway. The blue dotted–dashed line shows orbits with a perihelion distance of 12 au.

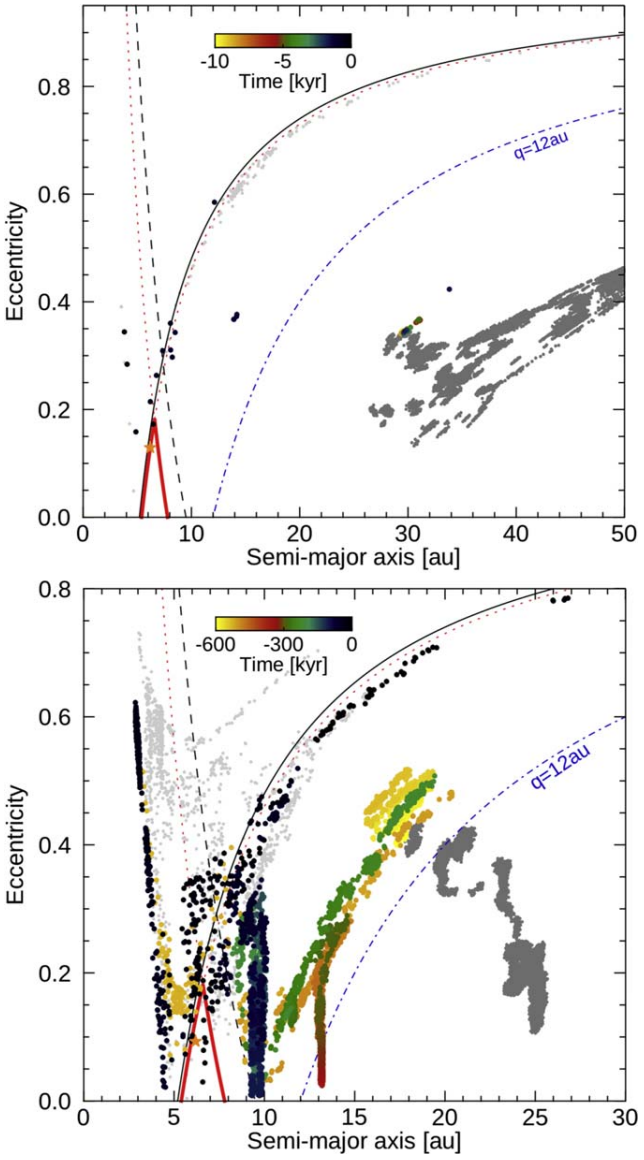


**Figure 6.** Orbital evolution of two clones of comet CL94 in the eccentricity–semimajor axis plane. As in Figure 4, the clone from the top panel underwent relatively little heating before approaching the orbit of comet CL94, whereas the clone from the bottom panel was strongly heated during close passages to the Sun. One data point is given every 100 yr of dynamical evolution: the color code provides the time evolution for the duration subsequently displayed in Figure 10. The orbital evolution prior and after this time subset is shown in dark and light gray, respectively. The black solid line shows orbits with a perihelion distance of 5.2 au, the black dashed line shows orbits with an aphelion distance of 9.4 au, and the red lines provide the limits of the gateway. The blue dotted–dashed line shows orbits with a perihelion distance of 12 au.

LD2 $5.24 < a < 5.34$ au
$0.08 < e < 0.18$
$10.56 < i < 12.^{\circ}56$
CL94 $6.10 < a < 6.20$ au
$0.07 < e < 0.17$
$7.3 < i < 9.^{\circ}3$

We find 10 clones which at some point of their lifetime had orbital elements similar to the observed 29P and LD2. For CL94, we find 21 clones whose orbital elements satisfy the conditions at some point of their lifetime. In the following, we only consider the orbital history of each object before it evolves into the relevant box as a proxy for the past orbital history of each Centaur. As a sanity check, we have searched for clones of each known active Centaur (i.e., 31 additional Centaurs, as displayed in Figure 1 bottom panel), with the same accepted range for each orbital element. For each active Centaur, we find a number of clones that satisfy our conditions: on average 18 clones per object, ranging from 2 clones for C/2012 Q1 (Kowalski) to 50 clones for P/2010 C1 (Scotti) (median at 14). We thus conclude that there is nothing particular with the orbital boxes defined for 29P, LD2, or CL94 that would have led to a significantly different number of

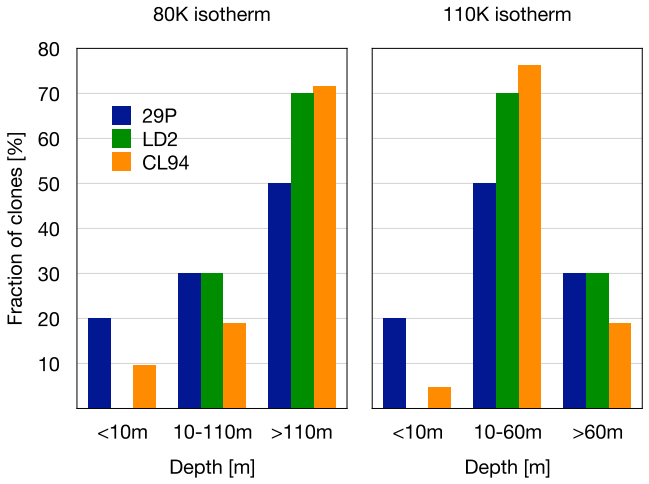


**Figure 7.** Temperature distributions of the clones of 29P (blue), LD2 (green), and CL94 (orange).

clones than the rest of the active objects in the giant-planet region.

### *4.3. Orbital Considerations*

For our three objects, several features of interest are observed. First, the lifetimes of clones span a wide range of values. For 29P, some clones transition from 30 au to the box as fast as ∼4.5 Myr, while others take much longer than 100 Myr to reach 29P's orbit from the outer solar system (the longest being 375.5 Myr). For LD2, the dynamical timescales range from 16.6 to 480.5 Myr, and for CL94, the lifetime range is even larger: from 9.3 to 878.1 Myr. Figures 4, 5, and 6 provide details on the evolution of the orbital elements of the clones of 29P, LD2, and CL94, respectively, before they enter the designated box. The dynamical behavior of each clone is unique and chaotic, with sometimes long periods spent in regions where phase transitions would be expected to occur (see Guilbert-Lepoutre 2012; Davidsson 2021; and Figures 4–6). Second, we see that before entering the designated box, most clones explored orbits with lower perihelion distances (either as JFCs or Jupiter-crossers). Indeed, once their orbital evolution is dominated by gravitational interactions with Jupiter, changes in the perihelion distance become more frequent and chaotic. Third, some clones can enter the orbital box defined for each object several times during their lifetime. Furthermore, we notice that clones can enter the orbital box of two different objects throughout their lifetime. For instance, we have one clone in common between 29P and LD2, three clones in common between 29P and CL94, and two clones in common between LD2 and CL94.

### *4.4. Thermal Evolution and Internal Structure*

Clones of individual objects experience a variety of timescales of residency in the giant-planet region, and of variations in orbital elements. This inevitably entails a diversity in thermal processing. The relationship between timescale and thermal processing is not straightforward though, and is clearly dependent upon the unique orbital track followed by each clone. In order to assess the degree of processing of each individual clone, we record the depth of the two isotherms of interest: their distributions in depth for clones of our three objects are shown in Figure 7. Visualizing how the heat propagates below the surface is also informative, so we show in Figures 8, 9, and 10 two examples of thermal evolution coupled to the dynamical evolution for clones of 29P, LD2, and CL94, respectively. These correspond to clones whose orbital evolutions are presented in Figures 4–6. For each Centaur of interest, we have selected one clone arriving relatively unaltered in the designated box, and one comparatively thermally processed clone.

Centaur 29P is the object, among our three, with the largest fraction of relatively unaltered clones: two of them, despite having quite long lifetimes (∼29 and 76.7 Myr, respectively), reach the 29P current position with an unaltered composition. Their interiors are barely heated above 80 K in the upper 10 m. Three clones have 80 and 110 K isotherms located around 50 and 10 m deep, respectively, while half of the 29P clones have been processed to the extent that the 110 K isotherm is located below 50 m, and the 80 K isotherm below 100 m or more (up to ∼360 m). For the clones of LD2, the depths for the 80 and 110 K isotherms are statistically greater than for 29P, since no LD2 clone reaches the orbital box as unprocessed as the two 29P clones mentioned above. Of the 10 clones of LD2, all are thus moderately to substantially processed, with the 80 and 110 K isotherms found at least below 10 m, and mostly below 100 m for the 80 K isotherm. For the two most-processed clones, with two different lifetimes of more than 480 Myr versus 40 Myr, the 80 K isotherm is located beyond 400 m when they arrive in the LD2 orbital box. Of the CL94 clones, only one remains relatively unprocessed (with the 80 and 110 K isotherms within the uppermost 10 m), while for most the 80 and 110 K isotherms are located beyond 110 m and 60 m, respectively.

## 5. Discussion

### *5.1. On Transitioning Through the Gateway*

By means of forward modeling of the dynamical cascade from trans-Neptunian Objects to JFCs, Sarid et al. (2019) suggested that a specific dynamical pathway should facilitate the transition between the Centaur and JFC populations. They found that 21% of Centaurs transition to JFC orbits through the gateway (30% when adding the gravitational perturbations from inner solar system planets). Because of stochastic gravitational perturbations from Jupiter, objects can jump in and out of the giant-planet region several times in their lifetime, so that more than $3/4$ of them would eventually go through the gateway, or nearly half of objects with a perihelion distance smaller than 3 au.

We use a sample of simulated active and visible JFCs, all with perihelion distances smaller than 2.5 au at some point in their lifetime. Our results can be directly compared with those of Sarid et al. (2019), as they provide statistics for clones reaching $q < 3$ au. They find that nearly half of those clones spend some time in the gateway, which is consistent with the 54.6% of clones we find. In terms of pure dynamical pathways, our results are thus completely aligned with those of Sarid et al. (2019).

However, when it comes to the pristine nature of these objects, the thermal processing sustained prior to their passage in the gateway, and hence the direction from which they enter the gateway, matters. When we constrain the origin of clones the first time they reach the gateway, we find that, strictly speaking, our population has only 20.9% of Centaurs which

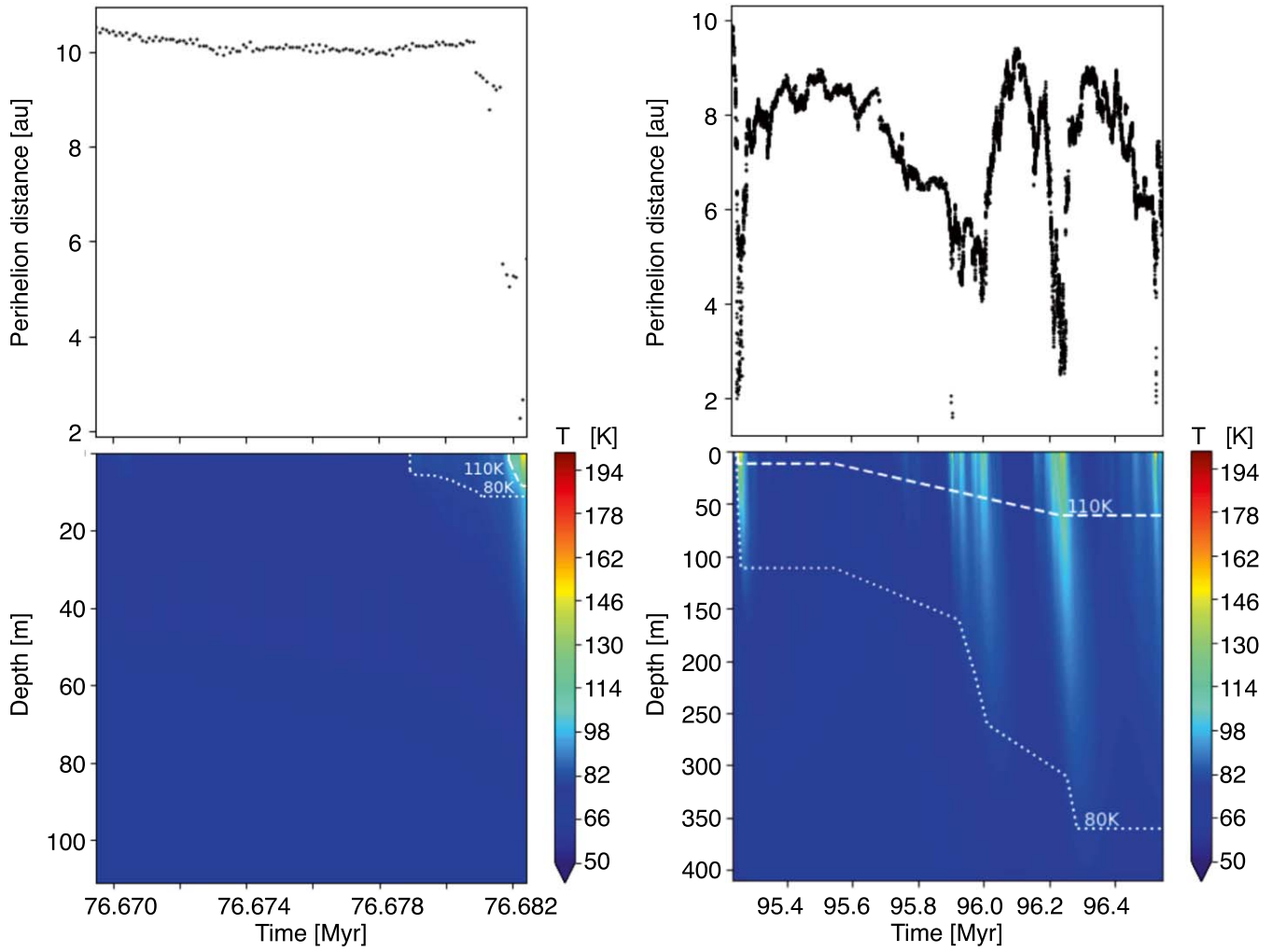


**Figure 8.** Distribution of the internal temperature as a function of depth and time for two clones of 29P, resulting from orbital evolution. The top panels show the evolution of the perihelion distance as a function of time. The bottom panels show the resulting evolution of the internal temperature. The least-processed clone of 29P is shown on the left. The timeline focuses on the last 100 kyr of thermal and dynamical evolution, before the clone's orbital elements match those of 29P. On the right, one of the most-processed clone is shown: the timeline focuses on the last 1 Myr of thermal and dynamical evolution, before the clone's orbital elements match those of 29P. The maximum depths of the 80 and 110 K isotherms are shown with a white dotted and dashed line, respectively.

actually go through the gateway prior to becoming JFCs for the first time, again consistent with Sarid et al. (2019). Since 159 clones (45.4%) never go through the gateway at any point of their lifetime, we find that most Centaurs (79.2%) transition from the giant-planet region to the JFC population outside of the gateway region.

As a result, objects in the gateway are statistically more prone to being thermally processed than other Centaurs crossing the orbit of Jupiter for the first time, because a higher fraction of gateway objects have already been processed as JFCs. Guilbert-Lepoutre et al. (2016) suggested that typical JFCs could have their subsurface altered down to a few hundred meters before entering the inner solar system. Gkotsinas et al. (2022) found that due to the stochastic nature of comet trajectories toward the inner solar system, JFCs can experience multiple heating events resulting in substantial chemical alteration of their upper layers, down to several hundred meters. Accessing material below this depth would require the cumulative erosion effect of multiple perihelion passages as JFCs (typically a few meters per perihelion passage; Prialnik et al. 2004; Huebner et al. 2006). Therefore, for most JFCs, outgassing observed today might occur from a layer thermally altered during the Centaur stage. Because several transitions between the Centaur and the JFC populations are possible (Sarid et al. 2019; Gkotsinas et al. 2022; and this work), the cumulative effect of multiple transitions should lead to a complex internal structure and composition. Our results suggest that statistically, there is a ∼50% chance that any object in the gateway is one of these processed bodies.

### 5.2. On Objects Currently in the Gateway

To illustrate the latter point, we focused on three objects of interest: Centaur 29P/Schwassmann-Wachmann 1 and comets P/2019 LD2 (ATLAS) and 423P/Lemmon (2008 CL94) currently residing in the gateway. For the first two, the dynamical evolution of many dynamical clones was integrated backwards in time (Sarid et al. 2019; Steckloff et al. 2020). This method can only inform a recent past, typically hundreds to thousands of years, before stochastic gravitational interactions with Jupiter make clones diverge. These backward integrations suggest that it is unlikely they should have spent any significant amount of time in the inner solar system. As a

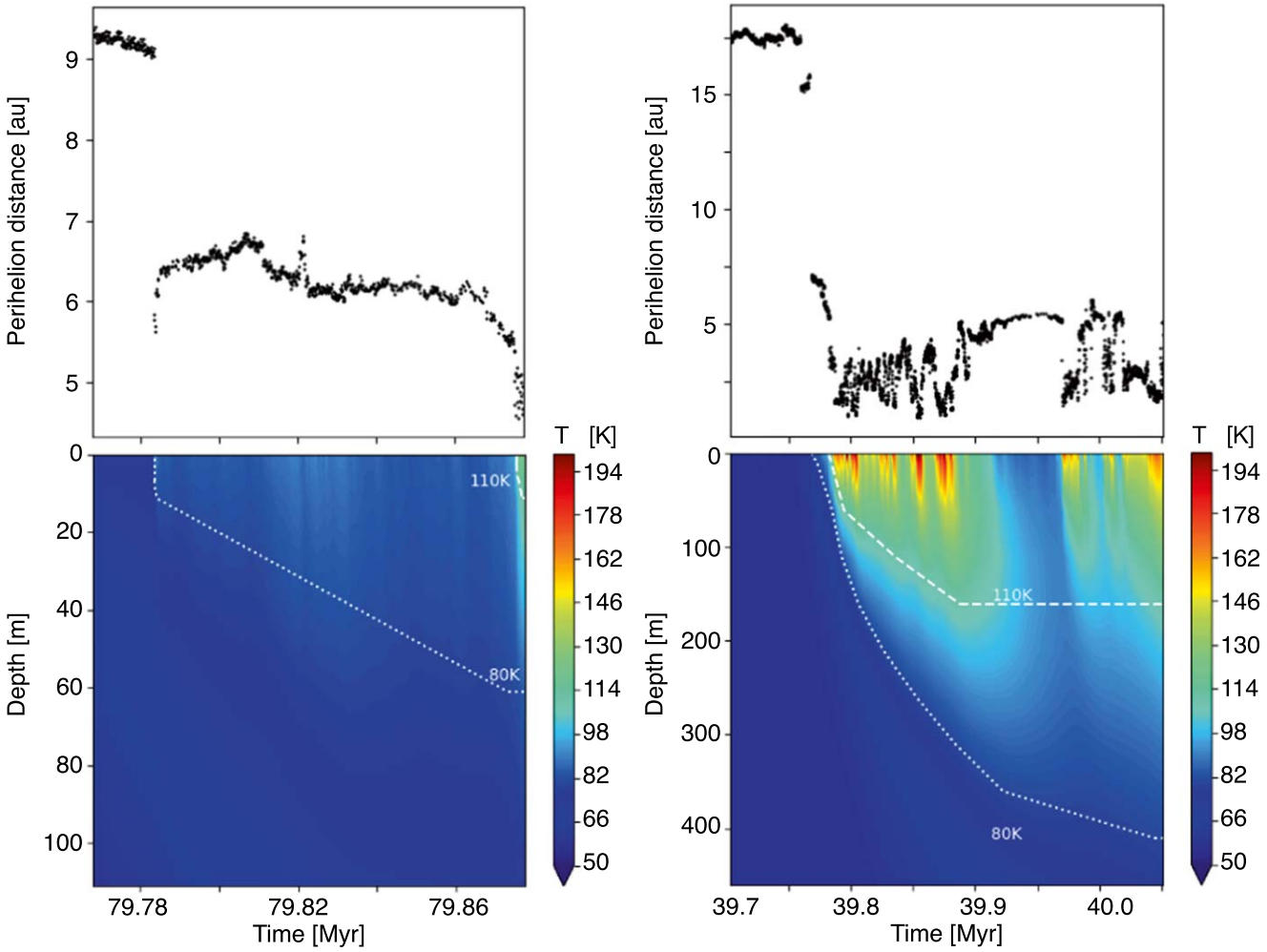


**Figure 9.** Distribution of the internal temperature as a function of depth and time for two clones of LD2, resulting from orbital evolution. The top panels show the evolution of the perihelion distance as a function of time. The bottom panels show the resulting evolution of internal temperature. The least-processed clone of LD2 is shown on the left. The timeline focuses on the last 100 kyr of thermal and dynamical evolution, before the clone's orbital elements match those of LD2. On the right, one of the most-processed clone is shown: the timeline focuses on the last 300 kyr of thermal and dynamical evolution, before the clone's orbital elements match those of LD2. The maximum depths of the 80 and 110 K isotherms are shown with a white dotted and dashed line, respectively.

result, they should not have experienced any significant thermophysical evolution, and their current activity would be representative of nearly pristine objects.

Our results stem from a different methodology, arguably the only reliable strategy, i.e., forward modeling of the dynamical evolution (Morbidelli et al. 2020). Our statistics are necessarily limited, given the number of clones for 29P and LD2 in particular. However, there are issues in using backward integrations to investigate the evolution of solar system objects, as detailed by Morbidelli et al. (2020). Therefore, even if the JFC clones from Nesvorný et al. (2017) yield a smaller number of clones for each individual object of interest compared to the aforementioned studies, the overall sample has strengths that cannot be excluded. For instance, our results span a much longer period, since our dynamical tracks follow objects from the time they leave the trans-Neptunian region for several million to hundred million years. Our analysis justifies that a broad look at the time spent in the giant-planet region is not sufficient for assessing the thermal evolution of Centaurs. Instead, the detailed orbital evolution, and the resulting thermal processing, must be constrained for each object. We find that each object of interest has a higher than 50% chance that the layer currently contributing to its observed activity has been physically and chemically altered, due to thermal processing sustained during previous stages of evolution.

### 5.3. Significance for the Centaur and JFC Populations

Understanding the mechanisms at the origin of Centaurs' activity is paramount to comprehend fully the extent of the post-formation thermal processing of JFCs. Current impediments for fulfilling that goal come, on one hand, from a lack of volatile detection in their coma. No strong detection of gaseous CO has been made to date (e.g., Drahus et al. 2017), except for 29P (Senay & Jewitt 1994; Crovisier et al. 1995; Gunnarsson et al. 2008; Wierzchos & Womack 2020). CO was marginally detected in the coma of 2060 Chiron at 8.5 au (Womack & Stern 1999; Womack et al. 2017), as well as in the coma of 174P/Echeclus during an outburst at 6.1 au (Wierzchos et al. 2017). These observations are consistent with the activity of Centaurs not being driven by the sublimation of CO, but such a limited data set does not allow one to constrain phase transitions at the source of outgassing from nuclei. This may be due to current observational sensitivities, which will

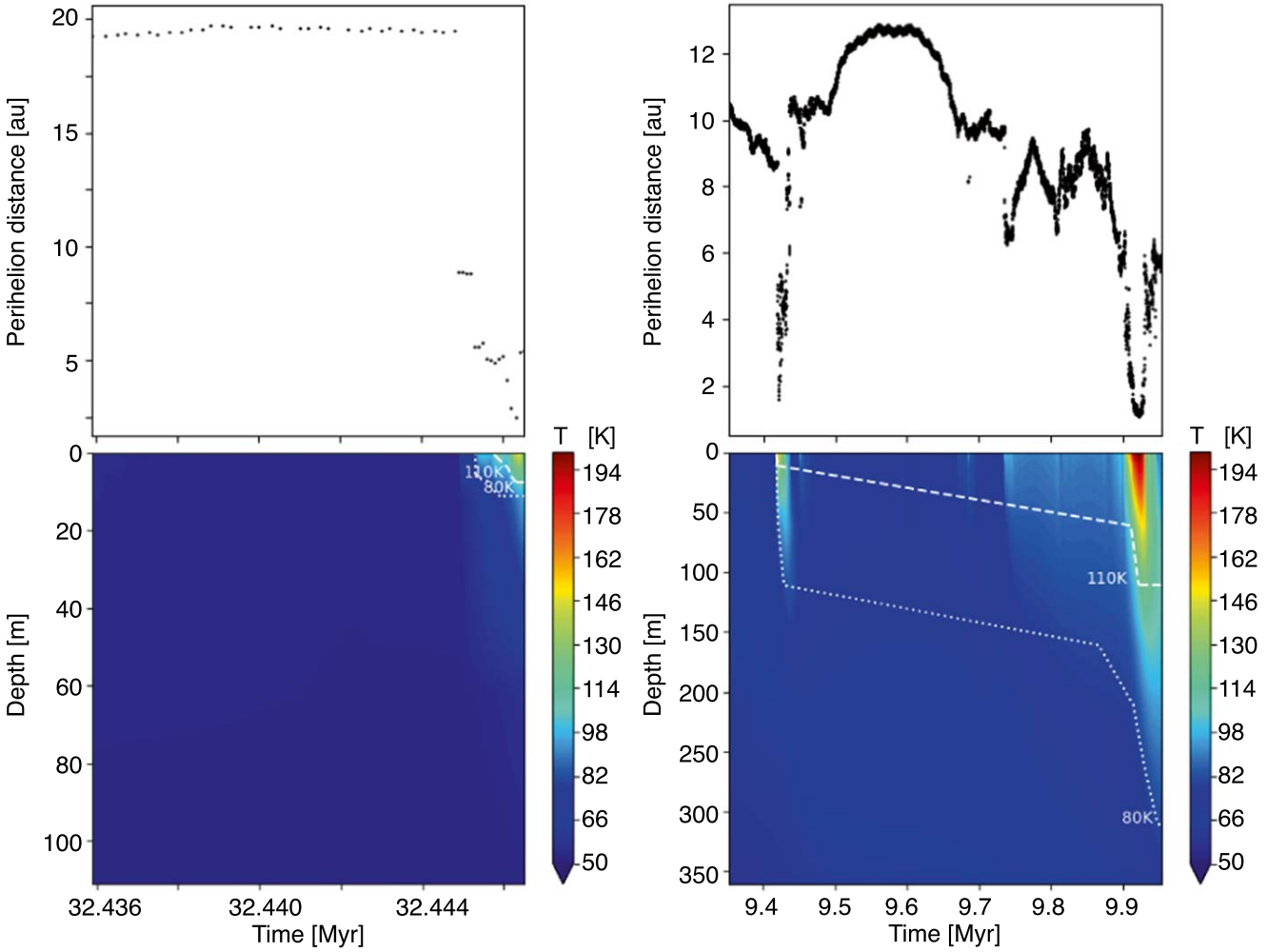


**Figure 10.** Distribution of the internal temperature as a function of depth and time for two clones of CL94, resulting from orbital evolution. The top panels show the evolution of perihelion distance as a function of time. The bottom panels show the resulting evolution of internal temperature. The least-processed clone of CL94 is shown on the left, with a lifetime of ∼32.4 Myr. The timeline focuses on the last 10 kyr of thermal and dynamical evolution, before the clone's orbital elements match those of CL94. On the right, the most-processed clone is shown, with a short lifetime (∼10 Myr). The timeline focuses on the last 500 kyr of thermal and dynamical evolution, before the clone's orbital elements match those of CL94. The maximum depths of the 80 and 110 K isotherms are shown with a white dotted and dashed line, respectively.

improve in the JWST and Atacama Large Millimeter/submillimeter Array (ALMA) era. On the other hand, Cabral et al. (2019) argued that we currently do not have an appropriate data set to constrain the origin of Centaurs' activity, because no survey has ever been dedicated to this population. Compared to trans-Neptunian objects, Centaurs have a different detectability in motion rate-dependent surveys. For instance, a survey such as the Outer Solar System Origins Survey (OSSOS; Bannister et al. 2016) has an observation cadence biased toward detecting dynamically stable orbits beyond Saturn (Tiscareno & Malhotra 2003; Di Sisto et al. 2010). As of today, no survey has adequately targeted the motion rate of objects in the 5–12 au region, where Centaurs with more unstable orbits can be found, and active Centaurs are currently observed, in a well-characterized manner.

As for any Centaur or JFC, the activities of 29P, LD2, and CL94 reflect the composition and structure inherited from their previous stages of evolution. As such, our results suggest that current outgassing likely arises from a layer significantly altered prior to observations. Depending on the thermophysical parameters, compositions, and other poorly constrained properties, it is still possible that the effects of such thermal processing could be limited to a modest near-surface layer, for 29P in particular. Because the degree of activity, reflected, for example, by production rates, may not be straightforwardly linked to the degree of processing experienced by comets prior to current observations, it is important to remain cautious when claiming that any active Centaur is representative of a pristine nucleus. Our results suggest that objects in the gateway may not have a particular significance, compared to other active Centaurs, for a better understanding of this population or the onset and development of activity in the giant-planet region. In any case, some caution ought to be applied when claiming that gateway Centaurs and their activity are representative of the onset of activity experienced by supposedly pristine objects, prior to their transition into JFC orbits

## 6. Summary

We aim to constrain the internal thermal structure resulting from the orbital evolution of Centaurs, prior to their transition in the JFC region, and whether this transition occurs through

the gateway or not. We use simulation outcomes of the coupled thermal and dynamical evolution from Gkotsinas et al. (2022), for a population of JFC clones from Nesvorný et al. (2017). We find that:

1. Only ∼20% Centaurs go through the gateway prior to transitioning into JFC orbits. Most Centaurs in our sample make their first transition to the JFC population from outside of this region.
2. More than half of the dynamical clones entering the gateway for the first time have already been JFCs. Statistically, objects in the gateway are thus more processed than the rest of the objects when they start transitioning into JFC orbits.
3. 29P/Schwassmann-Wachmann1, P/2019 LD2 (ATLAS), and P/2008 CL94 (Lemmon) have a higher than 50% chance to be thermally processed. As a result, the layer currently contributing to their observed activity could be physically and chemically altered, and not representative of the initial state of these objects.

We thank Darryl Seligman for his excellent review of our work, helping us to improve this manuscript. We warmly thank members of the International Space Science Institute (ISSI) team led by Rosita Kokotanekova, for constructive discussions on the Centaur population. This study is part of a project that has received funding from the European Research Council (ERC) under the European Union's Horizon 2020 research and innovation program (grant agreement No. 802699). We gratefully acknowledge support from the PSMN (Pôle Scientifique de Modélisation Numérique) of the ENS de Lyon for computing resources.

*Facilities:* PSMN, ENS de Lyon.

## Appendix

To illustrate the diversity of dynamical behaviors, we show in Figures 11, 12, and 13 the evolution of the perihelion distance for nine clones of 29P, LD2, and CL94, respectively.

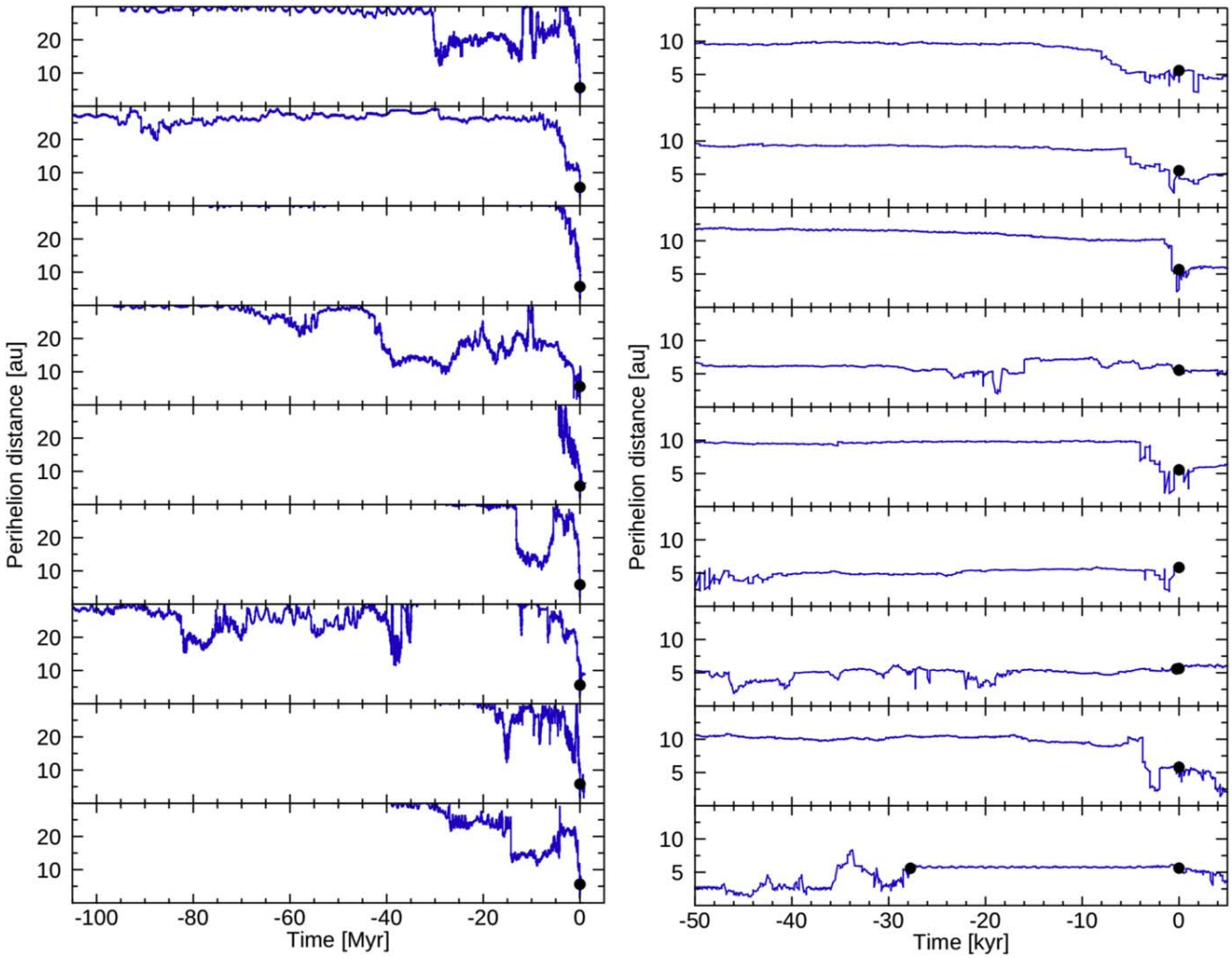


**Figure 11.** Evolution of the perihelion distance for nine clones of 29P, within the last 100 Myr (left) and 50 kyr (right) of their orbital evolution toward "becoming" 29P—marked as black dots. Reference time 0 is chosen as the last time the clone enters the "29P box" of accepted orbital elements.

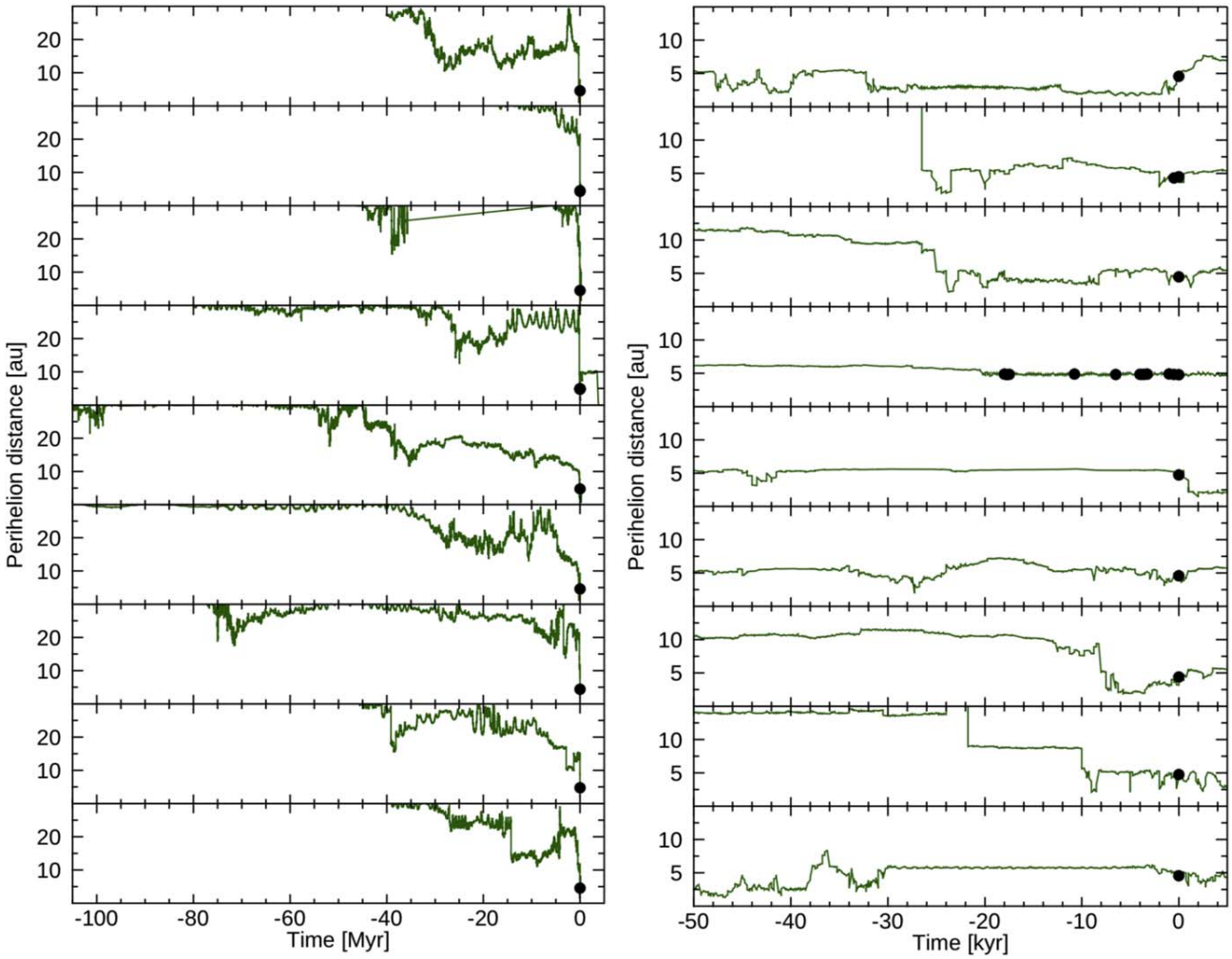


**Figure 12.** Evolution of the perihelion distance for nine clones of LD2, within the last 100 Myr (left) and 50 kyr (right) of their orbital evolution toward "becoming" LD2—marked as black dots. Reference time 0 is chosen as the last time the clone enters the "LD2 box" of accepted orbital elements.

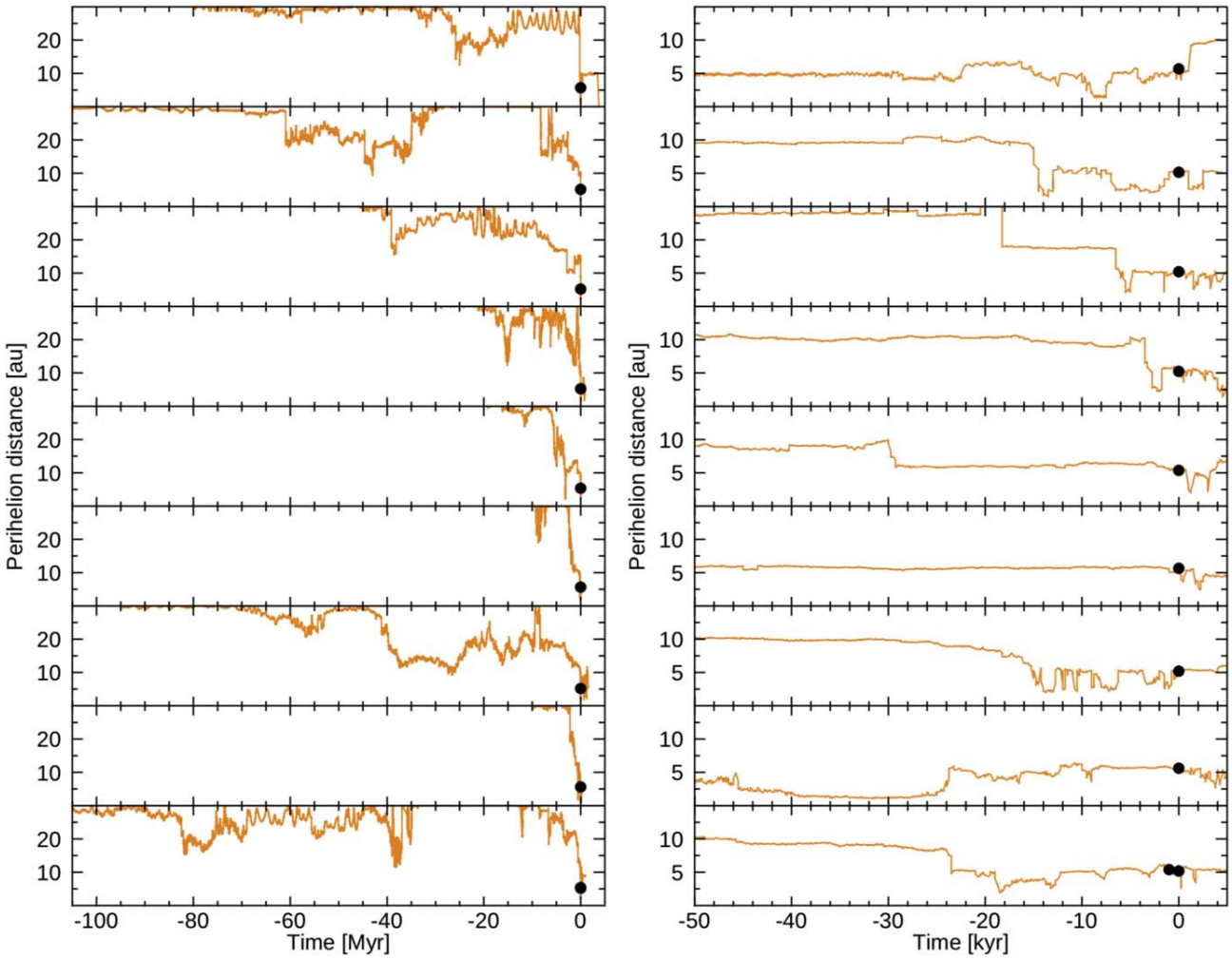


**Figure 13.** Evolution of the perihelion distance for nine clones of CL94, within the last 100 Myr (left) and 50 kyr (right) of their orbital evolution toward "becoming" CL94—marked as black dots. Reference time 0 is chosen as the last time the clone enters the "CL94 box" of accepted orbital elements.

## ORCID iDs

Aurélie Guilbert-Lepoutre https://orcid.org/0000-0003-2354-0766
Anastasios Gkotsinas https://orcid.org/0000-0002-1611-0381
Sean N. Raymond https://orcid.org/0000-0001-8974-0758
David Nesvorny https://orcid.org/0000-0002-4547-4301

## References

Bannister, M. T., Kavelaars, J. J., Petit, J.-M., et al. 2016, AJ, 152, 70
Cabral, N., Guilbert-Lepoutre, A., Fraser, W. C., et al. 2019, A&A, 621, A102
Capria, M. T., Coradini, A., De Sanctis, M. C., & Orosei, R. 2000, AJ, 119, 3112
Crovisier, J., Biver, N., Bockelee-Morvan, D., et al. 1995, Icar, 115, 213
Davidsson, B. J. R. 2021, MNRAS, 505, 5654
De Sanctis, M. C., Capria, M. T., Coradini, A., & Orosei, R. 2000, AJ, 120, 1571
Di Sisto, R. P., Brunini, A., & de Elía, G. C. 2010, A&A, 519, A112
Drahus, M., Yang, B., Lis, D. C., & Jewitt, D. 2017, MNRAS, 468, 2897
Duncan, M., Quinn, T., & Tremaine, S. 1988, ApJL, 328, L69
Fernandez, J. A. 1980, Icar, 42, 406
Fernández, J. A., Helal, M., & Gallardo, T. 2018, P&SS, 158, 6
Gkotsinas, A., Guilbert-Lepoutre, A., Raymond, S. N., & Nesvorny, D. 2022, ApJ, 928, 43
Guilbert-Lepoutre, A. 2012, AJ, 144, 97
Guilbert-Lepoutre, A., Lasue, J., Federico, C., et al. 2011, A&A, 529, A71
Guilbert-Lepoutre, A., Rosenberg, E. D., Prialnik, D., & Besse, S. 2016, MNRAS, 462, S146
Gunnarsson, M., Bockelée-Morvan, D., Biver, N., Crovisier, J., & Rickman, H. 2008, A&A, 484, 537
Hsieh, H. H., Fitzsimmons, A., Novaković, B., Denneau, L., & Heinze, A. N. 2021, Icar, 354, 114019
Huebner, W. F., Benkhoff, J., Capria, M.-T., et al. 2006, Heat and Gas Diffusion in Comet Nuclei (International Space Science Institute) (Noordwijk: ESA)
Jewitt, D. 2009, AJ, 137, 4296
Kareta, T., Woodney, L. M., Schambeau, C., et al. 2021, PSJ, 2, 48
Krause, M., Blum, J., Skorov, Y., & Trieloff, M. 2011, Icar, 214, 286
Kulyk, I., Korsun, P., Rousselot, P., Afanasiev, V., & Ivanova, O. 2016, Icar, 271, 314
Levison, H. F., & Duncan, M. J. 1997, Icar, 127, 13
Li, J., Jewitt, D., Mutchler, M., Agarwal, J., & Weaver, H. 2020, AJ, 159, 209
Lilly, E., Hsieh, H., Bauer, J., et al. 2021, PSJ, 2, 155
Méndez, A., & Rivera-Valentín, E. G. 2017, ApJL, 837, L1
Morbidelli, A., Batygin, K., Brasser, R., & Raymond, S. N. 2020, MNRAS Lett., 497, L46
Nesvorný, D. 2018, ARA&A, 56, 137
Nesvorný, D., & Morbidelli, A. 2012, AJ, 144, 117
Nesvorný, D., Vokrouhlický, D., Dones, L., et al. 2017, ApJ, 845, 27
Prialnik, D., Benkhoff, J., & Podolak, M. 2004, Modeling the Structure and Activity of Comet Nuclei (Tucson, AZ: Univ. Arizona Press), 359
Prialnik, D., Brosch, N., & Ianovici, D. 1995, MNRAS, 276, 1148
Sarid, G., Volk, K., Steckloff, J. K., et al. 2019, ApJL, 883, L25
Seligman, D. Z., Kratter, K. M., Levine, W. G., & Jedicke, R. 2021, PSJ, 2, 234
Senay, M. C., & Jewitt, D. 1994, Natur, 371, 229
Steckloff, J. K., Sarid, G., Volk, K., et al. 2020, ApJL, 904, L20
Tiscareno, M. S., & Malhotra, R. 2003, AJ, 126, 3122
Wierzchos, K., & Womack, M. 2020, AJ, 159, 136
Wierzchos, K., Womack, M., & Sarid, G. 2017, AJ, 153, 230
Williams, D. M., & Pollard, D. 2002, IJAsB, 1, 61
Womack, M., Sarid, G., & Wierzchos, K. 2017, PASP, 129, 031001
Womack, M., & Stern, S. A. 1999, SoSyR, 33, 187

# Appendix D

# Article AJ (2023)

Article published on the journal *The Astronomical Journal*: Gkotsinas et al., (2023), AJ, 165, 67, 10 pp.

The Astronomical Journal, 165:67 (10pp), 2023 February https://doi.org/10.3847/1538-3881/acaafd


# On Averaging Eccentric Orbits: Implications for the Long-term Thermal Evolution of Comets

Anastasios Gkotsinas[1], Aurélie Guilbert-Lepoutre[1], and Sean N. Raymond[2]
[1] Laboratoire de Géologie de Lyon: Terre, Planètes, Environnement, CNRS, UCBL, ENSL, F-69622 Villeurbanne, France; anastasios.gkotsinas@univ-lyon1.fr
[2] Laboratoire d'Astrophysique de Bordeaux, Univ. Bordeaux, CNRS, F-33615 Pessac, France
*Received 2022 October 18; revised 2022 December 8; accepted 2022 December 11; published 2023 January 24*

## Abstract

One of the common approximations in long-term evolution studies of small bodies is the use of circular orbits averaging the actual eccentric ones, facilitating the coupling of processes with very different timescales, such as the orbital changes and the thermal processing. Here we test a number of averaging schemes for elliptic orbits in the context of the long-term evolution of comets, aiming to identify the one that best reproduces the elliptic orbits' heating patterns and the surface and subsurface temperature distributions. We use a simplified thermal evolution model applied on simulated comets both on elliptic and on their equivalent averaged circular orbits, in a range of orbital parameter space relevant to the inner solar system. We find that time-averaging schemes are more adequate than spatial-averaging ones. Circular orbits created by means of a time average of the equilibrium temperature approximate efficiently the subsurface temperature distributions of elliptic orbits in a large area of the orbital parameter space, rendering them a powerful tool for averaging elliptic orbits.

*Unified Astronomy Thesaurus concepts:* Comets (280); Comet nuclei (2160); Comet interiors (272); Computational methods (1965)

## 1. Introduction

Considering comets' long lifetimes and complex dynamical histories, studying the long-term evolution of their nuclei is an essential step in understanding their current state and activity (Gkotsinas et al. 2022). One approach to assess long-term effects is to determine their thermal histories by coupling a thermal evolution model to orbital trajectories from dynamical simulations (Raymond et al. 2020; Gkotsinas et al. 2022). This coupling is challenging both from a physical and a numerical point of view (Gkotsinas et al. 2022) and demands a certain number of assumptions, as the processes involved operate on very different timescales. Thermal evolution processes such as phase transitions, heat or gas diffusion, depending on the temperature conditions, usually take place in minutes or hours or up to a few months in the case of the heat diffusion (Prialnik et al. 2004). The dynamical evolution of comets, on the other hand, is a billion-year process that requires *N*-body simulations with an output frequency on the order of hundreds to thousands of years (e.g., Nesvorný et al. 2017; Sarid et al. 2019), far longer than the short timescales of thermal processes.

One of the assumptions frequently used in these types of simulations is to simplify the dynamical pathways of comets by averaging their orbits (Prialnik & Rosenberg 2009; Guilbert-Lepoutre 2012; Snodgrass et al. 2017; Gkotsinas et al. 2022). Prialnik & Rosenberg (2009) proposed to replace elliptic orbits by equivalent circular ones; the radius of which was chosen to assure the same amount of total energy over the course of an orbital period. This is reinforced in other fields, as climate modeling of putative Earth-like planets on eccentric orbits has generally found that the controlling factor determining whether a planet may retain liquid water is the total energy received over a planet's orbit (Williams & Pollard 2002; Bolmont et al. 2016).

In this work we aim to compare and evaluate different methods for averaging elliptical orbits in the context of long-term simulations of comets' thermal evolution. In Section 2 we present the tested averaging schemes and we give a brief presentation of the thermal evolution model. In Section 3 we present the produced internal temperature distributions from the different schemes and a comparative study between them and elliptic orbits. In Section 4 we discuss the adequacy and the limits of validity of every scheme and highlight the scheme that worked better in the current context.

## 2. Methods

### 2.1. Averaging Eccentric Orbits

A variety of approaches have been proposed in order to average an elliptic orbit. The most common one is to estimate an average distance between the object and the focal point. This can be achieved in two ways: The first is to integrate the orbit equation over the true anomaly ($\theta$) throughout an orbital period to obtain a true-anomaly-averaged radius (e.g., Curtis 2014):

$$\bar{r}_\theta = a\sqrt{1-e^2}. \tag{1}$$

The second way is to integrate the orbit equation over the average angular velocity of the object over the course of an orbital period. This approach results in a time-averaged radius, which is always smaller than the true-anomaly-averaged radius (e.g., Curtis 2014):

$$\bar{r}_t = a\left(1+\frac{e^2}{2}\right). \tag{2}$$

Another widely used method is to integrate over a physical parameter, such as the flux received by an object over an orbital period. This is the most physically plausible way to approach

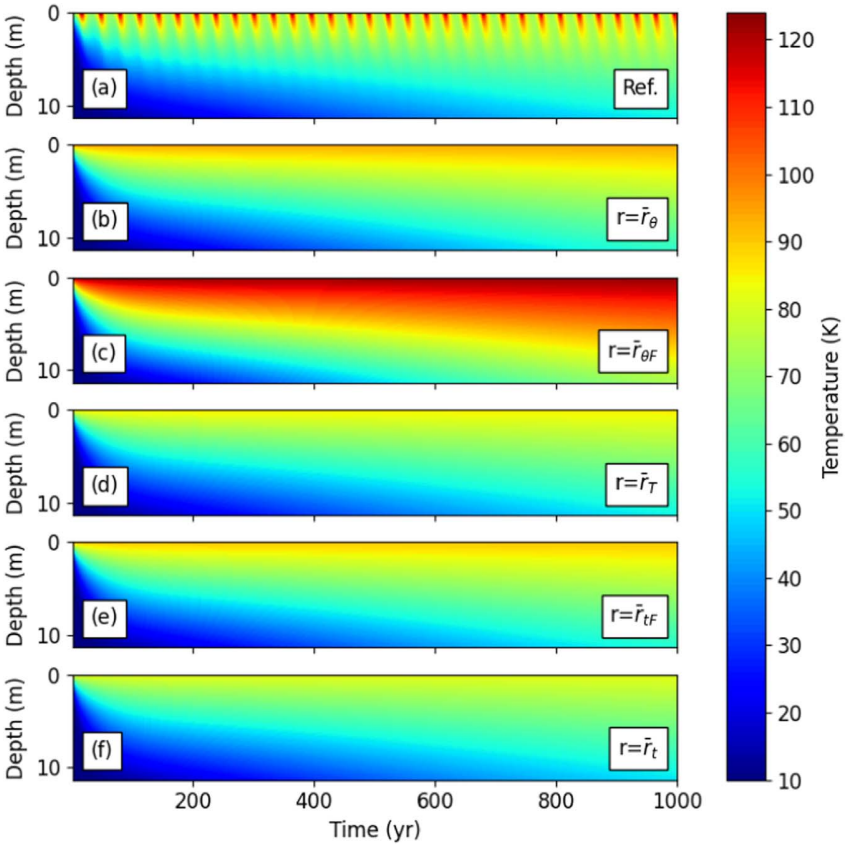


**Figure 1.** Subsurface temperature distributions for a layer of 10 m over a period of 1000 yr for (a) an elliptical orbit with $a = 10$ au and $e = 0.5$, (b) true-anomaly-averaged radius ($\bar{r}_\theta$), (c) true-anomaly-averaged flux ($\bar{r}_{\theta F}$), (d) effective thermal radius ($r_T$), (e) time-averaged flux ($\bar{r}_{tF}$), and (f) time-averaged radius ($\bar{r}_t$) equivalent circular orbits.

the problem, as it ensures that the total energy intercepted by an object over an orbit is not modified. Using Equations (1) and (2) we can calculate a true-anomaly-averaged and a time-averaged flux (Méndez & Rivera-Valentín 2017) from which we can obtain a new set of radii, the second of which is commonly used on planetary habitability studies (e.g., Bolmont et al. 2016):

$$\bar{r}_{\theta F} = \frac{a(1-e^2)}{\sqrt{2+e^2}}, \tag{3}$$

$$\bar{r}_{tF} = a(1-e^2)^{\frac{1}{4}}. \tag{4}$$

Recently, Méndez & Rivera-Valentín (2017) proposed a new effective thermal radius, calculated directly from the time average of the equilibrium temperature ($T_{\rm eq}$), guaranteeing the same average equilibrium temperature over an orbital period:

$$r_T = a\left[\frac{2\sqrt{1+e}}{\pi}E\sqrt{\frac{2e}{1+e}}\right]^{-2}, \tag{5}$$

$$\approx a\left(1+\frac{1}{8}e^2+\frac{21}{512}e^4+\mathcal{O}(e^6)\right), \tag{6}$$

where $E$ is the complete elliptic integral of the second order.

All of the proposed expressions are simple functions of the semimajor axis ($a$) and the eccentricity ($e$). In practice, this means that for an elliptic orbit with specified orbital parameters (i.e., an ($a$, $e$) couple), the orbit-averaging technique produces a circular orbit around the focal point with an "equivalent" radius. The differences in the averaging expressions imply different distances from the Sun. In fact for any given ($a$, $e$) couple the calculated radii are ordered as $\bar{r}_{\theta F} < \bar{r}_\theta < \bar{r}_{tF} < r_T < \bar{r}_t$. This means that true-anomaly-averaged flux expression ($\bar{r}_{\theta F}$) will always place an object closer to the Sun than the time-averaged radius ($\bar{r}_t$). As a consequence for the same ($a$, $e$) couple we produce different temperature profiles (panels (b) to (e) in Figure 1), raising the question "which one is better approximating the temperature distribution of the elliptic orbit?" (panel (a) in Figure 1). To answer we test these orbit-averaging schemes in the context of comets' thermal evolution. In order to test the validity limits of each scheme in a range of orbital parameter space relevant for the inner solar system (i.e., ~3–30 au) we use a total of 110 ($a$, $e$) couples. We sample the semimajor axis range logarithmically ($10^x$, with $x$ ranging between 0.5 and 1.5 with a step of 0.1) with more orbits close to the Sun, where the heating is stronger and the eccentricity is linear between 0 and 0.9 at increments of 0.1.

### 2.2. Thermal Evolution Model

We use a 1D version of the 3D thermal evolution model described in Guilbert-Lepoutre et al. (2011) to solve the heat diffusion equation in a spherical airless object:

$$\rho_{\rm bulk}\, c\, \frac{\partial T}{\partial t} + \mathrm{div}(-\kappa\, \overrightarrow{\mathrm{grad}}\, T) = \mathcal{S}, \tag{7}$$

where $\rho_{\rm bulk}$ is the object's bulk density (kg m$^{-3}$), $c$ is the material's heat capacity (J kg$^{-1}$ K$^{-1}$), $T$ is the temperature (K),

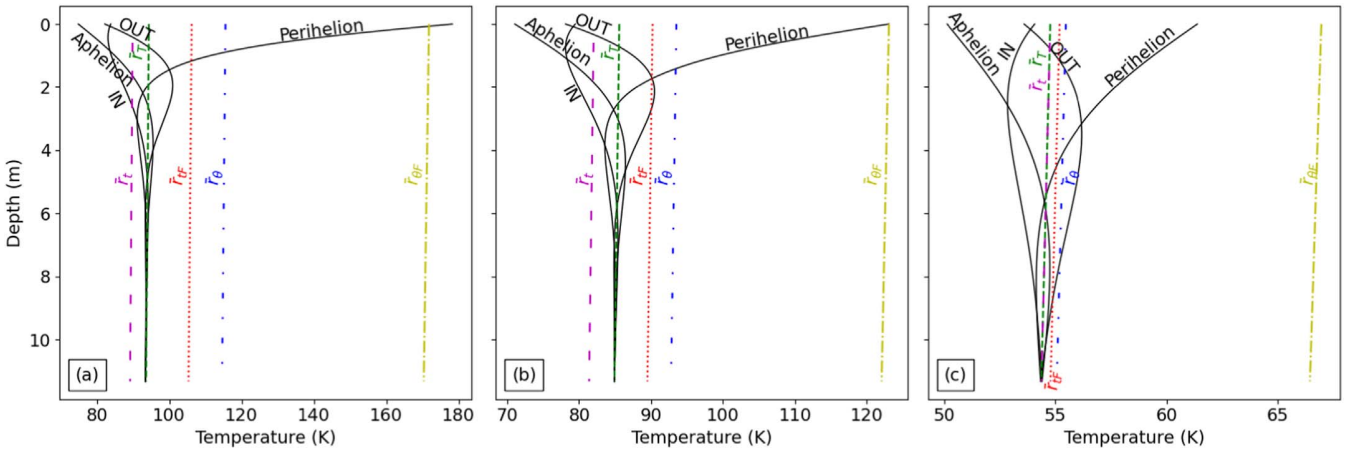


**Figure 2.** Temperature profiles for a subsurface layer of 10 m, ∼1 Myr after the start of the simulations, for three $a$, $e$ couples: (a) $a = 7.94$ au and $e = 0.7$, (b) $a = 10.0$ au and $e = 0.5$, and (c) $a = 25.11$ and $e = 0.2$. The solid black lines give the temperature profiles of elliptic orbits at perihelion, aphelion, and halfway through—time-wise—both inward and outward. The temperatures profiles for the equivalent orbits are true-anomaly-averaged radius ($\bar{r}_\theta$) (blue loosely dashed–dotted line), true-anomaly-averaged flux ($\bar{r}_{\theta F}$) (yellow dashed–dotted line), time-averaged radius ($\bar{r}_t$) (green dashed line), time-averaged flux ($\bar{r}_{tF}$) (red dotted line), and effective thermal radius ($r_T$) (purple loosely dashed line).

$\kappa$ is the material's effective thermal conductivity (W K$^{-1}$ m$^{-1}$), and $\mathcal{S}$ is the heat sources and sinks.

The surface boundary condition for Equation (7) is

$$(1 - \mathcal{A})\frac{L_\odot}{4\pi d_H^2} = \varepsilon\sigma T^4 + \kappa\frac{\partial T}{\partial z}, \tag{8}$$

where the received solar energy is given as a function of Bond's albedo ($\mathcal{A}$), the solar constant ($L_\odot$) in W m$^{-2}$, and the heliocentric distance ($d_H$) in au; the nucleus' thermal emission as a function of the emissivity ($\varepsilon$), the Stefan–Boltzmann constant ($\sigma$), and the temperature ($T$) in K; and the heat flux toward the interior given as a function of the surface's thermal conductivity ($\kappa$) in W K$^{-1}$ m$^{-1}$. We assume that the incident solar energy is uniformly distributed over the surface of the sphere, providing a spherical average of the energy received by the nucleus.

As the goal of this work is to compare elliptic to circular orbits, we chose a simplified setup for our model. Each comet is composed of dust without any ice, such that no phase transitions take place, removing any energy sources or sinks from Equation (7) ($\mathcal{S} = 0$). Without them the most important parameter in the model is the effective thermal conductivity ($\kappa$), as it controls the heat diffusion toward the interior. In the current configuration it is set at $5 \times 10^{-3}$ W m$^{-1}$ K$^{-1}$, in good agreement with laboratory measurements for porous dust aggregates (Krause et al. 2011). The rest of the model's parameters are widely used averages in the published literature (Huebner et al. 2006).

It is the value of the heliocentric distance ($d_H$) that changes between the different case studies, controlling the amount of energy received at the surface of our objects. In an elliptic orbit it changes following the constant increment of the eccentric anomaly as the object moves between the apsides. In the test cases it is constant, set on the distance calculated by Equations (1)–(6).

We run a total of 660 simulations: 110 reference simulations for all the ($a$, $e$) couples with objects on elliptic orbits, serving as basis for the comparisons with the 550 simulations for objects on equivalent circular orbits created from Equations (1)–(6) for the same ($a$, $e$) couples. The simulations run for ∼1 Myr, an arbitrary period selected to allow heat diffusion inside our objects. This allows us to study the temperature differences between elliptic and circular orbits, not only at the surface but in the interior as well, and look for any accumulative or propagation effects that might be introduced during long-term simulations.

## 3. Results

Figure 1 presents the internal temperature distribution produced by the different orbit-averaging schemes for a comet on an orbit with $a = 10$ au and $e = 0.5$. For clarity only the first 1000 yr of the 1 Myr simulation are presented, but this is sufficient to notice the averaging effects. Clearly, none of the averaged orbits reproduce the heating cycle of the elliptic orbit with the subsequent passages from the perihelion to the aphelion, i.e., the seasons. Instead, as the distance from the Sun is constant, the heat diffusion is steady and uniform throughout an orbital period.

Figure 2 presents temperature profiles in the interior of our simulated comets using different orbit-averaging methods, taken near the end of our simulations (∼1 Myr). The fact that the profiles are near-vertical stems from the assumption of a fixed, circular orbit with constant illumination. A profile from the reference elliptic orbit with the same orbital elements (i.e., $a$ and $e$) is shown at perihelion and aphelion, and at two points halfway in between at times coinciding with a quarter of its orbital period, both on its way inward (from aphelion to perihelion) and outward (from perihelion to aphelion). The three panels examine different orbits: (a) a highly eccentric and relatively short orbit with $a = 7.94$ au and $e = 0.7$; (b) a longer, less eccentric orbit with $a = 10$ au and $e = 0.5$; and (c) a long orbit ($a = 25.11$ au) with low eccentricity of 0.2.

The temperature profiles from Figure 2 help us to confirm some of the previous observations:

1. The true-anomaly-averaged flux ($\bar{r}_{\theta F}$) better approximates the effect of the perihelion passage (even for the less eccentric orbit, where the temperature difference at the surface is ∼6 K), but fails completely on the other positions both on the surface and the subsurface.

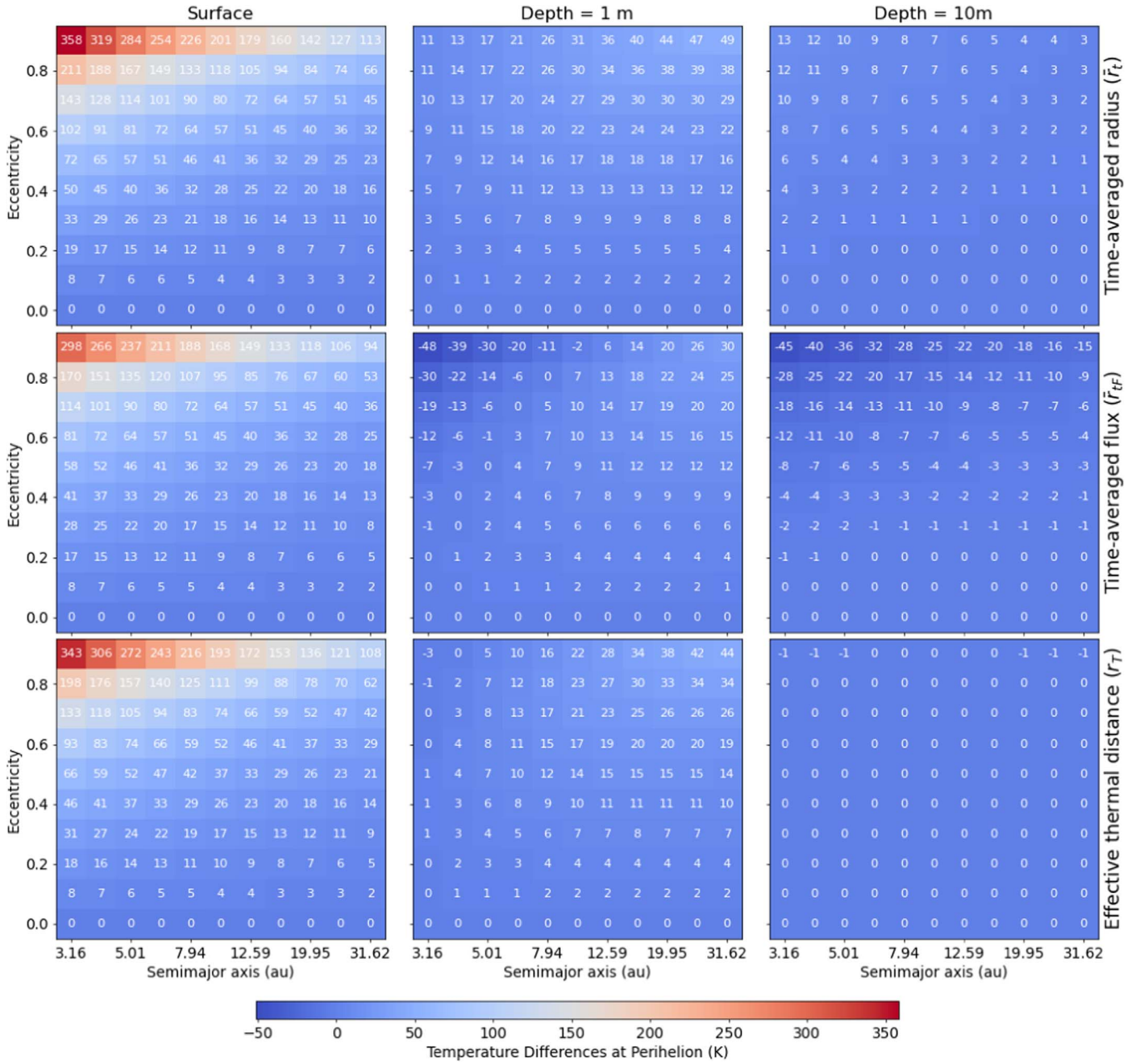


**Figure 3.** Temperature differences between the elliptic orbits at perihelion and the time-averaged radius ($\bar{r}_t$) (top row), the time-averaged flux ($\bar{r}_{tF}$) (middle row), and the effective thermal radius ($r_T$) equivalent orbits (bottom row) for three depths: surface (left column), 1 m (middle column), and 10 m (right column) for all the $a$, $e$ couples.

Divergences range from ∼6 K in the least eccentric to ∼80 K in the most eccentric orbit examined.

2. The true-anomaly-averaged radius ($\bar{r}_\theta$) works slightly better, with calculated surface temperatures between those of the two apsides and subsurface profiles closer to the reference ones, and with temperature differences ranging from ∼20 K in the most eccentric, to almost complete convergence in the least eccentric orbits.
3. Overall, the time-averaged expressions (Equations (2), (4), and (6)) work better in all cases. Despite their failure to reproduce the high surface temperatures encountered at perihelion, especially for the most eccentric orbit, these schemes better reproduce the cooling effect of the aphelion passage, leading to internal temperature distributions that converge to those of the reference orbit in all the examples of Figure 2.
4. The effective thermal radius ($r_T$) stands out as the scheme producing an internal temperature distribution converging almost perfectly to the reference distribution, close to the surface: below 6 m in the first two cases and 10 m in the last.

Given that the true-anomaly-averaged (or spatial) expressions failed in matching the reference simulations, we focus hereafter on the time-averaged formulas. We expand our study

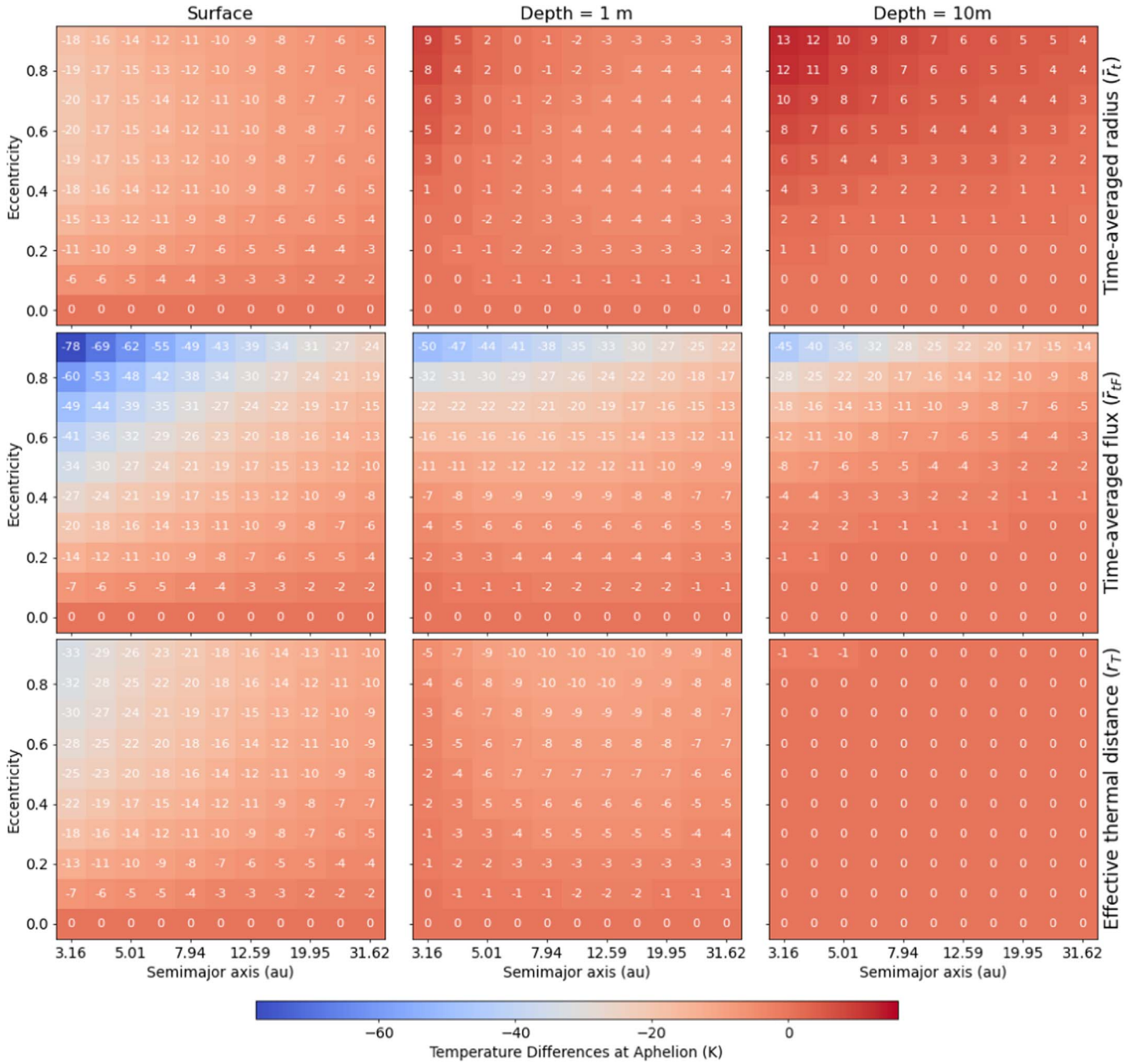


**Figure 4.** Temperature differences between the elliptic orbits at aphelion and the time-averaged radius ($\bar{r}_t$; top row), the time-averaged flux ($\bar{r}_{tF}$; middle row), and the effective thermal radius ($r_T$) equivalent orbits (bottom row) for three depths: surface (left column), 1 m (middle column), and 10 m (right column) for all the $a$, $e$ couples.

by examining the temperature differences from the reference elliptic orbits at the surface, 1 and 10 m below the surface at perihelion, at aphelion and halfway in between time-wise.

In Figure 3 we present the temperature differences ($\Delta T$) between the three time-averaged formulas ($\bar{r}_t$, $\bar{r}_{tF}$, and $r_T$) and the elliptic orbits at perihelion. All schemes underestimate the surface temperatures during the perihelion passage. The time-averaged radius ($\bar{r}_t$) deviates the most from the reference orbits (maximum $\Delta T$ of ∼358 K or in terms of relative difference by 73%), especially for very eccentric ($e > 0.5$) and short orbits ($a < 10$ au). It is followed by the effective thermal radius ($r_T$) with a maximum divergence of ∼343 K (relative difference of 70%). The time-averaged flux ($\bar{r}_{tF}$) presents a maximum $\Delta T$ of ∼298 K (or relative difference of 61%). These relative differences at the surface rise with the eccentricity, becoming important (∼20%) above $e = 0.3$, and really significant for high eccentricities (50% for $e = 0.7$ and ∼70% for $e = 0.9$) for the time-averaged and the effective thermal radius, highlighting their failure to represent the perihelion passage. The time-averaged flux ($\bar{r}_{tF}$) has slightly smaller relative deviations especially above $e > 0.4$ where it is constantly lower than the other time-averaged schemes by ∼4%–9%.

All three schemes are more robust in the objects' interiors (middle and right panels of Figure 3). At 1 m below the surface the time-averaged radius ($\bar{r}_t$) differences converge quickly for all orbits (maximum $\Delta T$ of ∼26 K) except for distant ($a > 10$ au) and highly eccentric ($e > 0.5$) orbits for which the maximum $\Delta T$ is ∼49 K. The same stands for the effective

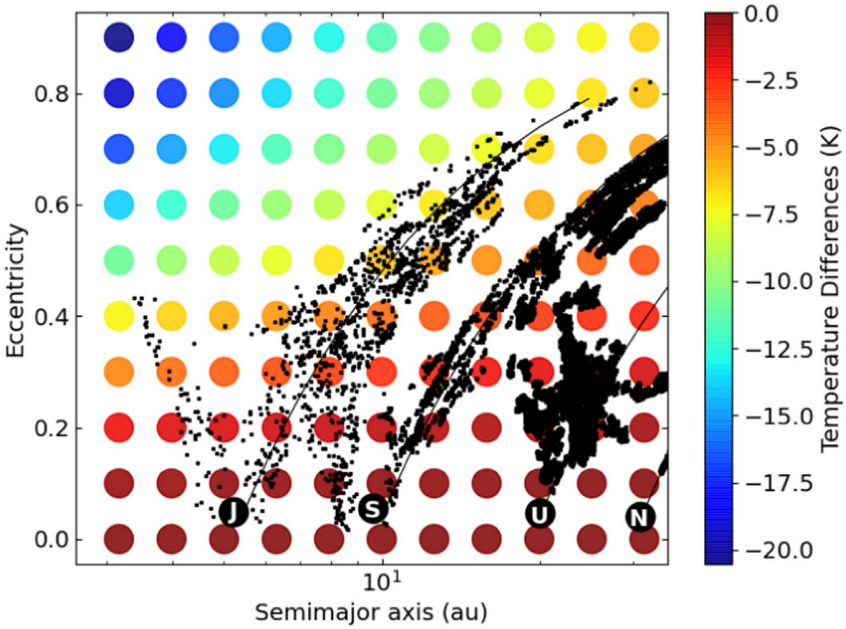


**Figure 5.** A typical Jupiter-family comet trajectory taken from Gkotsinas et al. (2022) plotted over the temperature differences between elliptic orbits and an average of the effective thermal radius ($r_T$) inward and outward for all the $a$, $e$ couples. Each circle represents a point in our orbital parameter space sampling. The color code gives the scale of the temperature difference.

thermal radius ($r_T$) only with better convergence for short ($a < 10$ au) and low-eccentric orbits ($e < 0.5$). For distant ($a > 10$ au) and highly eccentric ($e > 0.5$) orbits the problem remains but is slightly less pronounced (with a maximum $\Delta T$ of ∼44 K). Long-period orbits with prolonged excursions into hot areas around perihelion allow the heatwave to advance deeper in the interior and extend the temperature differences well below the surface. In these cases underestimating the perihelion temperature remains problematic, unlike the cases of short orbits ($a < 10$ au) where the heating, although more intense, takes place in a shorter period of time that is not sufficient for its diffusion in the interior (panel (a) versus panel (b) in Figure 2, for example). These differences almost completely disappear 10 m below the surface in the case of the effective thermal radius ($r_T$; $\Delta T_{\max} = -1$ K for $e = 0.9$; lower right panel in Figure 3) and the time-averaged radius ($\bar{r}_t$; with the exception of very short, $a < 10$ au, and highly eccentric orbits, $e > 0.7$). On the contrary, the time-averaged flux ($\bar{r}_{tF}$) differences at the interior (middle panels in Figure 3) fail to achieve convergence in high eccentricities ($e \geqslant 0.5$), whether it is a short or a long orbit. In addition these deviations persist at larger depths (middle right panel of Figure 3), as there is still no convergence for highly eccentric orbits ($e \geqslant 0.5$) and the differences on low-eccentricity orbits are higher than those of the effective thermal radius and the time-averaged radius.

At the aphelion the temperatures are overestimated by the averaging schemes (Figure 4). The time-averaged radius ($\bar{r}_t$) works better than the other methods in the surface and the close subsurface area ($\Delta T_{\max} = 20$ K versus $\Delta T_{\max} = -78$ K for $\bar{r}_{tF}$ and $\Delta T_{\max} = 33$ K for $r_T$ at the surface and $\Delta T_{\max} = 9$ K versus $\Delta T_{\max} = 50$ K and $\Delta T_{\max} = 10$ K, respectively, 1 m below the surface). However, at 10 m below the surface the convergence for the effective thermal radius is almost complete ($\Delta T_{\max} = -1$ K in only three short and eccentric orbits) unlike for the time-averaged radius and the time-averaged flux where there is still no convergence. For completeness, similar representations for the temperature differences halfway through inward and outward presented in Figure 2 are given in Figures 6 and 7. As expected the temperature differences are less important comparing to those of the two apsides, but we can still observe the efficiency of the time-averaged and especially of the effective thermal radius over the time-averaged flux method.

## 4. Discussion

Overall the time-averaged schemes work better than the true-anomaly or spatial-averaged ones. This is because the true-anomaly formulas are restricted to the calculation of an average distance from the focal point. Although this seems to be a sufficient assumption, it ignores crucial information: the different time spent by an object at different distances from the focal point. In fact an object in an elliptic orbit will move much faster close to perihelion than close to aphelion, implying —in our case—more time in colder regions. This information is integrated in temporal expressions rendering them more appropriate in the approximation of elliptic orbits. With that in mind, the surface temperatures obtained from the time-averaged schemes, closer to the aphelion temperatures of an elliptic orbit, are more appropriate than an average of the perihelion–aphelion temperatures calculated by the spatial-averaged schemes.

When it comes to the time-averaged orbits, we demonstrated (Figures 3 and 4) that the time-averaged ($\bar{r}_t$) and the effective thermal radius ($r_T$) better approximate the temperature distributions of elliptic orbits with the exception of the surface temperatures at perihelion. These two distances are increasing functions of the eccentricity, whereas the time-averaged flux ($\bar{r}_{tF}$) is a decreasing one (Méndez & Rivera-Valentín 2017). This implies that for a given ($a$, $e$) couple, the time-averaged flux will place an object closer to the perihelion, leading to a systematic overestimation of the surface temperature. On the other hand, the time-averaged and the effective thermal radius

(very close by definition; see Equations (2) and (6)) place the object closer to the aphelion accounting better for the lower temperatures reigning during the biggest part of an orbit (especially for highly eccentric ones), managing better to represent the internal temperature distribution. Interestingly, there is no clear distinction on the efficiency between these two formulas, as the time-averaged radius, as expected by its definition, works better at aphelion and halfway through both inward and outward at the surface and 1 m below, but fails to convergence as quickly as the effective thermal radius that manages to converge in all cases at maximum 10 m below the surface.

We tested the equivalent semimajor axis proposed by Prialnik & Rosenberg (2009), deriving also from a time-averaging integral ($a_c = a(1 - e^2)$). As this average distance provides the same energy per orbit as the real eccentric one, it is reliable only when orbital periods are very close. Otherwise significant deviations are observed (for very eccentric orbits for instance), with a systematic overestimation of the internal temperatures. Its validity thus remains limited to low-eccentricity orbits ($e < 0.3$) or limited timescales, as done in Guilbert-Lepoutre (2012), Snodgrass et al. (2017), and Gkotsinas et al. (2022).

When the actual orbital trajectory of a typical comet is accounted for, it is clear that orbit averaging remains a viable technique for the long-term cometary thermal evolution. Figure 5 shows the orbital changes of a simulated Jupiter-family comet during its trajectory toward the inner solar system (taken from Gkotsinas et al. 2022 with dynamical trajectories from Nesvorný et al. 2017), over an average of the inward and outward surface temperature differences for the effective thermal radius ($r_T$). With the exception of short and highly eccentric orbits ($a < 10$ au and $e > 0.5$), which are very rare, the averaging is very efficient in all the other areas of the orbital parameter space. Even in the area of long and highly eccentric orbits ($a > 10$ au and $e > 0.5$), the temperature divergences do not overcome the $\sim$10 K. This suggests that using the effective thermal radius to average elliptic orbits is a very effective tool with a large area of validity in the orbital parameter space and not important discrepancies outside of this area (as even for the short and highly eccentric orbits the divergence is not bigger than 20 K).

We therefore recommend the use of the effective thermal radius scheme, $r_T \approx a(1 + \frac{1}{8}e^2 + \frac{21}{512}e^4 + \mathcal{O}(e^6))$, in long-term thermal evolution studies, as it can efficiently approximate the internal temperature distribution of an airless dusty body with low thermal inertia, such as a comet or an asteroid, evolving in eccentric orbits.

This study is part of a project that has received funding from the European Research Council (ERC) under the European Union's Horizon 2020 research and innovation program (grant agreement No. 802699). We gratefully acknowledge support from the PSMN (Pôle Scientifique de Modélisation Numérique) of the ENS de Lyon for computing resources. The authors would like to thank Benoit Carry for his useful comments on previous work, which provided the background for the current paper.

*Facilities:* PSMN, ENS de Lyon.

## Appendix
## Supplementary Figures

In Figures 6 and 7 we present, for completeness"the temperatures differences, as presented in Figures 3 and 4 of the main text"for the halfway points inward and outward, respectively.

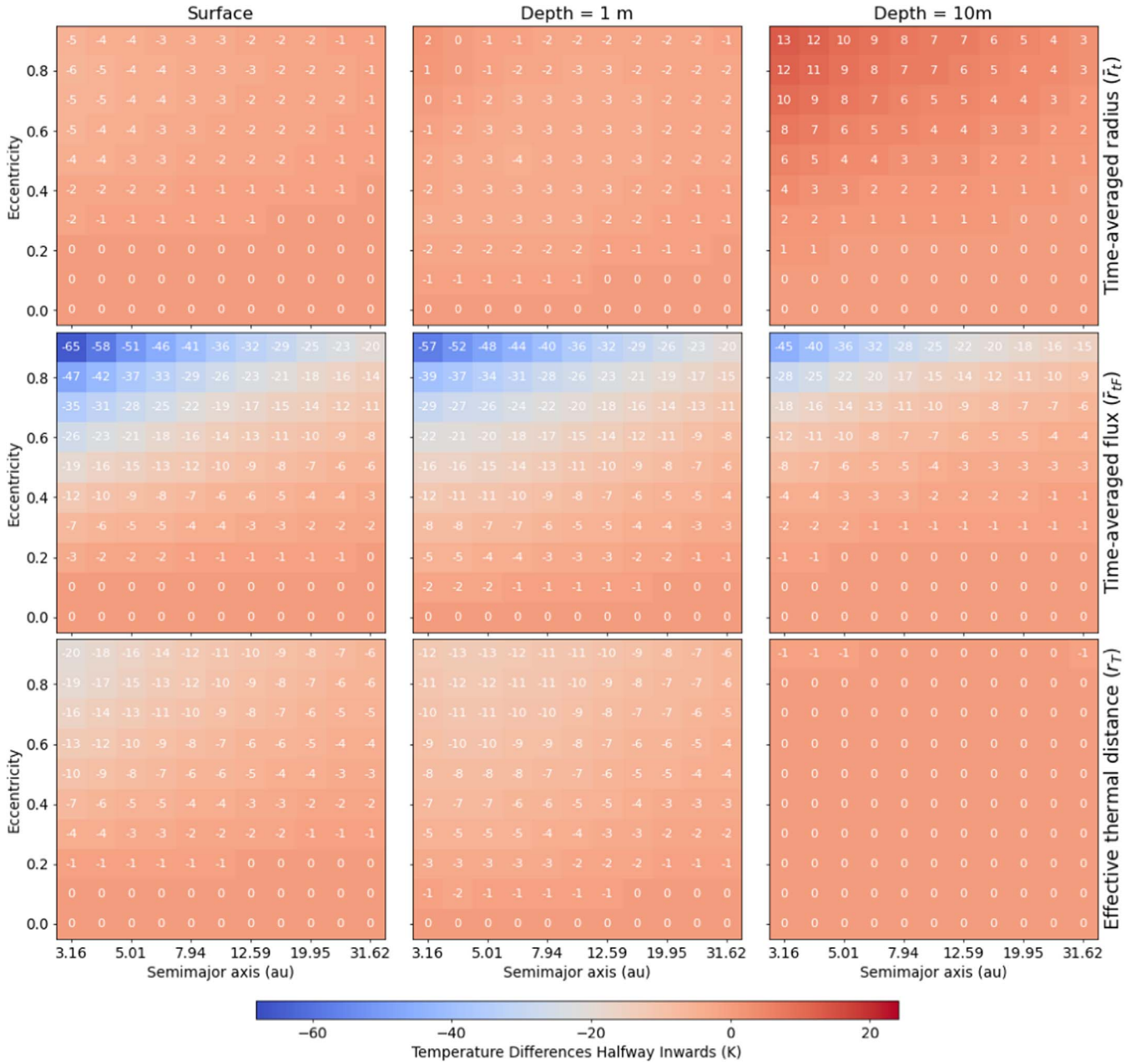


**Figure 6.** Temperature differences between the elliptic orbits halfway through inward (time-wise) and the time-averaged radius ($\bar{r}_t$; top row), the time-averaged flux ($\bar{r}_{tF}$; middle row), and the effective thermal radius ($r_T$) equivalent orbits (bottom row) for three depths: surface (left column), 1 m (middle column), and 10 m (right column) for all the $a$, $e$ couples.

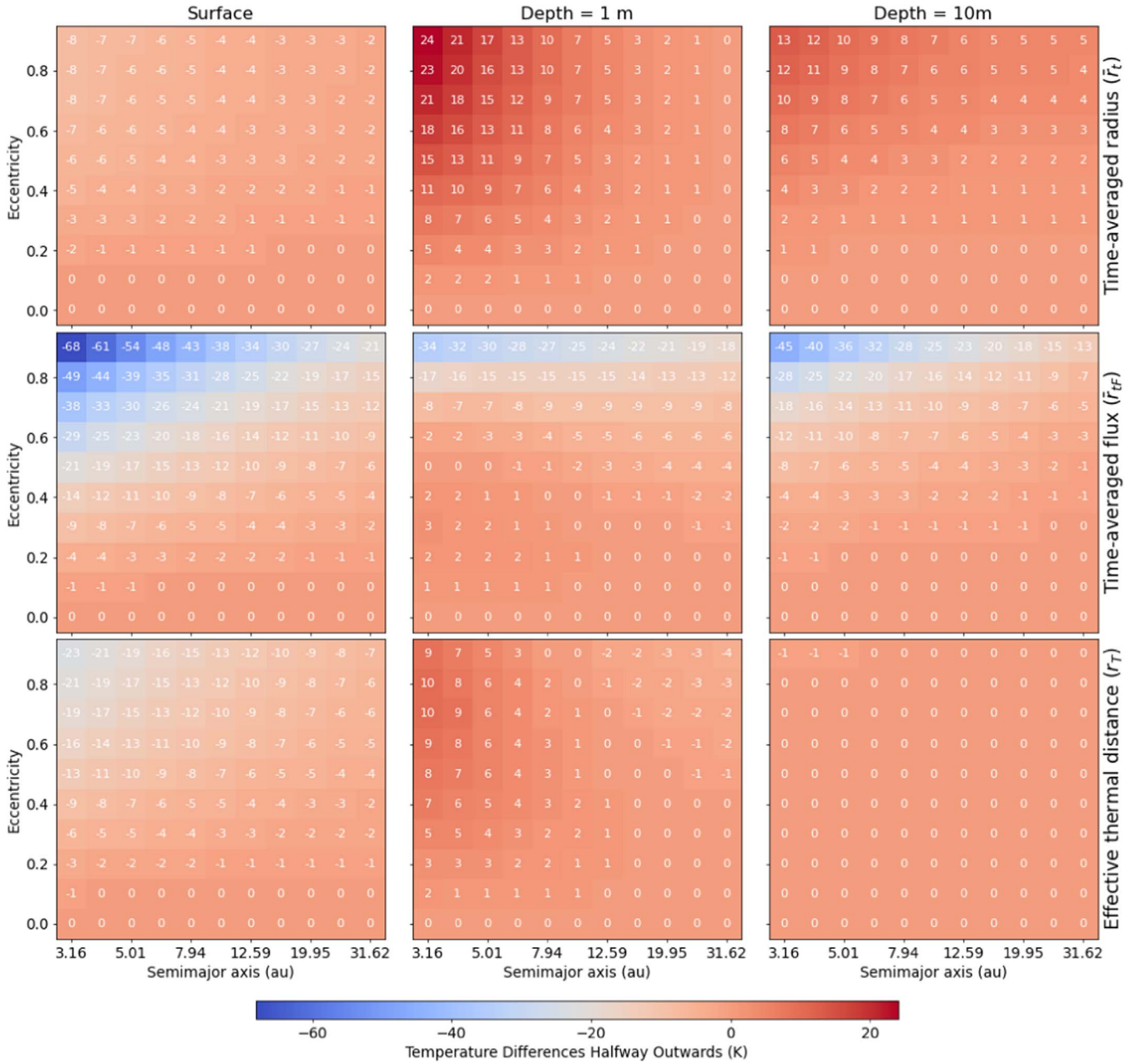


**Figure 7.** Temperature differences between the elliptic orbits halfway through outward (time-wise) and the time-averaged radius ($\bar{r}_t$; top row), the time-averaged flux ($\bar{r}_{tF}$; middle row), and the effective thermal radius ($r_T$) equivalent orbits (bottom row) for three depths: surface (left column), 1 m (middle column), and 10 m (right column) for all the $a$, $e$ couples.

## ORCID iDs

Anastasios Gkotsinas https://orcid.org/0000-0002-1611-0381
Aurélie Guilbert-Lepoutre https://orcid.org/0000-0003-2354-0766
Sean N. Raymond https://orcid.org/0000-0001-8974-0758

## References

Bolmont, E., Libert, A.-S., Leconte, J., & Selsis, F. 2016, A&A, 591, A106
Curtis, H. D. 2014, in Orbital Mechanics for Engineering Students (Third Edition), ed. H. D. Curtis (3rd ed.; Boston, MA: Butterworth-Heinemann) doi:10.1016/B978-0-08-097747-8.00002-5
Gkotsinas, A., Guilbert-Lepoutre, A., Raymond, S. N., & Nesvorny, D. 2022, ApJ, 928, 43
Guilbert-Lepoutre, A. 2012, AJ, 144, 97
Guilbert-Lepoutre, A., Lasue, J., Federico, C., et al. 2011, A&A, 529, A71
Huebner, W. F., Benkhoff, J., Capria, M.-T., et al. 2006, Heat and Gas Diffusion in Comet Nuclei (Bern: International Space Science Institute)
Krause, M., Blum, J., Skorov, Y., & Trieloff, M. 2011, Icar, 214, 286
Méndez, A., & Rivera-Valentín, E. G. 2017, ApJL, 837, L1
Nesvorný, D., Vokrouhlický, D., Dones, L., et al. 2017, The, ApJ, 845, 27
Prialnik, D., Benkhoff, J., & Podolak, M. 2004, in Comets II, ed. M. C. Festou & H. . Keller, Vol. 374 (Tucson, AZ: Univ. of Arizona Press)
Prialnik, D., & Rosenberg, E. D. 2009, MNRAS, 399, L79
Raymond, S. N., Kaib, N. A., Armitage, P. J., & Fortney, J. J. 2020, ApJL, 904, L4
Sarid, G., Volk, K., Steckloff, J. K., et al. 2019, ApJL, 883, L25
Snodgrass, C., Agarwal, J., Combi, M., et al. 2017, A&ARv, 25, 5
Williams, D. M., & Pollard, D. 2002, IJAsB, 1, 61

# References


'Oumuamua ISSI Team et al. (July 2019). "The natural history of 'Oumuamua". In: *Nature Astronomy* 3, pp. 594–602.

A'Hearn, M. F. et al. (Mar. 2005). "Deep Impact: A Large-Scale Active Experiment on a Cometary Nucleus". In: *Space Science Reviews* 117(1-2), pp. 1–21.

Allen, R. L., G. M. Bernstein, and R. Malhotra (Mar. 2001). "The Edge of the Solar System". In: *The Astrophysical Journal* 549(2), pp. L241–L244.

Altwegg, K., H. Balsiger, and S. A. Fuselier (Aug. 2019). "Cometary Chemistry and the Origin of Icy Solar System Bodies: The View After Rosetta". In: *Annual Review of Astronomy and Astrophysics* 57, pp. 113–155.

Altwegg, K. et al. (July 2017). "Organics in comet 67P - a first comparative analysis of mass spectra from ROSINA-DFMS, COSAC and Ptolemy". In: *Monthly Notices of the Royal Astronomical Society* 469, S130–S141.

Bailey, B. L. and R. Malhotra (Sept. 2009). "Two dynamical classes of Centaurs". In: *Icarus* 203(1), pp. 155–163.

Bar-Nun, A., G. Notesco, and T. Owen (Oct. 2007). "Trapping of N $_2$, CO and Ar in amorphous ice—Application to comets". In: *Icarus* 190(2), pp. 655–659.

Bar-Nun, A. and D. Prialnik (Jan. 1988). "The Possible Formation of a Hydrogen Coma around Comets at Large Heliocentric Distances". In: *The Astrophysical Journal Letters* 324, p. L31.

Bar-Nun, A. et al. (Sept. 1985). "Trapping and release of gases by water ice and implications for icy bodies". In: *Icarus* 63(3), pp. 317–332.

Bardyn, A. et al. (July 2017). "Carbon-rich dust in comet 67P/Churyumov-Gerasimenko measured by COSIMA/Rosetta". In: *Monthly Notices of the Royal Astronomical Society* 469, S712–S722.

Bauer, J. M. et al. (Feb. 2021). "NEOWISE Observed CO and $CO_2$ Production Rates of 46P/Wirtanen During the 2018-2019 Apparition". In: *The Planetary Science Journal* 2(1), 34, p. 34.

Bear, J. (1988). *Dynamics of Fluids in Porous Media*. Dover, New York. ISBN: 9780486656755.

Behar, E. et al. (Aug. 2018). "The root of a comet tail: Rosetta ion observations at comet 67P/Churyumov-Gerasimenko". In: *Astronomy and Astrophysics* 616, A21.

Benkhoff, J. and W. F. Huebner (Apr. 1995). "Influence of the Vapor Flux on Temperature, Density, and Abundance Distributions in a Multicomponent, Porous, Icy Body". In: *Icarus* 114(2), pp. 348–354.

Benkhoff, J. and T. Spohn (Feb. 1991). "Thermal histories of the KOSI samples". In: *Geophysical Research Letters* 18(2), pp. 261–264.

Benkhoff, J. and D. C. Boice (July 1996). "Modeling the thermal properties and the gas flux from a porous, ice-dust body in the orbit of P/Wirtanen". In: *Planetary and Space Science* 44(7), pp. 665–673.

Benseguane, S. et al. (Dec. 2022). "Evolution of pits at the surface of 67P/Churyumov- Gerasimenko". In: *Astronomy and Astrophysics* 668, A132.

Bergner, J. B. and D. Z. Seligman (Mar. 2023). "Acceleration of 1I/ 'Oumuamua from radiolytically produced $H_2$ in $H_2O$ ice". In: *Nature* 615(7953), pp. 610–613.

Biver, N. and D. Bockelée-Morvan (Oct. 2016). "Chemical diversity in the comet population". In: *IAU Focus Meeting* 29A, pp. 228–232.

Biver, N. et al. (June 2002). "The 1995 2002 Long-Term Monitoring of Comet C/1995 O1 (HALE BOPP) at Radio Wavelength". In: *Earth Moon and Planets* 90(1), pp. 5–14.

Biver, N. et al. (July 2021). "Molecular composition of short-period comets from millimetre-wave spectroscopy: 21P/Giacobini-Zinner, 38P/Stephan-Oterma, 41P/Tuttle-Giacobini-Kresák, and 64P/Swift-Gehrels". In: *Astronomy and Astrophysics* 651, A25, A25.

Biver, N. et al. (July 2022). "Chemistry of comet atmospheres". In: *arXiv e-prints*, arXiv:2207.04800.

Blum, J., D. Bischoff, and B. Gundlach (July 2022). "Formation of Comets". In: *Universe* 8(7), pp. 381–415.

Blum, J. et al. (July 2017). "Evidence for the formation of comet 67P/Churyumov- Gerasimenko through gravitational collapse of a bound clump of pebbles". In: *Monthly Notices of the Royal Astronomical Society* 469, S755–S773.

Bockelée-Morvan, D. and N. Biver (May 2017). "The composition of cometary ices". In: *Philosophical Transactions of the Royal Society of London Series A* 375(2097), 20160252, p. 11.

Bockelée-Morvan, D. et al. (2004). "The composition of cometary volatiles". In: *Comets II*. Ed. by M. C. Festou, H. U. Keller, and H. Weaver. University of Arizona Press, pp. 391–424.

Bockelée-Morvan, D. et al. (Nov. 2015). "First observations of $H_2O$ and $CO_2$ vapor in comet 67P/Churyumov-Gerasimenko made by VIRTIS onboard Rosetta". In: *Astronomy and Astrophysics* 583, A6.

Bockelée-Morvan, D. et al. (Nov. 2016). "Evolution of $CO_2$, $CH_4$, and OCS abundances relative to $H_2O$ in the coma of comet 67P around perihelion from Rosetta/VIRTIS-H observations". In: *Monthly Notices of the Royal Astronomical Society* 462, S170–S183.

Bockelée-Morvan, D. et al. (Aug. 2022). "Water, hydrogen cyanide, carbon monoxide, and dust production from distant comet 29P/Schwassmann-Wachmann 1". In: *Astronomy and Astrophysics* 664, A95.

Bodewits, D. et al. (Apr. 2020). "The carbon monoxide-rich interstellar comet 2I/Borisov". In: *Nature Astronomy* 4, pp. 867–871.

Boehnhardt, H. (2004). "Split comets". In: *Comets II*. Ed. by M. C. Festou, H. U. Keller, and H. Weaver. University of Arizona Press, pp. 301–316.

Boehnhardt, H. et al. (May 2017). "The Philae lander mission and science overview". In: *Philosophical Transactions of the Royal Society of London Series A* 375(2097), p. 20160248.

Boehnke, P. and T. M. Harrison (Sept. 2016). "Illusory Late Heavy Bombardments". In: *Proceedings of the National Academy of Science* 113(39), pp. 10802–10806.

Bolmont, E. et al. (June 2016). "Habitability of planets on eccentric orbits: Limits of the mean flux approximation". In: *Astronomy and Astrophysics* 591, A106.

Bottke, W. F. and M. D. Norman (Aug. 2017). "The Late Heavy Bombardment". In: *Annual Review of Earth and Planetary Sciences* 45(1), pp. 619–647.

Brasser, R. and A. Morbidelli (July 2013). "Oort cloud and Scattered Disc formation during a late dynamical instability in the Solar System". In: *Icarus* 225(1), pp. 40–49.

Brasser, R. and J. .-.-H. Wang (Jan. 2015). "An updated estimate of the number of Jupiter-family comets using a simple fading law". In: *Astronomy and Astrophysics* 573, A102.

Brasser, R. et al. (Nov. 2009). "Constructing the secular architecture of the solar system II: the terrestrial planets". In: *Astronomy and Astrophysics* 507(2), pp. 1053–1065.

Brasser, R. et al. (Jan. 2012). "Reassessing the formation of the inner Oort cloud in an embedded star cluster". In: *Icarus* 217(1), pp. 1–19.

Brown, G. N. J. and W. T. Ziegler (1980). "Vapor Pressure and Heats of Vaporization and Sublimation of Liquids and Solids of Interest in Cryogenics Below 1-atm Pressure". In: *Advances in Cryogenic Engineering, Vol. 25*. Ed. by K. D. Timmerhaus and H. A. Snyder. Springer Science+Business Media, LLC, New York, pp. 662–670.

Brown, M. E. (May 2001). "The Inclination Distribution of the Kuiper Belt". In: *The Astronomical Journal* 121(5), pp. 2804–2814.

Brown, M. E., C. A. Trujillo, and D. Rabinowitz (Dec. 2004). "Discovery of a Candidate Inner Oort Cloud Planetoid". In: *The Astrophysical Journal* 617(1), pp. 645–649.

Brownlee, D. E. et al. (Oct. 2003). "Stardust: Comet and interstellar dust sample return mission". In: *Journal of Geophysical Research (Planets)* 108(E10), p. 8111.

Cabral, N. et al. (Jan. 2019). "OSSOS. XI. No active centaurs in the Outer Solar System Origins Survey". In: *Astronomy and Astrophysics* 621, A102.

Capaccioni, F. et al. (Jan. 2015). "The organic-rich surface of comet 67P/ Churyumov- Gerasimenko as seen by VIRTIS/ Rosetta". In: *Science* 347, aaa0628.

Capria, M. T. et al. (Sept. 1996). "A P/Wirtanen evolution model". In: *Planetary and Space Science* 44(9), pp. 987–1000.

Capria, M. T. et al. (June 2000). "Chiron Activity and Thermal Evolution". In: *The Astronomical Journal* 119(6), pp. 3112–3118.

Capria, M. T. et al. (Sept. 2009). "Thermal modeling of the active Centaur P/2004 A1 (LONEOS)". In: *Astronomy and Astrophysics* 504(1), pp. 249–258.

Carusi, A., Ľ. Kresák, and G. B. Valsecchi (Jan. 1995). "Conservation of the Tisserand Parameter at Close Encounters of Interplanetary Objects with Jupiter". In: *Earth Moon and Planets* 68(1-3), pp. 71–94.

Cazaux, S. et al. (Nov. 2017). "CO Depletion: A Microscopic Perspective". In: *The Astrophysical Journal* 849(2), 80, p. 12.

Charnoz, S. and A. Morbidelli (Nov. 2003). "Coupling dynamical and collisional evolution of small bodies:. an application to the early ejection of planetesimals from the Jupiter-Saturn region". In: *Icarus* 166(1), pp. 141–156.

Chiang, E. and A. N. Youdin (May 2010). "Forming Planetesimals in Solar and Extrasolar Nebulae". In: *Annual Review of Earth and Planetary Sciences* 38, pp. 493–522.

Choi, Y.-J. et al. (Dec. 2002). "Long-Term Evolution of Objects in the Kuiper Belt Zone—Effects of Insolation and Radiogenic Heating". In: *Icarus* 160(2), pp. 300–312.

Choukroun, M. et al. (Apr. 2020). "Dust-to-Gas and Refractory-to-Ice Mass Ratios of Comet 67P/Churyumov-Gerasimenko from Rosetta Observations". In: *Space Science Reviews* 216(3), p. 44.

Clayton, J. O. and W. F. Giauque (Jan. 1932). "The heat capacity and entropy of carbon monoxide: Heat of vaporization. Vapor pressures of solid and liquid. Free energy to 5000 K from spectroscopic data". In: *Journal of the American Chemical Society* 54, pp. 2610–2626.

Clement, M. S. et al. (Sept. 2018). "Mars' growth stunted by an early giant planet instability". In: *Icarus* 311, pp. 340–356.

Cochran, A. L. et al. (Dec. 2015). "The Composition of Comets". In: *Space Science Reviews* 197(1-4), pp. 9–46.

Collings, M. P. et al. (Feb. 2003). "Carbon Monoxide Entrapment in Interstellar Ice Analogs". In: *The Astrophysical Journal* 583(2), pp. 1058–1062.

Cook, R. D. (1995). *Finite Element Modeling for Stress Analysis*. John Wiley & Son, Inc. ISBN: 0-471-10774-3.

Coradini, A. et al. (Oct. 1997). "Transition Elements between Comets and Asteroids". In: *Icarus* 129(2), pp. 317–336.

Cordiner, M. A. et al. (Apr. 2020). "Unusually high CO abundance of the first active interstellar comet". In: *Nature Astronomy* 4, pp. 861–866.

Crank, J. and P. Nicolson (1947). "A practical method for numerical evaluation of solutions of partial differential equations of the heat-conduction type". In: *Mathematical Proceedings of the Cambridge Philosophical Society* 43(1), pp. 50–67.

Cremonese, G. et al. (Dec. 1997). "Neutral Sodium from Comet Hale-Bopp: A Third Type of Tail". In: *The Astrophysical Journal Letters* 490(2), pp. L199–L202.

Cremonese, G. et al. (Jan. 2002). "Neutral sodium tails in comets". In: *Advances in Space Research* 29(8), pp. 1187–1197.

Crovisier, J. et al. (Mar. 1997). "The spectrum of comet Hale-Bopp (C/1995 O1) observed with the infrared space observatory at 2.9 astronomical units from the sun." In: *Science* 275, pp. 1904–1907.

Curtis, H. D. (2014). *Orbital Mechanics for Engineering Students*. Third Edition. Elsevier Butterworth-Heinemann. ISBN: 978-0-08-097747-8.

Cuzzi, J. N., R. C. Hogan, and W. F. Bottke (Aug. 2010). "Towards initial mass functions for asteroids and Kuiper Belt Objects". In: *Icarus* 208(2), pp. 518–538.

Cuzzi, J. N., R. C. Hogan, and K. Shariff (Nov. 2008). "Toward Planetesimals: Dense Chondrule Clumps in the Protoplanetary Nebula". In: *The Astrophysical Journal* 687(2), pp. 1432–1447.

Davidsson, B. J. R. (Aug. 2021). "Thermophysical evolution of planetesimals in the primordial disc". In: *Monthly Notices of the Royal Astronomical Society* 505(4), pp. 5654–5685.

Davidsson, B. J. R. and Y. V. Skorov (Sept. 2002). "On the Light-Absorbing Surface Layer of Cometary Nuclei. II. Thermal Modeling". In: *Icarus* 159(1), pp. 239–258.

Davidsson, B. J. R. et al. (July 2016). "The primordial nucleus of comet 67P/Churyumov-Gerasimenko". In: *Astronomy and Astrophysics* 592, A 63, A63.

De la Fuente Marcos, C. et al. (May 2021). "The active centaur 2020 $MK_4$". In: *Astronomy and Astrophysics* 649, A85.

De Sanctis, M. C., M. T. Capria, and A. Coradini (May 2001). "Thermal Evolution and Differentiation of Edgeworth-Kuiper Belt Objects". In: *The Astronomical Journal* 121(5), pp. 2792–2799.

De Sanctis, M. C., M. T. Capria, and A. Coradini (Dec. 2005). "Thermal evolution model of 67P/Churyumov-Gerasimenko, the new Rosetta target". In: *Astronomy and Astrophysics* 444(2), pp. 605–614.

De Sanctis, M. C. et al. (Sept. 2000). "Thermal Evolution of the Centaur Object 5145 Pholus". In: *The Astronomical Journal* 120(3), pp. 1571–1578.

Dello Russo, N. et al. (Nov. 2016). "Emerging trends and a comet taxonomy based on the volatile chemistry measured in thirty comets with high-resolution infrared spectroscopy between 1997 and 2013". In: *Icarus* 278, pp. 301–332.

Di Sisto, R. P. and A. Brunini (Sept. 2007). "The origin and distribution of the Centaur population". In: *Icarus* 190(1), pp. 224–235.

Di Sisto, R. P., A. Brunini, and G. C. de Elia (Sept. 2010). "Dynamical evolution of escaped plutinos, another source of Centaurs". In: *Astronomy and Astrophysics* 519, A112.

Di Sisto, R. P., J. A. Fernández, and A. Brunini (Sept. 2009). "On the population, physical decay and orbital distribution of Jupiter family comets: Numerical simulations". In: *Icarus* 203(1), pp. 140–154.

Dodson-Robinson, S. E. et al. (Apr. 2009). "Ice lines, planetesimal composition and solid surface density in the solar nebula". In: *Icarus* 200(2), pp. 672–693.

Dones, L., H. F. Levison, and M. Duncan (Jan. 1996). "On the Dynamical Lifetimes of Planet-Crossing Objects". In: *Completing the Inventory of the Solar System*. Ed. by T. Rettig and J. M. Hahn. Vol. 107. Astronomical Society of the Pacific Conference Series, pp. 233–244.

Dones, L. et al. (2004). "Oort cloud formation and dynamics". In: *Comets II*. Ed. by M. C. Festou, H. U. Keller, and H. Weaver. University of Arizona Press, pp. 153–174.

Dones, L. et al. (Dec. 2015). "Origin and Evolution of the Cometary Reservoirs". In: *Space Science Reviews* 197(1-4), pp. 191–269.

Douglas, J. J. and J. B. F. Jones (1963). "On Predictor-Corrector Methods for Nonlinear Parabolic Differential Equations". In: *Journal of the Society for Industrial and Applied Mathematics* 11(1), pp. 195–204.

Drążkowska, J., Y. Alibert, and B. Moore (Oct. 2016). "Close-in planetesimal formation by pile-up of drifting pebbles". In: *Astronomy and Astrophysics* 594, A105.

Drążkowska, J. and C. P. Dullemond (Dec. 2014). "Can dust coagulation trigger streaming instability?" In: *Astronomy and Astrophysics* 572, A78.

Drozdovskaya, M. N. et al. (Oct. 2016). "Cometary ices in forming protoplanetary disc midplanes". In: *Monthly Notices of the Royal Astronomical Society* 462(1), pp. 977–993.

Duncan, M. J. and H. F. Levison (June 1997). "A scattered comet disk and the origin of Jupiter family comets". In: *Science* 276, pp. 1670–1672.

Duncan, M. J., H. F. Levison, and S. M. Budd (Dec. 1995). "The Dynamical Structure of the Kuiper Belt". In: *The Astronomical Journal* 110, pp. 3073–3081.

Duncan, M., T. Quinn, and S. Tremaine (Nov. 1987). "The Formation and Extent of the Solar System Comet Cloud". In: *The Astronomical Journal* 94, p. 1330.

Duncan, M., T. Quinn, and S. Tremaine (May 1988). "The Origin of Short-Period Comets". In: *The Astrophysical Journal Letters* 328, p. L69.

Dybczyński, P. A. and M. Królikowska (Mar. 2015). "Near-parabolic comets observed in 2006-2010 - II. Their past and future motion under the influence of the Galaxy field and known nearby stars". In: *Monthly Notices of the Royal Astronomical Society* 448(1), pp. 588–600.

Edgeworth, K. E. (July 1943). "The evolution of our planetary system". In: *Journal of the British Astronomical Association* 53, pp. 181–188.

Edgeworth, K. E. (Jan. 1949). "The origin and evolution of the Solar System". In: *Monthly Notices of the Royal Astronomical Society* 109, pp. 600–609.

Eisenberg, D. and W. Kauzmann (2005). *The Structure and Properties of Water*. Oxford University Press. ISBN: 9780198570264.

Ellsworth, K. and G. Schubert (June 1983). "Saturn's icy satellites: Thermal and structural models". In: *Icarus* 54(3), pp. 490–510.

Emel'yanenko, V. V., D. J. Asher, and M. E. Bailey (Jan. 2003). "A new class of trans-Neptunian objects in high-eccentricity orbits". In: *Monthly Notice of the Royal Astronomical Society* 338(2), pp. 443–451.

Enzian, A., H. Cabot, and J. Klinger (Mar. 1997). "A 2 1/2 D thermodynamic model of cometary nuclei. I. Application to the activity of comet 29P/ Schwassmann- Wachmann 1." In: *Astronomy and Astrophysics* 319, pp. 995–1006.

Escribano, R. M. et al. (Aug. 2013). "Crystallization of CO2 ice and the absence of amorphous CO2 ice in space". In: *Proceedings of the National Academy of Science* 110(32), pp. 12899–12904.

Espinasse, S. et al. (Dec. 1989). "A method of estimating temperature profiles and chemical differentiation in the near surface layers of porous comet nuclei - first results for comet P/Churyumov-Gerasimenko." In: *Physics and Mechanics of Cometary Materials*. Ed. by J. J. Hunt and T. D. Guyenne. Vol. 302. ESA Special Publication, pp. 185–190.

Espinasse, S. et al. (Aug. 1991). "Modeling of the thermal behavior and of the chemical differentiation of cometary nuclei". In: *Icarus* 92(2), pp. 350–365.

Espinasse, S. et al. (June 1993). "Thermal evolution and differentiation of a short-period comet". In: *Planetary and Space Science* 41(6), pp. 409–427.

Faggi, S. et al. (Jan. 2023). "Strongly Depleted Methanol and Hypervolatiles in Comet C/2021 A1 (Leonard): Signatures of Interstellar Chemistry?" In: *The Planetary Science Journal* 4(1), p. 8.

Fanale, F. P. and J. R. Salvail (Dec. 1984). "An idealized short-period comet model: Surface insolation, $H_2O$ flux, dust flux, and mantle evolution". In: *Icarus* 60(3), pp. 476–511.

Fanale, F. P. and J. R. Salvail (Dec. 1987). "The loss and depth of CO $_2$ ice in comet nuclei". In: *Icarus* 72(3), pp. 535–554.

Fanale, F. P. and J. R. Salvail (Apr. 1990). "The influence of CO ice on the activity and near-surface differentiation of comet nuclei". In: *Icarus* 84(2), pp. 403–413.

Fanale, F. P. and J. R. Salvail (Feb. 1997). "The Cometary Activity of Chiron: A Stratigraphic Model". In: *Icarus* 125(2), pp. 397–405.

Farnham, T. L., M. S. P. Kelley, and J. M. Bauer (Dec. 2021). "Early Activity in Comet C/2014 UN271 Bernardinelli-Bernstein as Observed by TESS". In: *The Planetary Science Journal* 2(6), p. 236.

Fayolle, E. C. et al. (May 2011). "Laboratory $H_2O$:$CO_2$ ice desorption data: entrapment dependencies and its parameterization with an extended three-phase model". In: *Astronomy and Astrophysics* 529, A74, A74.

Feistel, R. and W. Wagner (Jan. 2007). "Sublimation pressure and sublimation enthalpy of H $_2$O ice Ih between 0 and 273.16 K". In: *Geochimica et Cosmochimica Acta* 71(1), pp. 36–45.

Fernández, J. A. (Sept. 1997). "The Formation of the Oort Cloud and the Primitive Galactic Environment". In: *Icarus* 129(1), pp. 106–119.

Fernández, J. A. (2005). *Comets - Nature, Dynamics, Origin and their Cosmological Relevance*. First Edition. Springer Dordrecht. ISBN: 978-1-4020-3490-9.

Fernández, J. A., M. Helal, and T. Gallardo (Sept. 2018). "Dynamical evolution and end states of active and inactive Centaurs". In: *Planetary and Space Science* 158, pp. 6–15.

Fernández, Y. R. (Aug. 2009). "That's the way the comet crumbles: Splitting Jupiter-family comets". In: *Planetary and Space Science* 57(10), pp. 1218–1227.

Festou, M. C., H. U. Keller, and H. A. Weaver (2004). "A brief conceptual history of cometary science". In: *Comets II*. Ed. by M. C. Festou, H. U. Keller, and H. Weaver. University of Arizona Press, pp. 3–16.

Filacchione, G. et al. (Jan. 2016a). "Exposed water ice on the nucleus of comet 67P/Churyumov-Gerasimenko". In: *Nature* 529(7586), pp. 368–372.

Filacchione, G. et al. (Dec. 2016b). "Seasonal exposure of carbon dioxide ice on the nucleus of comet 67P/Churyumov-Gerasimenko". In: *Science* 354(6319), pp. 1563–1566.

Filacchione, G. et al. (Feb. 2019). "Comet 67P/CG Nucleus Composition and Comparison to Other Comets". In: *Space Science Reviews* 215(1), p. 19.

Fornasier, S. et al. (Dec. 2016). "Rosetta's comet 67P/ Churyumov- Gerasimenko sheds its dusty mantle to reveal its icy nature". In: *Science* 354, pp. 1566–1570.

Fornasier, S. et al. (Apr. 2023). "Volatile exposures on the 67P/Churyumov-Gerasimenko nucleus". In: *Astronomy and Astrophysics* 672, A136.

Fouchard, M. et al. (July 2011). "The key role of massive stars in Oort cloud comet dynamics". In: *Icarus* 214(1), pp. 334–347.

Fouchard, M. et al. (Aug. 2017). "On the present shape of the Oort cloud and the flux of ;new; comets". In: *Icarus* 292, pp. 218–233.

Fraser, W. C. et al. (Oct. 2022). "The Transition from the Kuiper Belt to the Jupiter-Family (Comets)". In: *arXiv e-prints*, arXiv:2210.16354.

Fray, N. and B. Schmitt (Dec. 2009). "Sublimation of ices of astrophysical interest: A bibliographic review". In: *Planetary and Space Science* 57(14-15), pp. 2053–2080.

Fulle, M. (2004). "Motion of cometary dust". In: *Comets II*. Ed. by M. C. Festou, H. U. Keller, and H. Weaver. University of Arizona Press, p. 565575.

Fulle, M. et al. (Jan. 2019). "The refractory-to-ice mass ratio in comets". In: *Monthly Notices of the Royal Astronomical Society* 482(3), pp. 3326–3340.

Gerakines, P. A. et al. (Sept. 1999). "Observations of Solid Carbon Dioxide in Molecular Clouds with the Infrared Space Observatory". In: *The Astrophysical Journal* 522(1), pp. 357–377.

Ghormley, J. A. and C. J. Hochanadel (Jan. 1971). "Amorphous Ice: Density and Reflectivity". In: *Science* 171(3966), pp. 62–64.

Giauque, W. F. and C. J. Egan (Jan. 1937). "Carbon Dioxide. The Heat Capacity and Vapor Pressure of the Solid. The Heat of Sublimation. Thermodynamic and Spectroscopic Values of the Entropy". In: *The Journal of Chemical Physics* 5(1), pp. 45–54.

Giauque, W. F. and J. W. Stout (Jan. 1936). "The entropy of water and third law of thermodynamics. The heat capacity of ice from 15 to 273K". In: *Journal of the American Chemical Society* 58, pp. 1144–1144.

Gkotsinas, A., A. Guilbert-Lepoutre, and S. N. Raymond (Feb. 2023). "On Averaging Eccentric Orbits: Implications for the Long-term Thermal Evolution of Comets". In: *The Astronomical Journal* 165(2), p. 67.

Gkotsinas, A. et al. (Mar. 2022). "Thermal Processing of Jupiter-family Comets during Their Chaotic Orbital Evolution". In: *The Astrophysical Journal* 928(1), p. 43.

Gladman, B., B. G. Marsden, and C. Vanlaerhoven (2008). "Nomenclature in the Outer Solar System". In: *The Solar System Beyond Neptune*. Ed. by M. A. Barucci et al. University of Arizona Press, pp. 43–57.

Gladman, B. et al. (July 2012). "The Resonant Trans-Neptunian Populations". In: *The Astronomical Journal* 144(1), p. 23.

Goesmann, F. et al. (July 2015). "Organic compounds on comet 67P/ Churyumov- Gerasimenko revealed by COSAC mass spectrometry". In: *Science* 349(6247), p. 2.689.

Golabek, G. J. and M. Jutzi (July 2021). "Modification of icy planetesimals by early thermal evolution and collisions: Constraints for formation time and initial size of comets and small KBOs". In: *Icarus* 363, p. 114437.

Goldreich, P. and W. R. Ward (Aug. 1973). "The Formation of Planetesimals". In: *The Astrophysical Journal* 183, pp. 1051–1062.

Gomes, R. S. (Feb. 2003). "The origin of the Kuiper Belt high-inclination population". In: *Icarus* 161(2), pp. 404–418.

Gomes, R. S. et al. (May 2005). "Origin of the cataclysmic Late Heavy Bombardment period of the terrestrial planets". In: *Nature* 435(7041), pp. 466–469.

Gómez, P. C., M. Á. Satorre Aznar, and R. Escribano (Apr. 2020). "Density and porosity of amorphous water ice by DFT methods". In: *Chemical Physics Letters* 745, 137222, p. 137222.

Groussin, O. et al. (June 2019). "The Thermal, Mechanical, Structural, and Dielectric Properties of Cometary Nuclei After Rosetta". In: *Space Science Reviews* 215(4), p. 29.

Guilbert-Lepoutre, A. (Oct. 2012). "Survival of Amorphous Water Ice on Centaurs". In: *The Astronomical Journal* 144(4), 97, p. 97.

Guilbert-Lepoutre, A. (Mar. 2014). "Survival of water ice in Jupiter Trojans". In: *Icarus* 231, pp. 232–238.

Guilbert-Lepoutre, A. et al. (May 2011). "New 3D thermal evolution model for icy bodies application to trans-Neptunian objects". In: *Astronomy and Astrophysics* 529, A71, A71.

Guilbert-Lepoutre, A. et al. (Nov. 2016). "Modelling the evolution of a comet subsurface: implications for 67P/Churyumov-Gerasimenko". In: *Monthly Notices of the Royal Astronomical Society* 462, S146–S155.

Guilbert-Lepoutre, A. et al. (Jan. 2023). "The Gateway from Centaurs to Jupiter-family Comets: Thermal and Dynamical Evolution". In: *The Astrophysical Journal* 942(2), p. 92.

Guillot, M. and S. McCool (2015). "Effect of boundary condition approximation on convergence and accuracy of a finite volume discretization of the transient heat conduction equation". In: *International Journal of Numerical Methods for Heat and Fluid Flow* 25(4), pp. 950–972.

Gundlach, B. and J. Blum (June 2012). "Outgassing of icy bodies in the Solar System - II: Heat transport in dry, porous surface dust layers". In: *Icarus* 219(2), pp. 618–629.

Gundlach, B. et al. (Oct. 2018). "Sintering and sublimation of micrometre-sized water-ice particles: the formation of surface crusts on icy Solar System bodies". In: *Monthly Notices of the Royal Astronomical Society* 479(4), pp. 5272–5287.

Gutiérrez, P. J. et al. (Mar. 2000). "A study of water production and temperatures of rotating irregularly shaped cometary nuclei". In: *Astronomy and Astrophysics* 355, pp. 809–817.

Guzik, P. et al. (Jan. 2020). "Initial characterization of interstellar comet 2I/Borisov". In: *Nature Astronomy* 4, pp. 53–57.

Harker, D. E., C. E. Woodward, and D. H. Wooden (Oct. 2005). "The Dust Grains from 9P/Tempel 1 Before and After the Encounter with Deep Impact". In: *Science* 310(5746), pp. 278–280.

Harrington Pinto, O. et al. (Nov. 2022). "A Survey of CO, $CO_2$, and $H_2O$ in Comets and Centaurs". In: *The Planetary Science Journal* 3(11), p. 247.

Hartmann, W. K., D. J. Tholen, and D. P. Cruikshank (Jan. 1987). "The relationship of active comets, "extinct" comets, and dark asteroids". In: *Icarus* 69(1), pp. 33–50.

Haruyama, J. et al. (Aug. 1993). "Thermal history of comets during residence in the Oort cloud: Effect of radiogenic heating in combination with the very low thermal conductivity of amorphous ice". In: *Journal of Geophysical Research* 98(E8), pp. 15079–15090.

Hassig, M. et al. (Jan. 2015). "Time variability and heterogeneity in the coma of 67P/Churyumov-Gerasimenko". In: *Science* 347(6220), aaa0276, aaa0276.

Heisler, J. and S. Tremaine (Jan. 1986). "The influence of the Galactic tidal field on the Oort comet cloud". In: *Icarus* 65(1), pp. 13–26.

Henke, S. et al. (Jan. 2012). "Thermal evolution and sintering of chondritic planetesimals". In: *Astronomy and Astrophysics* 537, A45.

Herique, A. et al. (Nov. 2016). "Cosmochemical implications of CONSERT permittivity characterization of 67P/CG". In: *Monthly Notices of the Royal Astronomical Society* 462, S516–S532.

Herman, G. and M. Podolak (Feb. 1985). "Numerical simulation of comet nuclei I. Water-ice comets". In: *Icarus* 61(2), pp. 252–266.

Hills, J. G. (Nov. 1981). "Comet showers and the steady-state infall of comets from the Oort cloud." In: *The Astronomical Journal* 86, pp. 1730–1740.

Horner, J., N. W. Evans, and M. E. Bailey (Nov. 2004a). "Simulations of the population of Centaurs - I. The bulk statistics". In: *Monthly Notices of the Royal Astronomical Society* 354(3), pp. 798–810.

Horner, J., N. W. Evans, and M. E. Bailey (Dec. 2004b). "Simulations of the population of Centaurs - II. Individual objects". In: *Monthly Notices of the Royal Astronomical Society* 355(2), pp. 321–329.

Hudson, R. L. and B. Donn (Dec. 1991). "An experimental study of the sublimation of water ice and the release of trapped gases". In: *Icarus* 94(2), pp. 326–332.

Huebner, W. F. et al. (Jan. 1999). "Results from the Comet Nucleus Model Team at the International Space Science Institute, Bern, Switzerland". In: *Advances in Space Research* 23(7), pp. 1283–1298.

Huebner, W. F. et al. (2006). *Heat and Gas Diffusion in Comet Nuclei.* Vol. 133. International Space Science Institute Bern.

Hui, M.-T., D. Farnocchia, and M. Micheli (Apr. 2019). "C/2010 U3 (Boattini): A Bizarre Comet Active at Record Heliocentric Distance". In: *The Astronomical Journal* 157(4), p. 162.

Izidoro, A., B. Bitsch, and R. Dasgupta (July 2021). "The Effect of a Strong Pressure Bump in the Sun's Natal Disk: Terrestrial Planet Formation via Planetesimal Accretion Rather than Pebble Accretion". In: *The Astrophysical Journal* 915(1), p. 62.

Jewitt, D. (May 2009). "The Active Centaurs". In: *The Astronomical Journal* 137(5), pp. 4296–4312.
Jewitt, D. (Dec. 2015). "Color Systematics of Comets and Related Bodies". In: *The Astronomical Journal* 150(6), pp. 201–219.
Jewitt, D. and J. Luu (Apr. 1993). "Discovery of the candidate Kuiper belt object 1992 $QB_1$". In: *Nature* 362(6422), pp. 730–732.
Jewitt, D. et al. (Oct. 2017). "A Comet Active Beyond the Crystallization Zone". In: *The Astrophysical Journal Letters* 847(2), p. L19.
Jewitt, D. et al. (Jan. 2020). "The Nucleus of Interstellar Comet 2I/Borisov". In: *The Astrophysical Journal Letters* 888(2), p. L23.
Jewitt, D. et al. (Apr. 2021). "Cometary Activity Begins at Kuiper Belt Distances: Evidence from C/2017 K2". In: *The Astronomical Journal* 161(4), p. 188.
Johansen, A. and A. Youdin (June 2007). "Protoplanetary Disk Turbulence Driven by the Streaming Instability: Nonlinear Saturation and Particle Concentration". In: *The Astrophysical Journal* 662(1), pp. 627–641.
Jorda, L. et al. (Oct. 2016). "The global shape, density and rotation of Comet 67P/Churyumov-Gerasimenko from preperihelion Rosetta/OSIRIS observations". In: *Icarus* 277, pp. 257–278.
Julian, W. H., N. H. Samarasinha, and M. J. S. Belton (Mar. 2000). "Thermal Structure of Cometary Active Regions: Comet 1P/Halley". In: *Icarus* 144(1), pp. 160–171.
Kaib, N. A. (Apr. 2022). "Comet fading begins beyond Saturn". In: *Science Advances* 8(13), eabm9130.
Kaib, N. A. and T. Quinn (Sept. 2008). "The formation of the Oort cloud in open cluster environments". In: *Icarus* 197(1), pp. 221–238.
Kaib, N. A. and T. Quinn (Sept. 2009). "Reassessing the Source of Long-Period Comets". In: *Science* 325(5945), p. 1234.
Kaib, N. A., R. Roškar, and T. Quinn (Oct. 2011). "Sedna and the Oort Cloud around a migrating Sun". In: *Icarus* 215(2), pp. 491–507.
Kaib, N. A. and S. S. Sheppard (Nov. 2016). "Tracking Neptune's Migration History through High-perihelion Resonant Trans-Neptunian Objects". In: *The Astronomical Journal* 152(5), p. 133.
Keller, H. U. (Dec. 1989). "Comets - dirty snowballs or icy dirtballs?" In: *Physics and Mechanics of Cometary Materials*. Ed. by J. J. Hunt and T. D. Guyenne. Vol. 302. ESA Special Publication, pp. 39–45.
Keller, H. U. et al. (May 1986). "First Halley Multicolour Camera imaging results from Giotto". In: *Nature* 321, pp. 320–326.
Keller, H. U. et al. (Nov. 2015). "Insolation, erosion, and morphology of comet 67P/Churyumov-Gerasimenko". In: *Astronomy and Astrophysics* 583, A34, A34.
Kelley, M. S. P. et al. (Mar. 2017). "Mid-infrared spectra of comet nuclei". In: *Icarus* 284, pp. 344–358.

Kelley, M. S. P. et al. (July 2022). "A Look at Outbursts of Comet C/2014 $UN_{271}$ (Bernardinelli-Bernstein) near 20 au". In: *The Astrophysical Journal Letters* 933(2), p. L44.

Kelley, M. S. et al. (Oct. 2013). "Dust Properties of Three Oort Cloud Comets and Comet 67P/Churyumov-Gerasimenko". In: *AAS/Division for Planetary Sciences Meeting Abstracts #45*. Vol. 45. AAS/Division for Planetary Sciences Meeting Abstracts, p. 413.08.

Kissel, J. and F. R. Krueger (Apr. 1987). "The organic component in dust from comet Halley as measured by the PUMA mass spectrometer on board Vega 1". In: *Nature* 326(6115), pp. 755–760.

Kissel, J. et al. (May 1986a). "Composition of comet Halley dust particles from Giotto observations". In: *Nature* 321, pp. 336–337.

Kissel, J. et al. (May 1986b). "Composition of comet Halley dust particles from Vega observations". In: *Nature* 321, pp. 280–282.

Kissel, J. et al. (June 2004). "The Cometary and Interstellar Dust Analyzer at Comet 81P/Wild 2". In: *Science* 304(5678), pp. 1774–1776.

Klinger, J. (July 1980). "Influence of a Phase Transition of Ice on the Heat and Mass Balance of Comets". In: *Science* 209(4453), pp. 271–272.

Knight, M. M., R. Kokotanekova, and N. H. Samarasinha (Apr. 2023). "Physical and Surface Properties of Comet Nuclei from Remote Observations". In: *arXiv e-prints*, arXiv:2304.09309.

Kofman, W. et al. (July 2015). "Properties of the 67P/Churyumov-Gerasimenko interior revealed by CONSERT radar". In: *Science* 349(6247), p. 2.639.

Kokotanekova, R. et al. (Oct. 2021). "Observations of the newly discovered comet C/2014 UN271 (Bernardinelli-Bernstein) active beyond 20 au". In: *AAS/Division for Planetary Sciences Meeting Abstracts*. Vol. 53. AAS/Division for Planetary Sciences Meeting Abstracts, p. 301.04.

Kossacki, K. J., S. Ł. Szutowicz, and J. Leliwa-Kopystyński (Nov. 1999a). "Comet 46P/Wirtanen: Evolution of the Subsurface Layer". In: *Icarus* 142(1), pp. 202–218.

Kossacki, K. J. et al. (May 1994). "The influence of grain sintering on the thermoconductivity of porous ice". In: *Planetary and Space Science* 42(5), pp. 383–389.

Kossacki, K. J. et al. (Dec. 1999b). "Sublimation coefficient of water ice under simulated cometary-like conditions". In: *Planetary and Space Science* 47(12), pp. 1521–1530.

Kossacki, K. J. et al. (Nov. 2015). "Comet 67P/Churyumov-Gerasimenko: Hardening of the sub-surface layer". In: *Icarus* 260, pp. 464–474.

Kouchi, A. et al. (Apr. 1992). "Extremely Low Thermal Conductivity of Amorphous Ice: Relevance to Comet Evolution". In: *Astrophysical Journal Letters* 388, p. L73.

Kral, Q. et al. (Sept. 2021). "A molecular wind blows out of the Kuiper belt". In: *Astronomy and Astrophysics* 653, p. L11.

Krause, M. et al. (July 2011). "Thermal conductivity measurements of porous dust aggregates: I. Technique, model and first results". In: *Icarus* 214(1), pp. 286–296.

Kravchenko, Y. and I. Krupskii (1986). "Thermal conductivity of solid N2O and CO2". In: *Sov. J. Low Temperature Physics* 12, pp. 46–48.

Królikowska, M. and P. A. Dybczyński (Dec. 2017). "Oort spike comets with large perihelion distances". In: *Monthly Notices of the Royal Astronomical Society* 472(4), pp. 4634–4658.

Krueger, F. R., A. Korth, and J. Kissel (Apr. 1991). "The Organic Matter of Comet Halley as Inferred by Joint Gas Phase and Solid Phase Analyses". In: *Space Science Reviews* 56(1-2), pp. 167–175.

Kuhrt, E. (Dec. 1984). "Temperature profiles and thermal stresses in cometary nuclei". In: *Icarus* 60(3), pp. 512–521.

Kuhrt, E. and H. U. Keller (May 1994). "The Formation of Cometary Surface Crusts". In: *Icarus* 109(1), pp. 121–132.

Kuiper, G. P. (Jan. 1951). "On the Origin of the Solar System". In: *Proceedings of the National Academy of Science* 37(1), pp. 1–14.

Lamy, P. L., A. Herique, and I. Toth (Dec. 2015). "The Subsurface Structure and Density of Cometary Nuclei". In: *Space Science Reviews* 197(1-4), pp. 85–99.

Lasue, J. et al. (Dec. 2008). "Quasi-3-D model to describe topographic effects on non-spherical comet nucleus evolution". In: *Planetary and Space Science* 56(15), pp. 1977–1991.

Lecar, M. et al. (Apr. 2006). "On the Location of the Snow Line in a Protoplanetary Disk". In: *The Astrophysical Journal* 640(2), pp. 1115–1118.

Levasseur-Regourd, A.-C. et al. (Apr. 2018). "Cometary Dust". In: *Space Science Reviews* 214(3), p. 64.

Levison, H. F. (Jan. 1996). "Comet Taxonomy". In: *Completing the Inventory of the Solar System*. Ed. by T. Rettig and J. M. Hahn. Vol. 107. Astronomical Society of the Pacific Conference Series, pp. 173–191.

Levison, H. F. and M. J. Duncan (Mar. 1994). "The Long-Term Dynamical Behavior of Short-Period Comets". In: *Icarus* 108(1), pp. 18–36.

Levison, H. F. and M. J. Duncan (May 1997). "From the Kuiper Belt to Jupiter-Family Comets: The Spatial Distribution of Ecliptic Comets". In: *Icarus* 127(1), pp. 13–32.

Levison, H. F. and A. Morbidelli (Nov. 2003). "The formation of the Kuiper belt by the outward transport of bodies during Neptune's migration". In: *Nature* 426(6965), pp. 419–421.

Levison, H. F. et al. (July 2009). "Contamination of the asteroid belt by primordial trans-Neptunian objects". In: *Nature* 460(7253), pp. 364–366.

Levison, H. F. et al. (June 2010). "Capture of the Sun's Oort Cloud from Stars in Its Birth Cluster". In: *Science* 329(5988), pp. 187–190.

Levison, H. F. et al. (Nov. 2011). "Late Orbital Instabilities in the Outer Planets Induced by Interaction with a Self- gravitating Planetesimal Disk". In: *The Astronomical Journal* 142(5), p. 152.

Li, J.-Y. et al. (Feb. 2013). "Photometric properties of the nucleus of Comet 103P/Hartley 2". In: *Icarus* 222(2), pp. 559–570.

Li, J. et al. (May 2020). "Hubble Space Telescope Search for Activity in High-perihelion Objects". In: *The Astronomical Journal* 159(5), p. 209.

Lilly, E. et al. (Aug. 2021). "No Activity among 13 Centaurs Discovered in the Pan-STARRS1 Detection Database". In: *The Planetary Science Journal* 2(4), p. 155.

Lin, H. W. et al. (May 2014). "Pan-STARRS 1 Observations of the Unusual Active Centaur P/2011 S1(Gibbs)". In: *The Astronomical Journal* 147(5), p. 114.

Lisse, C. M. et al. (Mar. 2021). "On the origin & thermal stability of Arrokoth's and Pluto's ices". In: *Icarus* 356, p. 114072.

Lisse, C. M. et al. (May 2022). "A Predicted Dearth of Majority Hypervolatile Ices in Oort Cloud Comets". In: *The Planetary Science Journal* 3(5), p. 112.

Liu, B., S. N. Raymond, and S. A. Jacobson (Apr. 2022). "Early Solar System instability triggered by dispersal of the gaseous disk". In: *Nature* 604(7907), pp. 643–646.

Loveless, S., D. Prialnik, and M. Podolak (Mar. 2022). "On the Structure and Long-term Evolution of Ice-rich Bodies". In: *The Astrophysical Journal* 927(2), p. 178.

Luna, R. et al. (Apr. 2008). "Thermal desorption of $CH_4$ retained in $CO_2$ ice". In: *Astrophysics and Space Science* 314(1-3), pp. 113–119.

Luna, R. et al. (Aug. 2022). "Density and Refractive Index of Carbon Monoxide Ice at Different Temperatures". In: *The Astrophysical Journal* 935(2), 134, p. 134.

Malamud, U. and D. Prialnik (Jan. 2015). "Modeling Kuiper belt objects Charon, Orcus and Salacia by means of a new equation of state for porous icy bodies". In: *Icarus* 246, pp. 21–36.

Malamud, U. et al. (Aug. 2022). "Are there any pristine comets? Constraints from pebble structure". In: *Monthly Notices of the Royal Astronomical Society* 514(3), pp. 3366–3394.

Malhotra, R. (Oct. 1993). "The origin of Pluto's peculiar orbit". In: *Nature* 365(6449), pp. 819–821.

Malhotra, R. (July 1995). "The Origin of Pluto's Orbit: Implications for the Solar System Beyond Neptune". In: *The Astronomical Journal* 110, p. 420.

Marboeuf, U. et al. (June 2012). "A cometary nucleus model taking into account all phase changes of water ice: amorphous, crystalline and clathrate". In: *Astronomy and Astrophysics* 542, A82, A82.

Mazzotta Epifani, E. et al. (Jan. 2017). "Nucleus of the active Centaur C/2011 P2 (PANSTARRS)". In: *Astronomy and Astrophysics* 597, A59.
Mazzotta Epifani, E. et al. (Dec. 2018). "523676 (2013 UL10): the first active red centaur". In: *Astronomy and Astrophysics* 620, A93.
Meech, K. J. and J. Svoren (2004). "Using cometary activity to trace the physical and chemical evolution of cometary nuclei". In: *Comets II*. Ed. by M. C. Festou, H. U. Keller, and H. Weaver. University of Arizona Press, pp. 317–335.
Meech, K. J. et al. (June 2009). "Activity of comets at large heliocentric distances pre-perihelion". In: *Icarus* 201(2), pp. 719–739.
Meech, K. J. et al. (Dec. 2017a). "A brief visit from a red and extremely elongated interstellar asteroid". In: *Nature* 552(7685), pp. 378–381.
Meech, K. J. et al. (Nov. 2017b). "CO-driven Activity in Comet C/2017 K2 (PANSTARRS)". In: *The Astrophysical Journal Letters* 849(1), p. L8.
Mekler, Y., D. Prialnik, and M. Podolak (June 1990). "Evaporation from a Porous Cometary Nucleus". In: *The Astrophysical Journal* 356, p. 682.
Mellon, M. T. (Nov. 1996). "Limits on the CO $_2$Content of the Martian Polar Deposits". In: *Icarus* 124(1), pp. 268–279.
Mendez, A. and E. G. Rivera-Valentin (Mar. 2017). "The Equilibrium Temperature of Planets in Elliptical Orbits". In: *The Astrophysical Journal Letters* 837(1), p. L1.
Mendis, D. A. and G. D. Brin (Dec. 1977). "Monochromatic Brightness Variations of Comets. II: Core-Mantle Model". In: *The Moon* 17(4), pp. 359–372.
Merk, R. and D. Prialnik (June 2003). "Early Thermal and Structural Evolution of Small Bodies in the Trans-Neptunian Zone". In: *Earth Moon and Planets* 92(1), pp. 359–374.
Merk, R. and D. Prialnik (Aug. 2006). "Combined modeling of thermal evolution and accretion of trans-neptunian objects—Occurrence of high temperatures and liquid water". In: *Icarus* 183(2), pp. 283–295.
Milani, A., A. M. Nobili, and M. Carpino (Jan. 1987). "Secular variations of the semimajor axes - Theory and experiments". In: *Astronomy and Astrophysics* 172(1-2), pp. 265–279.
Molaro, J. L. et al. (Feb. 2019). "The Microstructural Evolution of Water Ice in the Solar System Through Sintering". In: *Journal of Geophysical Research (Planets)* 124(2), pp. 243–277.
Morbidelli, A. et al. (May 2005). "Chaotic capture of Jupiter's Trojan asteroids in the early Solar System". In: *Nature* 435(7041), pp. 462–465.
Morbidelli, A. et al. (Nov. 2007). "Dynamics of the Giant Planets of the Solar System in the Gaseous Protoplanetary Disk and Their Relationship to the Current Orbital Architecture". In: *The Astronomical Journal* 134(5), pp. 1790–1798.
Morbidelli, A. et al. (Dec. 2009). "Asteroids were born big". In: *Icarus* 204(2), pp. 558–573.

Morbidelli, A. et al. (May 2018). "The timeline of the lunar bombardment: Revisited". In: *Icarus* 305, pp. 262–276.

Morbidelli, A. et al. (Jan. 2022). "Contemporary formation of early Solar System planetesimals at two distinct radial locations". In: *Nature Astronomy* 6, pp. 72–79.

Moukalled, F., L. Mangani, and M. Darwish (2015). *The Finite Volume Method in Computational Fluid Dynamics: An Advanced Introduction with OpenFOAM and Matlab*. Springer International Publishing. ISBN: 978-3-319-16873-9.

Mousis, O. et al. (Apr. 2017). "Impact of Radiogenic Heating on the Formation Conditions of Comet 67P/Churyumov-Gerasimenko". In: *The Astrophysical Journal Letters* 839(1), L4, p. L4.

Muñoz Caro, G. M. et al. (May 2016). "Photodesorption and physical properties of CO ice as a function of temperature". In: *Astronomy and Astrophysics* 589, A19, A19.

Nesvorný, D. (Sept. 2015). "Evidence for Slow Migration of Neptune from the Inclination Distribution of Kuiper Belt Objects". In: *The Astronomical Journal* 150(3), p. 73.

Nesvorný, D. (Sept. 2018). "Dynamical Evolution of the Early Solar System". In: *Annual Review of Astronomy and Astrophysics* 56, pp. 137–174.

Nesvorný, D. and A. Morbidelli (Oct. 2012). "Statistical Study of the Early Solar System's Instability with Four, Five, and Six Giant Planets". In: *The Astronomical Journal* 144(4), 117, p. 117.

Nesvorný, D. and D. Vokrouhlický (July 2016). "Neptune's Orbital Migration Was Grainy, Not Smooth". In: *The Astrophysical Journal* 825(2), p. 94.

Nesvorný, D., D. Vokrouhlický, and A. Morbidelli (May 2007). "Capture of Irregular Satellites during Planetary Encounters". In: *The Astronomical Journal* 133(5), pp. 1962–1976.

Nesvorný, D., D. Vokrouhlický, and F. Roig (Aug. 2016). "The Orbital Distribution of Trans-Neptunian Objects Beyond 50 au". In: *The Astrophysical Journal Letters* 827(2), p. L35.

Nesvorný, D. et al. (Aug. 2017). "Origin and Evolution of Short-period Comets". In: *The Astrophysical Journal* 845(1), 27, p. 27.

Notesco, G. and A. Bar-Nun (July 1996). "Enrichment of CO over N $_2$by Their Trapping in Amorphous Ice and Implications to Comet P/Halley". In: *Icarus* 122(1), pp. 118–121.

Oort, J. H. (Jan. 1950). "The structure of the cloud of comets surrounding the Solar System and a hypothesis concerning its origin". In: *Bulletin of the Astronomical Institutes of the Netherlands* 11, pp. 91–110.

Ootsubo, T. et al. (June 2012). "AKARI Near-infrared Spectroscopic Survey for $CO_2$ in 18 Comets". In: *The Astrophysical Journal* 752(1), 15, p. 15.

Orosei, R. et al. (June 1999). "Numerically improved thermochemical evolution models of comet nuclei". In: *Planetary and Space Science* 47(6-7), pp. 839–853.

Parhi, A. and D. Prialnik (June 2023). "Sublimation of ices during the early evolution of Kuiper belt objects". In: *Monthly Notices of the Royal Astronomical Society* 522(2), pp. 2081–2088.

Patankar, S. V. (1980). *Numerical Heat Transfer and Fluid Flow*. Hemisphere Publishing Corporation. ISBN: 0-07-048740-5.

Patankar, S. V. and B. R. Baliga (1978). "A new finite-diference scheme for parabolic differential equations". In: *Numerical Heat Transfer Part A-applications* 1, pp. 27–37.

Pfalzner, S. et al. (Aug. 2018). "Outer Solar System Possibly Shaped by a Stellar Fly-by". In: *The Astrophysical Journal* 863(1), p. 45.

Poch, O. et al. (Mar. 2020). "Ammonium salts are a reservoir of nitrogen on a cometary nucleus and possibly on some asteroids". In: *Science* 367(6483), aaw7462.

Pommerol, A. et al. (Nov. 2015). "OSIRIS observations of meter-sized exposures of $H_2O$ ice at the surface of 67P/Churyumov-Gerasimenko and interpretation using laboratory experiments". In: *Astronomy and Astrophysics* 583, A25.

Portegies Zwart, S. et al. (Aug. 2021). "Oort cloud Ecology. II. the chronology of the formation of the Oort cloud". In: *Astronomy and Astrophysics* 652, A144.

Preusker, F. et al. (Nov. 2015). "Shape model, reference system definition, and cartographic mapping standards for comet 67P/ Churyumov-Gerasimenko - Stereo - photogrammetric analysis of Rosetta/OSIRIS image data". In: *Astronomy and Astrophysics* 583, A33, A33.

Prialnik, D. (Mar. 1992). "Crystallization, Sublimation, and Gas Release in the Interior of a Porous Comet Nucleus". In: *The Astrophysical Journal* 388, p. 196.

Prialnik, D. (Oct. 2021). "Modeling sublimation of ices during the early evolution of Kuiper Belt objects". In: *AAS/Division for Planetary Sciences Meeting Abstracts*. Vol. 53. AAS/Division for Planetary Sciences Meeting Abstracts, p. 307.10.

Prialnik, D. and A. Bar-Nun (Feb. 1987). "On the Evolution and Activity of Cometary Nuclei". In: *The Astrophysical Journal* 313, p. 893.

Prialnik, D. and A. Bar-Nun (May 1988). "The formation of a permanent dust mantle and its effect on cometary activity". In: *Icarus* 74(2), pp. 272–283.

Prialnik, D., A. Bar-Nun, and M. Podolak (Aug. 1987). "Radiogenic Heating of Comets by 26Al and Implications for Their Time of Formation". In: *The Astrophysical Journal* 319, p. 993.

Prialnik, D., J. Benkhoff, and M. Podolak (2004). "Modeling the structure and activity of comet nuclei". In: *Comets II*. Ed. by M. C. Festou, H. U. Keller, and H. Weaver. University of Arizona Press, pp. 359–388.

Prialnik, D. and D. Jewitt (Sept. 2022). "Amorphous ice in comets: evidence and consequences". In: *arXiv e-prints*, arXiv:2209.05907.

Prialnik, D. and M. Podolak (Oct. 1995). "Radioactive heating of porous comet nuclei." In: *Icarus* 117(2), pp. 420–430.

Prialnik, D. and E. D. Rosenberg (Oct. 2009). "Can ice survive in main-belt comets? Long-term evolution models of comet 133P/Elst-Pizarro". In: *Monthly Notices of the Royal Astronomical Society: Letters* 399(1), pp. L79–L83.

Prialnik, D. and A. Bar-Nun (Nov. 1990). "Gas Release in Comet Nuclei". In: *The Astrophysical Journal* 363, p. 274.

Prialnik, D. and R. Merk (Sept. 2008). "Growth and evolution of small porous icy bodies with an adaptive-grid thermal evolution code. I. Application to Kuiper belt objects and Enceladus". In: *Icarus* 197(1), pp. 211–220.

Price, E. M. et al. (May 2021). "Ice-coated Pebble Drift as a Possible Explanation for Peculiar Cometary $CO/H_2O$ Ratios". In: *The Astrophysical Journal* 913(1), p. 9.

Raettig, N., H. Klahr, and W. Lyra (May 2015). "Particle Trapping and Streaming Instability in Vortices in Protoplanetary Disks". In: *The Astrophysical Journal* 804(1), p. 35.

Raymond, S. N., P. J. Armitage, and D. Veras (Mar. 2018a). "Interstellar Object 'Oumuamua as an Extinct Fragment of an Ejected Cometary Planetesimal". In: *The Astrophysical Journal Letters* 856(1), p. L7.

Raymond, S. N. and A. Izidoro (Nov. 2017). "Origin of water in the inner Solar System: Planetesimals scattered inward during Jupiter and Saturn's rapid gas accretion". In: *Icarus* 297, pp. 134–148.

Raymond, S. N., A. Izidoro, and A. Morbidelli (2020a). "Solar System Formation in the Context of Extrasolar Planets". In: *Planetary Astrobiology*. Ed. by V. S. Meadows et al., p. 287.

Raymond, S. N. et al. (Oct. 2009). "Building the terrestrial planets: Constrained accretion in the inner Solar System". In: *Icarus* 203(2), pp. 644–662.

Raymond, S. N. et al. (May 2018b). "Implications of the interstellar object 1I/'Oumuamua for planetary dynamics and planetesimal formation". In: *Monthly Notices of the Royal Astronomical Society* 476(3), pp. 3031–3038.

Raymond, S. N. et al. (Nov. 2020b). "Survivor Bias: Divergent Fates of the Solar System's Ejected versus Persisting Planetesimals". In: *The Astrophysical Journal Letters* 904(1), p. L4.

Reinhard, R. (Jan. 1982). "The Giotto mission to Halley's comet". In: *Advances in Space Research* 2(12), pp. 97–107.

Rickman, H., J. A. Fernandez, and B. A. S. Gustafson (Oct. 1990). "Formation of stable dust mantles on short-period comet nuclei". In: *Astronomy and Astrophysics* 237(2), pp. 524–535.

Rickman, H. et al. (Sept. 2008). "Injection of Oort Cloud comets: the fundamental role of stellar perturbations". In: *Celestial Mechanics and Dynamical Astronomy* 102(1-3), pp. 111–132.

Roberts, A. C. and M. A. Muñoz-Gutiérrez (Apr. 2021). "Dynamics of small bodies in orbits between Jupiter and Saturn". In: *Icarus* 358, p. 114201.

Rodgers, S. D. et al. (2004). "Physical processes and chemical reactions in cometary comae". In: *Comets II*. Ed. by M. C. Festou, H. U. Keller, and H. Weaver. University of Arizona Press, pp. 505–522.

Rosenberg, E. D. and D. Prialnik (Oct. 2007). "A fully 3-dimensional thermal model of a comet nucleus". In: *New Astronomy* 12(7), pp. 523–532.

Russell, H. W. (1935). "Principles of heat flow in porous insulators". In: *Journal of the American Ceramic Society* 18(1-12), pp. 1–5.

Safrit, T. K. et al. (Feb. 2021). "The Formation of Bilobate Comet Shapes through Sublimative Torques". In: *The Planetary Science Journal* 2(1), 14, p. 14.

Sarid, G. et al. (Sept. 2019). "29P/Schwassmann-Wachmann 1, A Centaur in the Gateway to the Jupiter-family Comets". In: *The Astrophysical Journal Letters* 883(1), p. L25.

Satorre, M. Á. et al. (Nov. 2008). "Density of $CH_4$, $N_2$ and $CO_2$ ices at different temperatures of deposition". In: *Planetary and Space Science* 56(13), pp. 1748–1752.

Satorre, M. Á. et al. (Feb. 2009). "Volatiles retained in icy surfaces dominated by CO $_2$ after energy inputs". In: *Planetary and Space Science* 57(2), pp. 250–258.

Schmitt, B. et al. (Dec. 1989). "Laboratory studies of cometary ice analogues." In: *Physics and Mechanics of Cometary Materials*. Ed. by J. J. Hunt and T. D. Guyenne. Vol. 302. ESA Special Publication, pp. 65–69.

Schorghofer, N. (July 2008). "The Lifetime of Ice on Main Belt Asteroids". In: *The Astrophysical Journal* 682(1), pp. 697–705.

Schorghofer, N. (Aug. 2010). "Fast numerical method for growth and retreat of subsurface ice on Mars". In: *Icarus* 208(2), pp. 598–607.

Schorghofer, N. (Sept. 2016). "Predictions of depth-to-ice on asteroids based on an asynchronous model of temperature, impact stirring, and ice loss". In: *Icarus* 276, pp. 88–95.

Schwamb, M. E. (Mar. 2014). "Solar System: Stranded in no-man's-land". In: *Nature* 507(7493), pp. 435–436.

Seiferlin, K. et al. (July 1996). "Line heat-source measurements of the thermal conductivity of porous H $_2$O ice, CO $_2$ ice and mineral powders under space conditions". In: *Planetary and Space Science* 44(7), pp. 691–704.

Seligman, D. Z. and G. Laughlin (June 2020). "Evidence that 1I/2017 U1 ('Oumuamua) was Composed of Molecular Hydrogen Ice". In: *The Astrophysical Journal Letters* 896(1), p. L8.

Seligman, D. Z. and A. Moro-Martin (Apr. 2023). "Interstellar Objects". In: *arXiv e-prints*, arXiv:2304.00568.

Seligman, D. Z. et al. (Dec. 2021). "A Sublime Opportunity: The Dynamics of Transitioning Cometary Bodies and the Feasibility of In Situ Obser-

vations of the Evolution of Their Activity". In: *The Planetary Science Journal* 2(6), p. 234.

Seligman, D. Z. et al. (July 2022). "The Volatile Carbon-to-oxygen Ratio as a Tracer for the Formation Locations of Interstellar Comets". In: *The Planetary Science Journal* 3(7), p. 150.

Sheppard, S. S. and C. A. Trujillo (Dec. 2016). "New Extreme Trans- Neptunian Objects: Toward a Super- Earth in the Outer Solar System". In: *The Astronomical Journal* 152(6), p. 221.

Sheppard, S. S. et al. (Apr. 2019). "A New High Perihelion Trans-Plutonian Inner Oort Cloud Object: 2015 TG387". In: *The Astronomical Journal* 157(4), p. 139.

Shoshany, Y., D. Prialnik, and M. Podolak (May 2002). "Monte Carlo Modeling of the Thermal Conductivity of Porous Cometary Ice". In: *Icarus* 157(1), pp. 219–227.

Shulman, L. M. (Mar. 2004). "The heat capacity of water ice in interstellar or interplanetary conditions". In: *Astronomy and Astrophysics* 416, pp. 187–190.

Sierks, H. et al. (Jan. 2015). "On the nucleus structure and activity of comet 67P/Churyumov-Gerasimenko". In: *Science* 347(6220), aaa1044, aaa1044.

Simon, A. et al. (Sept. 2019). "Entrapment of CO in $CO_2$ Ice". In: *The Astrophysical Journal* 883(1), 21, p. 21.

Simon, J. B. et al. (May 2016). "The Mass and Size Distribution of Planetesimals Formed by the Streaming Instability. I. The Role of Self-gravity". In: *The Astrophysical Journal* 822(1), p. 55.

Snodgrass, C. and G. H. Jones (Nov. 2019). "The European Space Agency's Comet Interceptor lies in wait". In: *Nature Communications* 10, p. 5418.

Snodgrass, C. et al. (Nov. 2017). "The Main Belt Comets and ice in the Solar System". In: *The Astronomy and Astrophysics Review* 25(1), p. 5.

Spohn, T. and J. Benkhoff (Oct. 1990). "Thermal history models for KOSI sublimation experiments". In: *Icarus* 87(2), pp. 358–371.

Spohn, T., K. Seiferlin, and J. Benkhoff (Dec. 1989). "Thermal conductivities and diffusivities of porous ice samples at low pressures and temperatures and possible modes of heat transfer in near surface layers of comets." In: *Physics and Mechanics of Cometary Materials*. Ed. by J. J. Hunt and T. D. Guyenne. Vol. 302. ESA Special Publication, pp. 77–81.

Steckloff, J. K., G. Sarid, and B. C. Johnson (Jan. 2023). "The Effects of Early Collisional Evolution on Amorphous Water Ice Bodies". In: *The Planetary Science Journal* 4(1), p. 4.

Steckloff, J. K. et al. (Dec. 2020). "P/2019 LD2 (ATLAS): An Active Centaur in Imminent Transition to the Jupiter Family". In: *The Astrophysical Journal Letters* 904(2), p. L20.

Steckloff, J. K. et al. (Mar. 2021). "The sublimative evolution of (486958) Arrokoth". In: *Icarus* 356, p. 113998.

Steiner, G. (Dec. 1990). "Two considerations concerning the free molecular flow of gases in porous ices". In: *Astronomy and Astrophysics* 240(2), pp. 533–536.

Steiner, G. and N. I. Kömle (Mar. 1991). "A model of the thermal conductivity of porous water ice at low gas pressures". In: *Planetary and Space Science* 39(3), pp. 507–513.

Stern, S. A. (Aug. 2003). "The evolution of comets in the Oort cloud and Kuiper belt". In: *Nature* 424(6949), pp. 639–642.

Sugita, S. et al. (Oct. 2005). "Subaru Telescope Observations of Deep Impact". In: *Science* 310(5746), pp. 274–278.

Sumarokov, V. V., P. Stachowiak, and A. JeŻowski (May 2003). "Low-temperature thermal conductivity of solid carbon dioxide". In: *Low Temperature Physics* 29(5), pp. 449–450.

Sumarokov, V. V. et al. (Mar. 2019). "The thermal diffusivity of molecular cryocrystals". In: *Low Temperature Physics* 45(343), pp. 391–394.

Swinkels, F. B. and M. F. Ashby (Feb. 1981). "A second report on sintering diagrams". In: *Acta Metallurgica* 29(2), pp. 259–281.

Tancredi, G. (July 1995). "The dynamical memory of Jupiter family comets." In: *Astronomy and Astrophysics* 299, pp. 288–292.

Tancredi, G. (Mar. 1998). "Chaotic dynamics of planet-encountering bodies". In: *Celestial Mechanics and Dynamical Astronomy* 70(3), pp. 181–200.

Tancredi, G., H. Rickman, and J. M. Greenberg (June 1994). "Thermochemistry of cometary nuclei I. The Jupiter family case." In: *Astronomy and Astrophysics* 286, pp. 659–682.

Tannehill, J. C., D. A. Anderson, and R. H. Pletcher (1997). *Computational Fluid Mechanics and Heat Transfer*. 2nd ed. Taylor & Francis. ISBN: 1-56032-046-X.

Tera, F., D. A. Papanastassiou, and G. J. Wasserburg (Apr. 1974). "Isotopic evidence for a terminal lunar cataclysm". In: *Earth and Planetary Science Letters* 22(1), pp. 1–21.

Thomas, L. H. (1949). "Elliptic problems in linear differential equations over a network". In: *Watson Sci. Comput. Lab. Rept., Columbia University, New York* 1, p. 71.

Thommes, E. W., M. J. Duncan, and H. F. Levison (Dec. 1999). "The formation of Uranus and Neptune in the Jupiter-Saturn region of the Solar System". In: *Nature* 402(6762), pp. 635–638.

Tiscareno, M. S. and R. Malhotra (Dec. 2003). "The Dynamics of Known Centaurs". In: *The Astronomical Journal* 126(6), pp. 3122–3131.

Torbett, M. V. (Oct. 1989). "Chaotic motion in a comet disk beyong Neptune : the delivery of short-period comets." In: *The Astronomical Journal* 98, pp. 1477–1481.

Tremaine, S. (Jan. 1993). "The distribution of comets around stars." In: *Planets Around Pulsars*. Ed. by J. A. Phillips, S. E. Thorsett, and S. R.

Kulkarni. Vol. 36. Astronomical Society of the Pacific Conference Series, pp. 335–344.

Trujillo, C. and S. S. Sheppard (Mar. 2014). "A Sedna-like body with a perihelion of 80 astronomical units". In: *Nature* 507(7493), pp. 471–474.

Tsiganis, K. et al. (May 2005). "Origin of the orbital architecture of the giant planets of the Solar System". In: *Nature* 435(7041), pp. 459–461.

Versteeg, H. and W. Malalasekera (2007). *An Introduction to Computational Fluid Dynamics - The Finite Volume Method*. 2nd ed. Pearson Education Limited. ISBN: 0-13-127498-8.

Vincent, J.-B. et al. (June 2019). "Local Manifestations of Cometary Activity". In: *Space Science Reviews* 215(4), p. 30.

Vokrouhlický, D., D. Nesvorný, and L. Dones (May 2019). "Origin and Evolution of Long-period Comets". In: *The Astronomical Journal* 157(5), p. 181.

Volk, K. and R. Malhotra (Nov. 2008). "The Scattered Disk as the Source of the Jupiter Family Comets". In: *The Astrophysical Journal* 687(1), pp. 714–725.

Walsh, K. J. et al. (July 2011). "A low mass for Mars from Jupiter's early gas-driven migration". In: *Nature* 475(7355), pp. 206–209.

Weidenschilling, S. J. (Aug. 2011). "Initial sizes of planetesimals and accretion of the asteroids". In: *Icarus* 214(2), pp. 671–684.

Weidenschilling, S. J. et al. (Aug. 1997). "Accretional Evolution of a Planetesimal Swarm". In: *Icarus* 128(2), pp. 429–455.

Weissman, P. R., J. Bottke W. F., and H. F. Levison (2002). "Evolution of Comets into Asteroids". In: *Asteroids III*. Ed. by W. F. Bottke et al. University of Arizona Press, pp. 669–686.

Weissman, P. R. and H. H. Kieffer (Sept. 1981). "Thermal modeling of cometary nuclei". In: *Icarus* 47(3), pp. 302–311.

Weissman, P. et al. (Jan. 2020). "Origin and Evolution of Cometary Nuclei". In: *Space Science Reviews* 216(1), p. 6.

Wetherill, G. W. (Jan. 1975). "Late heavy bombardment of the moon and terrestrial planets." In: *Lunar and Planetary Science Conference Proceedings* 2, pp. 1539–1561.

Whipple, F. L. (Mar. 1950). "A comet model. I. The acceleration of Comet Encke". In: *The Astrophysical Journal* 111, pp. 375–394.

Wiegert, P. and S. Tremaine (Jan. 1999). "The Evolution of Long-Period Comets". In: *Icarus* 137(1), pp. 84–121.

Wierzchos, K. and M. Womack (Apr. 2020). "CO Gas and Dust Outbursts from Centaur 29P/Schwassmann-Wachmann". In: *The Astronomical Journal* 159(4), p. 136.

Wierzchos, K., M. Womack, and G. Sarid (May 2017). "Carbon Monoxide in the Distantly Active Centaur (60558) 174P/Echeclus at 6 au". In: *The Astronomical Journal* 153(5), p. 230.

Williams, D. M. and D. Pollard (Jan. 2002). "Earth-like worlds on eccentric orbits: excursions beyond the habitable zone". In: *International Journal of Astrobiology* 1(1), pp. 61–69.

Wilson, J. K., J. Baumgardner, and M. Mendillo (Feb. 1998). "Three tails of comet Hale-Bopp". In: *Geophysical Research Letters* 25(3), pp. 225–228.

Womack, M., G. Sarid, and K. Wierzchos (Mar. 2017). "CO in Distantly Active Comets". In: *Publications of the Astronomical Society of the Pacific* 129(973), p. 031001.

Wyatt, M. C. et al. (Jan. 2017). "How to design a planetary system for different scattering outcomes: giant impact sweet spot, maximizing exocomets, scattered discs". In: *Monthly Notices of the Royal Astronomical Society* 464(3), pp. 3385–3407.

Wysoczańska, R., P. A. Dybczyński, and M. Królikowska (Jan. 2020). "First stars that could significantly perturb comet motion are finally found". In: *Monthly Notices of the Royal Astronomical Society* 491(2), pp. 2119–2128.

Yang, B. et al. (June 2021). "Discovery of Carbon Monoxide in Distant Comet C/2017 K2 (PANSTARRS)". In: *The Astrophysical Journal Letters* 914(1), p. L17.

Yang, C.-C., A. Johansen, and D. Carrera (Oct. 2017). "Concentrating small particles in protoplanetary disks through the streaming instability". In: *Astronomy and Astrophysics* 606, A80.

Yeomans, D. K. et al. (2004). "Cometary orbit determination and nongravitational forces". In: *Comets II*. Ed. by M. C. Festou, H. U. Keller, and H. Weaver, pp. 137–152.

Youdin, A. N. and J. Goodman (Feb. 2005). "Streaming Instabilities in Protoplanetary Disks". In: *The Astrophysical Journal* 620(1), pp. 459–469.

Zellner, N. E. B. (Sept. 2017). "Cataclysm No More: New Views on the Timing and Delivery of Lunar Impactors". In: *Origins of Life and Evolution of the Biosphere* 47(3), pp. 261–280.

Zhang, Q. et al. (June 2022). "Dust Evolution in the Coma of Distant, Inbound Comet C/2017 K2 (PANSTARRS)". In: *The Planetary Science Journal* 3(6), p. 135.

Zolensky, M. E. et al. (Dec. 2006). "Mineralogy and Petrology of Comet 81P/Wild 2 Nucleus Samples". In: *Science* 314(5806), p. 1735.

# List of Figures

# List of Tables